

**HIGHLY INTEGRATED THREE DIMENSIONAL MILLIMETER-WAVE
PASSIVE FRONT-END ARCHITECTURES USING SYSTEM-ON-
PACKAGE (SOP) TECHNOLOGIES FOR BROADBAND
TELECOMMUNICATIONS AND MULTIMEDIA/SENSING
APPLICATIONS**

A Dissertation
Presented to
The Academic Faculty

by

Jong-Hoon Lee

In Partial Fulfillment
of the Requirements for the Degree
Doctor of Philosophy in the
School of Electrical and Computer Engineering



Georgia Institute of Technology
August 2007

Copyright © 2007 by Jong-Hoon Lee

**HIGHLY INTEGRATED THREE DIMENSIONAL MILLIMETER-WAVE
PASSIVE FRONT-END ARCHITECTURES USING SYSTEM-ON-
PACKAGE (SOP) TECHNOLOGIES FOR BROADBAND
TELECOMMUNICATIONS AND MULTIMEDIA/SENSING
APPLICATIONS**

Approved by:

Dr. Manos M. Tentzeris, Advisor
Associate Professor, School of ECE
Georgia Institute of Technology

Dr. John Papapolymerou
Associate Professor, School of ECE
Georgia Institute of Technology

Dr. Joy Laskar
Professor, School of ECE
Georgia Institute of Technology

Dr. Kevin T. Kornegay
Professor, School of ECE
Georgia Institute of Technology

Dr. Chang-Ho Lee
Director, RF IC Design Center
Samsung Electro-Mechanics

Date Approved: June 4, 2007

ACKNOWLEDGEMENTS

First, I would like to express my most sincere gratitude and honor to my Lord, Jesus Christ. Since I met him personally, he has been always with me, strengthened me and helped me whenever I fear and am dismayed in my life. He has done it because of nothing but his fulfilled and unlimited love. And his love has driven me to his purpose for my life no matter how my being is reflected to him because he knows that his purpose is just perfect to me. Now I once again confess that Jesus Christ is everything to me and promised that I will run to you and live for you to glorify your name to the earth until my life is eventually given to you.

I would like to acknowledge the enthusiastic supervision of my research advisor, Professor Manos M. Tentzeris. He has motivated me to provide the excellence and the novelty in this research area and guided me to reach the outstanding outcomes in the most right way. For that, I am eternally grateful to him. In addition, my researches in the Georgia Tech could not be completed without the excellent guidance and the consistent help of Dr. Stephane Pinel. He was surely one of the amazing mentors, whom I ever met, both technically and mentally. I express my gratitude to Professor Joy Laskar and Professor John Papapolymerou for the great assistance they gave me regarding their technical discussion and guidance. I truly appreciate my ATHENA group members and multi-gigabit group members with respect to their significant impact on me in one and another way.

Finally, I sincerely acknowledge my parents, Woo-Jong Lee and Min-Ja Shin, my beloved wife, Hana Kim, and God's precious gifts, Eunice H. Lee and Eun-Hyool Lee, for their constant love, patience, trust, encouragement, hope, prayer, and, most of all, their beings just as they are. I love you all with all my heart.

TABLE OF CONTENTS

ACKNOWLEDGMENTS	iii
LIST OF TABLES	vii
LIST OF FIGURES	viii
LIST OF SYMBOLS AND ABBREVIATIONS	xiv
SUMMARY	xvi
 <u>CHAPTER</u>	
1: INTRODUCTION	1
2: BACKGROUND ON TECHNOLOGIES FOR MILLIMETER-WAVE PASSIVE FRONT-ENDS	14
2.1: 3D Integrated SOP Concept	14
2.2: LTCC Multilayer Technology	17
2.3: Integrated Cavity Structures	20
2.4: 60 GHz Transmitter/Receiver Modules	26
3: MICROSTRIP-TYPE INTEGRATED PASSIVES.....	30
3.1: Patch Resonator Filters and Duplexers	30
3.1.1: Single Patch Resonator	30
3.1.2: Duplexer (41 GHz/61 GHz)	37
3.1.3: Three- and Five-Pole Resonator Filters	43
3.2: Quasi-Elliptic Filter	49
4: CAVITY-TYPE INTEGRATED PASSIVES.....	56
4.1: Rectangular Cavity Resonator	56
4.2: Cavity Feeding Structures.....	60

4.2.1: Slot Excitation with a Shorting Via.....	60
4.2.2: Slot Excitation Using a $\lambda_g/4$ Open Stub.....	66
4.2.3: Probe Excitation.....	72
4.2.4: Discussion.....	76
4.3: Three-Pole Cavity Filters.....	79
4.4: Vertically Stacked Cavity Filters and Duplexers.....	86
4.4.1: Design of Cavity Resonator.....	86
4.4.2: Design of Three-Pole Cavity Bandpass Filter.....	88
4.2.3: Duplexer (60 GHz / 62.8 GHz).....	99
4.5: Cavity-Based Dual-Mode Filters.....	106
4.5.1: Dual-Mode Cavity Filters.....	107
4.5.1.1: Single Dual-Mode Cavity Resonator.....	107
4.5.1.2: Internal Coupling.....	109
4.5.1.3: External Coupling.....	113
4.5.1.4: Transmission Zero	114
4.5.1.5: Quasi-Elliptic Dual-Mode Cavity Filter.....	121
4.5.2: Multi-Pole Dual-Mode Cavity Filters.....	126
4.5.2.1: Quasi-Elliptic Filter with a Rectangular Slot.....	128
4.5.1.2: Quasi-Elliptic Filter with a Cross Slot.....	133
5: 3D ANTENNA ARCHITECTURES	136
5.1: Patch Antenna Using Soft-Surface Structure	136
5.1.1: Investigation of an Ideal Compact Soft Surface Structure.....	136
5.1.2: Implementation of the Soft-Surface Structure in LTCC.....	140
5.2: High-Gain Patch Antenna Using Soft-Surface Structure and Stacked Cavity.....	147

5.2.1: Antenna Structure Using a Soft-Surface and Stacked Cavity.....	147
5.2.2: Simulation and Measurement Results.....	151
5.3: Dual-Polarized Cross-Shaped Microstrip Antenna.....	155
5.3.1: Cross-Shaped Antenna Structure.....	155
5.3.2: Simulation and Measurement Results.....	156
5.4: Series-Fed Antenna Array.....	159
5.4.1: Antenna Array Structure.....	159
5.4.2: Simulation and Measurement Results.....	161
6: FULLY INTEGRATED 3D PASSIVE FRONT-ENDS	163
6.1: Passive Front-Ends for 60 GHz Time-Division Duplexing (TDD) Applications.....	163
6.1.1: Topologies.....	163
6.1.2: Performance Discussion	165
6.2: Passive Front-Ends for 60 GHz Frequency-Division Duplexing (FDD) Applications.....	165
6.2.1: Topologies.....	166
6.2.2: Performance Discussion	170
7: CONCLUSIONS.....	173
REFERENCES	179

LIST OF TABLES

Table 1: Material comparison	7
Table 2: Design Parameters of Cavity Resonators using three different excitation techniques (1. slot excitation with a shorting vis, 2.slot excitation with an open stub, 3.Probe Excitation).....	77
Table 3: Comparison of measured results of three different excitation techniques (1. slot excitation with a shorting vis, 1.slot excitation with an open stub, 3.Probe Excitation).....	77
Table 4: Design parameters of three-pole cavity filter using an open stub	85
Table 5: Design Parameters of Cavity Resonators	97
Table 6: Design Parameters of Cavity Duplexers	103
Table 7: Performance of Cavity Duplexers	105
Table 8: Total phase shifts for two different paths in the dual-mode cavity filter	117
Table 9: Design parameters of quasi-elliptic dual-mode cavity filters	125
Table 10: Total phase shifts for three different signal paths in the vertically stacked dual-mode cavity filter with a rectangular slot	130
Table 11: Design parameters of multi-pole dual-mode cavity filters with two types of inter- coupling slots	131
Table 12: Total phase shifts for three different signal paths in the vertically stacked dual-mode cavity filter with a cross slot	134

LIST OF FIGURES

Figure 1: (a) 3D integrated module concept view (b) Rx and Tx board block diagram	16
Figure 2: Geometry of a rectangular cavity [46]	21
Figure 3: Field patterns for (a) TE, and (b) TM modes in a rectangular cavity [46]	24
Figure 4: (a) Fabricated dielectric waveguide filter with CPW input and output ports (b) Filter mounted in the ceramic package. The metal cover is attached on the filter [47]	25
Figure 5: Top view of (a) conventional $\lambda/2$ square patch (b) Miniaturized patch resonator	31
Figure 6. Side view of 60GHz slotted patch resonator	31
Figure 7: The photograph of the fabricated filters with coplanar waveguide (CPW) pads at 60 GHz	31
Figure 8: Simulated responses of center frequency (f_0) and insertion loss ($ S_{21} $) as a function of transverse cut (L_{cl})	32
Figure 9: Simulated 3-dB bandwidth as function of Overlap distance of 60 GHz slotted patch resonator	34
Figure 10: Measured and simulated S-parameters of 60 GHz slotted patch resonator	35
Figure 11: Side view of 39 GHz slotted patch resonator	36
Figure 12: Measured and simulated S-parameters of 39 GHz slotted patch resonator	37
Figure 13: Top view of the dual-band compact duplexer	38
Figure 14: Side view of the dual-band compact duplexer	38
Figure 15: Photograph of the fabricated duplexer	40
Figure 16: Measured and simulated insertion loss for both channels of duplexer	41
Figure 17: Measured and simulated return loss for both channels of duplexer	42
Figure 18: Measured and simulated channel to channel isolation	42
Figure 19: The top view of (a) three-pole slotted patch bandpass filter (b) five-pole slotted patch bandpass filter	43

Figure 20: The side view of (a) three-pole slotted patch bandpass filter (b) five-pole slotted patch bandpass filter	44
Figure 21: (a) External quality factor (Q_{ext}) evaluated as a function of overlap distance (L_{over}) (b) Coupling coefficient, k_{12} , as a function of coupling spacing (d_{12}) between 1 st resonator and 2 nd resonator	45
Figure 22: Measured and simulated S-parameters of three-pole slotted patch bandpass filter ...	46
Figure 23: Measured and simulated S-parameters of five-pole slotted patch bandpass filter	48
Figure 24: (a) Top view and (b) cross-section view of 4-pole quasi-elliptic bandpass filter consisting of open-loop resonators fabricated on LTCC. All dimensions indicated in (a) are in μm	50
Figure 25: Design curve (a) Magnetic coupling. (b) Electric coupling. (c) Mixed coupling. (d) External quality factor	52
Figure 26: The comparison between measured and simulated S-parameters (S_{21} & S_{11}) of the four-pole quasi-elliptic bandpass filter composed of open-loop resonators	54
Figure 27: Cavity resonator utilizing via fences as side walls	56
Figure 28: LTCC cavity resonator employing slot excitation with a shorting via (a) top view of feeding structures, (b) 3D overview and (c) side view of the proposed resonator	61
Figure 29: (a) Electric field distribution and (b) Magnetic field distribution inside the cavity (<i>substrate 2-4</i> in Fig. 28 (c)) using shorting vias at resonant frequency (=59.4 GHz) (c) Electric field distribution of the top substrate layer (<i>substrate 1</i> in Fig. 28 (c))	63
Figure 30: The photograph of the fabricated cavity resonator using slot excitation with a shorting via	64
Figure 31: The comparison between measured and simulated S-parameters (S_{11} & S_{21}) of a cavity resonator using slot excitation with a shorting via	65
Figure 32: LTCC cavity resonator employing slot excitation with an open stub (a) the top view of feeding structure (b) the side view of the proposed resonator	67
Figure 33: (a) Electric field distribution inside the cavity using slot excitation with an open stub at resonant frequency (=59.2 GHz) (b) Electric field distribution of the top substrate layer (<i>substrate 1</i> in Fig. 32 (b))	68
Figure 34: The photograph of the fabricated cavity resonator using slot excitation with an open stub	69
Figure 35: S-parameters (S_{11} & S_{21}) of a resonator using slot excitation with an open stub (simulation with $\epsilon_r = 5.4$ vs. measurement)	70

Figure 36: S-parameters (S11 & S21) of a resonator using slot excitation with an open stub (simulation with $\epsilon_r = 5.5$ vs. measurement)	71
Figure 37: LTCC cavity resonator employing probe excitation: (a) top view of feeding structure (b) side view of the proposed resonator	73
Figure 38: (a) Electric field distribution inside the cavity using probe excitation at resonant frequency (=59.8 GHz) (b) Electric field distribution of the top substrate layer (substrate 1 in Fig. 37 (b))	74
Figure 39: The photograph of the fabricated cavity resonator using probe excitation	75
Figure 40: The comparison between measured and simulated S-parameters (S11 & S21) of a cavity resonator using probe excitation	76
Figure 41: LTCC 3-pole cavity bandpass filter employing slot excitation with an open stub: (a) 3D overview, (b) side view of the proposed filter	79
Figure 42: The comparison between measured and simulated S-parameters (S11 & S21) of 0.5 mm-height cavity resonator using slot excitation with an open stub	80
Figure 43: (a) External quality factor (Q_{ext}) evaluated as a function of external slot width (SW_{ext}) (b) Inter-resonator coupling coefficient (k_{jj+1}), as a function of internal slot width (SW_{int})	82
Figure 44: The comparison between measured and simulated (a) S21 and (b) S11 of three-pole cavity bandpass filter using slot excitation with an open stub	84
Figure 45: The 3D overview of LTCC cavity resonator employing slot excitation with microstrip feedlines on the different metal layers (<i>metal 1 and 4</i>)	86
Figure 46: (a) 3D overview (b) sideview of the vertically stacked three-pole cavity bandpass filter. (c) top view of the feeding structure (d) top view of the inter-resonator coupling structure	90
Figure 47: External quality factor (Q_{ext}) evaluated as a function of external slot length (SL)	91
Figure 48: (a) Two characteristic frequencies (f_{p1}, f_{p2}) of the coupled cavities to calculate the internal coupling coefficients (k_{jj+1}) (b) Inter-resonator coupling coefficient (k_{jj+1}), as a function of internal slot length (CL)	92
Figure 49: (a) 3D overview of vertically stacked 3-pole cavity bandpass filter with CPW pads and vertical transitions. (b) The photograph of the cavity bandpass filter fabricated on LTCC	94
Figure 50: The comparison between measured and simulated S-parameters (S11 & S21) of Rx 3-pole cavity band filter (a) measurement vs. simulation with $\epsilon_r = 5.4$ and originally designed cavity size ($1.95 \times 1.284 \times 0.1 \text{ mm}^3$) (b) measurement vs. simulation with $\epsilon_r =$	

5.5 and modified cavity size ($2.048 \times 1.348 \times 0.1 \text{ mm}^3$)	95
Figure 51: The comparison between measured and simulated S-parameters (S11 & S21) of Tx three-pole cavity band filter (simulation with $\epsilon_r = 5.5$ and modified cavity size ($2.048 \times 1.266 \times 0.1 \text{ mm}^3$) vs. measurement)	98
Figure 52: (a) 3D overview (b) top view of the proposed LTCC cavity duplexers using microstrip T-junction	100
Figure 53: (a) S21 response in the 1 st channel of the duplexer (measurement vs. simulation with $\epsilon_r = 5.5$ and modified cavity size ($2.048 \times 1.354 \times 0.1 \text{ mm}^3$)) (b) S31 response in the 2 nd channel of the duplexer (measurement vs. simulation with $\epsilon_r = 5.5$ and modified cavity size ($2.048 \times 1.261 \times 0.1 \text{ mm}^3$))	102
Figure 54: (a) S11 response of the duplexer (measurement vs. simulation with $\epsilon_r = 5.5$ and modified cavity sizes) (b) Measured S32 response in the isolation between the 1 st and 2 nd channels	104
Figure 55: (a) The 3D overview (b) The top view of a quasi-elliptic dual-mode single cavity filter	108
Figure 56: Magnitude of electric field distribution (TE_{102}) on horizontal plane inside the dual-mode cavity at the resonant frequency ($=62.9 \text{ GHz}$) (a) when $C_o = 0 \text{ mm}$ (b) when $C_o = 0.6 \text{ mm}$	110
Figure 57: (a) Magnetic vector of the odd mode (b) Magnetic vector of the even mode	111
Figure 58: Internal coupling coefficient k_{jj+1} as a function of the centerline offset C_o of the feeding structures	112
Figure 59: External quality factor Q_{ext} evaluated as a function of external slot length E_L	114
Figure 60: (a) Equivalent circuit model of the quasi-elliptic dual-mode cavity filter (b) Multi-coupling diagram for the quasi-elliptic dual-mode cavity filter	115
Figure 61: The simulated $S21$ parameter response of a dual mode filter as a function of the centerline offset C_o of the feeding structures	118
Figure 62: Simulated responses of (a) 3-dB bandwidth and (b) center frequency f_c as a function of the centerline offset C_o of the feeding structure	119
Figure 63: The simulated $S21$ parameter response of a dual mode filter as a function of the source-to-load distance D_s	121
Figure 64: Measured and simulated S-parameters of the dual-mode cavity filter for a Rx channel	122

Figure 65: (a) Simulated S-parameters of the dual-mode cavity filter using equivalent-circuit model in Fig. 60 (a). (b) Measured and simulated S-parameters of the dual-mode cavity filter for a Tx channel	124
Figure 66: (a) The 3D overview (b) The top view of a vertically stacked multi-pole dual-mode cavity filter (c) Inter-coupling rectangular slot (d) Inter-coupling cross slot.....	127
Figure 67: Multi-coupling diagram for the vertically stacked multi-pole dual-mode cavity filter with rectangular slot for inter-coupling between two cavities	124
Figure 68: Measured and simulated S-parameters of the quasi-elliptic dual-mode cavity filter with a rectangular slot for inter coupling between cavities	127
Figure 69: Multi-coupling diagram for the vertically stacked multi-pole dual-mode cavity filter with rectangular slot for inter-coupling between two cavities	134
Figure 70: Measured and simulated S-parameters of the quasi-elliptic dual-mode cavity filter with a rectangular slot for inter coupling between cavities	135
Figure 71: Patch antenna surrounded by an ideal compact soft surface structure which consists of a ring of metal strip and a ring of shorting wall (I_s =the surface current on the top surface of the soft surface ring, Z_s =the impedance looking into the shorted metal strip)	137
Figure 72: Simulated electric field distributions on the top surface of the substrate for the patch antennas with and without the soft surface ($\epsilon_r = 5.4$)	138
Figure 73: Layout and prototype of a stacked-patch antenna surrounded by a compact soft surface structure implemented on LTCC technology	141
Figure 74: Comparison of return loss between simulated and measured results for the stacked-patch antennas with and without the soft surface implemented on LTCC technology	143
Figure 75: Comparison between simulated and measured radiation patterns for the stacked-patch antennas with and without the soft surface implemented on LTCC technology ($f_0=17$ GHz)	146
Figure 76: (a) The 3D overview (b) cross-section view (c) cross-section view of a patch antenna with the soft surface and sacked cavity	144
Figure 77: Comparison of return loss between simulated and measured results for a patch antenna with the soft surface and the stacked cavity implemented on LTCC technology	146
Figure 78: The radiation characteristics at 61.5 GHz of patch antennas (a) with the soft surface and (b) with the soft surface and the stacked cavity	152

Figure 79: Comparison of simulated and measured gains at broadside between the stacked-patch antennas with and without the soft surface implemented on LTCC technology	153
Figure 80: Cross-Shaped Antenna Structure in LTCC	156
Figure 81: (a) Simulated and (b) measured S-Parameter data versus frequency	157
Figure 82: (a) Top view and (b) cross-section view of a series fed 1×4 linear array of four microstrip patches. All dimensions indicated in (a) are in mm	155
Figure 83: Measured and simulated return loss (S11) at 61.5 GHz of the series fed 1×4 antenna array	156
Figure 84: Simulated radiation patterns at 61.5 GHz of the series fed 1×4 antenna array	157
Figure 85: (a) Top view and (b) cross-section view of a series fed 1×4 linear array of four microstrip patches. All dimensions indicated in (a) are in mm	164
Figure 86: The comparison between measured and simulated return loss (S11) of the integrated filter and antenna functions	165
Figure 87: (a) 3D overview and (b) cross-section view of the 3D integration of the filters and antennas using LTCC multilayer technologies	167
Figure 88: The photograph of the top view of the integrated function of Rx/Tx cavity filters and cross-shaped patch antenna with the air cavity top	169
Figure 89: The comparison between measured and simulated return loss (a) S11 of the 1 st channel (b) S22 of the 2 nd channel	171
Figure 90: The measured channel-to-channel isolation (S21) of the integrated structure	172

LIST OF SYMBOLS AND ABBREVIATIONS

2D	Two Dimensional
2.5D	Two and Half Dimensional
3D	Three Dimensional
Ag	Silver
Al ₂ O ₃	Aluminum Oxide
BGA	Ball Grid Array
CAD	Computer-aided Design
CMOS	Complementary Metal-Oxide Semiconductor
CPW	Coplanar Waveguide
EBG	Electromagnetic Band-Gap
EIRP	Equivalent Isotropically Radiated Power
EM	Electromagnetic
FCC	Federal Communications Commission
FEM	Finite Element Method
FET	Field Effect Transistor
GSM	Global System of Mobile Communications
GaAs	Gallium Arsenide
HFSS	High Frequency System Simulator
HTCC	High Temperature Co-Fired Ceramic
IC	Integrated Circuit
InP	Indium Phosphide
I/O	Input/Output
ISM	Industrial-Scientific-Medical
ISS	Impedance Standard Substrates
Ku-Band	11 GHz -18 GHz
LCP	Liquid Crystal Polymer
LCRN	Local Cellular Radio Networks
LNA	Low Noise Amplifier
LRRM	Line-Reflect-Reflect-Match
LTCC	Low Temperature Co-fired Ceramic
LTTC-M	Low Temperature Co-Fired Ceramics on Metal
L-Band	390 MHz – 1.55 GHz
μBGA	Micro Ball Grid Array
MCM	Multi-Chip Module
MEMS	Micro-Electro-Mechanical Systems
MLO	Multilayer Organic
MMIC	Monolithic Microwave Integrated Circuit
Mo	Molybdenum
MoM	Method of Moments
PBG	Periodic Bandgap
PCS	Personal Communication Services
pHEMT	Pseudomorphic High Electron Mobility Transistor

RF	Radio Frequency
Q	Quality Factor
Q_{ext}	External Quality Factor
Q_l	Loaded Quality Factor
Q_u	Unloaded Quality Factor
Rx	Receiver
S-Band	2 – 4 GHz
SiGe	Silicon Germanium
SIP	System-in-a-Package
SMA	SubMiniature version A
SMD	Surface Mount Device
SOLT	Short, Open, Load, and Thru
SOC	System-on-Chip
SOP	System-on-Package
T/R	Transmitter/Receiver
TE	Transverse Electric
TM	Transverse Magnetic
TOS	Tape on Substrate
Tx	Transmitter
V-Band	55 – 65 GHz
VCO	Voltage Control Oscillator
W	Tungsten
WLAN	Wireless Local Area Networks
WPAN	Wireless Personal Area Networks
X-band	8 – 12 GHz

SUMMARY

The objective of the proposed research is to present a compact system-on-package (SOP)-based passive front-end solution for millimeter-wave wireless communication/sensor applications, that consists of fully integrated three dimensional (3D) cavity filters/duplexers and antenna. The presented concept is applied to the design, fabrication and testing of V-band transceiver front-end modules using multilayer low temperature co-fired (LTCC) technology.

The millimeter-wave front-end module is the foundation of 60 GHz (V-band) wireless systems for short-range multimedia applications, such as high-speed internet access, video streaming and content download. Its integration poses stringent challenges in terms of high performance, large number of embedded passive components, low power consumption, low interference between integrated components and compactness. To overcome these major challenges, a high level of integration of embedded passive functions using low-cost and high-performance materials that can be laminated in 3D, such as the multilayer LTCC, is significantly critical in the module-level design.

In this work, various compact and high-performance passive building blocks have been developed in both microstrip and cavity configurations and their integration, enabling a complete passives integration solution for 3D low-cost wireless millimeter-wave front-end modules. It is worthy to note that most of the designs implemented comes away with novel ideas and is presented as the first extensive state-of-art components, entirely validated by measured data at 60 GHz bands.

CHAPTER 1

INTRODUCTION

The rapid growth of wireless local area and personal communication networks, as well as sensor applications, has led to a dramatic increase of interest in the regimes of radio frequency (RF)/microwave/millimeter-wave systems [1]. Especially, the 60 GHz band is of much interest since this is the band in which massive amounts of spectrum space (7 GHz) have been allocated worldwide for dense wireless local communications [2]. There are a number of multimedia applications for short-range communications such as high-speed internet access, video streaming, content downloads, and wireless data bus for cable replacement [3]. Such emerging applications with data rate greater than 2 Gb/s require real estate efficiency, low-cost manufacturing, and excellent performance achieved by a high level of integration of embedded functions [2]. However, the band around 60 GHz has been limited in use based on the difficulties associated with traditional radio propagation models and the cost of producing commercial products. Since the mid-90's, many examples of monolithic-integrated circuit (MMIC) chipset have been reported for 60 GHz radio applications using Gallium Arsenide (GaAs) Field Effect Transistor FET and Indium Phosphide (InP) Pseudomorphic High Electron Mobility Transistor (pHEMT) technologies [2]. Despite their commercial availability and their outstanding performance, these technologies struggle to enter the market because of their prohibitive cost and their limited capability to integrated advanced base-band processing. The combination of a low-cost highly producible module technology, featuring low loss, and embedded passive functions is required to enable a commercial use of the 60 GHz systems.

Considering the importance of the above-mentioned new applications at 60 GHz, a paradigm change in the system integration of millimeter-wave applications from high budgets

and low volumes toward to low costs and high volumes is underway. With respect to millimeter-wave front-end, this leads to great challenges for both transceiver circuitry and antenna. Today's packaging technology of complex RF products based on traditional Chip & Wire approach on the single-layer structured ceramics and soft substrates assembled into metallic boxes with complex geometrics, hermetic sealing and ceramic coaxial feedthroughs cannot be the answer for high-volume production.

A complete reformation of this issue leads to the so-called 3D SOP concept [1], wherein the traditional approach with sub-unit substrate is replaced by a common package base architecture with a common multilayer substrate. This approach takes advantage of the passive integration, especially eliminating the individual passive components packages which usually occupy the 90% of the system. Using SOP, the passive elements are converted to bare, thin-film components only micrometers thick and embedded into the multilayer system package. Such thin-film components can be scaled anywhere from a thousandth to a millionth of their original packaged size [34]. Further, we can eliminate the bulky integrated circuit (IC) packages, too, by embedding their base chips in the SOP package [1]. In addition, the 3D integration, combining multiple layers of planar devices with a high density of both in-plane and out-of-plane interconnects, is a promising approach to extending performance improvements beyond devices and interconnect scaling limits [85]. The 3D integration provides high device integration density, high interconnectivity, reduction of long global wires and their power consumption, and novel compact architectures. By layer stacking and having functional connectivity in the vertical direction, 3D integration can provide excellent functionality in a small footprint with reduced wiring lengths, thus reducing interconnect-driven signal delay and power consumption. Since the concept of 3D integration was first introduced in the 1980s [86]-[89], several 3D fabrication

techniques (sequential [86]-[89], parallel [90], multilayer with buried structure (MLBS) [85]) have been demonstrated to realize 3D ICs. Also, 3D integration of microprocessors and memories (SRAM and DRAM) allows larger on-chip memory and on-chip interconnects, thus allowing substantial performance improvement in system due to improved memory hierarchy [91]. However, past 3D integration researches are still based on relatively low-density hybrid assembly technologies.

For more than 40 years, circuit designers have counted on the steady increase in transistor density in their pursuit of convergence. For example, engineers at Texas Instruments are building entire signal-processing subsystems with diverse functions on a chip of silicon, which is called a system-on-chip or SOC. However, a SOC has its technical problems if digital logic and memory for computation must be combined with analog and RF communications circuitry, specifically, on a single piece of silicon. These dissimilar circuits not only operate at different voltages but also require different processing steps during manufacturing. As a result, design and complexity, along with fabrication costs and time to market, can increase. With SOP, we are not limited to any particular technology. Therefore, the time it takes to design and fabricate a system is much shorter than before, and time to market is shorter as well. Also, SOP with its multi-functions will be more compact than the bulky package of an SOC, which cannot combine nearly as many technologies as we can. To build a highly integrated package for a mixed-signal, multifunction system, IBM's multi-chip module (MCM) technology was proposed with copper wiring for interconnecting ICs twenty years ago. The advent of the MCM offered an alternative to the restrictions of integrating components on the same chip by integrating multiple ICs (optical, radio frequency (RF), and digital) on a substrate using ball grid arrays (BGAs). This system approach alleviates issues of crosstalk between ICs by allowing the chips to perform their

functions independent of each other. However, MCM has no embedded thin-film components as does an SOP and requires a system board, resulting in a relatively bulky system. As another miniaturization technique for a system package, the system-in-a-package (SIP) was introduced approximately a decade ago. In SIP approach, bare or packaged IC chips are stacked on top of each other in a 3D arrangement that allows more compact modules to be produced. But SIP still employs the bulky passive components and must plug into a traditional system board. SOP allows the reduction of the overall substrate area required and a lower number of interfaces (lower loss). It also enables integration of matching structures, lumped and distributed passives, and antennas that is the so-called passive integration. Advantages of integrated passives over surface mount devices are (1) improved package efficiency (2) improved electrical high-frequency performance due to the reduced parasitics, leading to better performance or lower power consumption (3) elimination of a separate package for passives yielding the lower cost, reduced profile and weight (4) no assembly to board and thus reduced cost (5) improved reliability due to reduced solder joint failures. Integration of RF elements with digital and low-frequency analog circuits on the same substrate is also essential to reduce the overall cost and physical dimensions of the entire system. The proposed approach also opens the perspective to integrate micro-electro-mechanical systems (MEMS) circuits.

Despite its inherent advantages, passive integration has received only limited application in mass production [4]. A major obstacle to passive integration is identifying a suitable technology, which can encompass both the rich variety of passive component types required and cope with their scattered placement in an application. In common, a passive integration technology is built up from a multi-layer stack of a limited number of similar layers, which inherently limits the range passive component performance can be integrated. As an example, a dielectric layer with

a particular specific capacitance density typically allows two to three decades of integrated capacitor value to be covered before it becomes either too small for the process technology or too large to be economically viable. The capacitance tolerance is a function of the process control of the dielectric layer and cannot be improved by component selection as with low tolerance surface mount device (SMD) components. Only a limited range of passive component types and values can be efficiently integrated in any passive integration technology. It follows that different technologies are suited for different applications depending on the match between the integrated passive component capability and requirement.

In passive integration, an integrated antenna into transmitter/receiver (T/R) module is a very interesting alternative for applications where compact, low cost and high volume are important factors. However, integration of antennas or antenna arrays in a single substrate module is usually difficult because technological requirements driven by their performance characteristics (radiation efficiency, bandwidth) are opposite to those of non-radiation systems, where radiation effects are undesirable. Present solutions of T/R systems with antennas are mainly hybrid integration. They are bulky, often demand waveguides and introduce extra parasitics at the transition between antenna and transceiver. Monolithic integration of planar antennas in a few millimeter-size MMICs was also shown to be possible above approximately 60 GHz [5]-[7]. It provides the possibility of reduced interconnect parasitics, small size and light weight. Nevertheless, it is expensive and causes parasitic radiating coupling between antenna and circuit because of very limited space available. Larger arrays are also impossible due to the same reason. The high dielectric constants of MMIC semiconductor materials imply that the surface waves are more easily triggered in the substrate, thus, generally deteriorating antenna radiation properties, especially radiation efficiency.

To overcome the limitations and drawbacks mentioned above, the active researches of materials and process in packaging area have been performed. Both ceramic and organic technologies are candidates for the 3D integration of miniaturized RF/microwave/millimeter-wave systems. LTCC has been widely used as a packaging material because of its process maturity/stability and its relatively high dielectric constant that enables a significant reduction in the module/function dimensions. The very mature 3D multilayer fabrication capabilities of LTCC up to as many as metal layers make LTCC attractive for 3D integrated embedded components such as filters and antennas in a compact and cost-effective manner to meet millimeter-wave design requirements [8]. Although it has gained more popularity in RF module implementation, LTCC suffers from a couple of main drawbacks such as the shrinkage of ceramic tapes during firing process and a coarse metal definition. More details will be discussed in section 2.2. As an alternative, liquid crystal polymer (LCP) is an organic material that offers a unique combination of electrical, chemical, and mechanical properties, enabling high-frequency designs due to its ability to act as both the substrate and the package for flexible and conformal multilayer functions [8]. It is a fairly new, low-cost thermoplastic material, and its performance as an organic material is comparable to ceramic-based substrates that are widely used in RF and microwave applications (Table 1) [9].

LCP offers a large area processing capability that leads to tremendous cost reduction compared to LTCC substrates. Using vertical space allows the passive elements in RF front-ends to be efficiently integrated. However, processing challenges such as LCP-metal adhesion, bond registration and vias processing have delayed widespread LCP implementation in packaging area, compared to relatively mature and stable LTCC technology.

Table 1: Material comparison.

	FR4	LTCC	LCP
ϵ_r	4	3.9-9.1	2.9-3.2
$\tan \delta$	0.025	0.0012-0.0063	0.002-0.0045
CTE	15-20	3.4-7	3-17
Cost	Very Low	Low/Medium	Low

The development of multilayer substrates makes it possible to bring the concept of 3D integration into RF systems implementation to meet the stringent needs in wireless communication area. The 3D integration approach using multilayer LTCC technologies has emerged as an attractive solution for these systems because of its high level of compactness and mature multilayer fabrication capability. Numerous publications [10] – [18] have dealt with the development of 3D LTCC passive components for lower microwave frequency range than millimeter-wave frequencies. A compact functional 14 GHz LTCC-based transmitter module has featured an integrated stripline filter for Ku-band applications [15]. In addition, LTCC packaged ridge waveguide filters have been modeled via the mode-matching method and have proven the feasibility of the 3D filter embedding in the LTCC package with experimental verification [18]. However, recently reported structures occupy large real estate without any miniaturization mechanism applied, while being hardly scalable to millimeter-wave dual-band, wideband, or multiplexing applications. On-package integrated cavity filters using LTCC multilayer technology are a very attractive option for 3D RF front-end modules up to the millimeter-wave frequency range because of their relatively high quality factor (Q) compared to

stripline/microstrip [19]-[20] or lumped element type filters [21]. The 3D low-loss and high-Q resonators/bandpass filters utilizing electromagnetic band-gap (EBG) substrates and micromachined technology have been developed with a great potential to be integrated into the modules. In particular, the recent development of duroid-based EBG cavity resonators and filters [22]-[23] has demonstrated the advantages of implementing EBG instead of fully conducting metals [24] as side walls in terms of reconfigurability and inexpensive mass production. The idea of using rows of stacked vias as side walls has been applied to produce high unloaded quality factor (Q_u) (over 1000) cavity resonators at Ku-band [25] and low-loss quasi-planar two-pole filters based on capacitive loaded cavities at Q-band [26] using LTCC technology. Also, narrow-band two-pole filters, which can be embedded inside packaging, have been implemented in LTCC by employing capacitive loading techniques at X-band [27].

However, there have been a few researches above 50 GHz undertaken worldwide in multi-chip module technology leading to comprehensive feasibility study of a SOP concept for the V-band. The reason is that short wavelengths and increased reflections at discontinuities require a technology with very tight tolerance. For V-band applications, planar alumina waveguide filters with coplanar waveguide (CPW) input/output (I/O) ports have exhibited low insertion loss (<3dB) and good stop-band rejection [28]. A bandpass filter composed of three harmonic cavity resonators has been demonstrated with great integration potential for V-band applications [10]. However, those devices occupy large real estate because of the two dimensional (2D) arrangement of the resonators.

With the development of the passive components, the optimal integration of RF passives including duplexers and antennas into 3D 60 GHz front-end module is significantly challenging since the electrical performance can be degraded by severe parasitic, interconnection and

radiation losses. Also, the stringent isolation requirement between receiver (Rx) and transmitter (Tx) channel signals of 60 GHz transceivers requires the design of a highly integrated duplexer consisting of on-package low-loss, narrow-band and high-selectivity filters. The duplexer not only serves as a 3D interconnect between the T/R MMIC chipsets and the antenna, but also as an effective means to minimize the level of the interference between two channels. The development of 60 GHz-band modules for stringent system specifications has been demonstrated in a SIP transmitter integrating LTCC patch arrayed antennas [29] and compact wireless transceiver modules for Gigabit data-rate transmission [30]-[32]. However, the previously reported transmitter and receiver modules could suffer from the spurious and image signals because only antennas are integrated into modules without using any band-select filters or duplexers in passive front-ends. Moreover, two separate antennas for the Tx and Rx channels are used and occupy large area, which contradicts the size requirements of compact 60 GHz modules.

On the basis of the above analysis, the three objectives underlying this thesis can be formulated as follows:

1. To develop the complete library of the 3D filters and duplexers in both microstrip and cavity configurations for compact, low-cost, and high-performance millimeter-wave front-end modules using LTCC technologies.
2. To develop 60 GHz compact, high-data rate, high-gain, and directive antennas with the array configurations or innovative radiation improvement techniques.
3. To present the complete 3D integration of all passive building blocks such as the cavity duplexers and the antennas developed, enabling the complete passive front-end solution for compact 3D 60 GHz-band transceiver modules.

This dissertation is organized as follows:

As a starting point, today's available, state-of-art integration and passive technologies, that could be taken into account as candidates for the realization of millimeter-wave modules, are summarized in chapter 2. Their brief historical background and fundamental theory are thoroughly discussed, specifically addressing their potential to realize the passive front-end modules in V-band. A set of the considered technologies includes SOP, LTCC, integrated cavities, and T/R modules.

Chapter 3 focuses on the development of 3D fully integrated microstrip filters, enabling a complete passive solution for compact, low-cost, wireless, front-end modules to be used in millimeter-wave frequency ranges. In order to realize compact and highly integrated bandpass filters, the performance of single-mode, slotted, patch resonators is first investigated at two operating frequencies (59.3GHz, 38.6GHz). After ensuring their excellent performance based on simulated and experimental results, one compact multilayer duplexer, which uses a via junction as a common input, has been realized to cover two bands (39.8 GHz/ 59GHz) for dual-band mobile communication systems, such as wireless radio local area networks (WLAN) or local cellular radio networks (LCRN) [3]. To provide a wide bandwidth, a novel compact geometry of three- and five-pole bandpass filters has been implemented by cascading single-mode patch resonators on different layers with optimized inter-resonator coupling separation. Also, we discuss the development of a four-pole cross-coupled quasi-elliptic filter, targeting high selectivity and compactness.

In chapter 4, we present the extensive report, entirely validated by measured data on low-loss cavity resonators, three-pole bandpass filters and duplexers that can be the other candidates of a complete passive solution for 3D, compact, low-cost, wireless, front-end modules in LTCC at 60 GHz. First, the performance of the three topologies of cavity feeding structures (slot

excitation with a shorting via, slot excitation with a $\lambda_g/4$ open stub, probe excitation) is comparatively evaluated in terms of S-parameters, bandwidth, external coupling (Q_{ext}), Q_u , and fabrication accuracy/simplicity based on electromagnetic simulations and experimental results. Details of the design procedure of each technique are discussed. After ensuring the performance of the excitation techniques at V-band, the strongly coupled, cavity resonator excited by a $\lambda_g/4$ open stub is developed. Two types of the 3D, three-pole, bandpass filters have been implemented by vertically deploying three identical cavity resonators coupled together with moderate external and inter-resonator couplings for 60GHz, WLAN applications. The presented cavity bandpass filters are applied to the design, fabrication and testing of V-band (Rx: 59-61.5 GHz, Tx: 61.5-64GHz) transceiver front-end module using multilayer LTCC technology. Vertically stacked, 3D, low-loss, cavity bandpass filters are developed for Rx and Tx channels to realize a fully integrated compact duplexer. The fabrication tolerances contributing to the resonant frequency experimental downshift were investigated and taken into account in the simulations of the rest devices. The developed cavity filters are utilized to realize the compact duplexers by using microstrip T-junctions. Then, a novel concept of 3D integrated V-band dual-mode cavity filters, which permit the realization of a variety of quasi-elliptic responses by creating transmission zeros, has been demonstrated using multilayer LTCC technology. A single cavity resonator is designed to generate a degenerate resonance of two orthogonal modes (TE_{102} and TE_{201}), enabling dual-mode operation. The appearance and elimination of transmission zeros have been analyzed through the multi-path coupling diagrams and lumped elements models. Then, the quasi-elliptic, dual-mode filters with the appropriate locations of the transmission zeros are developed for receiver and transmitter channels of a V-band transceiver module. Two pre-synthesized, dual-mode cavity filters are vertically stacked with two types of inter-coupling slots

(1. rectangular 2. cross) to realize the multi-pole filters for 60 GHz WLAN narrowband applications. These proposed filters are the first to be reported and have great potential to be integrated into miniaturized V-band LTCC transceiver modules.

Chapter 5 focuses on three important necessities for successful 3D integration of antennas using SOP technologies: the improvement of radiation patterns (high gain), compactness, and high data rate. We apply the concept of the modern soft surface to improve the radiation pattern of patch antennas. A single square ring of the shorted quarter-wavelength metal strips is employed to form a soft surface and to surround the patch antenna for the suppression of outward propagating surface waves, thus alleviating the diffraction at the edge of the substrate. Since only a single ring of metal strips is involved, the formed soft surface structure is compact and easily integrable with 3D modules. Then, we further improve this technique by adding cavity-based feeding structure on the bottom LTCC layers of an integrated module to increase the gain and to reduce further the backside radiation. The back radiation is significantly reduced, and the maximum gain for the patch antenna with the soft surface and the stacked cavity is approximately 7.6 dBi which is 2.4 dB higher than 5.2 dBi for the “soft-enhanced” antenna without the backing cavity at 60 GHz. For the transmission and reception of signals that cover two bands between 59-64 GHz, a cross-shaped antenna has been designed. The first band (channel 1) covers 59-61.25 GHz, while the second band (channel 2) covers 61.75-64 GHz. This antenna can be easily integrated within a wireless millimeter-wave module containing the components of the previous section. Its structure is dual-polarized for the purpose of doubling the data output rate transmitted and received by the antenna. The cross-shaped geometry was utilized to decrease the cross-polarization which contributes to unwanted side lobes in the

radiation pattern [33]. Finally, a high-gain and directive series fed 1×4 linear antenna array of four microstrip patches covering 59-64 GHz has been designed.

The above proposed passive designs have been combined together, leading to the complete integration of passives with a high level of compactness and performance over the band of interest in chapter 6. The complete integration of the selected microstrip-type structures, such as quasi-elliptic four-pole filter and the series-fed 1×4 linear antenna array, was successfully implemented with a planar transition. Then, the presented fully integrated Rx and Tx cavity filters and the dual-polarized cross-shaped patch antenna functions demonstrate a novel 3D deployment of embedded components equipped with an air cavity on the top. The excellent overall performance of the fully integrated passive front-ends is verified through measured data.

Finally, chapter 7 summarizes the dissertation with conclusions and addresses future work.

CHAPTER 2

BACKGROUND ON TECHNOLOGIES FOR MILLIMETER-WAVE PASSIVE FRONT-ENDS

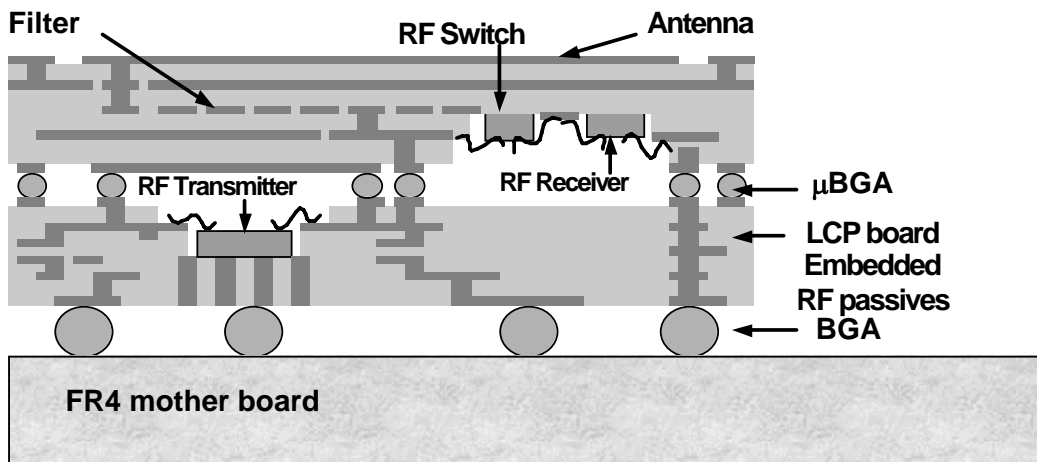
2.1 3D Integrated SOP Concept

The SOP is a single component, multifunction package solution providing the necessary system functions that include analog, digital, RF, optical and MEMS. The SOP also allows efficient integration of complete passive RF front-end functional building blocks, such as filters and antennas. The recent development of thin-film RF materials makes it possible to bring the concept of SOP into the RF world to meet stringent needs in wireless communication [34]-[36]. Major barriers that need to be addressed over a wide frequency range include wideband and low-loss interconnects; high-Q multilayer passives including resistors, inductors, and capacitors [37]-[39]; board-compatible embedded antennas and switches [39]; low-loss and low-cost boards; efficient partitioning of MMICs; low-crosstalk embedded transmission lines and single-mode packages; as well as design rules for vertically integrated transceivers. In addition, there exists a gap in the area of hybrid computer-aided design (CAD) needed for novel functions that require fast and accurate modeling of electromagnetic, circuit, solid-side, thermal, and mechanical effects. Multilayer ceramic (LTCC) and multilayer organic (MLO) structures with LCP technology [38] are used to embed passives efficiently, including high-Q inductors, capacitors, matching networks, lowpass and bandpass filters, baluns, combiners, and antennas. The 3D design approach using multilayer topologies leads to high-quality and compact components to support multiband, wider bandwidth, and multi-standards with high compactness and low cost.

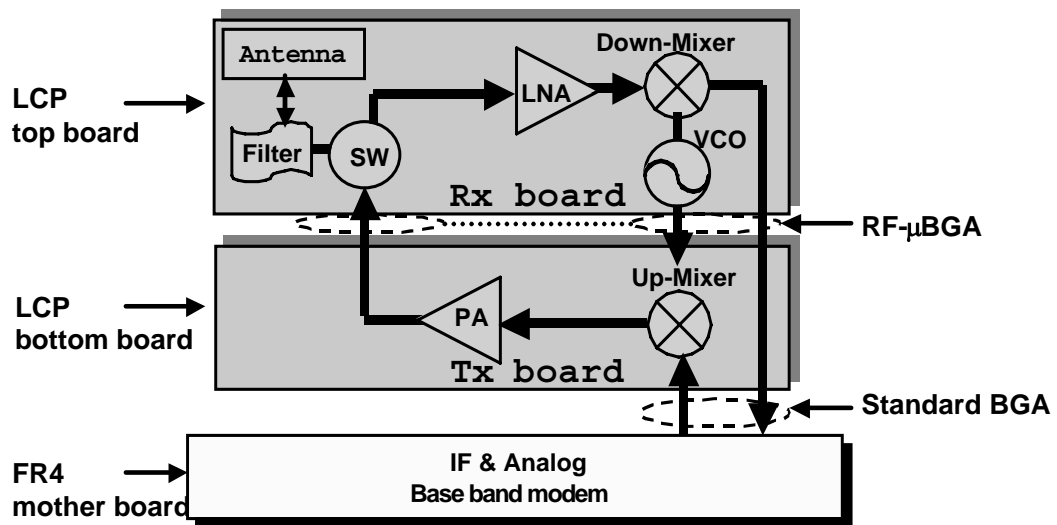
Figure 1 (a) illustrates the proposed 3D multilayer module concept [40]. Two stacked SOP multilayer substrates are used, and board-to-board, vertical transition is ensured by micro ball

grid array (μ BGA) balls. Standard alignment equipment is used to stack the boards and thus provide a compact, high-performance, and low-cost assembly process. Multi-stepped cavities in the SOP boards provide spacing for embedded RF active device (RF switch, RF receiver, and RF transmitter) chipsets and thus lead to significant volume reduction by minimizing the gap between the boards. Active devices can be flip-chipped as well as wire-bonded. Cavities also provide an excellent opportunity for the easy integration of RF MEMS devices, such as MEMS switches or tuners. Passive components, off-chip matching networks, embedded filters, and antennas are implemented directly into the SOP boards by using multilayer technologies [41]-[42]. Standard ball grid array (BGA) balls ensure the effective broadband interconnection of this high-density module with motherboards such as the FR4 board. The top and bottom substrates are dedicated to the receiver and transmitter building blocks, respectively, of the RF front-end module.

Figure 1 (b) shows the RF block diagram of each board. The receiver board includes an antenna, BPF, active switch, and RF receiver chipset (low noise amplifier (LNA), voltage control oscillator (VCO), and down conversion mixer). The transmitter board includes an RF transmitter chipset (up conversion mixer and power amplifier) and off-chip matching networks. Ground planes and vertical via walls are used to address the isolation issues between the transmitter and the receiver functional blocks. Arrays of vertical vias are added into the transmitter board to achieve better thermal management.



(a)



(b)

Figure 1: (a) 3D integrated module concept view (b) Rx and Tx board block diagram.

2.2 LTCC Multilayer Technology

The development of multilayer substrates makes it possible to bring the concept of 3D integration into RF system implementation to meet stringent needs in wireless communication. The 3D integration approach using multilayer LTCC technologies has emerged as an attractive solution for these systems. LTCC stands for a ceramic substrate system, which is applied in electronic circuits as a cost-effective and competitive substrate technology with a nearly arbitrary number of layers. In general, printed gold and silver conductors or alloys with platinum or palladium are used in general. Copper conductors are available as well. The metallization pastes will be screen-printed layer by layer upon the unfired and “green” ceramic foil, followed by stacking and lamination under pressure. The multilayer ceramic stack will be fired (sintered) in the final manufacturing step. The sintering temperature is below 900°C for the LTCC glass-ceramic. This relatively low temperature enables the co-firing of gold and silver conductors. The melting of Au and Ag are at 960°C and 1100°C, respectively.

The LTCC slurry is a mixture of re-crystallized glass and ceramic powder in binders and organic solvents. It is cast under “doctor blades” to obtain a certain tape thickness. The dried tape is coiled on a carrier tape and ready for production. In contrast, HTCC (high temperature co-fired ceramic) is an aluminum oxide substrate, also called alumina or Al_2O_3 . The sintering temperature of aluminum is 1600°C, which only allows co-firing conductors with a higher melting point like tungsten (W, 3370°C) and molybdenum (Mo, 2623°C). The drawback of these conductors is lower conductivity, which results in higher waveguide losses. The low line losses as well as competitive manufacturing costs are an advantage of LTCC for RF and microwave applications.

However, one of the main drawbacks of LTCC, limiting its accuracy, is the shrinkage of ceramic tapes during the firing process. Typically, the tapes shrink between 12-16% in the horizontal dimensions and 15-25% in the vertical. Typical shrinkage tolerances are +/-0.2% and +/-0.5% for both directions, respectively, and are dependent on the amount of conductor material on every layer. Fabricating multilayer structures with typical dimensions of 5"×5" results in length and width differences between layers as large as 250 μm, thus possibly leading to be opened and shorted in a high-density design incorporating fine lines and spacings. As a result, a dense packaging and miniaturization is achieved by exploiting the 3D capabilities of this technology. Unfortunately, this 3D configuration causes large modeling difficulties even at lower microwave frequencies, limiting the use of LTCC for practical circuit design. The realization of this 3D package scheme becomes difficult at millimeter-wave frequencies because of considerably higher coupling between elements in thick substrates.

Another basic limitation of the LTCC process is a coarse metal definition. The minimal line width and spaces that may be achieved with normal thick film techniques are typically 125 μm with a typical tolerance of +/-25 μm. The minimal conductor thickness is around 25 μm. The other two issues related to LTCC, which considerably influence millimeter-wave performance, are usually high loss tangent values on the order of 10^{-2} and low quality of surface finish. An additional disadvantage is that ceramic-based tapes show high dielectric constant, typically 7-10. This, combined with a high minimum feature size for thick-film patterning processes, results in low reproducibility of the millimeter-wave circuits. In the past, many efforts were undertaken to improve the quality of the LTCC process.

To eliminate shrinkage altogether, some manufacturers promoted tape on substrate technology (TOS) [43]-[44]. Shrinkage is virtually eliminated by laminating and firing each

layer of tape on a substrate made of Al_2O_3 , BeO or AlN . While this eliminates any component assembly alignment problems associated with shrinkage, TOS is a serial process requiring expensive ceramic substrate carriers, and thus resulting in higher manufacturing costs. Another approach to solving the shrinkage problem was the development of low-temperature co-fired ceramics on metal (LTTC-M) [45] with a specially formulated multilayer ceramic structure attached to a metal core. In this case, the ceramic firing and core attachment process occur in one and the same step, which is a more cost-effective solution than TOS. The resulting structure exhibits virtually no shrinkage in the plane of the substrate. However, vertical shrinkage is still an issue.

As long as the frequency is low or the system specifications are relaxed, LTCC may be successfully used. At the V-band, however, the application of this technology for practical integration of high-performance passive structures using planar transmission line media (microstrip and CPW) seems to be difficult. For microstrip realizations, the dielectric tapes should offer a very consistent and predictable thickness. The thin dielectric layers necessary for operation at the V-band impose an accuracy limit on the thickness of LTCC tapes that is difficult to achieve. Furthermore, the use of thin dielectric tapes involves the need for precisely defined narrow strips and spaces required for the repeatable performance of many passive structures. Taking into account a high dielectric constant of LTCC tapes, the realization of precise CPW structures with appropriately narrow ground-ground spacing, necessary for avoiding substantial coupling and leakage to substrate modes at the V-band, also seems to be impossible. In the 3D module integration, coefficient of thermal expansion (CTE) is also an important parameter as it affects the Si-based ICs integrated. The substrate is expected to exhibit CTE values close to Si ($\sim 4.2 \text{ ppm}/^\circ\text{C}$) in order to avoid deformation such as cracks, delaminations etc. between the

substrate and the attached components due to shrinkage mismatch. LTCC technology, which unites substrate thick-film-co-firing and device integration optimally, covers most of these requirements and it is, thus, still one of the few material systems employed for fabrication of 3D module systems.

To overcome the limitations of previous LTCC processes at millimeter-wave frequencies, Asahi Glass Co. developed and proposed an LTCC 044 $\text{SiO}_2\text{-B}_2\text{O}_3$ glass. The relative permittivity (ϵ_r) of the substrate is 5.4 and its loss tangent ($\tan\delta$) is 0.0015 at 35 GHz. The dielectric layer thickness per layer is 100 μm , and the metal thickness is 9 μm . The resistivity of metal (silver trace) is determined to be $2.7 \times 10^{-8} \Omega \cdot \text{m}$. The tolerance of XY shrinkage has been investigated to be $\pm 5\%$. To eliminate the shrinkage effect, a novel composite LTCC of a high dielectric constant ($\epsilon_r \sim 7.3$) and low dielectric constant ($\epsilon_r \sim 7.1$) has been proposed by Asahi Glass Co. The very mature multilayer fabrication capabilities of this novel process ($\epsilon_r = 7.1$ and 7.3 , $\tan\delta = 0.0019$ and 0.0024 , metal layer thickness: 9 μm , dielectric layer thickness: 53 μm , minimum metal line width and spacing: up to 75 μm) make it one of the leading competitive solutions to meet millimeter-wave design requirements in terms of the physical dimensions of the integrated passives. The proposed LTCC technologies can be very promising for the implementation of integrated cavities or waveguides at V-band or above with accurate via processing, substantially relaxing requirements on metal pattern accuracy.

2.3 Integrated Cavity Structures

The integrated cavity structures integrated into multilayer substrates is one of the more promising candidates for implementing of the filters and duplexers at millimeter-wave frequencies because of their relatively high-Q and high-power capability. Therefore, it would be valuable to review analytic solutions of cavity resonance to understand the physical phenomena

possibly observed in practical implementations. A general solution for transverse electric (TE) and transverse magnetic (TM) waves can be derived with Maxwell's equations [46]. The solution, known as the Helmholtz wave equation, is used to find TE and TM modes in rectangular waveguides by solving with the separation of variables procedure and applying electric boundary conditions. The TE and TM wave fields are then extended to find the cavity guided TE and TM modes by applying two additional electric boundary conditions.

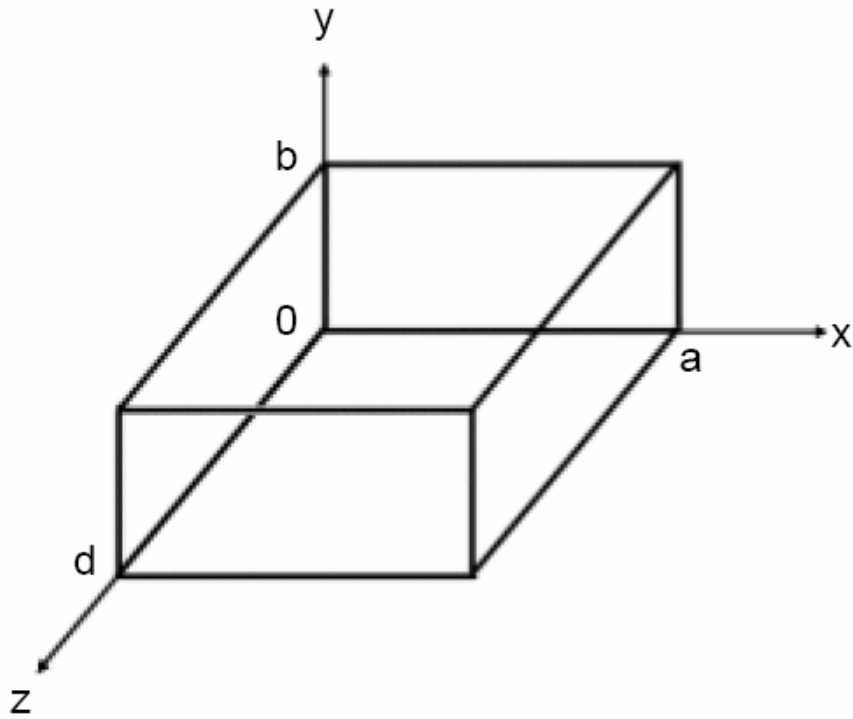


Figure 2: Geometry of a rectangular cavity [46].

Shorting the rectangular waveguide at $Z=[0, d]$ enforces a perfect electric boundary that sets $E_x=E_y=0$ on the end walls. The transverse electric fields (E_x, E_y) of the TE_{mn} or TM_{mn} rectangular waveguide mode can be written as

$$\vec{E}_t(x, y, z) = \vec{e}(x, y) \left[A^+ e^{-j\beta_{mn}z} + A^- e^{j\beta_{mn}z} \right] \quad (1)$$

where $\vec{e}(x, y)$ represents the transverse electric field components, and A^+ and A^- are arbitrary amplitudes of the waves moving in the $+z$ and $-z$ directions, and β is the propagation constant.

Applying the boundary condition setting $\vec{E}_t = 0$ at $z=[0, d]$ to equation (1) gives

$$\vec{E}_t(x, y, z) = -\vec{e}(x, y)A^+ 2j \sin \beta_{mn}d = 0 \quad (2)$$

If $A^+ \neq 0$, then a solution exists for

$$\beta_{mn}d = l\pi, l = 1, 2, 3, \dots, \quad (3)$$

which means the cavity supports resonant modes with integer multiples of half-guide wavelengths. No other wavelengths are supported, and the modes that are supported only exist at their discrete resonant frequencies.

The cutoff wavenumber for the rectangular cavity is then

$$k_{mnl} = \sqrt{\left(\frac{m\pi}{a}\right)^2 + \left(\frac{n\pi}{a}\right)^2 + \left(\frac{l\pi}{a}\right)^2} \quad (4)$$

Resonant modes of the cavity are referred to as TE_{mnl} or TM_{mnl} , where the m , n , and l indices refer to the number of guided half-wavelengths found in the standing wave pattern in the x , y , and z directions, respectively. The resonant frequency of the TE_{mnl} or TM_{mnl} mode is

$$f_{mnl} = \frac{ck_{mnl}}{2\pi\sqrt{\mu_r\epsilon_r}} = \frac{c}{2\pi\sqrt{\mu_r\epsilon_r}} \sqrt{\left(\frac{m\pi}{a}\right)^2 + \left(\frac{n\pi}{a}\right)^2 + \left(\frac{l\pi}{a}\right)^2} \quad (5)$$

Figure 2 shows the rectangular cavity convention, $b < a < d$; the dominant resonance mode (the mode with the lowest resonant frequency) is the TE_{101} mode shown in Fig. 3. This cavity resonant mode has a discrete resonant frequency different from the cutoff frequency associated

with a rectangular waveguide mode and is commonly used for cavity filter implementation in a multilayer package.

A planar dielectric waveguide filter with CPW ports for flip-bonding is reported and is demonstrated for 60 GHz applications [47]. The filter is formed, incorporating metalized through holes in an alumina substrate and mounted to a multilayer ceramic package with structures to suppress parasitically propagating electromagnetic waves. The photographs of the fabricated dielectric waveguide filter with CPW input and output ports and its ceramic packaging are shown in Fig. 4.

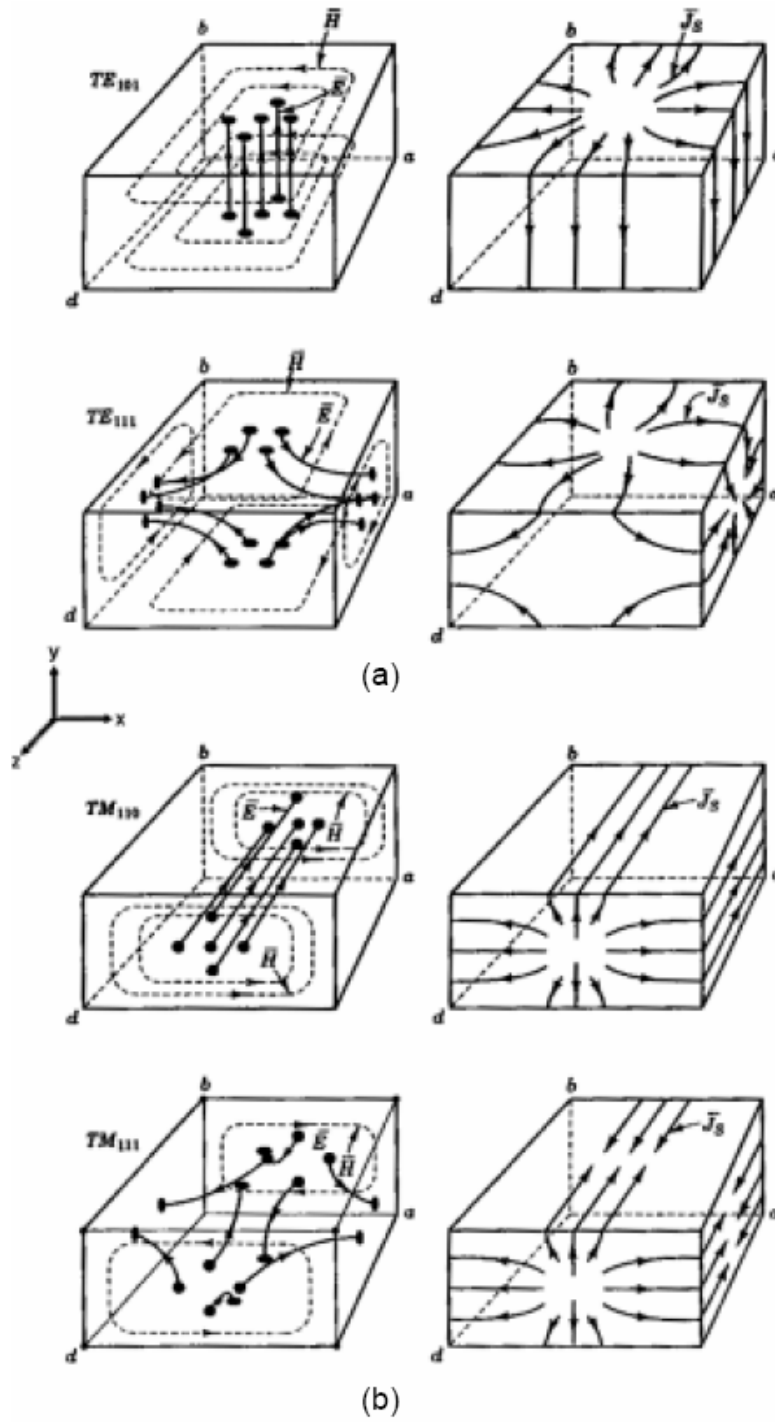
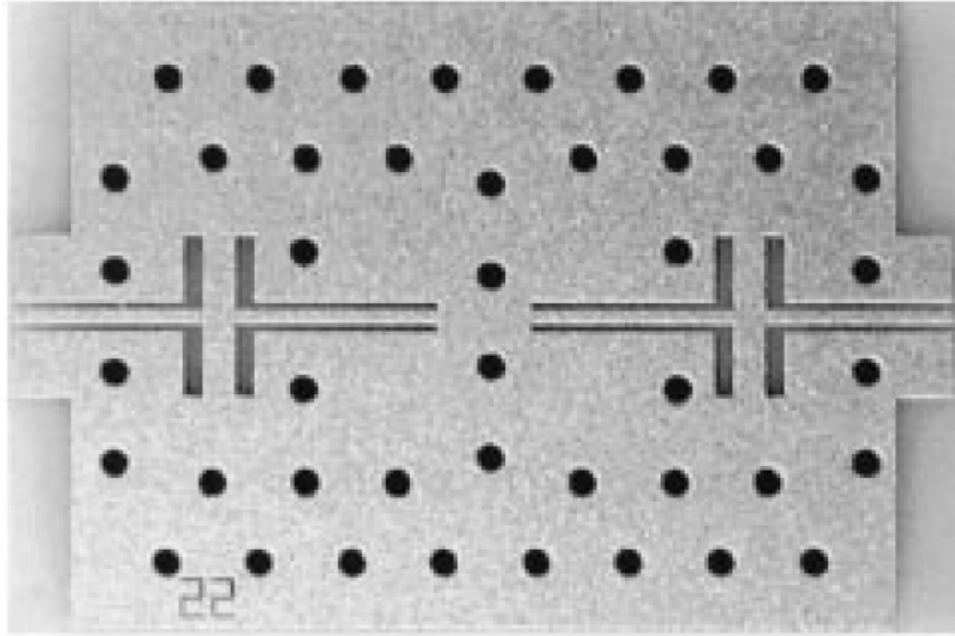
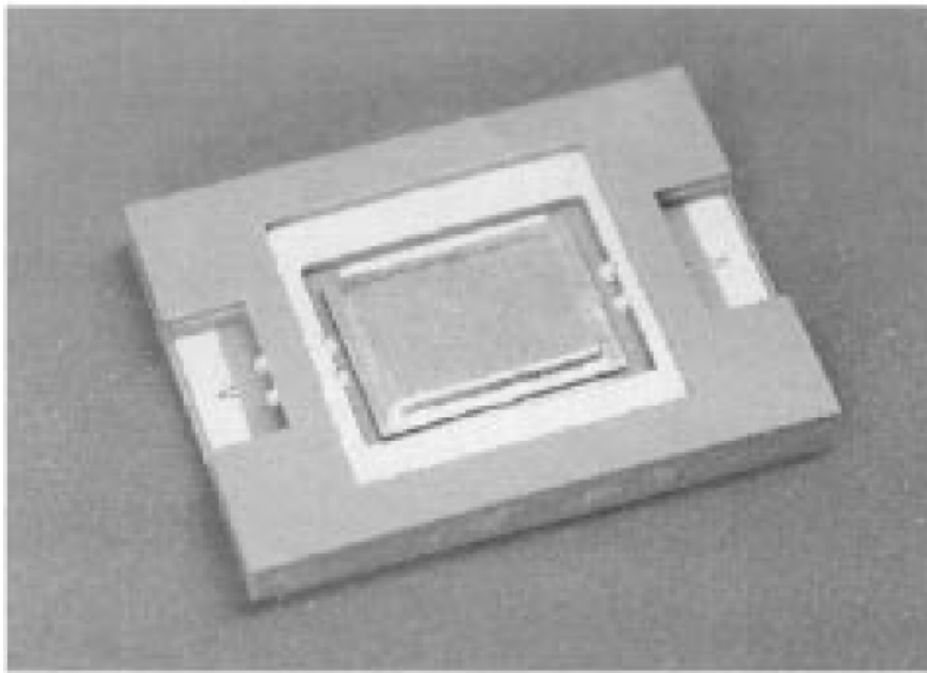


Figure 3: Field patterns for (a) TE, and (b) TM modes in a rectangular cavity [46].



(a)



(b)

Figure 4: (a) Fabricated dielectric waveguide filter with CPW input and output ports (b) Filter mounted in the ceramic package. The metal cover is attached on the filter [47].

2.4 60 GHz Transmitter/Receiver Modules

With the availability of 7 GHz of unlicensed spectra around 60 GHz, there is growing interest in using this resource for new consumer applications, such as high-speed Internet access, streaming content downloads, and wireless data bust for cable replacement, requiring very high-data-rate wireless transmission. The targeted data rate for these applications is greater than 2 Gb/s. Although the excessively high path loss at 60 GHz resulting from oxygen absorption precludes communication over distances greater than a few kilometers, short-range wireless personal area networks (WPAN) actually benefit from the attenuation, which provides extra spatial isolation and higher implicit security. Furthermore, because of oxygen absorption, Federal Communications Commission (FCC) regulations allow for up to 40 dBm equivalent isotropically radiated power (EIRP) for transmission, which is significantly higher than what is available for other WLAN/WPAN standards. The wide bandwidth and high allowable transmit power at 60 GHz enable multi-gigabit-per-second wireless transmission over typical indoor distances (~10 m). Moving to higher frequencies also reduces the form factor of the antennas, as antenna dimensions are inversely proportional to carrier frequency. Therefore, for a fixed area, more antennas can be used, and the antenna array can increase the antenna gain and help direct the electromagnetic energy to the intended target.

Assuming simple line-of-sight free-space communication, the Friis propagation is given by

$$\frac{P_r}{P_t} = \frac{D_1 D_2 \lambda^2}{(4\pi R)^2} \quad (6)$$

where the received power, P_r , normalized to the transmitted power, P_t , is seen to depend on the transmit and receive antenna directivities, $D_{1,2}$, the distance between the transmitter and receiver, R , and wavelength, λ . Assuming a single omnidirectional antenna at the transmitter and receiver,

the received power, P_r at a distance, R , decreases with increasing frequency, and an additional 20 dB loss is expected for a system operating at 60 GHz, compared to 6 GHz. This additional loss would render the system incapable of delivering gigabit-per-second data rates at 10 m given the limited output power and high noise figure of a 60 GHz transceiver implementation.

Fortunately, the antenna directivities, $D_{1,2}$, can be improved. While it is impossible to increase the antenna gain for a single antenna, it is more desirable to increase the directivity by employing an antenna array. For a fixed antenna aperture size, A , the directivity is simply

$$D = \frac{4\pi A}{\lambda^2}. \quad (7)$$

To implement a 60 GHz front-end module, several technologies have been investigated. In particular, GaAs FET technology has evolved to the point where 60 GHz GaAs MMICs are production-ready [92]. GaAs-based 60 GHz devices such as low-noise amplifiers, high-power amplifiers, multipliers, and switches can nowadays be ordered in large quantities in die form at prices on the order of \$10-20 apiece [93]. For application in WLAN equipment, however, this might still be too expensive. An alternative technology based on silicon germanium (SiGe) promises to provide relatively low-cost millimeter wave front-end MMICs while simultaneously maintaining the favorable performance of GaAs. Transceiver circuits using SiGe have been demonstrated to operate at 60 GHz with good performance [94]. However, digital Complementary Metal-Oxide Semiconductor (CMOS) technology is the lowest-cost option, and with its rapid improvement due to continual scaling, CMOS technology is becoming a viable option to address the millimeter-wave market. Today, 90 nm bulk CMOS technology is used to implement power and low-noise amplifiers at 60 GHz [95], Future bulk CMOS process at the 65 nm node are expected to provide even more gain at lower power consumption.

A 60 GHz receiver front-end realized in 130 nm CMOS technology has been successfully implemented with the low power consumption and compact size [96]. Also, the development of 60 GHz-band T/R modules for stringent system specifications has been demonstrated in a system-in-package (SIP) transmitter integrating LTCC patch-arrayed antennas [29] and compact wireless transceiver modules for Gigabit data-rate transmission [30]-[32]. However, the previously reported transmitter and receiver modules could suffer from the spurious signal and image signal because only antennas are integrated into modules without using any band-select filters or duplexers in passive front-ends. Moreover, two separate antennas for the Tx and Rx channels are used and occupy a large area, which contradicts the size requirements of compact 60 GHz modules.

Among some of major design concerns are the front-end module power consumption level, leading to prohibitive temperatures with detrimental impact on module's operation [97]. Thus, it is needed to optimize the thermal performance of the front-end module and to improve its reliability at reduced overall cost. The thermal performance of front-end module incorporating LTCC substrate has been investigated at L band [97]. It shows that the peak junction temperature for the power amplifier with LTCC substrate and silver paste metallization is around 130.1 °C, ~51% higher compared to the baseline case with 2-layer organic substrate. By increasing the metal thermal conductivity from 90 (silver past) to 150, 250, and 350 W/mK, a significant drop in peak temperature occurs, indicating its impact on PA's overall thermal performance. The thickness of the top metal (10 μm versus 30 μm) contributes only to 5% - 8% change in peak junction temperature. In addition, it has been shown that the vias placed under the die are the dominating mechanism removing the heat from the die through the substrate, while

the outer vias have no impact on the PA overall thermal performance. The material of vias placed under the die make a large impact to the module overall thermal performance.

CHAPTER 3

MICROSTRIP-TYPE INTEGRATED PASSIVES

3.1 Patch Resonator Filters and Duplexers

3.1.1 Single Patch Resonator

Integrating filter on-package in LTCC multilayer technology is a very attractive option for RF front-ends up to the millimeter-wave frequency range in terms of both miniaturization by vertical deployment of filter elements and reduction of the number of components and assembly cost by eliminating the demand for discrete filters. In millimeter-wave frequencies, the bandpass filters are commonly realized using slotted patch resonators because of their miniaturized size and their excellent compromise among size, power handling, and easy-to-design layout [13]. In this section, the design of a single-pole slotted patch filter is presented for two operating frequency bands (38-40 GHz and 58-60GHz). All designs have been simulated using the method of moments (MOM)-based, 2.5D full-wave solver IE3D.

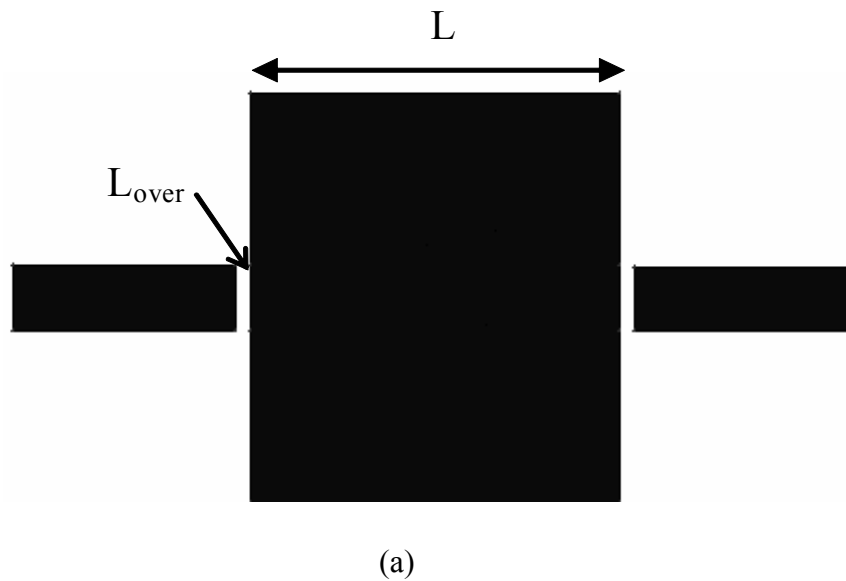
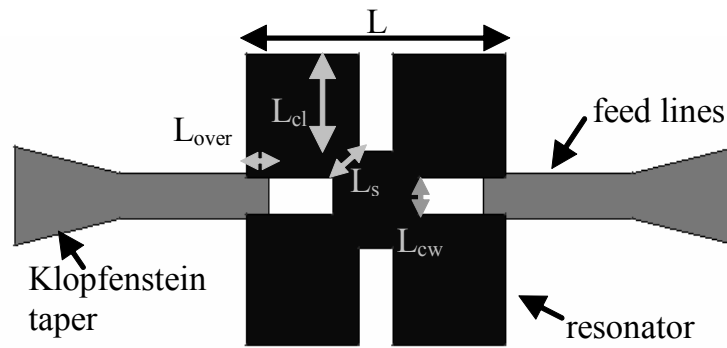


Figure 5: Top view of (a) conventional $\lambda/2$ square patch (b) Miniaturized patch resonator.



(b)

Figure 5: Continued.

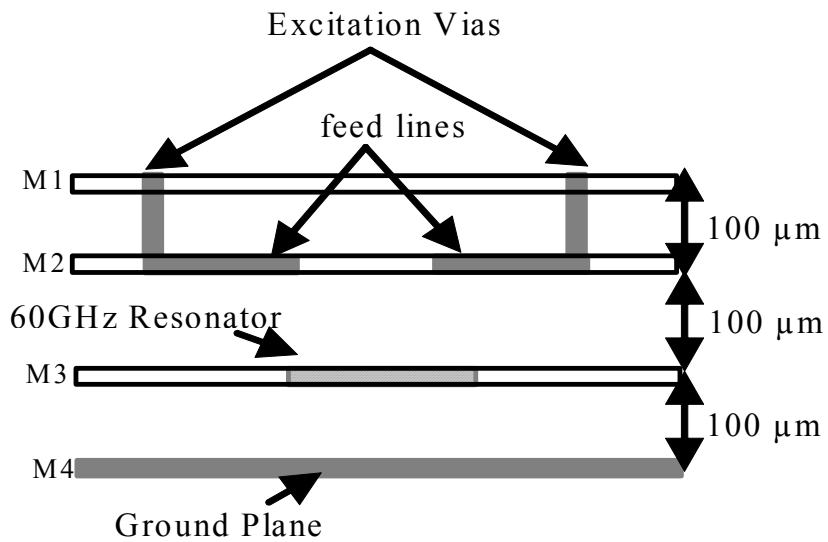


Figure 6: Side view of 60GHz slotted patch resonator.



Figure 7: The photograph of the fabricated filters with coplanar waveguide (CPW) pads at 60 GHz.

Figure 5 shows a top-view comparison between a basic half-wavelength ($\lambda/2$) square patch resonator ($L \times L = 0.996 \text{ mm} \times 0.996 \text{ mm}$) [48] (Fig. 5 (a)) and the new configuration ($L \times L = 0.616 \text{ mm} \times 0.616 \text{ mm}$) (Fig. 5 (b)), which is capable of providing good trade-offs between miniaturization and power handling. Side views and the photographs of the 60 GHz resonators are shown in Fig.6 and Fig.7, respectively. In the design of a $\lambda/2$ square patch, the planar single-mode patch and microstrip feedlines are located at metal 3 ($M3$ in Fig. 6) and use the end-gap capacitive coupling between the feedlines and the resonator itself to achieve 3% 3dB bandwidth and $<3\text{dB}$ insertion loss around the center frequency of 60 GHz. However, the required coupling capacitances to obtain design specifications could not be achieved because of the LTCC design rule limitations.

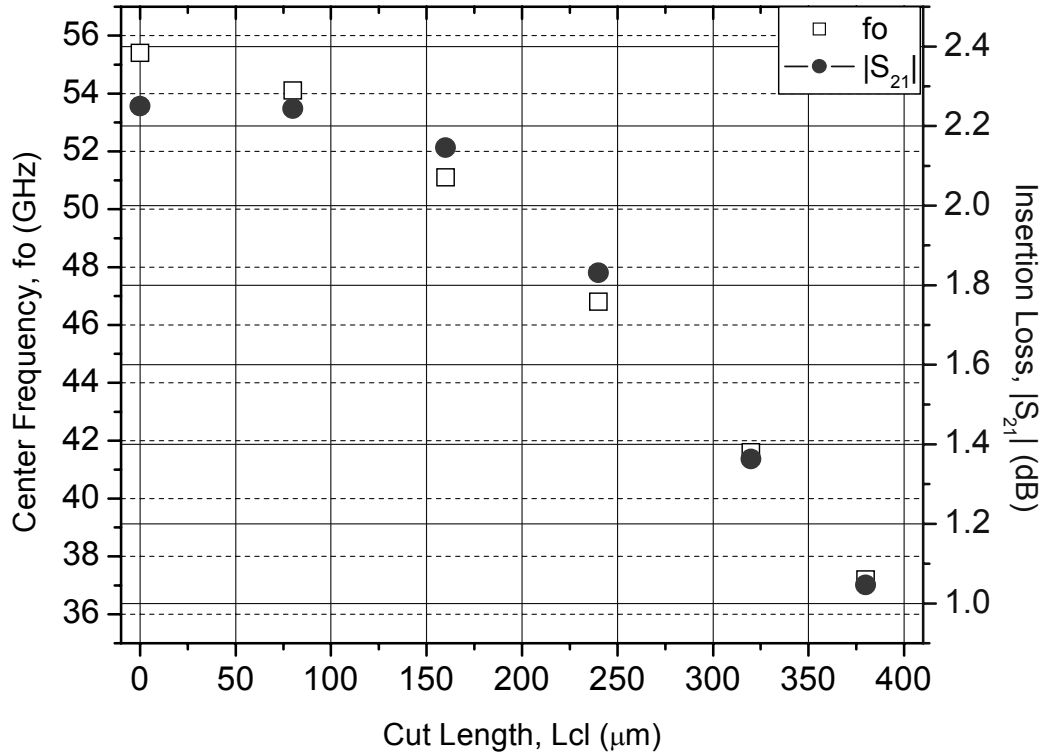


Figure 8: Simulated responses of center frequency (f_o) and insertion loss ($|S_{21}|$) as a function of transverse cut (L_{cl}).

To maximize the coupling strength while minimizing the effects of the fabrication, the proposed novel structure takes advantage of the vertical deployment of filter elements by placing the feedlines and the resonator into different vertical metal layers, as shown in Fig. 6. This transition also introduces a 7.6% frequency downshift resulting from the additional capacitive coupling effect compared to the basic $\lambda/2$ square patch resonator (Fig. 5 (a)) directly attached by feedlines. Transverse cuts have been added on each side of the patch to achieve significant miniaturization of the patch by adding additional inductance. Figure 8 shows the simulated response for the center frequency and the insertion loss as the length of cuts (L_{cl} in Fig. 5 (b)) increases, while the fixed width of cuts ($L_{cw}=L/8$ in Fig. 5 (b)) is determined by the fabrication tolerance. It can be observed that the operating frequency range shifts further downward about 33% as the length of the cut (L_{cl} in Fig. 5 (b)) increases by approximately 379 μm . Additional miniaturization is limited by the minimum distance (L_s in Fig. 5 (b)) between the corners of adjacent orthogonal cuts. Meanwhile, as the operating frequency decreases, the shunt conductance in the equivalent circuit of the single patch also decreases because its value is reciprocal to the exponential function of the operating frequency [48]. This fact additionally causes the reduction of radiation loss since it is proportionally related to the conductance in the absence of conductor loss [49]. Therefore, insertion loss at resonance is improved from 2.27 dB to 1.06 dB by an increase of L_{cl} in Fig. 5 (b).

The patch size is reduced significantly from 0.996 mm to 0.616 mm. The modification of bandwidth resulting from the patch's miniaturization can be compensated by adjusting the overlap distance (L_{over}). Figure 9 shows the simulated response for the 3-dB bandwidth as L_{over} increases.

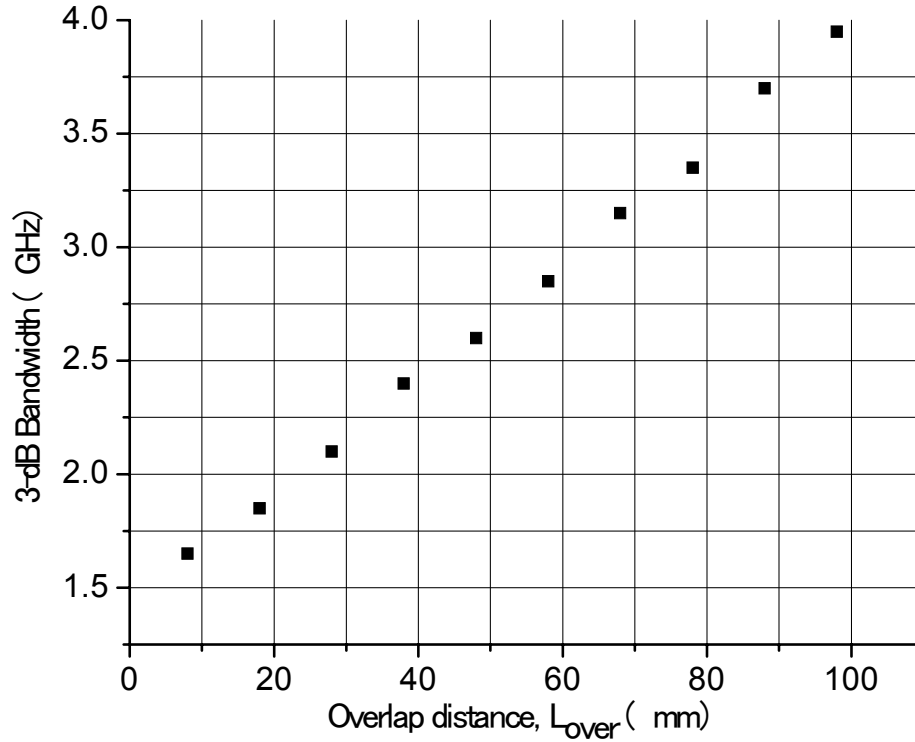


Figure 9: Simulated 3-dB bandwidth as function of Overlap distance of 60 GHz slotted patch resonator.

It is observed that the 3-dB bandwidth increases as L_{over} increases because of a stronger coupling effect, and then L_{over} is determined to be 18 μm corresponding to the 1.85 GHz 3-dB bandwidth.

The proposed embedded microstrip line filters are excited through vias connecting the CPW signal pads on the top metal layer ($M1$ in Fig. 6), reducing radiation loss compared to microstrip lines on the top (surface) layer. As shown in Fig. 5 (b), Klopfenstein impedance tapers are used to connect the 50 Ω feeding line and the via pad on the metal 2 ($M2$ in Fig. 6). The overlap ($L_{over} \approx L/31$) and transverse cuts ($L_{cv} \approx L/8$, $L_{cf} \approx L/3.26$) have been finally determined to achieve desired filter characteristics with the aid of IE3D. The filters with CPW pads were

fabricated in LTCC ($\epsilon_r=5.4$, $\tan\delta=0.0015$) with a dielectric layer thickness of 100 μm and metal thickness of 9 μm . The overall size is 4.018 mm \times 1.140 mm \times 0.3 mm, including the CPW measurement pads. As shown in Fig. 10, the experimental and the simulated results agree very well. It can be easily observed that the insertion loss is < 2.3 dB, the return loss >25.3 dB over the passband and the 3dB bandwidth is about 1 GHz. The center frequency shift from 59.85 GHz to 59.3 GHz can be attributed to the fabrication accuracy (vertical coupling overlap affected by the alignment between layers, layer thickness tolerance). This was the first fabrication iteration, and the differences could be corrected in the second and third iterations.

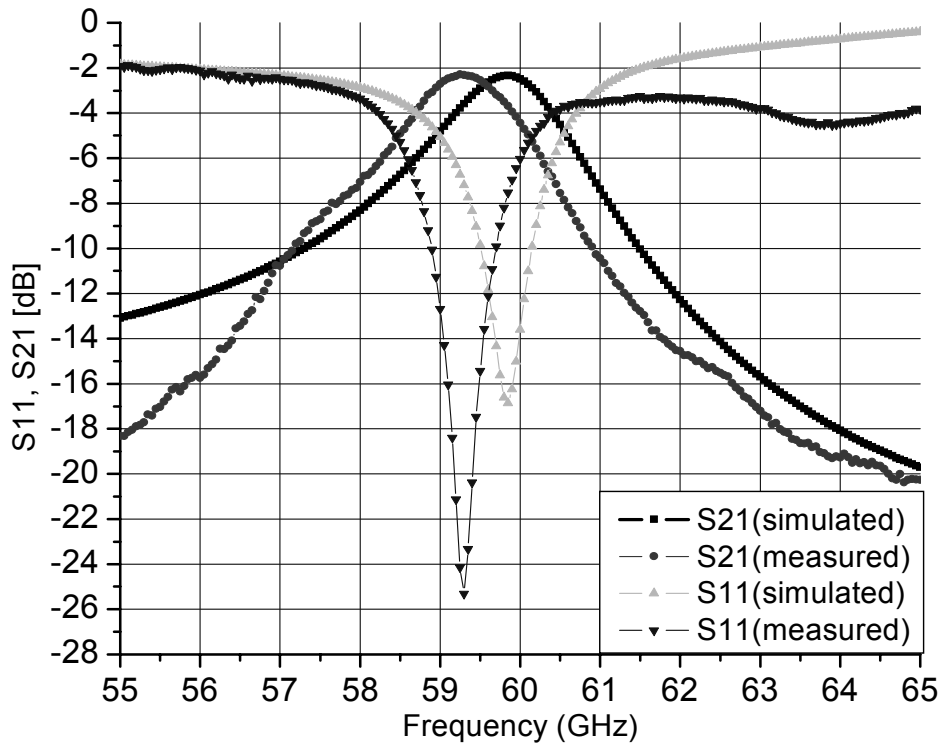


Figure 10: Measured and simulated S-parameters of 60 GHz slotted patch resonator.

The proposed slotted-patch filter architecture was also used in the design of mobile satellite communication systems around 39 GHz. The 39 GHz single-mode patch filter ($L \times L = 1.021\text{mm} \times 1.021\text{ mm}$) was designed for 3.08% bandwidth, 39 GHz center frequency, and $<3\text{dB}$ insertion loss. The design procedure was similar to that of the 60 GHz filter except for the fact that the resonator was placed on two layers (instead of one layer) beneath the feeding lines, as shown in the side view of Fig. 11. The overlap ($L_{\text{over}} \approx L/7$) and the transverse cuts ($L_{\text{cw}} \approx L/8.2$, $L_c \approx L/3$) were determined to achieve the desired filter characteristics. The overall size was $4.423\text{ mm} \times 1.140\text{ mm} \times 0.4\text{ mm}$ with CPW measurement pads. The fabricated filter exhibits a minimum insertion loss of 2.3 dB, a return loss of 18.2 dB, and a 3-dB bandwidth about 3%. (Fig. 12) The experimental error in the calculation of the center frequency can be attributed to the fabrication accuracy, as mentioned in the 60GHz case.

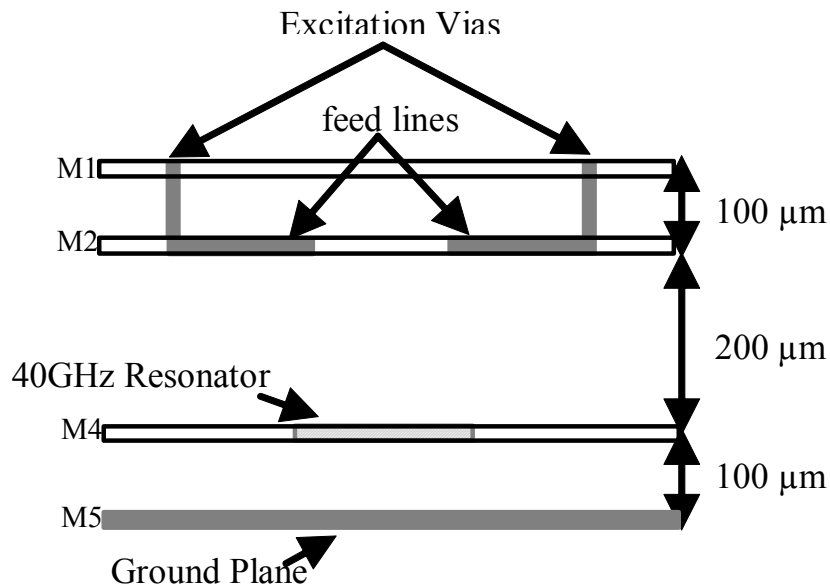


Figure 11: Side view of 39 GHz slotted patch resonator.

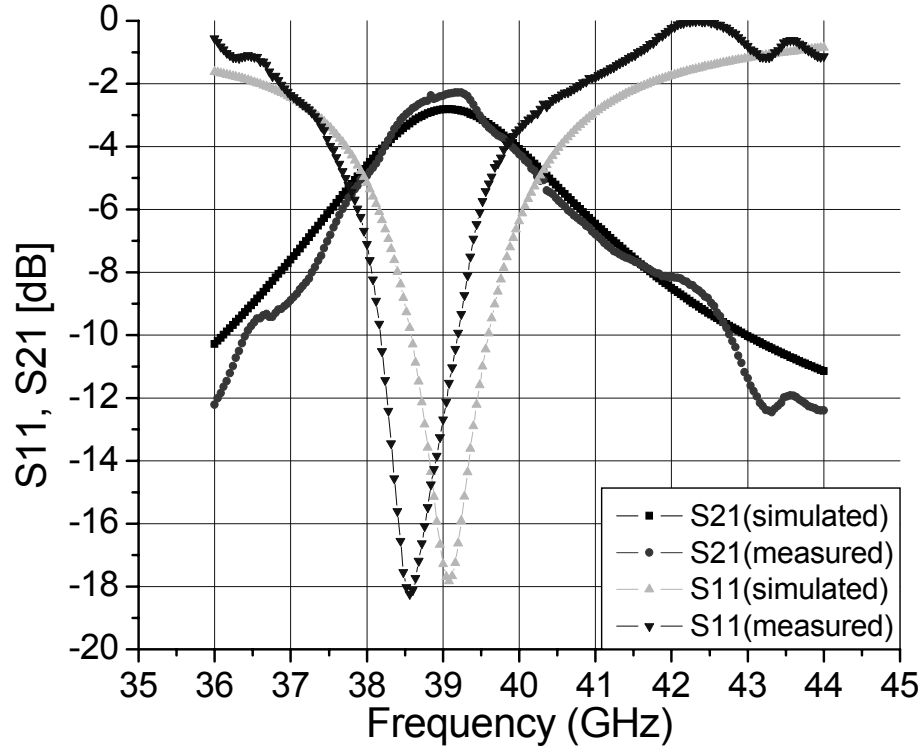


Figure 12: Measured and simulated S-parameters of 39 GHz slotted patch resonator.

3.1.2 Duplexer (41 GHz/61 GHz)

Recently, an X-band H-plane ridge waveguide duplexer was built in LTCC and experimentally succeeded [14]. Also, a global system of mobile communications (GSM) ($f_o = 0.92$ GHz)/ personal communication services (PCS) ($f_o = 1.77$ GHz) duplexer was implemented to be integrated into an LTCC switch/filter front-end module, with excellent performance, such as 0.5/0.9 dB insertion loss and 26.7 dB/ 27.9 dB return loss [15]. However, to the best knowledge of the authors, no duplexers of compact slotted patch resonator configurations operating at 40 and 60 GHz have ever been proposed. With the above reported development in the design of miniaturized patch resonators, it is now possible to realize compact duplexers using

LTCC multilayer technology that cover two bands of interest for mobile communications such as broadband WLAN and LCRN. These dual-band duplexers can be designed around the 41/61 GHz center frequencies (channel1/channel2) with <3dB insertion loss for both channels and 6% 3dB bandwidth below maximum insertion loss.

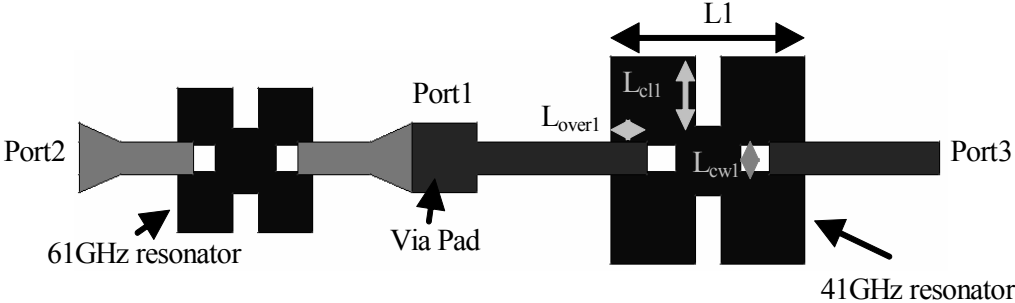


Figure 13: Top view of the dual-band compact duplexer.

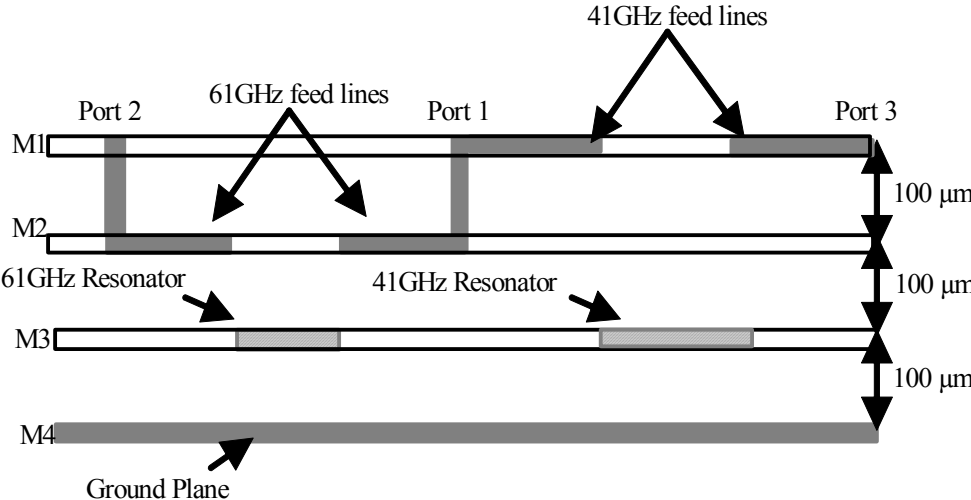


Figure 14: Side view of the dual-band compact duplexer.

The top and side views of the topology chosen for the slotted patch duplexer are shown in Figs. 13, 14, respectively. The two resonant patch filters are connected together with a via junction (*Port1* in Fig. 13), which constitutes the common input. The 61 GHz patch filter occupies the left portion of the duplexer and the 41 GHz filter the right portion in Fig 13. In comparison to the patch filter of Fig. 10 that occupies four dielectric layers, the whole 41GHz patch filter is shifted up by one dielectric/metal layer so that it remains only three dielectric layers. This modification of the structure not only realizes a compact multilayer 3D duplexer configuration, where the resonators are on the same metal layer while fed by strip lines on different layers (better isolation), but also makes it simpler to design by directly embedding the configuration designed in section 3.1.1. In channel 1, this type provides a narrower bandwidth and a higher insertion loss since radiation from microstrip feedlines on the top (surface) layer is higher than from embedded types. The overlap (L_{over1} in Fig. 13) works as the main control factor to improve the bandwidth, as demonstrated in Fig. 9. The overlap ($L_{over1} \approx L/8.3$) has been determined for a fixed dimension of the transverse cuts ($L_{cw1} \approx L/8.2$, $L_{cl1} \approx L/3$) with the aid of IE3D. The slot length (L_{cl1} in Fig. 13) is determined to fulfill the insertion and center frequency specifications in the same way as in section 3.1.1. In addition, the surface microstrip feedlines of channel 1 have been implemented in such a way as to achieve 50 Ω impedance matching, and Klopfenstein impedance tapers have been employed to annihilate the parasitic coupling in microstrip discontinuities and to achieve impedance matching between the 61 GHz feedline and the via pad, as shown in Fig. 13. The fabricated duplexer (Fig. 15) occupies an area of $5.719 \times 1.140 \times 0.3 \text{ mm}^3$, including the CPW measurement pads and the CPW-microstrip transition [51].

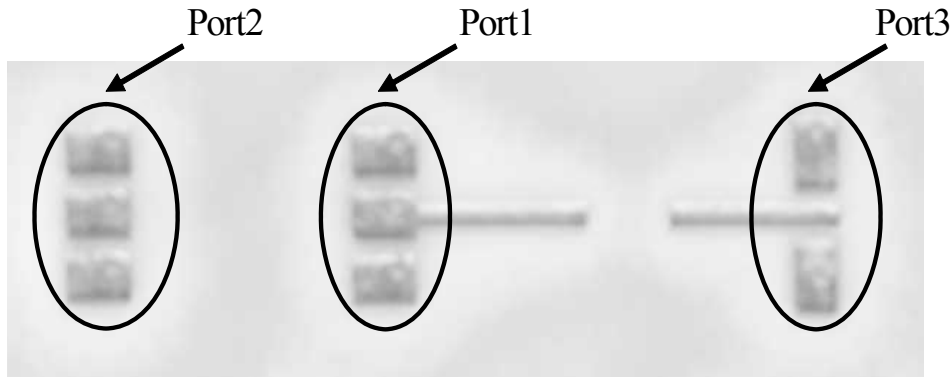


Figure 15: Photograph of the fabricated duplexer.

Figures 16 and 17 show respectively the simulated and measured insertion and return losses of the duplexer. The measured insertion loss for channel 1 is 3.10 dB, which is slightly higher than the simulated value, while the return loss, shown in Fig. 16, increases from -27 dB to -18.6 dB. The measured bandwidth is 4.8%, slightly smaller than the simulation results. Also, the center frequency is shifted to 39.8 GHz. For channel 2, the measured insertion loss is 3.41 dB slightly higher than the simulated value, while the return loss is -11.32 dB, a 6.68 dB decrease from the simulated value. The measured bandwidth was about 3.25%, which is quite smaller than the simulated values of 6%. The center frequency was also shifted to 59 GHz. The discrepancy between the simulated and measured insertion/return loss values can be attributed to several factors: (1) the fabrication accuracy of the feeding line/cut designs that have been computationally optimized for the original resonant frequencies and not for the shifted frequencies and (2) the additional conductor loss in measurements, because the simulations assume that the metals of the strip feeding lines are perfect electric conductors. In addition, the narrower bandwidth in measurements compared to the simulations might be due to the fabrication accuracy of the vertical-coupling overlap design that is optimized for the original

resonant frequencies and not for the shifted frequencies. The measured isolation agrees fairly well with the simulated values. The overall isolation is -29.5 dB at 39.8 GHz, -20.4 dB at 59 GHz, and better than -16.3 dB in the worst case, as shown in Fig. 18.

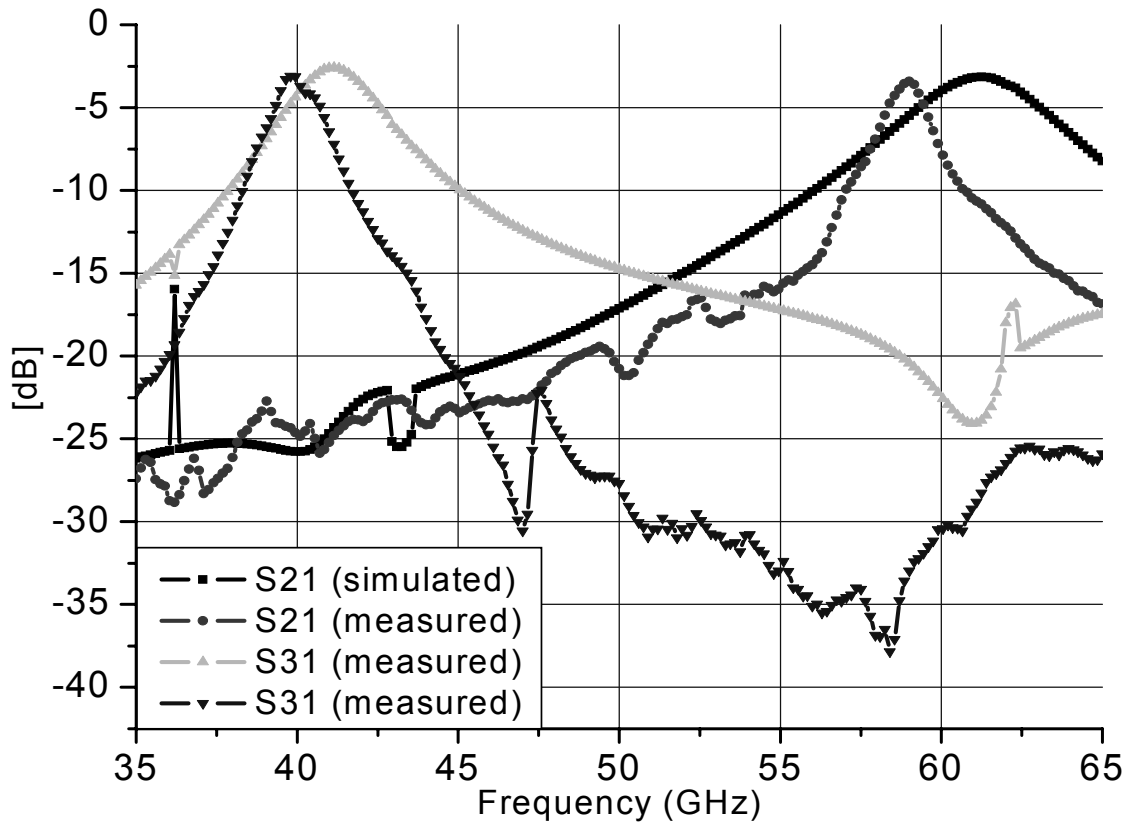


Figure 16: Measured and simulated insertion loss for both channels of duplexer.

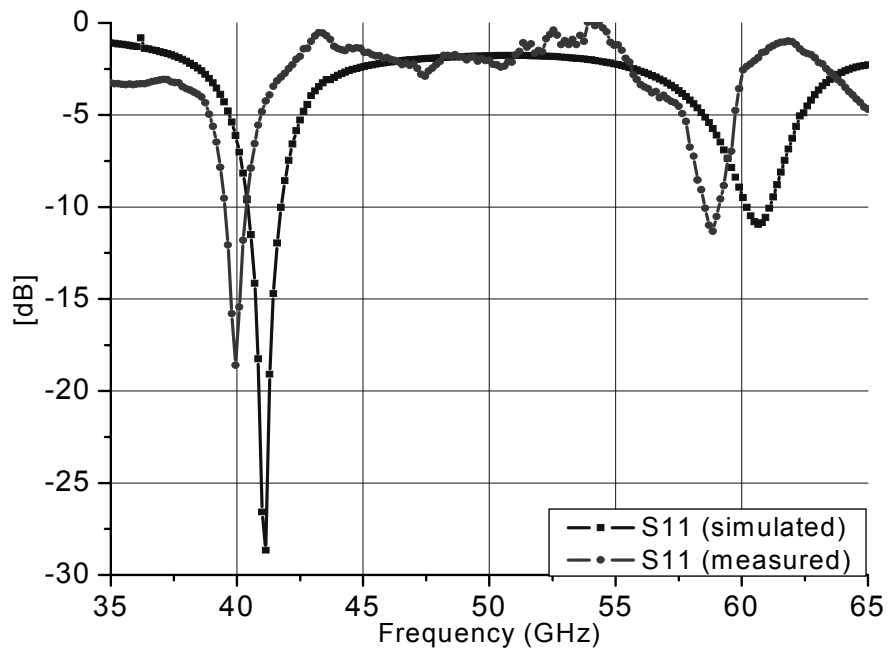


Figure 17: Measured and simulated return loss for both channels of duplexer.

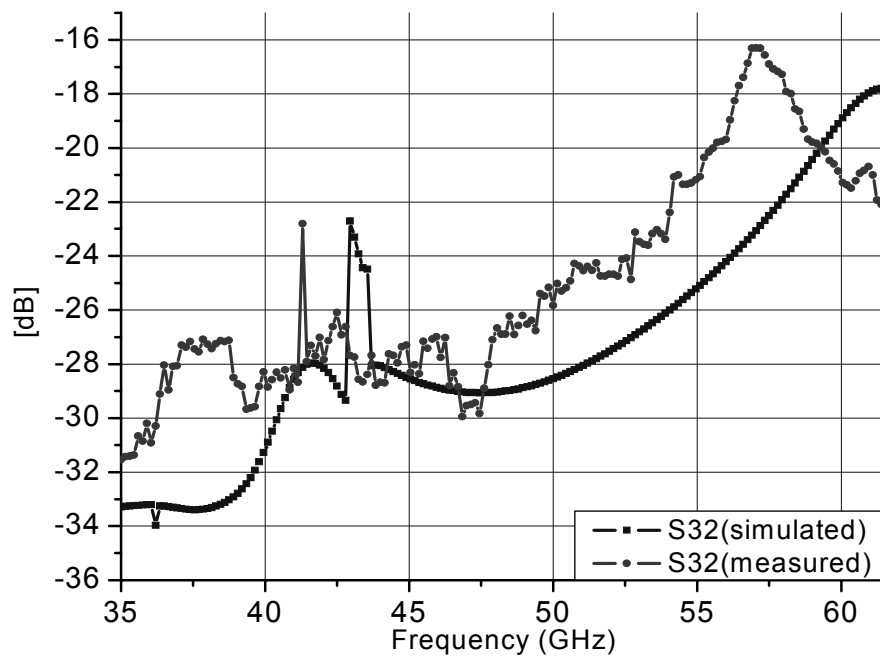


Figure 18: Measured and simulated channel to channel isolation.

3.1.3 Three- and Five-Pole Resonator Filters

We have designed and fabricated symmetrical three-pole and five-pole filters for inter-satellite wideband applications that consist of, respectively, three and five capacitively gap-coupled single-mode resonators, as shown Fig. 19 (a) and (b).

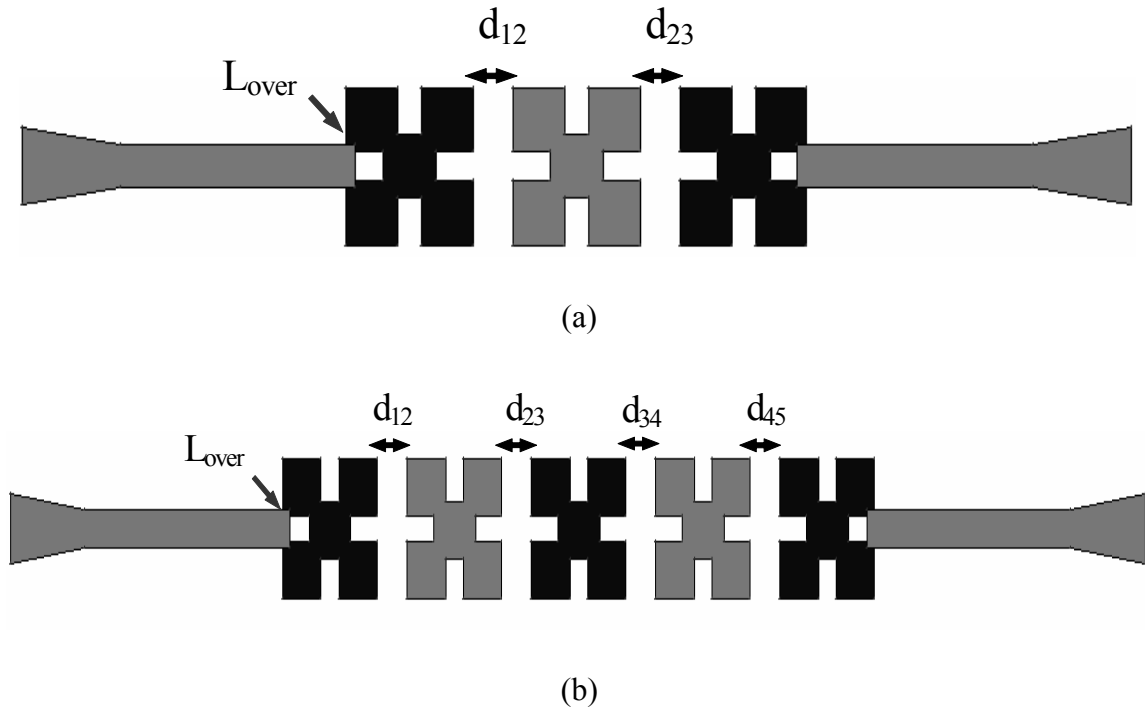


Figure 19: The top view of (a) three-pole slotted patch bandpass filter (b) five-pole slotted patch bandpass filter.

The first three-pole bandpass filter was developed for a center frequency of 59.6 GHz, 1dB insertion loss, 0.1 dB in band ripple, and 6.4% fractional bandwidth based on Chebyshev low-pass prototype filter. The design parameters, such as the external quality factors and the coupling coefficients, were decided to be

$$Q_{ext} = 15.4725$$

$$k_{12}=k_{23} = 0.06128.$$

To determine the physical dimensions, full-wave electromagnetic (EM) simulations (IE3D) were used to extract the coupling coefficients (k_{ii+1} , $i = 1 \text{ or } 2$) and external quality factors (Q_{ext}) based on a simple graphical approach as described in [52]. Feeding lines and slotted patch resonators were alternately located on different metal layers (feeding lines, 2nd resonator: $M2$; 1st resonator, 3rd resonator : $M3$) as shown in Fig. 20 (a) to achieve strong k_{ii+1} between resonators as well as desired Q_{ext} between resonator and feeding line with a moderate sensitivity to the LTCC fabrication tolerances.

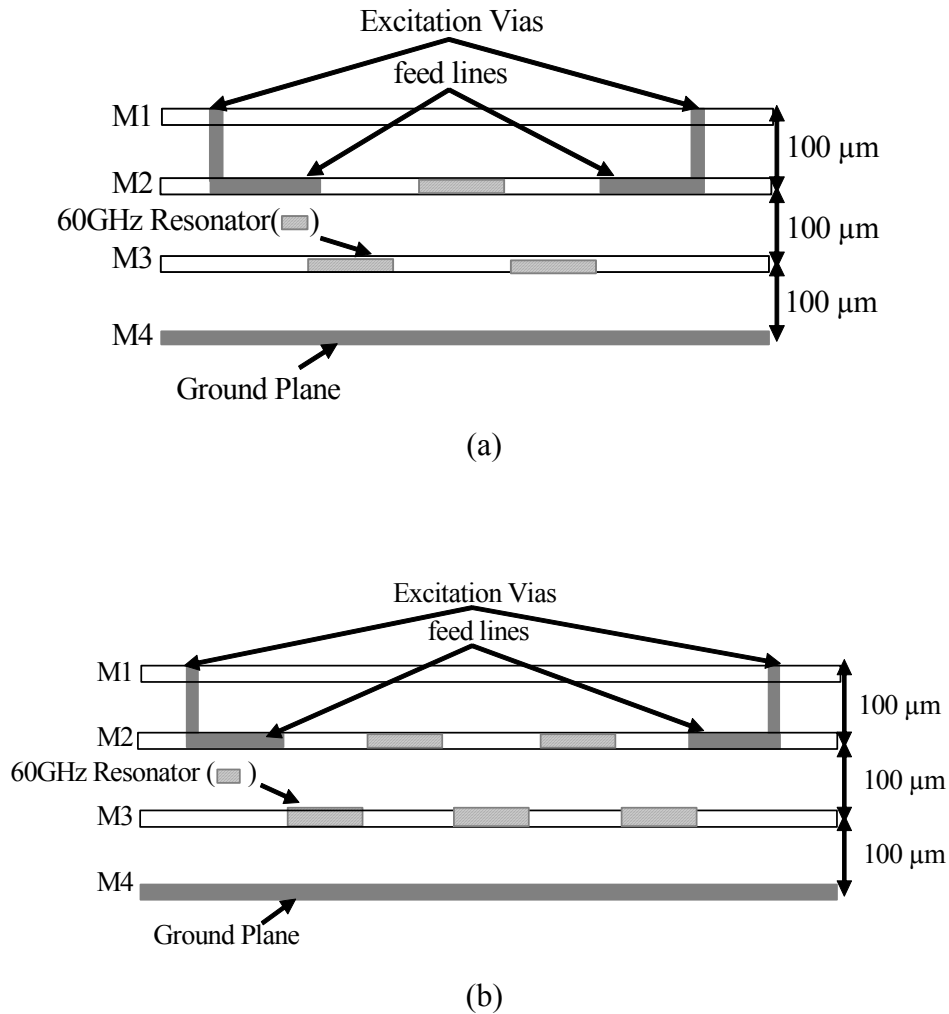
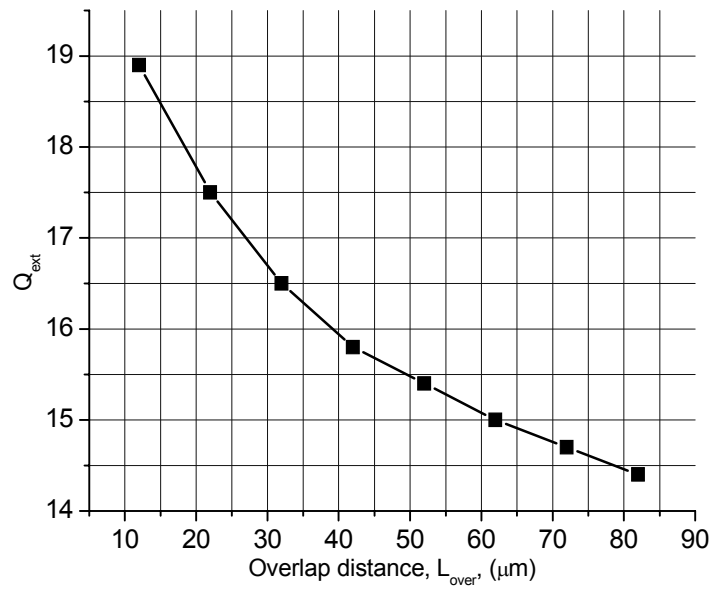
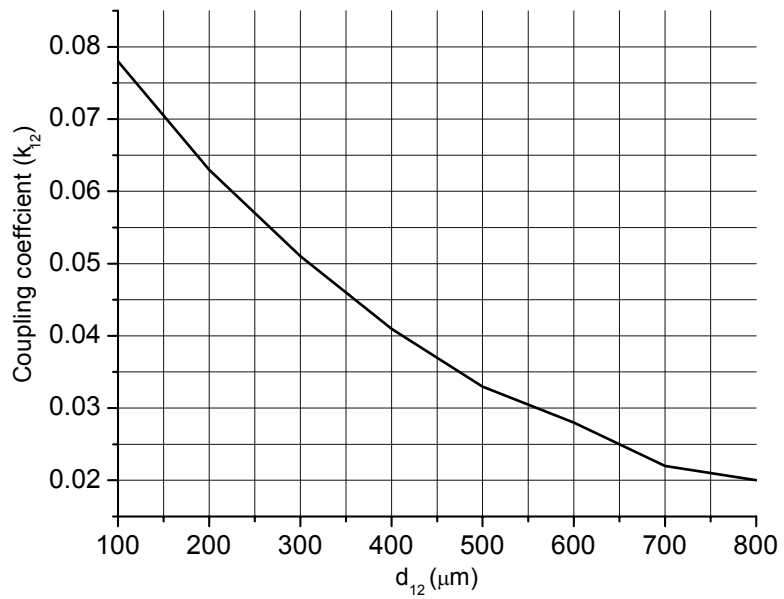


Figure 20: The side view of (a) three-pole slotted patch bandpass filter (b) five-pole slotted patch bandpass filter.



(a)



(b)

Figure 21: (a) External quality factor (Q_{ext}) evaluated as a function of overlap distance (L_{over}) (b) Coupling coefficient, k_{12} , as a function of coupling spacing (d_{12}) between 1st resonator and 2nd resonator.

Figure 21 (a) shows the Q_{ext} evaluated as a function of overlap distance (L_{over}). A larger L_{over} results in a stronger input/output coupling and smaller Q_{ext} . Then, the required k_{ij} is obtained against the variation of distance (d_{ij} in Fig. 19 (a)) for a fixed Q_{ext} at the input/output ports. Full-wave simulation was also employed to find two characteristic frequencies (f_{p1}, f_{p2}) that represent resonant frequencies of the coupled structure when an electrical wall or a magnetic wall, respectively, was inserted in the symmetrical plane of the coupled structure [52]. Characteristic frequencies were associated with the coupling between resonators as follows: $k = (f_{p2}^2 - f_{p1}^2) / (f_{p2}^2 + f_{p1}^2)$ [34]. The coupling spacing (d_{12} in Fig. 19 (a)) between the first and second resonators for the required k_{12} was determined from Fig 21 (b). k_{23} and d_{23} are determined in the same way as k_{12} and d_{12} since the investigated filter is symmetrical around its center.

Figure 22 shows the comparison of the simulated and the measured S-parameters of the three-pole slotted patch filter.

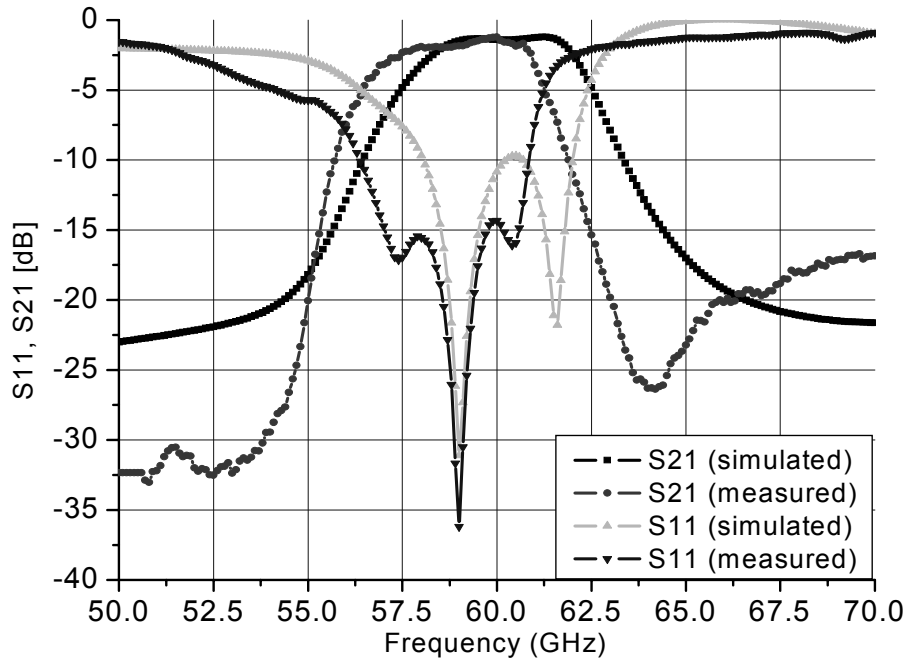


Figure 22: Measured and simulated S-parameters of three-pole slotted patch bandpass filter.

Good correlation is observed, and the filter exhibits an insertion loss < 1.23 dB, the return loss > 14.31 dB over passband, and the 3dB bandwidth about 6.6% at center frequency 59.1GHz. The selectivity on the high side of the passband is better than the EM simulation because an inherent attenuation pole occurs at the upper side. The latter is due to the fact that the space between fabricated nonadjacent resonators might be smaller than that in simulation so that stronger cross coupling might occur. In addition, the measured insertion loss is slightly higher than the theoretical result because of additional conductor loss and radiation loss from the feeding microstrip lines that cannot be de-embedded because of the nature of Short, Open, Load, and Thru (SOLT) calibration method. The dimension of the fabricated filter is $5.855 \text{ mm} \times 1.140 \text{ mm} \times 0.3 \text{ mm}$ with measurement pads.

A high-order filter design using five-slotted patches (Fig. 19 (b)) and having very similar coupling scheme as the three-pole filter was investigated. The Chebyshev prototype filter was designed for a center frequency of 61.5 GHz, 1.3 dB insertion loss, 0.1 dB band ripple, and 8.13% 3-dB bandwidth. The circuit parameters for this filter are

$$Q_{ext} = 14.106$$

$$k_{12} = k_{45} = 0.0648$$

$$k_{23} = k_{34} = 0.0494$$

Figure 20 (b) shows the side view of a five-pole slotted patch bandpass filter. The feeding lines and the open-circuit resonators have been inserted into the different metallization layers (feeding lines, 2nd resonator, 4th resonator: $M2$; 1st resonator, 3rd resonator, 5th resonator: $M3$) so that the spacing between adjacent resonators and the overlap between the feeding lines and the resonators work as the main parameters of the filter design to achieve the desired coupling coefficients and the external quality factor.

The same technique is applied to the design of five-pole bandpass filters. The filter layout parameters are $d_{12}=d_{45}\approx\lambda_{go}/16$, $d_{23}=d_{34}\approx\lambda_{go}/11$, $L_{over}\approx\lambda_{go}/26$ (Fig. 19 (b)), where λ_{go} is the guided wavelength and the filter size is $7.925\times 1.140\times 0.3\text{mm}^3$.

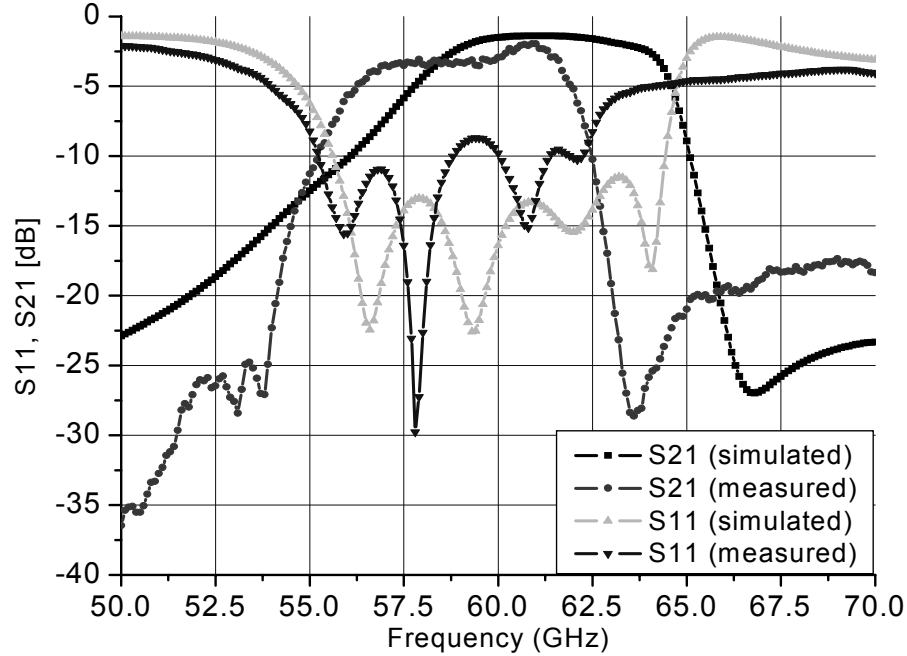


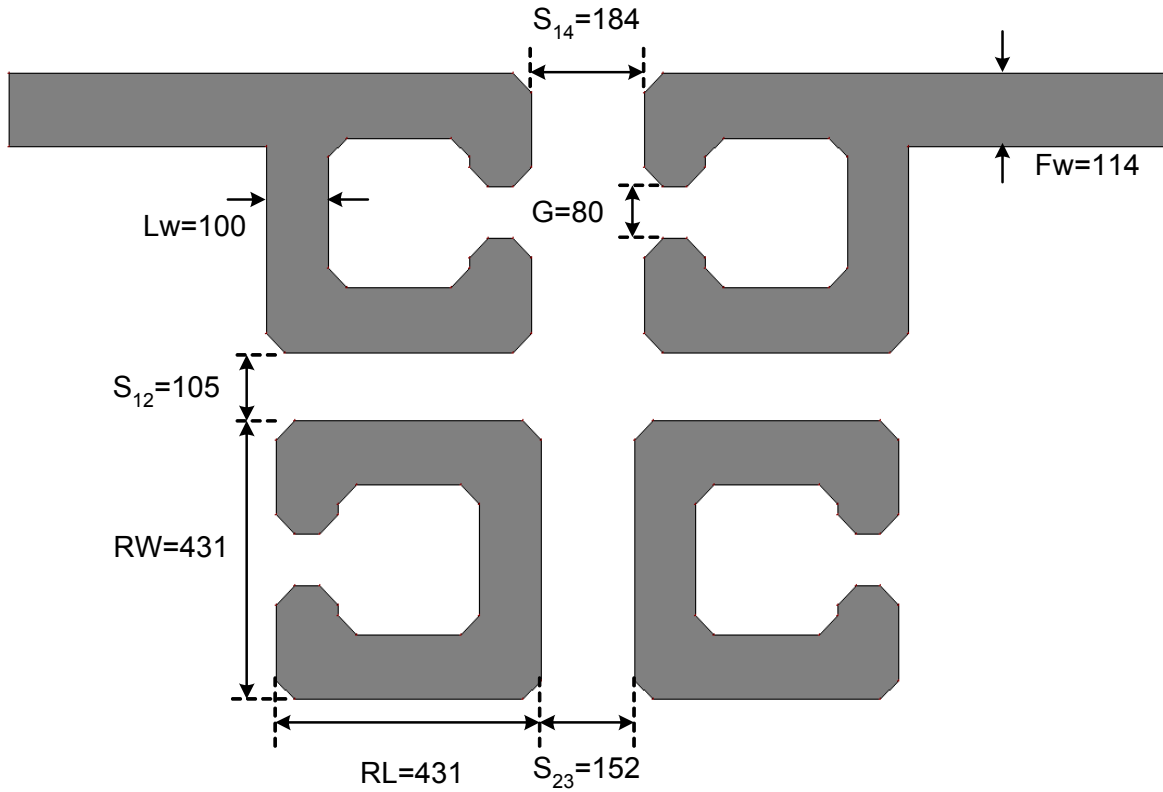
Figure 23: Measured and simulated S-parameters of five-pole slotted patch bandpass filter.

The measured insertion and reflection loss of the fabricated filter are compared with the simulated results in Fig. 23. The fabricated filter exhibits a center frequency of 59.15 GHz, an insertion loss of about 1.39 dB, and a 3-dB bandwidth of approximately 7.98%. These multi-pole filters can be used in the development of a multi-pole duplexer. The difference between the measurement and simulation is attributed to the fabrication tolerances, as mentioned in the case of the three-pole bandpass filter.

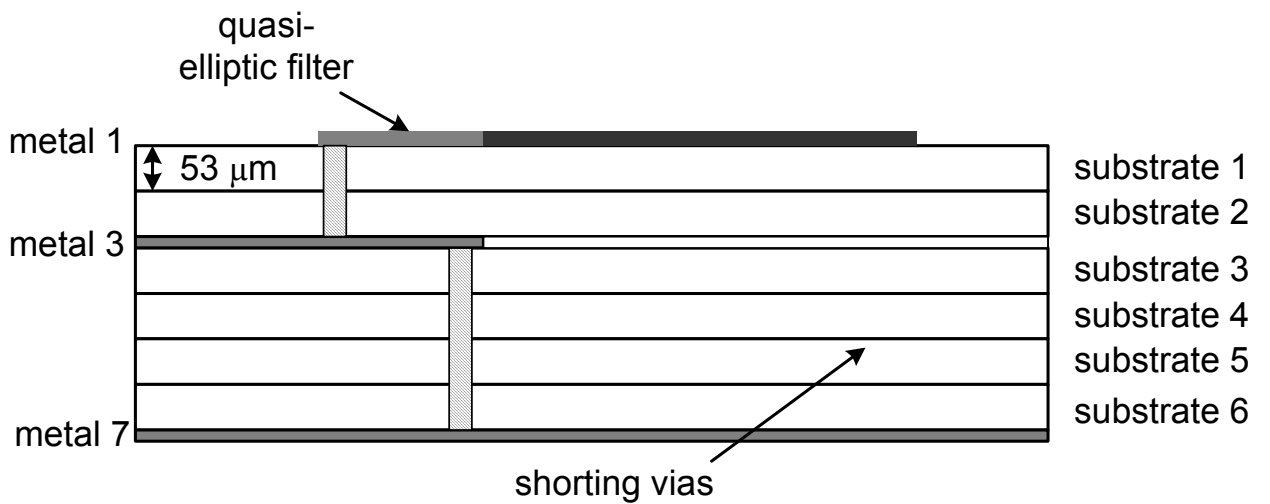
3.2 Quasi-Elliptic Filter

Numerous researchers [52]-[53] have demonstrated narrow bandpass filters employing open-loop resonators for current mobile communication services at L- and S- bands. In this section, the design of a four-pole quasi-elliptic filter is presented as a filter solution for LTCC 60 GHz front-end module because it exhibits a superior skirt selectivity by providing one pair of transmission zeros at finite frequencies, enabling a performance between that of the Chebyshev and elliptical-function filters [52]. The very mature multilayer fabrication capabilities of LTCC ($\epsilon_r=7.1$, $\tan\delta=0.0019$, metal layer thickness: 9 μm , number of layers: 6, dielectric layer thickness: 53 μm , minimum metal line width and spacing: up to 75 μm) make it one of the leading competitive solutions to meet millimeter-wave design requirements in terms of physical dimensions [52] of the open-loop resonators ($\approx 0.2\lambda_g \times 0.2\lambda_g$), achieving a significant miniaturization because of relatively high ϵ_r , and spacing ($\geq 80 \mu\text{m}$) between adjacent resonators that determine the coupling coefficient of the filter function. All designs have been simulated using the MOM-based, 2.5 full-wave solver IE3D.

Figure 24 (a) and (b) show the top and cross-section views of the microstrip quasi-elliptic bandpass filter, respectively. The filter was designed according to the filter synthesis proposed by Hong [52] to meet the following specifications: (1) center frequency: 62 GHz (2) fractional bandwidth: 5.61% ($\sim 3.5\text{GHz}$) (3) insertion loss: $< 3\text{dB}$ (4) 35 dB rejection bandwidth: 7.4 GHz. Its effective length (RL in Fig. 24 (a)) and width (RW in Fig. 24 (a)) has been optimized to be approximately $0.2\lambda_g$ using a full-wave simulator (IE3D) [52]. The design parameters, such as the coupling coefficients (C_{12} , C_{23} , C_{34} , C_{14}) and the Q_{ext} can be theoretically determined by the formulas [52]



(a)



(b)

Figure 24: (a) Top view and (b) cross-section view of 4-pole quasi-elliptic bandpass filter consisting of open-loop resonators fabricated on LTCC. All dimensions indicated in (a) are in μm .

$$Q_{ext} = \frac{g_1}{FBW}$$

$$C_{i,j+1} = C_{n-i,n-i+1} = \frac{FBW}{\sqrt{g_i g_{i+1}}} \quad \text{for } i=1 \text{ to } m-1 \quad (8)$$

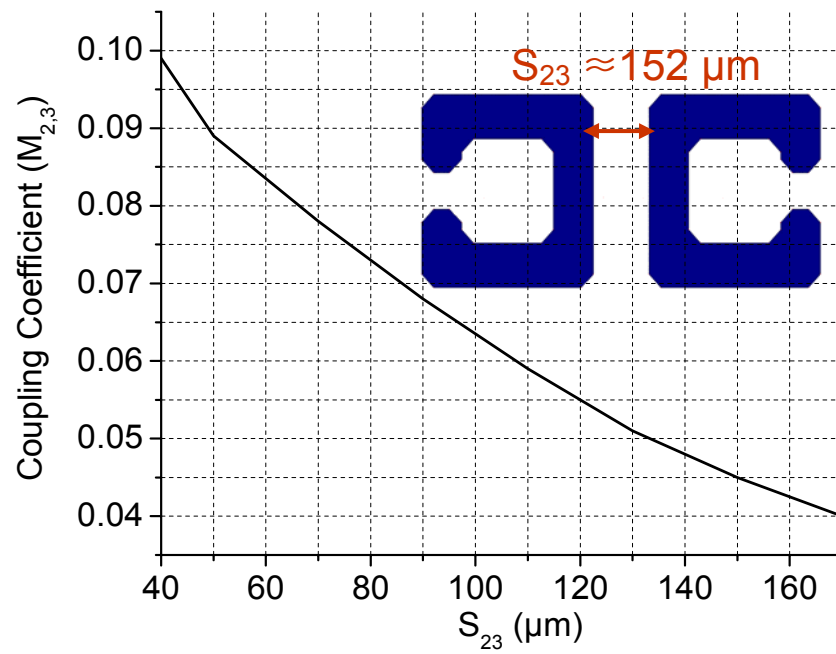
$$C_{m,m+1} = \frac{FBW \cdot J_m}{g_m}$$

$$C_{m-1,m+2} = \frac{FBW \cdot J_{m-1}}{g_{m-1}}$$

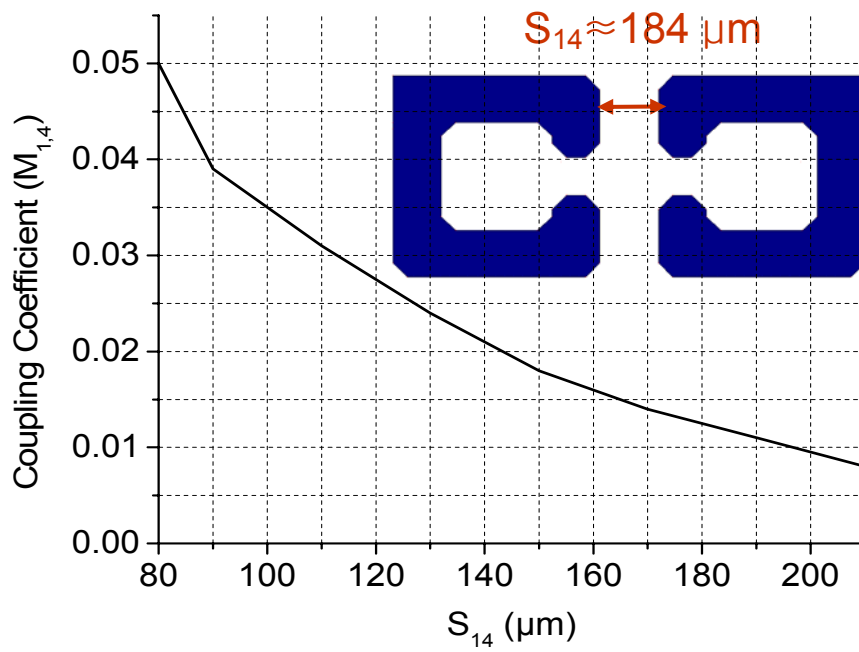
where g_i are the element values of the low pass prototype, FBW is the fractional bandwidth, and J_i are characteristic admittances of the filter. From (8), the design parameters of this bandpass filter are found

$$C_{1,2} = C_{3,4} = 0.048, \quad C_{1,4} = 0.012, \quad C_{2,3} = 0.044, \quad Q_{ext} = 18$$

Then, to determine the physical dimensions of the filter, the full-wave EM simulations are carried out to extract the theoretical values of coupling coefficients and external quality factors [52]. The simulated results are plotted in Fig. 25, where the size of each square microstrip open-loop resonator is $431 \times 431 \mu\text{m}^2$ ($RW \times RL$ in Fig. 24 (a)) with the line width of $100 \mu\text{m}$ (L_w in Fig. 20 (a)) on the substrate. The coupling gaps (S_{23} and S_{14} in Fig. 20 (a)) for the required $C_{2,3}$ and $C_{1,4}$ can be determined from Fig. 25 (a) for the magnetic coupling and Fig. 25 (b) for the electric coupling, respectively. The other coupling gaps (S_{12} and S_{34} in Fig. 24 (a)) for $C_{1,2}$ and $C_{3,4}$ can be found from Fig. 25 (c) for the mixed coupling. The tapered line position (T in Fig. 24 (d)) for the required Q_{ext} is determined from Fig. 25 (d).

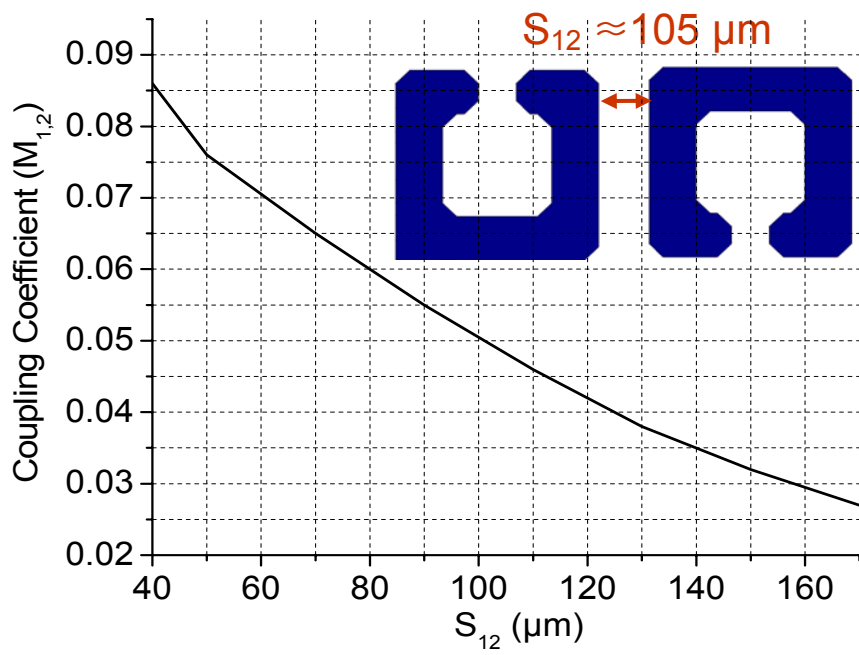


(a)

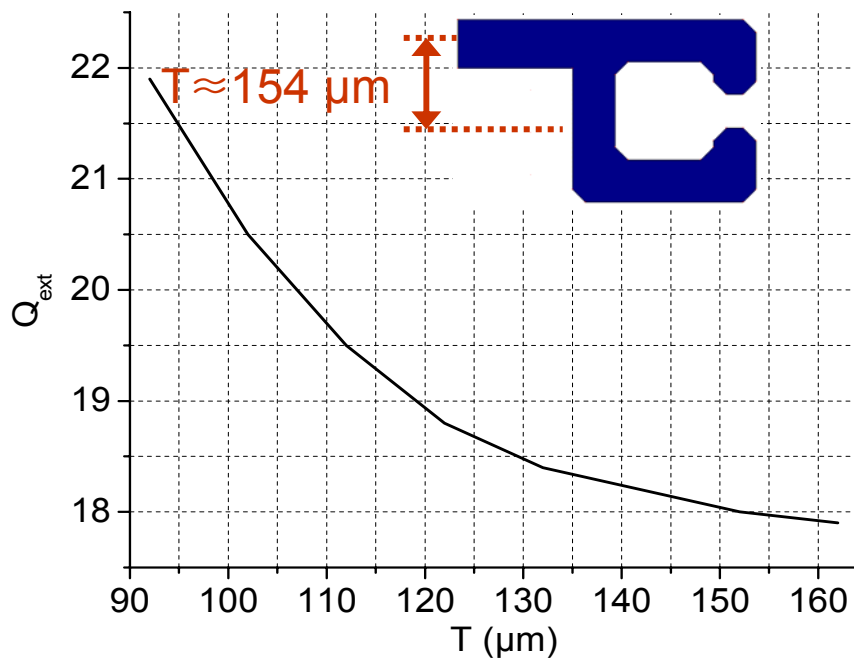


(b)

Figure 25: Design curve (a) Magnetic coupling. (b) Electric coupling. (c) Mixed coupling. (d) External quality factor.



(c)



(d)

Figure 25: Continued.

The quasi-elliptic filter was fabricated on the first metallization layer (*metal 1* in Fig 24. (b)), which is placed two substrate layers ($\sim 106 \mu\text{m}$) above the first ground plane on *metal 3*. That is the minimum substrate height to realize the 50Ω microstrip feeding structure on LTCC substrate. This ground plane is connected to the second ground plane located on the back side of the substrate through shorting vias (pitch: $390 \mu\text{m}$, diameter: $130 \mu\text{m}$), as shown in Fig. 24 (b) [54]. The four additional substrate layers (*substrate 3-6* in Fig. 24 (b)) are reserved for an integrated filter and antenna functions implementation, because antenna bandwidth requires higher substrate thickness than the filter.

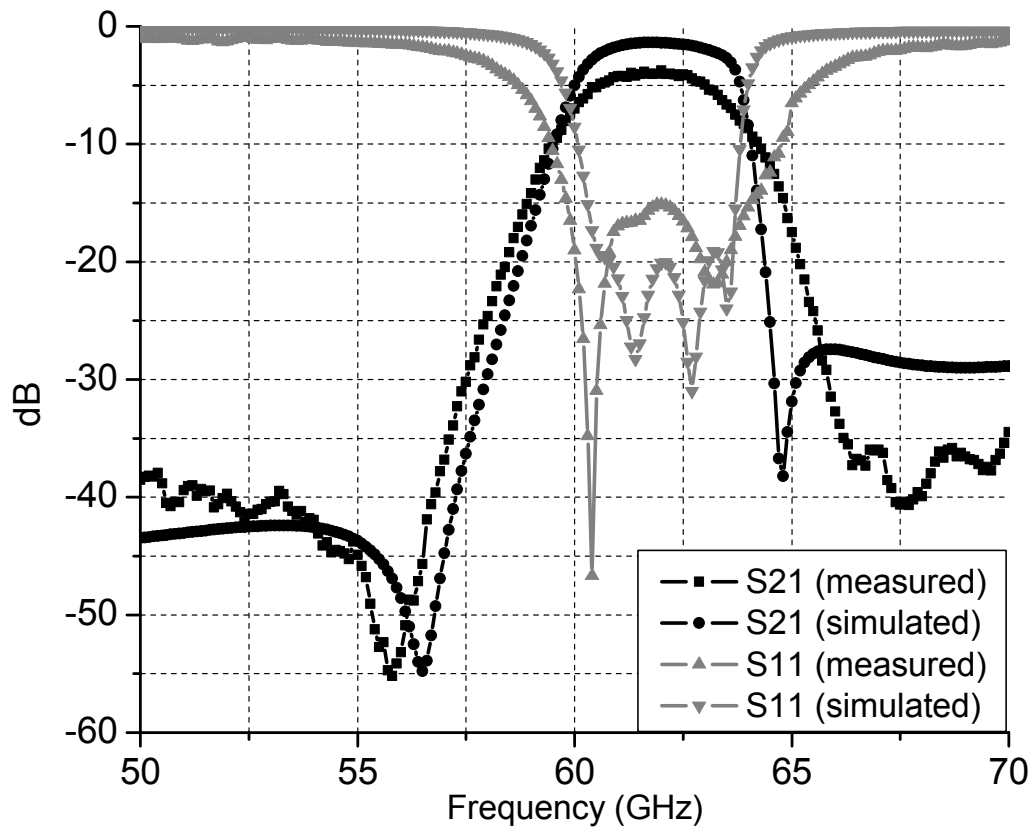


Figure 26: The comparison between measured and simulated S-parameters (S21 & S11) of the four-pole quasi-elliptic bandpass filter composed of open-loop resonators.

Figure 26 shows the comparison between the simulated and measured S-parameters of the bandpass filter. The filter exhibits an insertion loss < 3.5 dB which is higher than the simulated values of < 1.4 dB and a return loss > 15 dB compared to a simulated value of < 21.9 dB over the passband. The loss discrepancy can be attributed to conductor loss caused by the strip edge profile and the quality of the edge definition of metal traces since the simulations assume a perfect definition of metal strips. Also, the metallization surface roughness may influence the ohmic loss because the skin depth in a metal conductor is very low at these high frequencies. The measurement shows a slightly decreased 3-dB fractional bandwidth of 5.46 % (~ 3.4 GHz) at a center frequency of 62.3 GHz. The simulated results give a 3-dB bandwidth of 5.61 % (~ 3.5 GHz) at a center frequency 62.35 GHz. The transmission zeros are observed within less than 5 GHz away from the cut-off frequency of the passband. The discrepancy of the zero positions between the measurement and the simulation can be attributed to the fabrication tolerance. However, the overall response of the measurement correlates very well with the simulation.

CHAPTER 4

CAVITY-TYPE INTEGRATED PASSIVES

4.1 Rectangular Cavity Resonator

The proposed cavity resonators are based on the theory of rectangular cavity resonators [49], and all designs are optimized with the aid of a finite element method (FEM)-based full-wave simulator (HFSS).

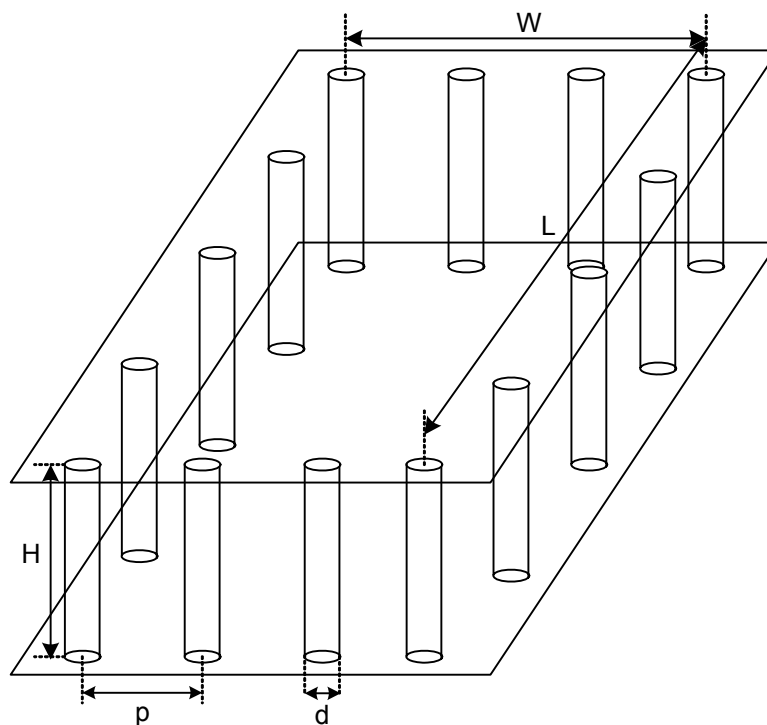


Figure 27: Cavity resonator utilizing via fences as side walls.

The cavity resonator is built utilizing conducting planes as horizontal walls and via fences as side walls, as shown in Fig. 27. The size (d in Fig. 23) and spacing (p in Fig. 23) of via posts are properly chosen to prevent electromagnetic field leakage and to achieve stop-band

characteristic at the desired resonant frequency [23]. The resonant frequency of the TE_{mnl} mode is obtained by [49]

$$f_{res} = \frac{c}{2\pi\sqrt{\epsilon_r}} \sqrt{\left(\frac{m\pi}{L}\right)^2 + \left(\frac{n\pi}{H}\right)^2 + \left(\frac{l\pi}{W}\right)^2} \quad (9)$$

where f_{res} is the resonant frequency, c the speed of light, ϵ_r the dielectric constant, L the length of cavity, W the width of cavity, and H the height of the cavity. Using (9), the initial dimensions of the cavity with perfectly conducting walls are determined for a resonant frequency of 60 GHz for the TE_{101} dominant mode by simply indexing $m=1$, $n=0$, $l=1$ and are optimized with a full-wave electromagnetic simulator ($L=1.95$ mm, $W=1.275$ mm, $H=0.3$ mm). Then, the design parameters of the feeding structures are slightly modified to achieve the best performance in terms of low insertion loss and accurate resonant frequency.

To decrease the metal loss and enhance the quality factor, the vertical conducting walls are replaced by a lattice of via posts. In our case, we use Cassivi's expressions [55] to get the preliminary design values, and then the final dimensions of the cavity are fine tuned with the HFSS simulator. The spacing (p) between the via posts of the sidewalls is limited to less than the half guided wavelength ($\lambda_g/2$) at the highest frequency of interest so that the radiation losses become negligible [23]. Also, it has been proven that smaller via sizes result in an overall size reduction of the cavity [23]. In our case, we used the minimum size of vias (d (via diameter) = 130 μm in Fig. 27) allowed by the LTCC design rules. Also, the spacing between the vias has been set to be the minimum via pitch (390 μm).

In the case of low external coupling, the unloaded Q, Q_u , is controlled by three loss mechanisms and defined by [48]

$$Q_u = \left(\frac{1}{Q_{cond}} + \frac{1}{Q_{dielec}} + \frac{1}{Q_{rad}} \right)^{-1} \quad (10)$$

where Q_{cond} , Q_{dielec} , and Q_{rad} take into account the conductor loss from the horizontal plates (the metal loss of the horizontal plates dominates especially for a thin substrate such as 0.3 mm), the dielectric loss from the filling substrates, and the leakage loss through the via walls, respectively. Since the gap between the via posts is less than $\lambda_g/2$ at the highest frequency of interest as mentioned, the leakage (radiation) loss can be negligible, as mentioned above, and the individual quantity of the two other quality factors can be obtained from [48]

$$Q_{cond} = \frac{(kWL)^3 H \eta}{2\pi^2 R_m (2W^3 H + 2L^3 H + W^3 L + L^3 W)} \quad (11)$$

where k is the wave number in the resonator ($(2\pi f_{res}(\epsilon_r)^{1/2})/c$), R_m is the surface resistance of the cavity ground planes ($(\pi f_{res} \mu / \sigma)^{1/2}$), η is the wave impedance of the LTCC resonator filling, L, W, H are the length, width, and height of the cavity resonator, respectively and

$$Q_{dielec} = \frac{1}{\tan(\delta)} \quad (12)$$

where $\tan\delta$ is the loss tangent (=0.0015) of the LTCC substrate. The quality factor equations (10)-(12) of a rectangular cavity can be used in the cavity using via-array sidewalls due to effective performance of the via-arrays, which almost matches the performance of the PEC's [22],[25].

The loaded quality factor (Q_l) can be obtained by adding the losses (Q_{ext}) of the external excitation circuit to the Q_u as expressed in [48]

$$Q_l = \left(\frac{1}{Q_u} + \frac{1}{Q_{ext}} \right)^{-1} . \quad (13)$$

The theoretical Q values can be extracted from the simulated performances of a weakly coupled cavity resonator using the following equations [48]

$$Q_l = \frac{f_{res}}{\Delta f} \quad (14)$$

$$S_{21}(dB) = 20 \log_{10} \left(\frac{Q_l}{Q_{ext}} \right) \quad (15)$$

$$Q_u = \left(\frac{1}{Q_l} - \frac{1}{Q_{ext}} \right)^{-1} \quad (16)$$

where Δf is the 3-dB bandwidth.

The weak external coupling ($S_{21} \sim 20$ dB) is imperative verifying the Q_u of the cavity resonator. The comparison between the theoretical and the HFSS-based Q_u values is discussed in section 4.2. The external coupling strength of three feeding techniques is also compared in section 4.2 based on the Q_{ext} measured from strongly coupled resonators using (14)-(15). All fabricated resonators were measured using the Agilent 8510C Network Analyzer and Cascade Microtech probe station with 250 μm pitch air coplanar probes. A standard SOLT method was employed for calibration.

4.2 Cavity Feeding Structures

4.2.1 Slot Excitation with a Shorting Via

Figure 28 shows (a) the top view, (b) a 3D overview, and (c) the side view of the proposed structure.

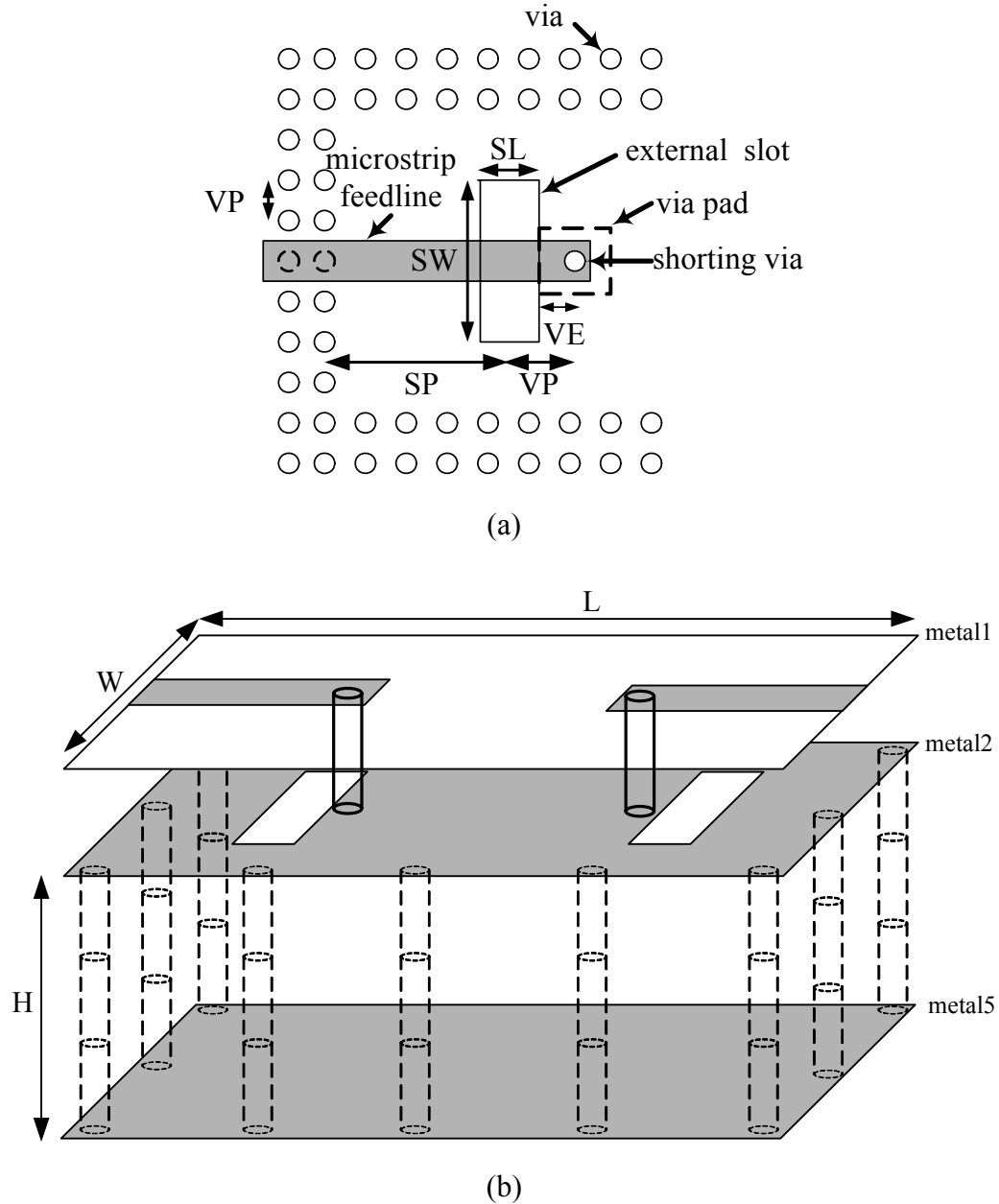
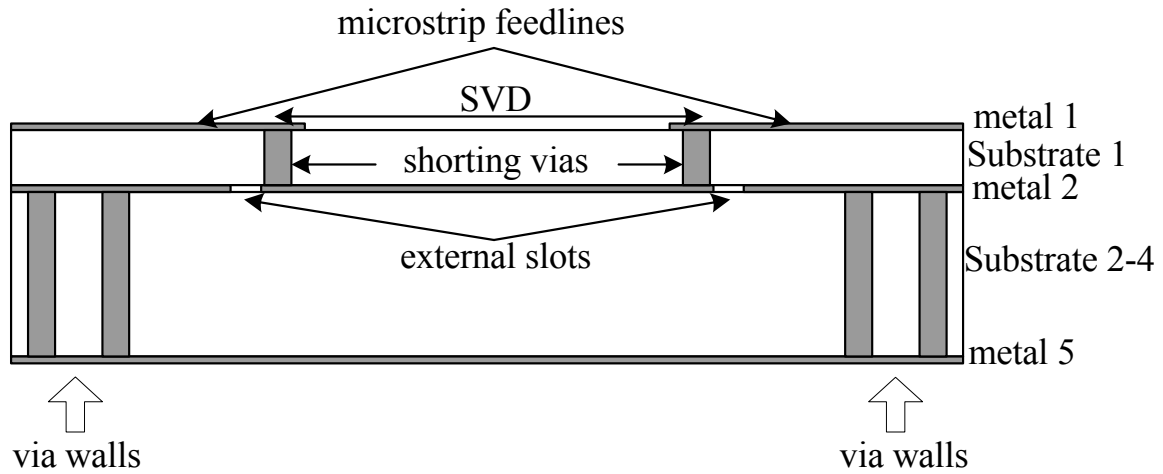


Figure 28: LTCC cavity resonator employing slot excitation with a shorting via (a) top view of feeding structures, (b) 3D overview and (c) side view of the proposed resonator.



(c)

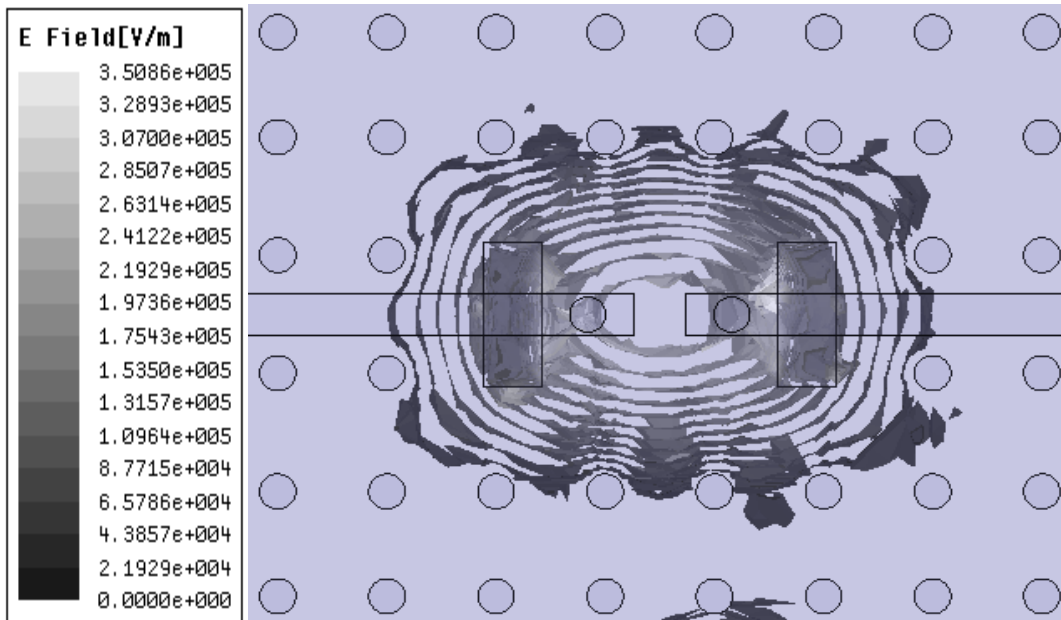
Figure 28: Continued.

Microstrip lines are utilized to excite the resonator through coupling slots etched in the top metal layer (*metal 2*) of the cavity, as shown in Fig. 28 (c). In order to maximize the magnetic coupling by maximizing magnetic currents, the microstrip lines are terminated with a physical short circuit realized by a metallic via. The spacing (VE in Fig. 28 (a)) between the center of the via and the edge of the slot is determined to be $165 \mu\text{m}$ according to the LTCC design rules we used.

The accurate design of the external coupling slots is a key issue to achieve a high- Q cavity resonator. The external coupling factor is directly related to the input resistance and reactance that can be controlled by the position and size of the coupling aperture [23]. To determine the dimensions of the slots for the optimum response, the coupling slots are initially located at a quarter of the cavity length (SP in Fig. 28 (a)) from the edge of the cavity to maximize the coupling, and then the slot width (SW in Fig. 28 (a)) is varied with the constant slot length ($SL \approx \lambda_g/4$ at 60 GHz in Fig. 28 (a)). As the slot width increases, the radius of the simulated

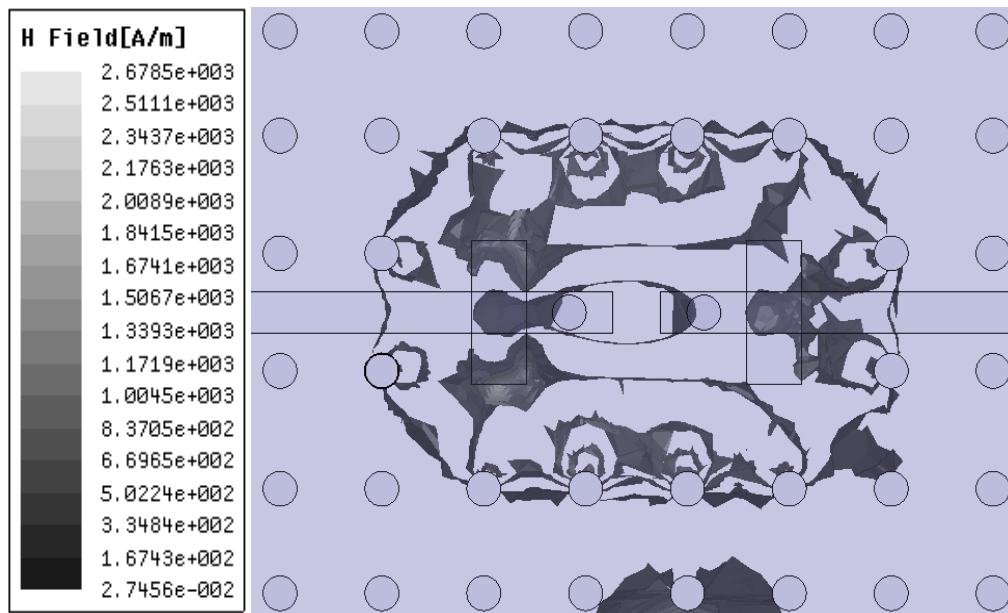
impedance locus increases, which denotes a strong external coupling. The dimensions of the coupling slots have been determined to be $0.538 \times 0.21 \text{ mm}^2$ ($\approx 0.21\lambda_g \times 0.08\lambda_g$). Then, the position of the slots is adjusted to obtain the desired insertion loss, resonant frequency, and input impedances. The optimized results for resonant frequency (59.9 GHz), insertion loss (1.07 dB), and bandwidth (1.5%) are obtained with $SP=0.4475 \text{ mm}$ ($\approx 0.19\lambda_g$) (Fig. 28 (a)).

The solid conducting sidewalls are replaced with rows of vias. The spacing between via rows is set to the minimum via pitch (390 μm). In this process, major filter characteristics such as resonant frequency and insertion loss are affected not only by the via pitch/diameter but also by the number of rows of vias. The resonator characteristics are investigated with the increase of the number of via rows (1 \rightarrow 3). Double and triple rows exhibit almost the same characteristics such as an insertion loss of 1.14 dB, while a single row exhibits 1 dB higher insertion loss as a result of a higher leakage.

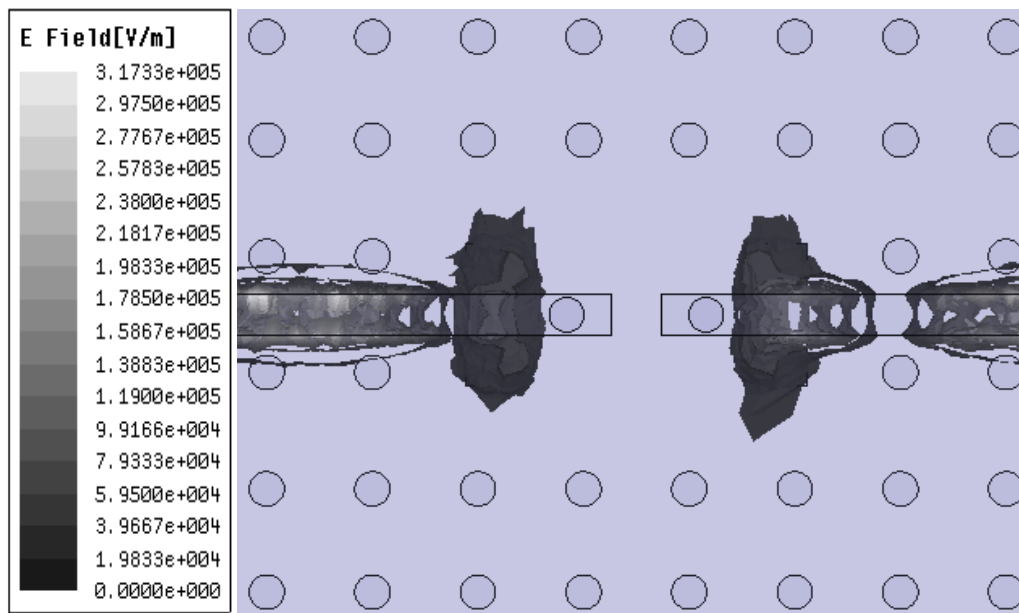


(a)

Figure 29: (a) Electric field distribution and (b) Magnetic field distribution inside the cavity (*substrate 2-4* in Fig. 28 (c)) using shorting vias at resonant frequency (=59.4 GHz) (c) Electric field distribution of the top substrate layer (*substrate 1* in Fig. 28 (c)).



(b)



(c)

Figure 29: Continued.

Figure 29 shows (a) the electric field distributions, (b) the magnetic field distributions inside the cavity surrounded by rows of vias, and (c) the electric field distributions of the top substrate. It is clearly observed that two rows of vias are sufficient to block the field leakage through vias in Fig. 29 (a). Nevertheless, in the fabrication, three rows of via posts were used to ensure a high level of leakage block with respect to both the simulation error and the fabrication accuracy. The simulation of the top substrate (Fig. 29 (c)) shows the decoupling between the two microstrip feedlines because of shorted vias providing the necessary shielding. All final design parameters are summarized in Table 2.

The proposed cavity resonator was fabricated in LTCC multilayer substrate ($\epsilon_r=5.4$, $\tan\delta=0.0015$). The dielectric thickness per layer is 100 μm , and the metal thickness is 9 μm . Its photograph is shown in Fig. 30. The overall size was 3.8 mm \times 3.2 mm \times 0.3 mm³ (including the CPW measurement pads).

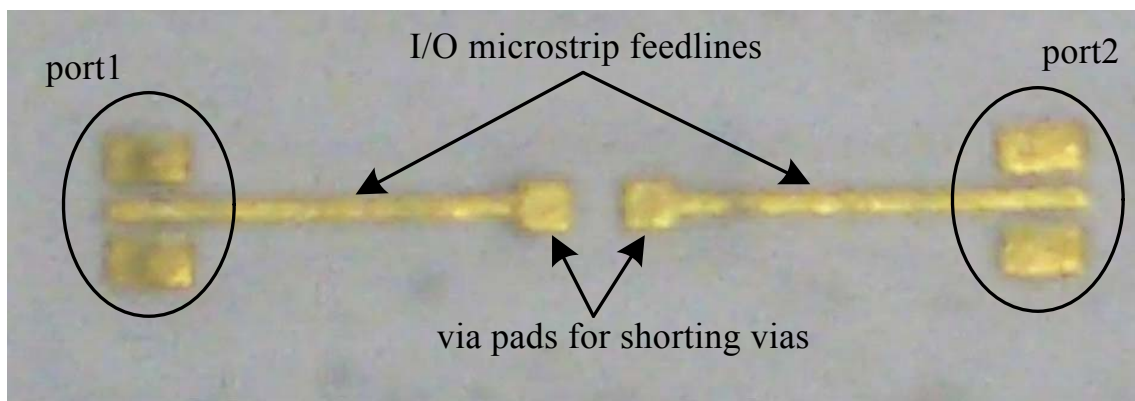


Figure 30: The photograph of the fabricated cavity resonator using slot excitation with a shorting via.

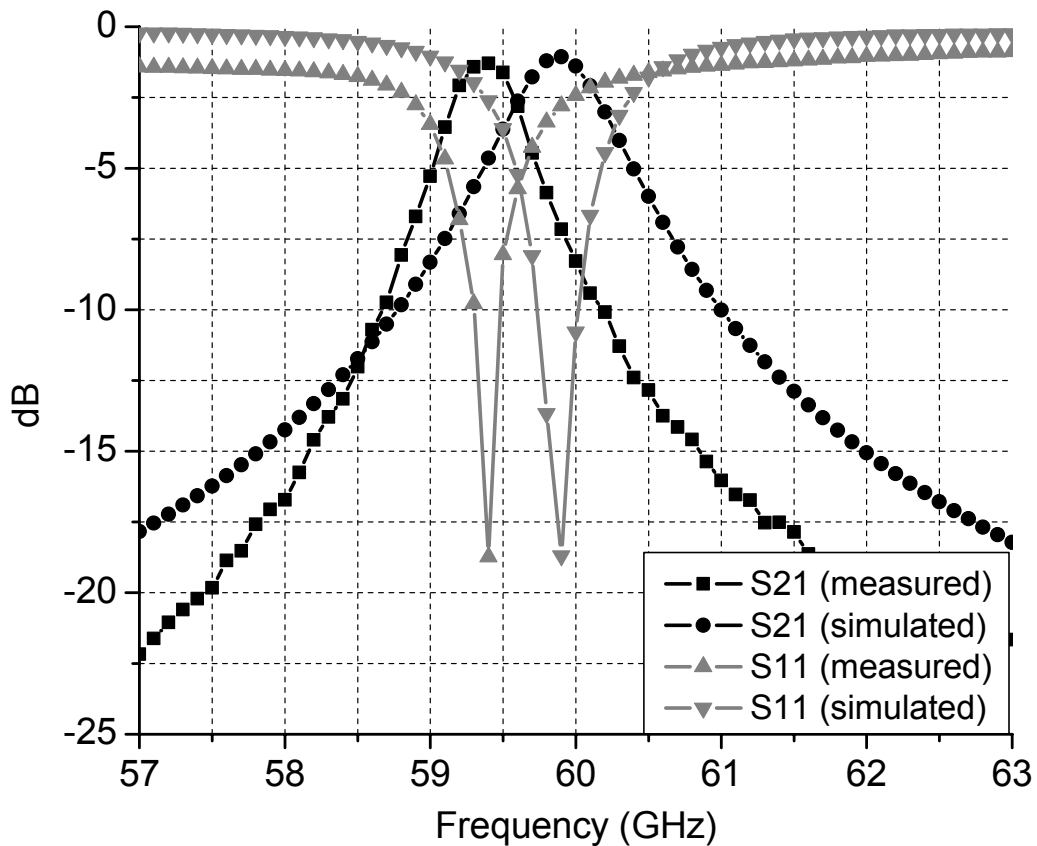


Figure 31: The comparison between measured and simulated S-parameters (S11 & S21) of a cavity resonator using slot excitation with a shorting via.

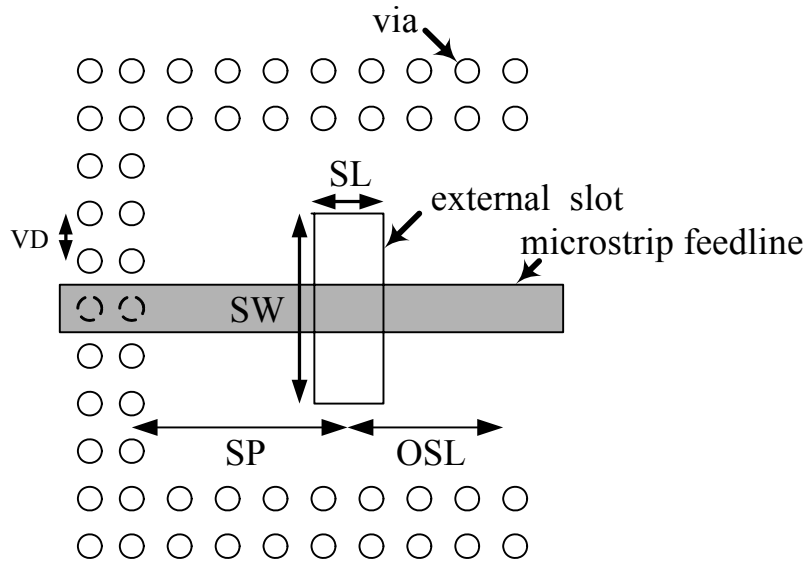
The measured insertion and reflection loss of the fabricated cavity are compared with the simulated results in Fig. 31. The measured insertion loss is 1.28 dB, which is 0.21 dB higher than the simulated value, while return losses match closely. The main source of this discrepancy might be the radiation loss from the feeding line. The center frequency shift from 59.9 GHz to 59.4 GHz can be attributed to the fabrication accuracy (dielectric constant variation, slot positioning affected by the alignment between layers, via positioning tolerance, shrinkage and layer thickness tolerance...). Also, the resonator exhibits a 3-dB bandwidth of about 1.18 % at the center frequency of 59.4 GHz, compared to 1.5% from the simulated model. The narrow

bandwidth in measurements might be due to the fabrication accuracy of the slot design that has been optimized for the original resonant frequency and not for the shifted frequency. Also, in the calibration task, the calibration kit containing information about the Cascade probes and Cascade impedance standard substrates (ISS) was loaded into SOLT dialog box supported by “Wincal” software. Wincal gives us the ability to de-embed capacitance effects of CPW open pads and inductive effects of short pads from device measurements, but it can not effectively remove all parasitic effects at this high frequency range so that we can expect the band-limiting effect to S21 performance as well. The extracted Q_u from the weakly coupled resonators in full-wave simulations was found to be 360 that is lower than the theoretical Q_u of 372 obtained using (10)-(12). The Q_{ext} was measured to be 73.23.

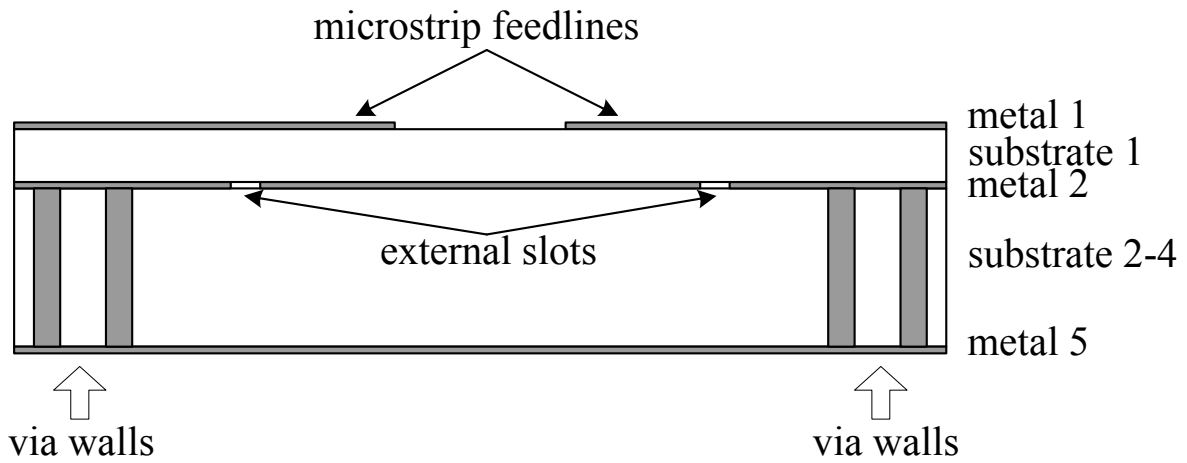
4.2.2 Slot Excitation Using a $\lambda_g/4$ Open Stub

Figure 32 shows (a) the top view of the feeding structure and (b) the side view of the microstrip-fed cavity resonator using a $\lambda_g/4$ open stub slot excitation technique. The structure is the same as in the previous section 4.2.1, except that the microstrip feedline is terminated with a $\lambda_g/4$ open stub beyond the slot.

In the design procedure, the length (OSL in Fig. 32 (a)) of the open stub is initially set up to $\lambda_g/4$. The fringing field generated by an open-end discontinuity can be modeled by an equivalent length of transmission line [56] which is determined to be about $\lambda_g/20$. Therefore, the optimum length of the stub is approximately $\lambda_g/5$. The optimum value, which maximizes the magnetic coupling, is determined using full-wave simulations.

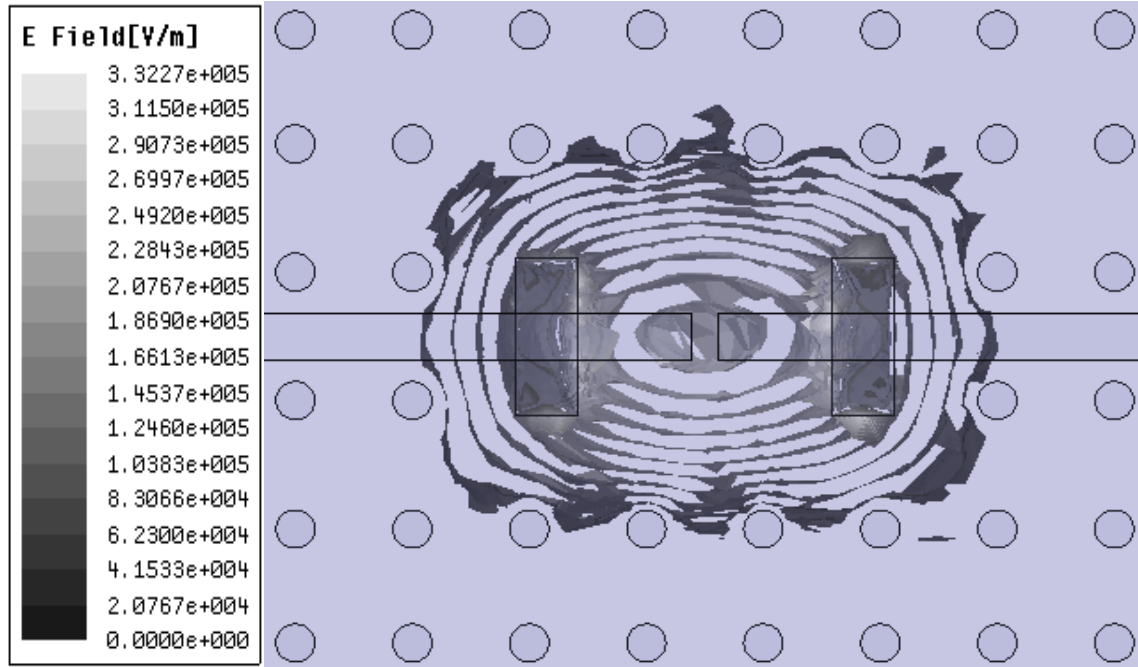


(a)

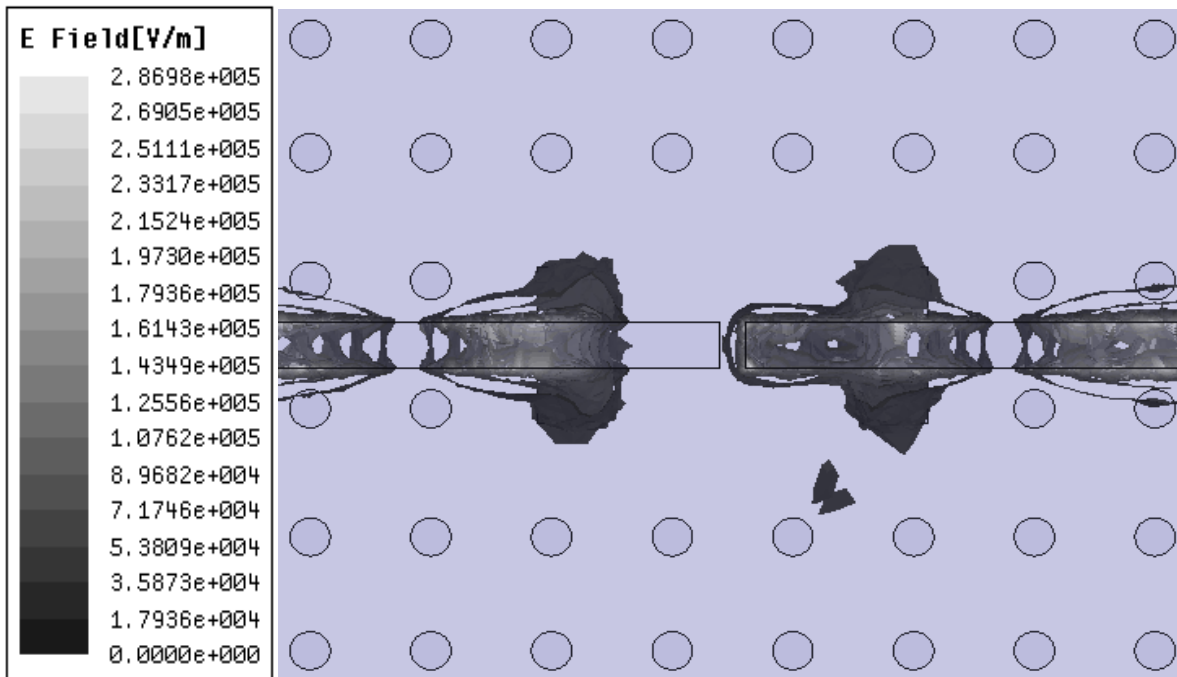


(b)

Figure 32: LTCC cavity resonator employing slot excitation with an open stub (a) the top view of feeding structure (b) the side view of the proposed resonator.



(a)



(b)

Figure 33: (a) Electric field distribution inside the cavity using slot excitation with an open stub at resonant frequency (≈ 59.2 GHz) (b) Electric field distribution of the top substrate layer (*substrate 1* in Fig. 32 (b)).

All design parameters are summarized in Table 2. The magnitude of the electric field distribution inside the cavity is simulated at the resonant frequency of 59.8GHz and its efficient containment is clearly observed in Fig. 33 (a). However, the extended stubs generate electrical coupling effects between the feed-lines and the substrate as shown in Fig. 33 (b). The photograph of the LTCC is shown in Fig. 34.

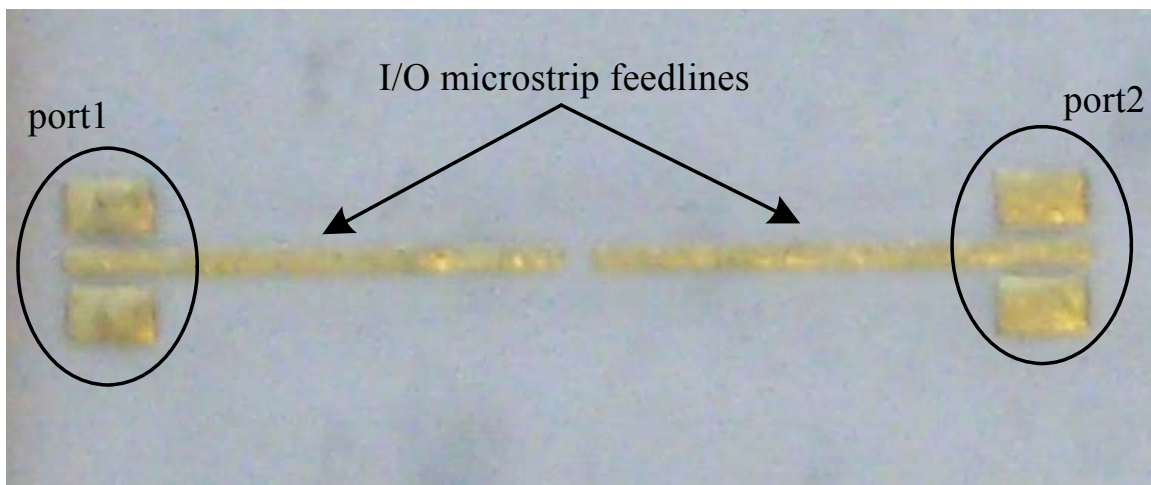


Figure 34: The photograph of the fabricated cavity resonator using slot excitation with an open stub.

Figure 35 shows the simulated and the measured S-parameters of the cavity resonator with open stubs. Good correlation is observed for insertion loss. The resonator measurements exhibit an insertion loss < 0.84 dB, a return loss about 20.59 dB at the center frequency of 59.2 GHz, and a 3-dB bandwidth about 1.5% at the center frequency. The simulation shows almost the same insertion loss and return loss but an increased bandwidth of 2.3% around the center frequency of 59.8 GHz. The narrow bandwidth in measurements might be due to the fabrication accuracy of the slot design that has been optimized for the original resonant frequencies and not for the shifted frequencies.

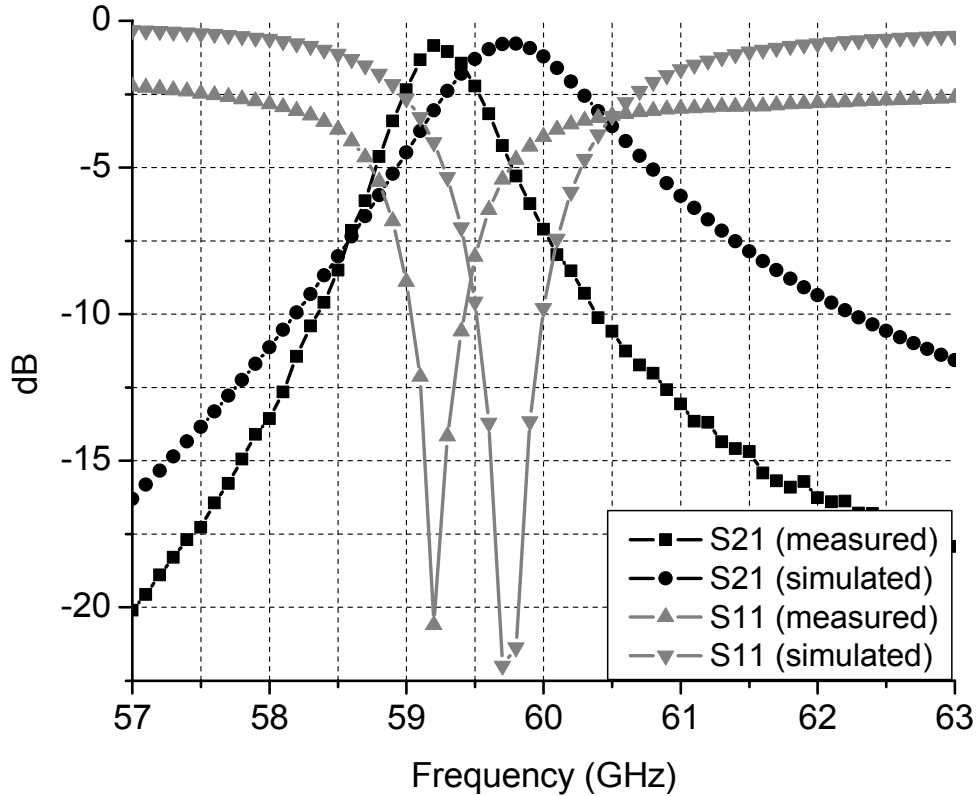


Figure 35: S-parameters (S11 & S21) of a resonator using slot excitation with an open stub (simulation with $\epsilon_r = 5.4$ vs. measurement).

The frequency downshift between measurements and simulations is similar to the one observed on section 4.2.1. The center frequency downshift can be attributed to the dielectric constant variation at these high frequencies. The preliminary HFSS simulation presumed that the averaged relative permittivity would be increased to 5.5 across 55-65 GHz. An expanded plot of a comparison of the simulation with $\epsilon_r = 5.5$ and the measurement is shown in Fig. 36. The coincidence between the center frequencies is observed in Fig. 36. The long input/output feedlines that are terminated with 0.085 mm gap between them could be responsible for the asymmetrical response due to the parasitic cross-coupling and substrate coupling effects as

shown in Fig. 33 (b). The excitation technique using a shorting via takes advantage of the significantly reduced coupling between the two microstrip feedlines because of the vias providing the necessary shielding. Using (14)-(16), the simulated Q_u was found to be 367, which is approximately 2% higher than that with a shorting via. The measured Q_{ext} was 60.52 which is lower than a shorting via ($Q_{ext} \sim 73.23$).

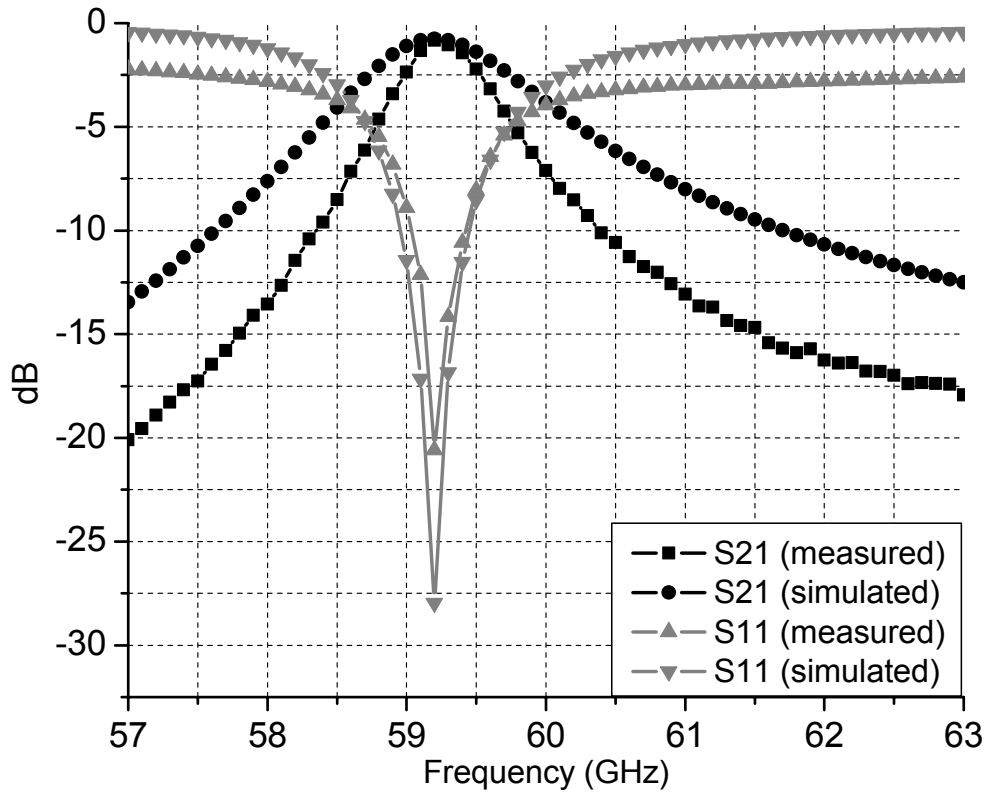


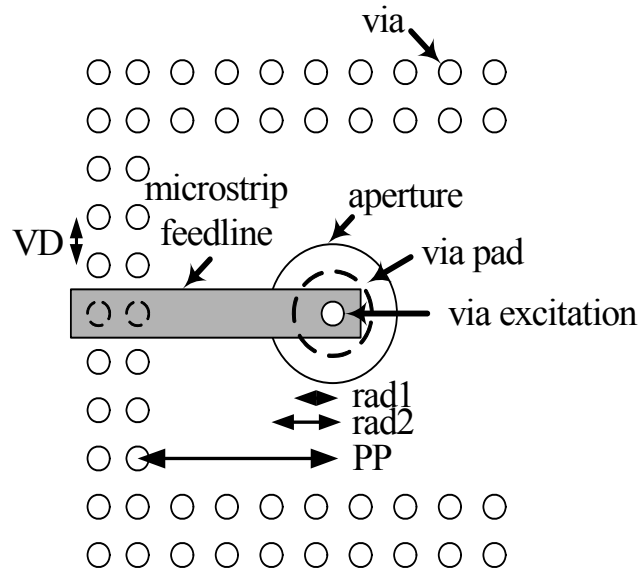
Figure 36: S-parameters (S11 & S21) of a resonator using slot excitation with an open stub (simulation with $\epsilon_r = 5.5$ vs. measurement).

4.2.3 Probe Excitation

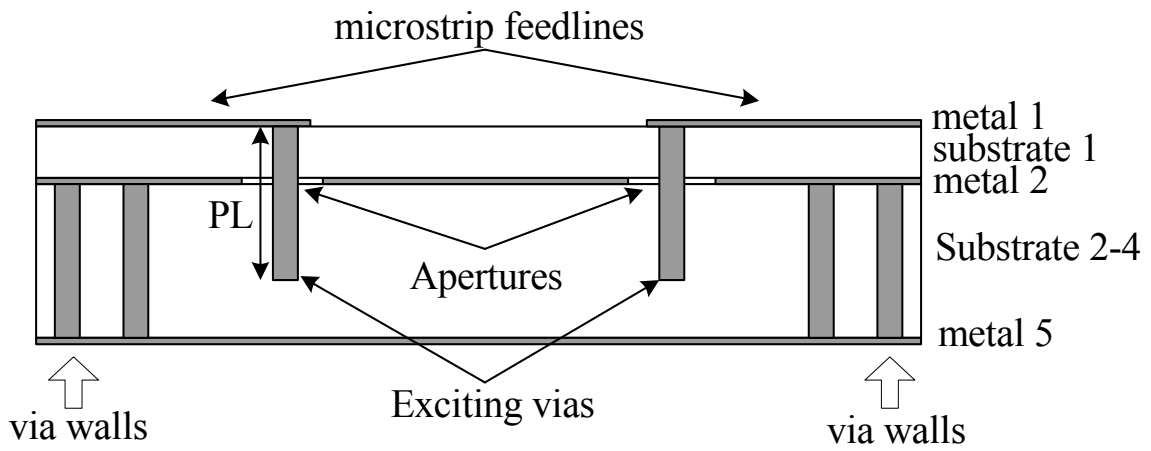
Figure 37 illustrates (a) the top view of the feeding structure and (b) the side view of via-fed cavity resonator. The probe length (PL in Fig. 37 (b)) and the probe position (PP in Fig. 37 (a)) are the dominant design factors to achieve the maximum coupling from the probe to the cavity and are investigated with the aid of HFSS. For maximum coupling with the TE_{101} mode in the cavity, the probe (*exciting vias* in Fig. 37 (b)) descends into the cavity through a circular aperture (*aperture* in Fig. 37 (a)) etched in the second metal layer (*metal 2* in Fig. 37 (b)) up to the location of the maximum electric field at a distance of half of the cavity height. In our design, the excitation probe consists of three vias vertically stacked and penetrates three substrate layers (*substrate 1 – 3* in Fig 37 (b)). The size of the via pads is kept to the minimum size allowed by the LTCC design rules to minimize the parasitic effects.

The effect of the probe position was investigated in terms of insertion loss, bandwidth, and input impedance. The probes were initially located at the edge of the cavity, and then moved toward the center to achieve the strongest coupling possible. The probe position (PP in Fig. 37 (a)) has been found to be optimum at the same location ($PP=0.4475$ mm) as the slot position in sections 4.2.1 and 4.2.2. The effect of the aperture size was also investigated. It was observed from the simulations that the bandwidth gets wider and the insertion loss lower with the decrease of the aperture radius ($rad2$ in Fig. 37 (a)).

The dimension of the cavity composed of the via walls was determined to be 1.95×1.276 mm² ($\approx 0.77\lambda_g \times 0.5\lambda_g$). The width of this cavity is 42 μ m smaller than the ones in section 4.2.1 and 4.2.2. The resonant frequency shifts down because of the probe perturbation. This perturbation can be characterized with induced dipole moments [49]. All design parameters are summarized in Table 2.

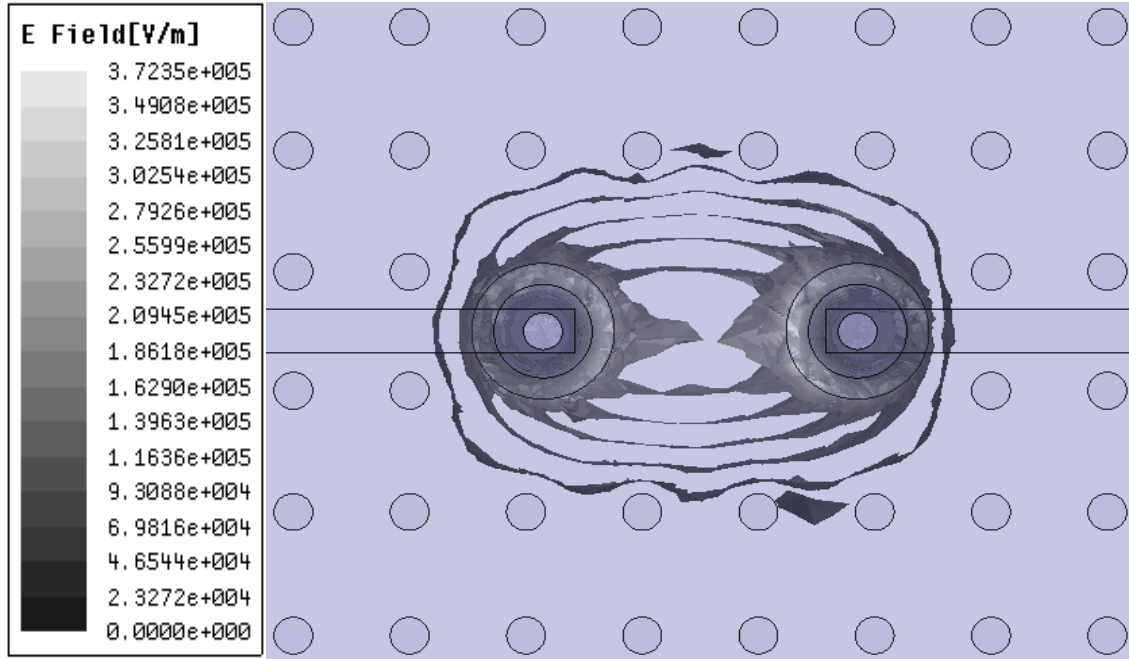


(a)

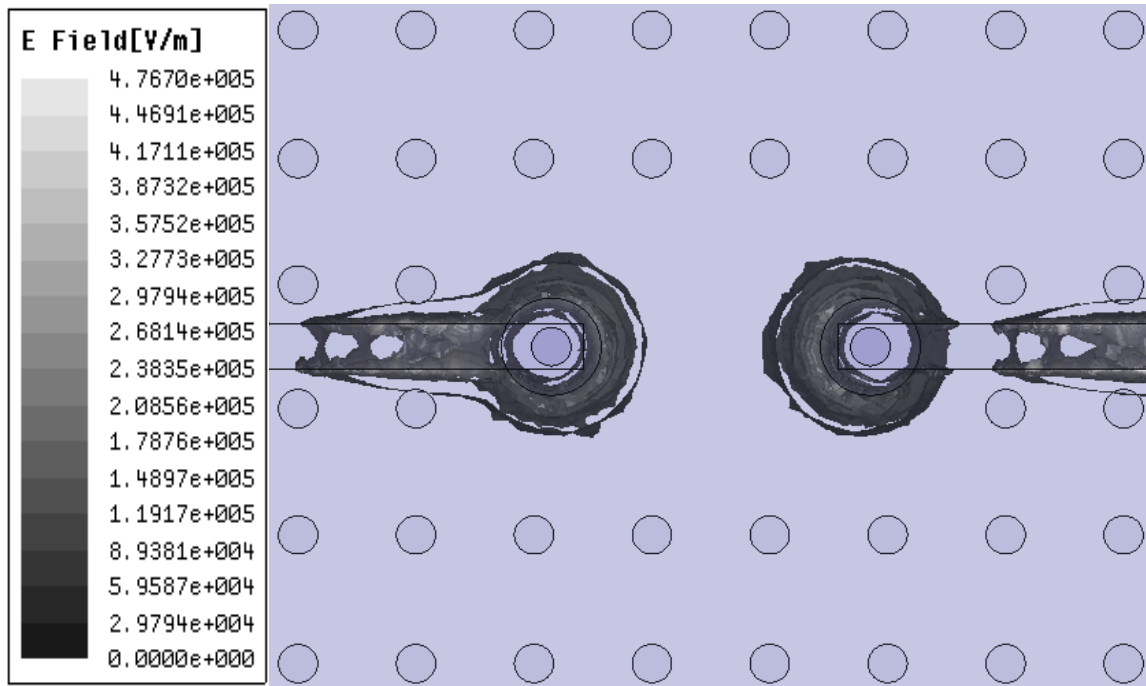


(b)

Figure 37: LTCC cavity resonator employing probe excitation: (a) top view of feeding structure (b) side view of the proposed resonator.



(a)



(b)

Figure 38: (a) Electric field distribution inside the cavity using probe excitation at resonant frequency ($=59.8$ GHz) (b) Electric field distribution of the top substrate layer (substrate 1 in Fig. 37 (b)).

The simulated electric field distributions, both inside the cavity and inside the top substrate, are shown in Figs. 38 (a) and (b), respectively. The efficient containment of the electric field and the perfect decoupling between the two feeding structures is observed. The cavity resonator using probe excitation was fabricated using LTCC technology and its photograph is shown in Fig. 39.

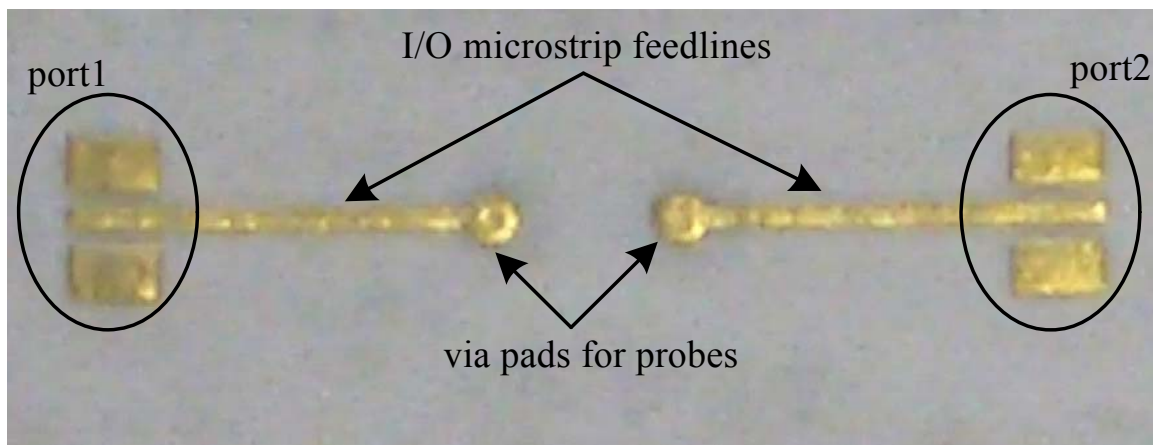


Figure 39: The photograph of the fabricated cavity resonator using probe excitation.

The S-parameter data from both the simulations and the measurements are shown in Fig. 40. The measured insertion loss of 0.95 dB is a little larger than the simulated value 0.67 dB but the measured bandwidth of 1.8% is narrower than the predicted value 3.74%. This difference might be due to a change in the external coupling caused by a misaligned probe position that can significantly affect the electromagnetic performance. No significant frequency shift in the operating frequencies of 59.8 GHz is observed. The simulated Q_u was found to be 355 compared to the theoretical Q_u of 362. The Q_{ext} was measured to be 49.8.

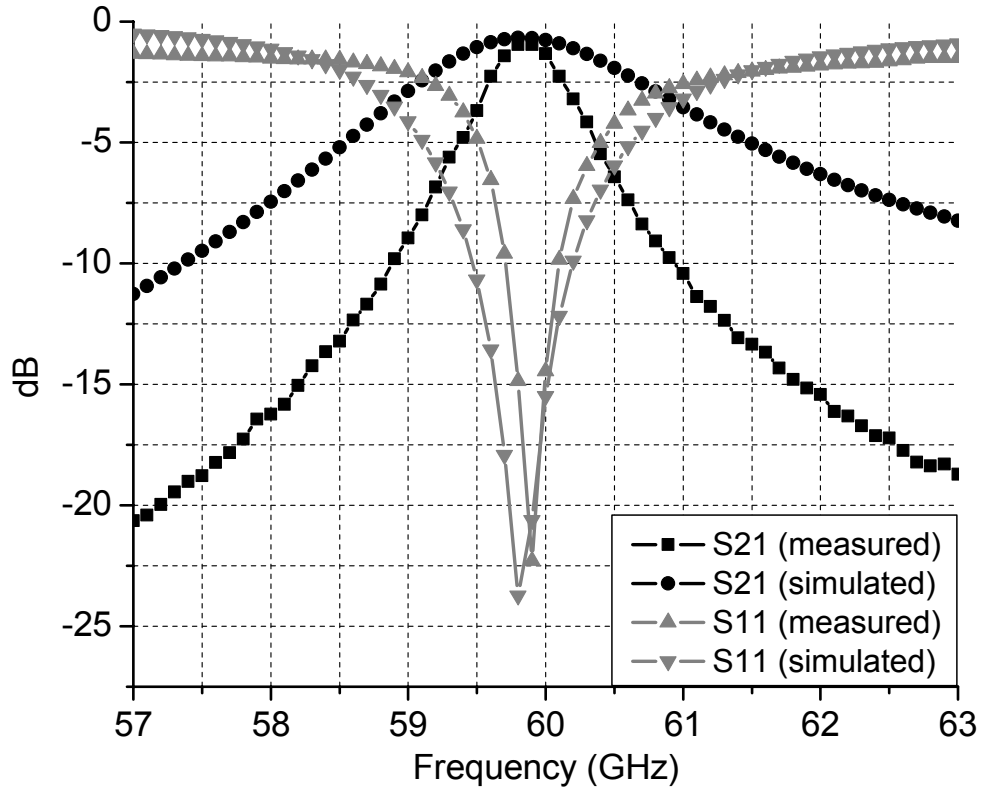


Figure 40: The comparison between measured and simulated S-parameters (S11 & S21) of a cavity resonator using probe excitation.

4.2.4 Discussion

Table 3 summarizes the experimental results of the three cavity excitation techniques. Based on experimental results, the probe excitation exhibits the strongest coupling in terms of the lowest Q_{ext} measured from the strongly coupled resonators by using (14)-(16). In addition, the probe excitation is an attractive option for wideband applications due to its relatively wide bandwidth performance, but it requires a mature fabrication capability (accurate via stacking and alignment) to implement the probe structure.

Table 2: Design parameters of cavity resonators using three different excitation techniques (1. slot excitation with a shorting via, 2.slot excitation with an open stub, 3.probe excitation).

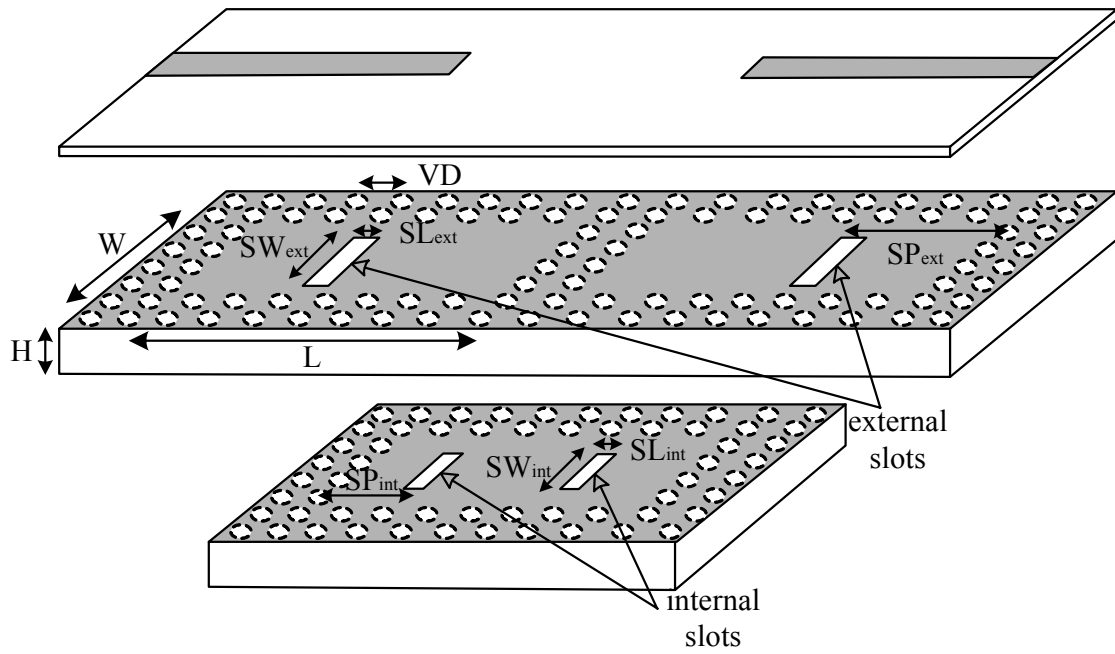
Cavity Resonator using Shorting Vias		Cavity Resonators using Open Stubs		Cavity Resonators using Probes	
<i>Design Parameters</i>	<i>Dimensions (mm)</i>	<i>Design Parameters</i>	<i>Dimensions (mm)</i>	<i>Design Parameters</i>	<i>Dimensions (mm)</i>
effective cavity length (L)	1.95	effective cavity length (L)	1.95	effective cavity length (L)	1.95
effective cavity width (W)	1.318	effective cavity width (W)	1.318	effective cavity width (W)	1.276
effective cavity height (H)	0.3	effective cavity height (H)	0.3	effective cavity height (H)	0.3
slot positioning (SP)	0.4475	slot positioning (SP)	0.4475	probe positioning (PP)	0.4475
shorted via positioning (VP)	0.7175	open stub length (OSL)	0.485	via pad radius (rad1)	0.165
slot length (SL)	0.538	slot length (SL)	0.538	aperture radius (rad2)	0.24
slot width (SW)	0.21	slot width (SW)	0.21		
via pitch (VD)	0.39	via pitch (VD)	0.39	Via pitch (VD)	0.39
via diameter	0.13	via diameter	0.13	via diameter	0.13
via rows	3	via rows	3	via rows	3

Table 3: Comparison of measured results of three different excitation techniques (1. slot excitation with a shorting via, 1.slot excitation with an open stub, 3.probe excitation).

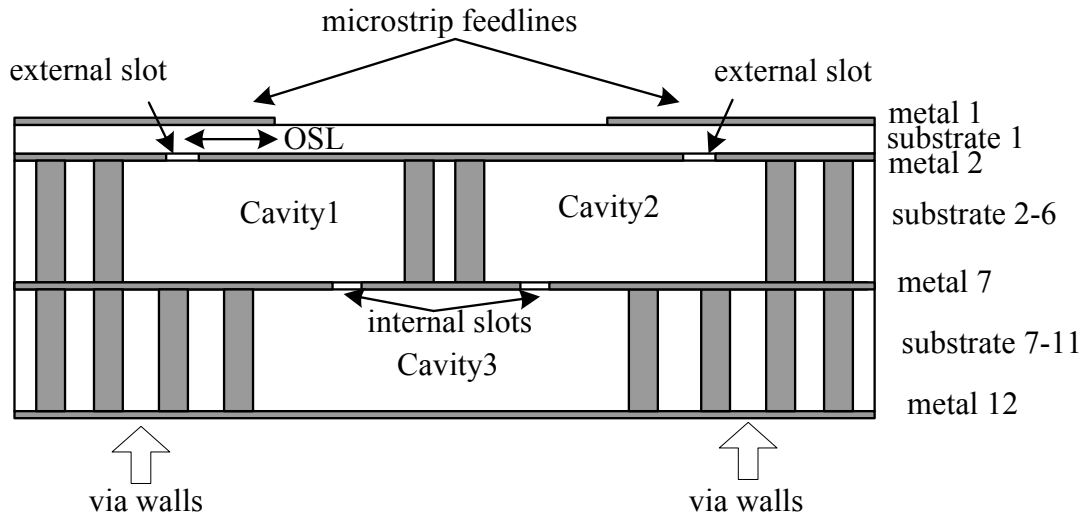
	slot excitation with a shorting via	slot excitation with an open stub	probe excitation
Resonant Frequency (f_{res})	59.4 GHz	59.2 GHz	59.8 GHz
Insertion Loss (S21)	1.28 dB	0.84 dB	0.95 dB
Return Loss (S11)	18 dB	20.59 dB	22.3 dB
Bandwidth (BW)	1.18 %	1.5 %	1.8 %
Simulated Unloaded Q (Q_u)	360	367	355
Measured External Q (Q_{ext})	73.23	60.52	49.80

The slot excitation with open stubs demonstrates the lowest insertion loss. An open stub contributes to fabrication simplicity with no need of drilling via holes to implement the feeding structures. Also, it avoids the loss and inductance effects generated by the via structure that could be serious in the millimeter-wave frequency range. However, the excitation techniques using a shorting via and vertically stacked vias (probe) take advantage of preventing electrical coupling between two microstrip feed-lines because of vias providing the necessary shielding, while reducing the substrate coupling effects generated from the extended open stub.

4.3 Three-Pole Cavity Filters



(a)



(b)

Figure 41: LTCC three-pole cavity bandpass filter employing slot excitation with an open stub: (a) 3D overview, (b) side view of the proposed filter

We have designed and fabricated three-pole filters using via walls for 60GHz WLAN narrowband (~ 1 GHz) applications that consist of three coupled cavity resonators (*Cavity1*, *Cavity2*, *Cavity3* in Fig. 41 (b)). The 3D overview (a) and side view (b) are illustrated in Fig. 41. The three-pole bandpass filter based on a Chebyshev lowpass prototype filter is developed for a center frequency of 60 GHz, < 3 dB insertion loss, 0.1 dB in band ripple and 1.67 % fractional bandwidth.

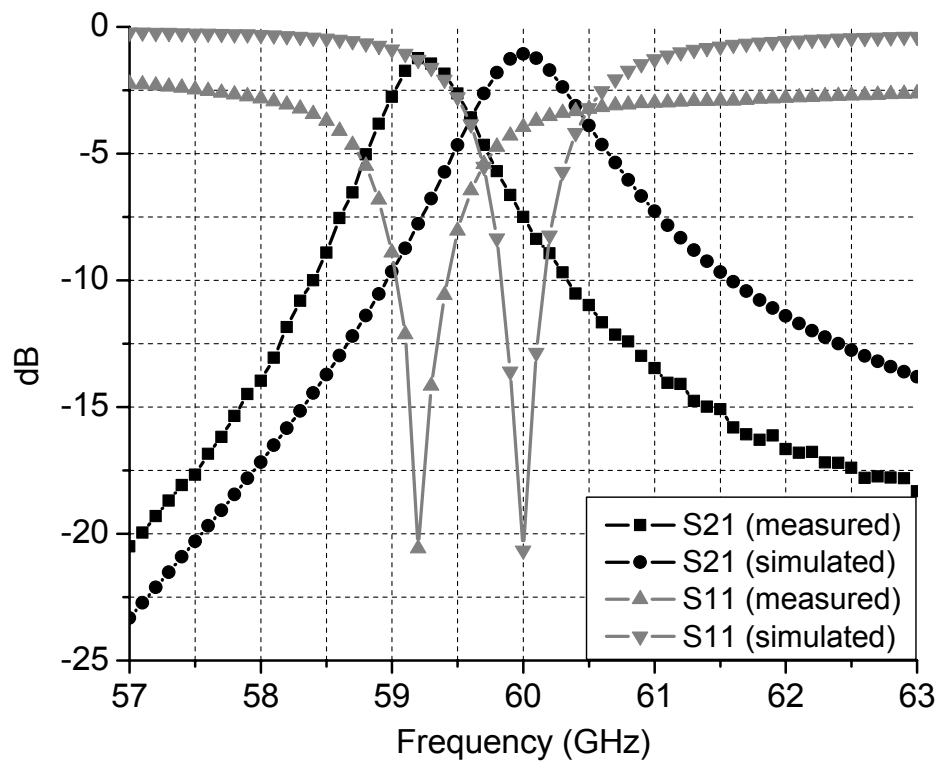


Figure 42: The comparison between measured and simulated S-parameters (S11 & S21) of 0.5 mm-height cavity resonator using slot excitation with an open stub.

To meet design specifications, the cavity height (H in Fig. 28 (b)) was increased to 0.5 mm (five substrate layers) to achieve a higher Q_u and consequently to obtain narrower bandwidth. The cavity resonator with 0.5 mm height has been fabricated in LTCC and measured. The

comparison between the simulation and the measurement is shown in Fig. 42. An insertion loss of 1.24 dB at the center frequency of 59.2 GHz and a narrow bandwidth of 1.35 % (~0.8 GHz) has been measured. The theoretical Q_u yields 426, and it is very close to the simulated Q_u of 424 from a weakly coupled cavity in HFSS.

After verifying the experimental performance of a single cavity resonator, the external coupling and the inter-resonator coupling are considered for the 3-pole filter design.

Firstly, Q_{ext} can be defined from the specifications as follows [56]

$$Q_{ext} = \frac{g_i g_{i+1} f_{res}}{FBW} \quad (17)$$

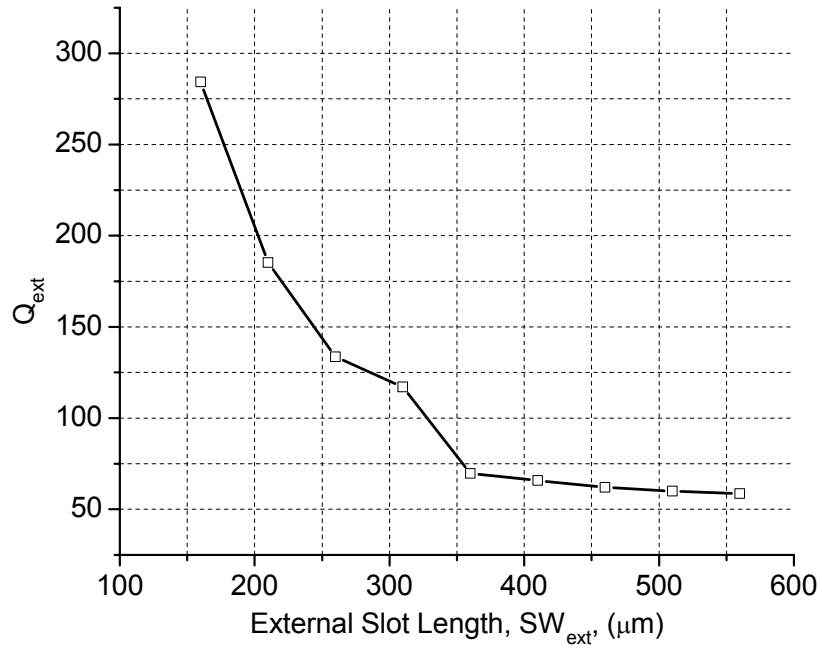
where g_i are the element values of the low pass prototype, f_{res} is the resonant frequency, and FBW is the fractional bandwidth of the filter. The input and output Q_{ext} were calculated to be 61.89. The position and size of the external slots (Fig. 41 (a)) are the main parameters to achieve the desired Q_{ext} . The slots have been positioned at a quarter of the cavity length ($L/4$) and their length has been fixed to $\lambda_g/4$ ($SL_{ext} \sim \lambda_g/4$ in Fig. 41 (a)). Then, Q_{ext} (shown in Fig. 43 (a)) has been (using full-wave simulations) evaluated as a function of the external slot width (SW_{ext} in Fig. 41 (a)) based on the following relationship [22]

$$Q_{ext} = \frac{f_{res}}{\Delta f_{\pm 90^\circ}} \quad (18)$$

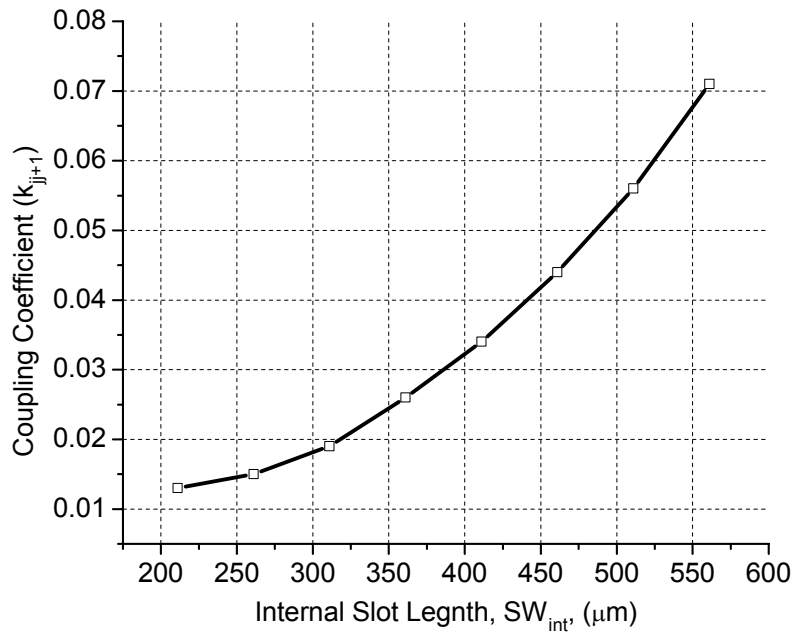
where $\Delta f_{\pm 90^\circ}$ is the frequency difference between $\pm 90^\circ$ phase response of S11.

Secondly, the inter-resonator coupling coefficients (k_{jj+1}) between the vertically adjacent resonators is determined by [56]

$$k_{jj+1} = \frac{BW}{f_{res}} \sqrt{\frac{1}{g_j g_{j+1}}} \quad (19)$$



(a)



(b)

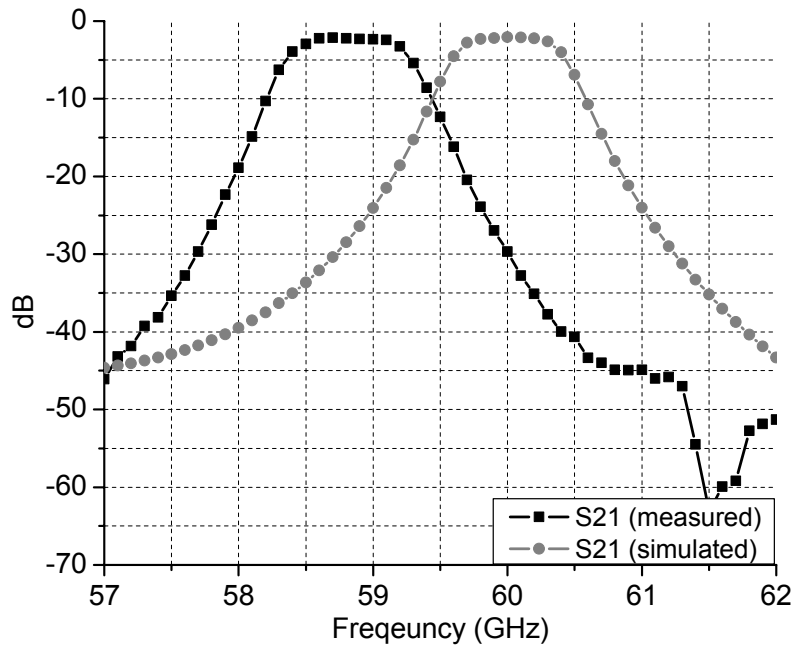
Figure 43: (a) External quality factor (Q_{ext}) evaluated as a function of external slot width (SW_{ext}) (b) Inter-resonator coupling coefficient (k_{jj+1}), as a function of internal slot width (SW_{int}).

where $j = 1$ or 2 because of the symmetrical nature of the filter. k_{jj+1} was calculated to be 0.0153. To extract the desired k_{jj+1} , the size of internal slots (Fig. 41 (a)) is optimized using full wave simulations to find the two characteristic frequencies (f_{p1} , f_{p2}) that are the frequencies of the peaks in the transmission response of the coupled structure when an electric wall or magnetic wall, respectively, is inserted in the symmetrical plane [56]. Then, k_{jj+1} can be determined by measuring the amount that the two characteristic frequencies deviate from the resonant frequency. The relationship between k_{jj+1} and the characteristic frequencies (f_{p1} , f_{p2}) is defined as follows: [56].

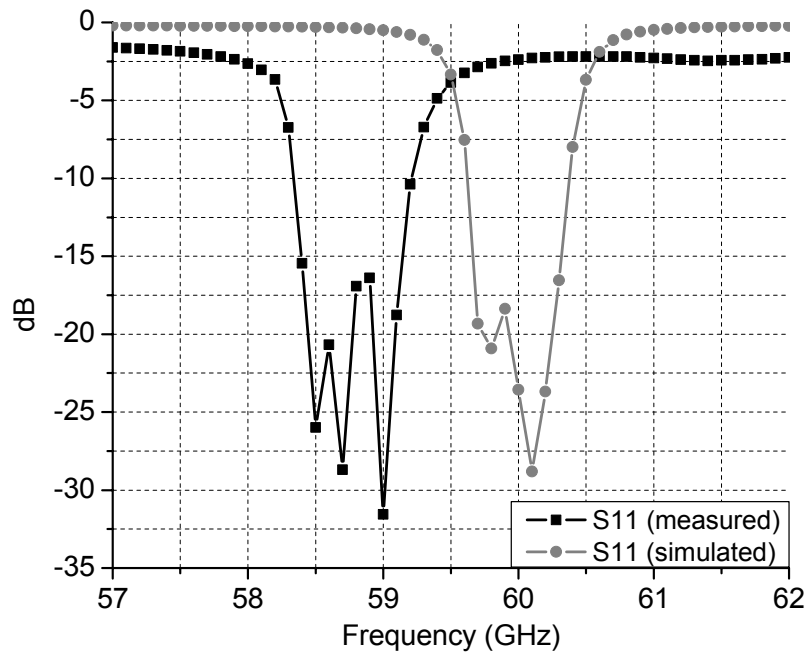
$$k_{jj+1} = \frac{f_{p2}^2 - f_{p1}^2}{f_{p2}^2 + f_{p1}^2} \quad (20)$$

Based on the above theory, the physical dimensions of internal slots were determined by using a simple graphical approach displaying two distinct peaks of character frequencies for a fixed Q_{ext} . Figure 43 (b) shows the graphical relationship between k_{jj+1} and internal slot width (SW_{int} in Fig. 41 (a)) variation with the fixed slot length ($SL_{int} \approx \lambda_g/4$ in Fig. 41 (a)). SW_{int} was determined to be 0.261 mm corresponding to the required $k_{jj+1} (\approx 0.0153)$ from Fig. 43 (b). After determining the initial dimensions of the external/internal slots, the other design parameters such as the open stub length (OSL in Fig. 41 (b)) and the cavity length and width (L and W in Fig. 41 (a)) using via walls are determined under the design guidelines described in section 4.1 and 4.2.

The initial dimensions of the external/internal slot widths are set up as optimal variables and fine tuned to achieve the desired frequency response using HFSS simulators. The summary of all design parameters for the three-pole filter is given in Table 4. Figures 44 (a) and (b) show the comparison between the simulated and the measured S-parameters of the bandpass filter. In the measurements, the parasitic effects from the I/O open pads were de-embedded with the aid of



(a)



(b)

Figure 44: The comparison between measured and simulated (a) S_{21} and (b) S_{11} of three-pole cavity bandpass filter using slot excitation with an open stub.

Table 4: Design parameters of three-pole cavity filter using an open stub.

<i>Design Parameters</i>	<i>Dimensions (mm)</i>
effective cavity resonator ($L \times W \times H$)	1.95×1.32×0.5
external slot position (SP_{ext})	0.4125
external slot ($SL_{ext} \times SW_{ext}$)	0.46 ×0.538
internal slot position (SP_{int})	0.3915
internal slot ($SL_{int} \times SW_{int}$)	0.261×0.4
open stub length (OSL)	0.538
via spacing	0.39
via diameter	0.13
via rows	3

WinCal 3.0 software. The filter exhibits an insertion loss <2.14 dB which is slightly higher than the simulated value of <2.08 dB, and a return loss > 16.39 dB compared to a simulated value > 18.37 dB over the pass band, as shown in Figs. 44 (a) and (b), respectively. In Fig. 44 (a), the measurement shows a slightly increased 3 dB fractional bandwidth of about 1.53 % (≈ 0.9 GHz) at a center frequency 58.7 GHz. The simulated results give a 3-dB bandwidth of 1.47 % (≈ 0.88 GHz) at a center frequency 60 GHz. The center frequency downshift can be attributed to the fabrication accuracy such as slot positioning affected by the alignment between layers, layer thickness tolerance, and higher dielectric constant at this high frequency range (55-65GHz) than 5.4 that is the relative permittivity at 35 GHz as mentioned in section 4.2.2. The overall response of the measurement is in excellent agreement with the simulation except a frequency shift of 1.3 GHz ($\sim 2\%$). This three-pole filter can be used in the development of three-pole duplexers for millimeter-wave wireless systems.

4.4 Vertically Stacked Cavity Filters and Duplexers

The proposed vertically stacked cavity bandpass filter is designed in a way that allows for its easy integration with a V-band multilayer module due to its compactness and its 3D interconnect feature as a duplexer between the active devices on the top of the LTCC board and the antenna integrated on the back side. High level of compactness can be achieved by vertically stacking three identical cavity resonators with the microstrip feedlines vertically coupled through rectangular slots etched on the input and output resonators. The proposed devices were fabricated in a LTCC by Asahi Glass Co. The relative permittivity (ϵ_r) of the substrate is 5.4 and its loss tangent ($\tan\delta$) is 0.0015. The dielectric layer thickness per layer is $100\ \mu\text{m}$, and the metal thickness is $9\ \mu\text{m}$. The resistivity of metal (silver trace) is determined to be $2.7 \times 10^{-8}\ \Omega \cdot \text{m}$. All designs are optimized with the aid of a FEM-based full-wave simulator (HFSS).

4.4.1 Design of Cavity Resonator

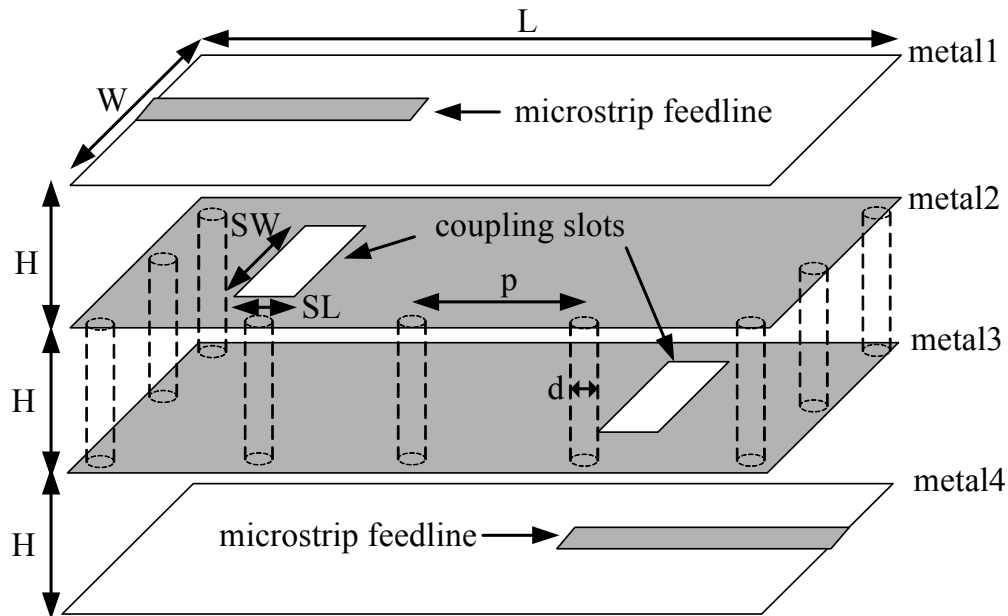


Figure 45: The 3D overview of LTCC cavity resonator employing slot excitation with microstrip feedlines on the different metal layers (*metal 1 and 4*).

The cavity resonator that is the most fundamental component of the cavity filter is built based on the conventional rectangular cavity resonator approach investigated in section 4.1. The cavity resonator shown in Fig. 45 consists of one LTCC cavity, two microstrip lines for input and output, and two vertically coupling slots etched on the ground planes of the cavity. The resonant frequency of the fundamental TE_{101} mode can be determined by (9). The resonant frequency at 60.25 GHz establishes the initial dimensions of the cavity resonator enclosed by perfectly conducting walls. For the purpose of compactness, the height (H) is determined to be 0.1 mm (one substrate layer). Then, the vertical conducting walls are replaced by double rows of via posts that are sufficient to suppress the field leakage and to enhance the Q . In addition, the size and spacing of via posts are properly chosen to prevent electromagnetic field leakage and to achieve stop-band characteristic at the desired resonant frequency according to the guidelines specified in section 4.1. In our work, the minimum value ($390 \mu\text{m} = p$ in Fig. 45) of center-to-center vias spacing and the minimum value ($130 \mu\text{m} = d$ in Fig. 45) of via diameter of the LTCC design rules are used. The final dimensions of the via-based cavity are determined by using a tuning analysis of HFSS full-wave simulator ($L=1.95\text{mm}$, $W=1.275\text{mm}$, $H=0.1\text{mm}$).

With the cavity size determined, microstrip lines are utilized as the feeding structure to excite the cavity via coupling slots that couple energy magnetically from the microstrip lines into the cavity. For a preliminary testing of the vertical inter-coupling of three-pole cavity bandpass filter, the input and output feedlines are placed on *metal 1* and *metal 4*, respectively, as shown in Fig. 45. The coupling coefficient can be controlled by the location and size of the coupling slots etched on *metal 2* and *metal 3* in Fig. 45.

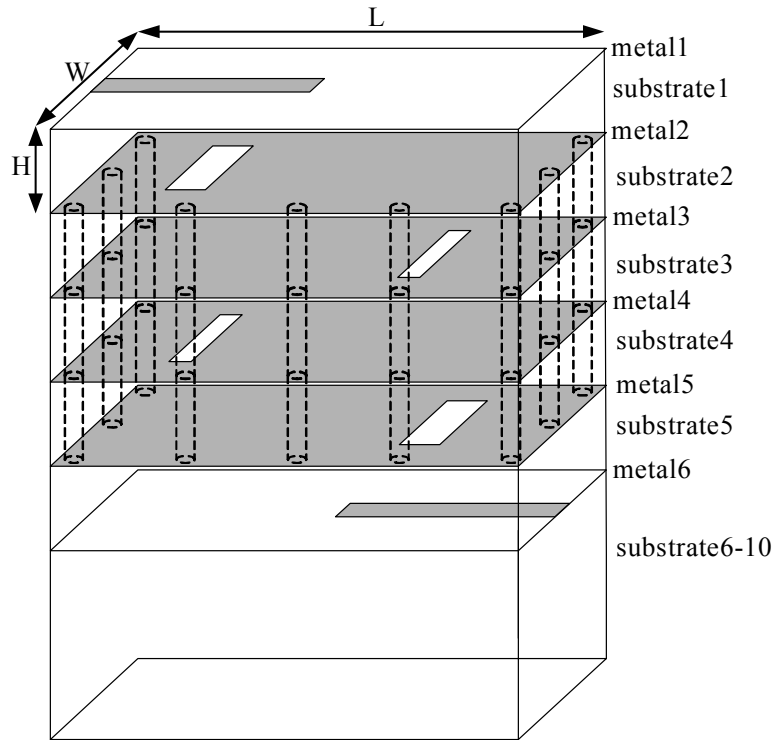
To accurately estimate the Q_u , the weakly coupled cavity resonator [57] with a relatively small value of the slot length (SL in Fig. 45) is implemented in HFSS simulator. The Q_u can be

extracted from the Q_{ext} and the Q_l using (14)-(16). The simulated value of Q_u was calculated to be 623 at 60.25 GHz.

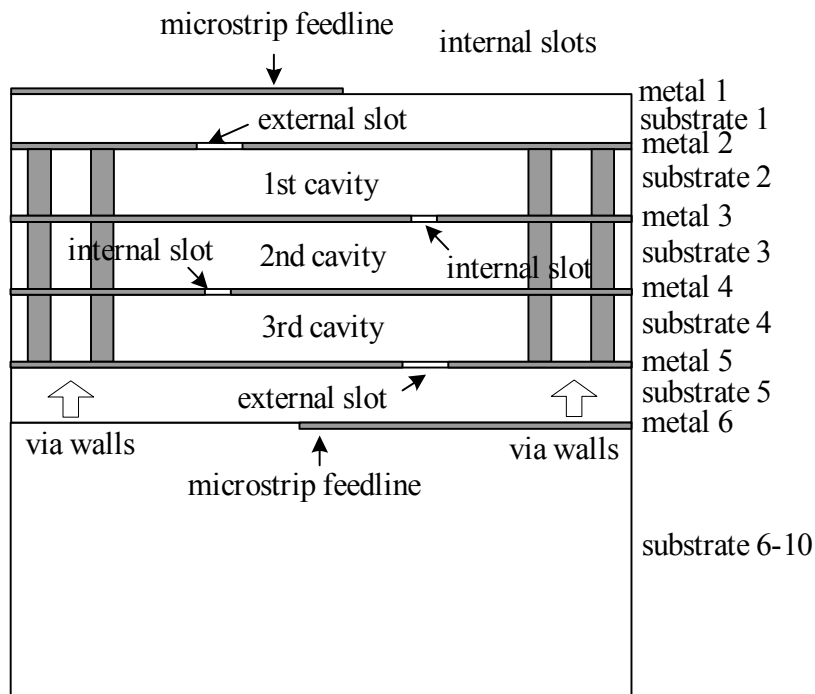
4.4.2 Design of Three-Pole Cavity Bandpass Filter

A vertically stacked LTCC three-pole cavity bandpass filter is developed for 3D integrated 59-64 GHz Industrial, Scientific and Medical (ISM) band transceiver front-end modules. The center frequencies of 60.25 GHz and 62.75 GHz in the band are selected for the Rx channel and the Tx channel, respectively.

First, the cavity bandpass for the Rx channel selection is designed with a 60.25 GHz center frequency, a < 3 dB insertion loss, a 0.1 dB ripple, and a 4.15% (≈ 2.5 GHz) fractional bandwidth based on a Chebyshev lowpass prototype. The filter schematic is implemented with ten substrate layers of LTCC tape. Its 3D overview (a), side view (b) and top view of the feeding structure (c) and inter-resonator coupling structure (d) are illustrated in Fig. 46. The top five substrate layers (*substrate 1-5* in Fig. 46 (b)) are occupied by the Rx filters, and the remaining layers are reserved for the antenna and the RF active devices, that could be integrated into front-end modules. The microstrip lines on *metal 1* and *6* are utilized as the feeding structure to excite the 1^{st} and 3^{rd} cavities, respectively. Three identical cavity resonators (1^{st} cavity, 2^{nd} cavity, 3^{rd} cavity in Fig. 42 (b)) designed in section 4.4.1 are vertically stacked and coupled through slots to achieve the desired the frequency response with high level of compactness. This filter is also an effective solution to connect the active devices on the top of the LTCC board and the antenna integrated on the back side.



(a)



(b)

Figure 46: (a) 3D overview (b) sideview of the vertically stacked three-pole cavity bandpass filter. (c) top view of the feeding structure (d) top view of the inter-resonator coupling structure.

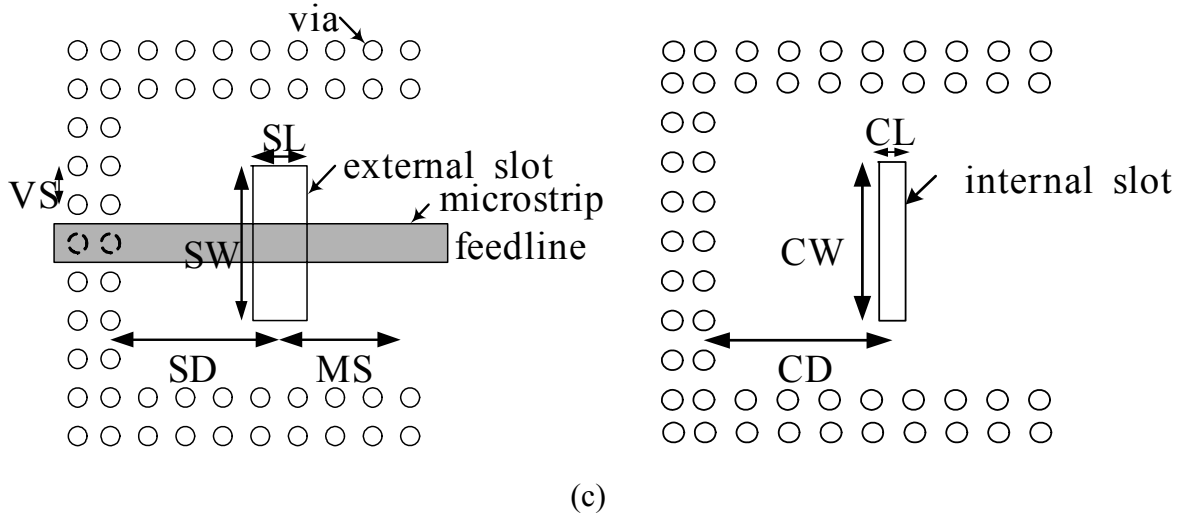


Figure 46: Continued.

Two external slots (Fig. 46 (a)) on metal layers 2 and 5 are dedicated to magnetically couple the energy from the I/O microstrip lines into the 1st and 3rd cavity resonators, respectively. To maximize magnetic coupling by maximizing the current, the microstrip feedlines are terminated with a $\lambda_g/4$ open stub beyond the center of each external slot. The fringing field generated by an open-end discontinuity can be modeled by an equivalent length of transmission line, which is determined to be about $\lambda_g/20$. Therefore the optimum length of the stub is approximately $\lambda_g/5$ (MS in Fig. 46 (c)). The position and size of the external slots are the main design parameters to provide the necessary Q_{ext} . The external quality factor (Q_{ext}) that controls the insertion loss and ripple over the pass band can be defined by (17).

The calculated Q_{ext} is 24.86. The external slot is initially positioned at $L/4$ from the edge of the cavity, and the width (SW in Fig. 46 (c)) of the slot is fixed to $\lambda_g/4$. Then, the length (SL in Fig. 46 (c)) of the slot is tuned until the simulated Q_{ext} converges to the prototype requirement. Figure 47 shows the relationship between the length variation of the external slots and the Q_{ext} extracted from the simulation using (18).

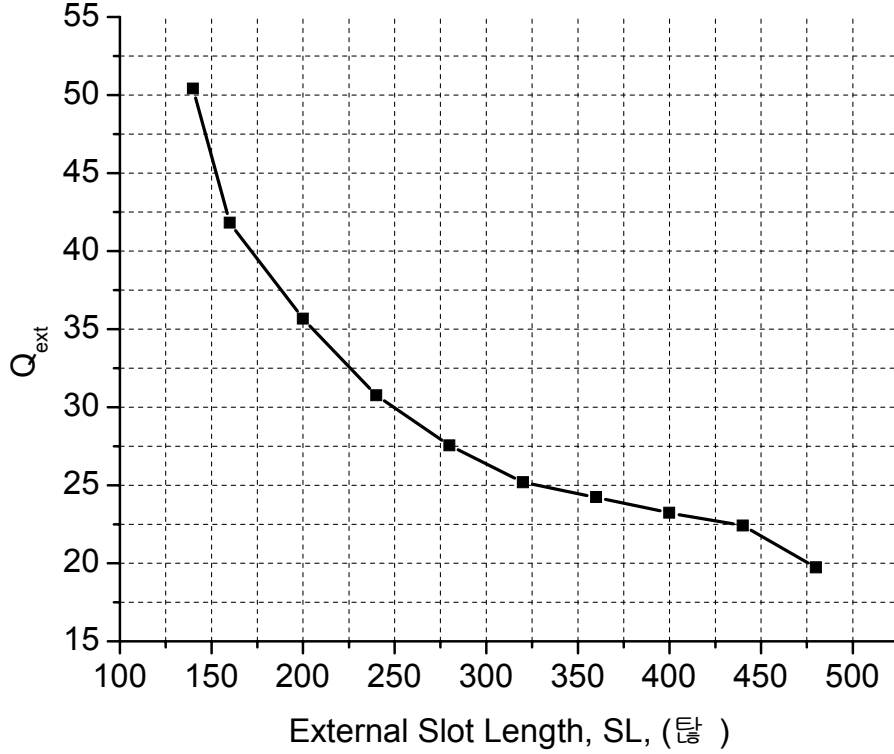
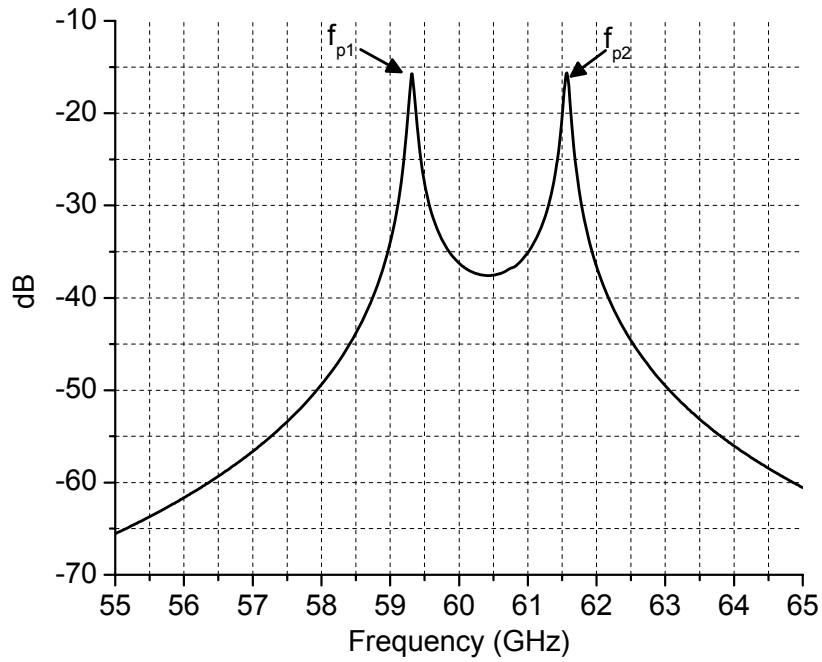
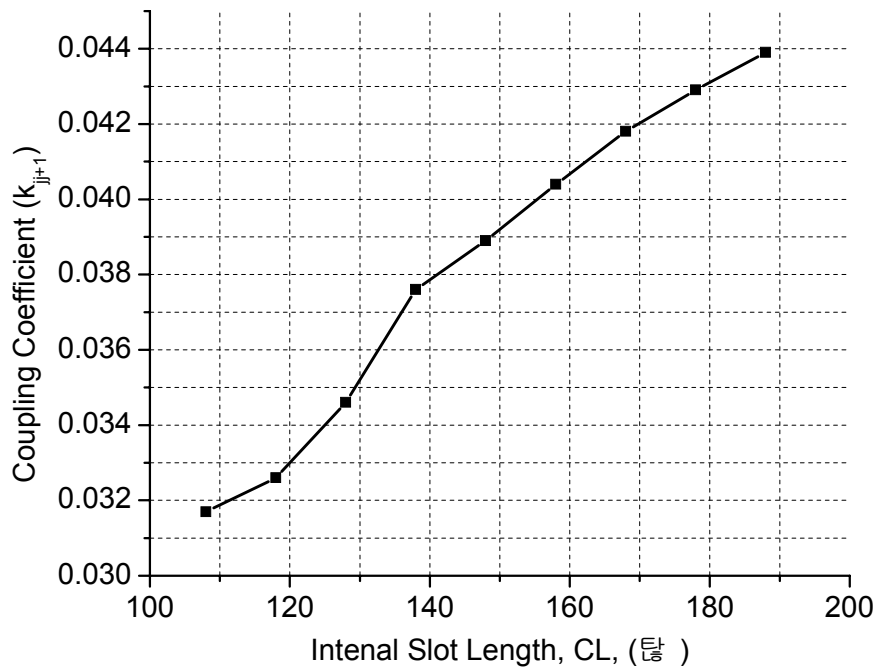


Figure 47: External quality factor (Q_{ext}) evaluated as a function of external slot length (SL).

The latter internal slots on *metal 3 and 4* (Fig. 46 (b)) are employed to couple energy from the 1st and 3rd cavity resonators into the 2nd resonator, and their design procedure is similar to that of the external slots. The internal slots are located a quarter of the cavity length from the sides. The desired inter-resonator coupling coefficients ($k_{12}=k_{23}=0.0381$) are obtained by (19). This desired prototype k_{jj+1} can be physically realized varying the slot length (CL in Fig. 46 (d)) with a fixed slot width ($CW \approx \lambda_g/4$ in Fig. 46 (d)). Full-wave simulations are employed to find the two characteristic frequencies (f_{p1}, f_{p2}) that are the resonant frequencies in the transmission response of the coupled structure [56] and its plot versus frequency is shown in Fig. 48 (a). These characteristic frequencies are associated to the inter-resonator coupling between the cavity resonators according to (20).



(a)



(b)

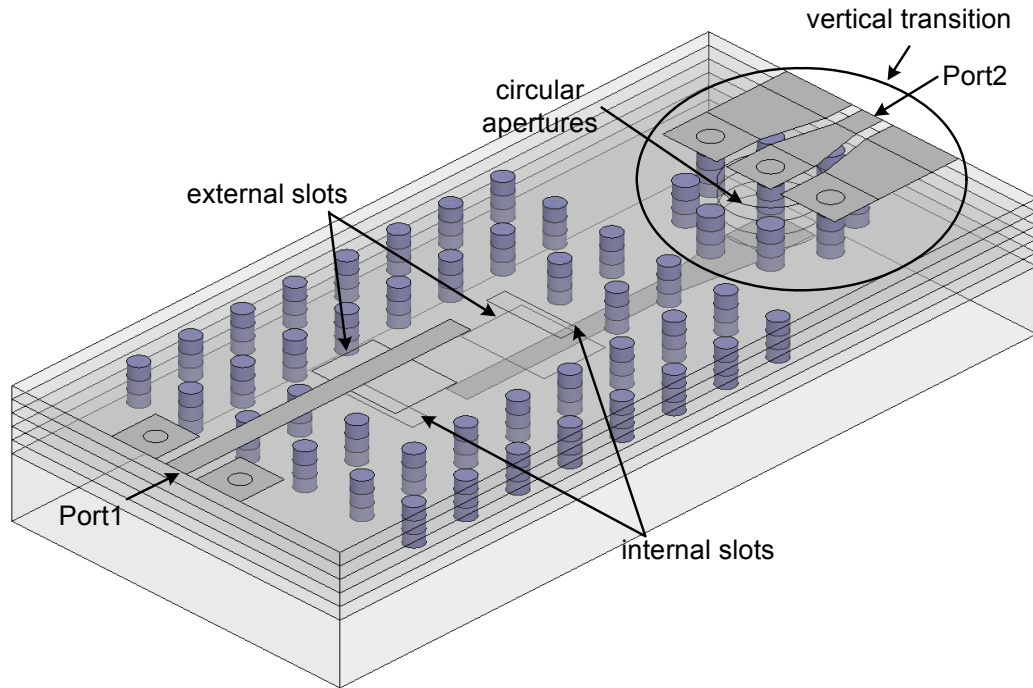
Figure 48: (a) Two characteristic frequencies (f_{p1} , f_{p2}) of the coupled cavities to calculate the internal coupling coefficients (k_{jj+1}) (b) Inter-resonator coupling coefficient (k_{jj+1}), as a function of internal slot length (CL).

Figure 48 (b) shows the internal coupling as a function of the variation of the internal slot length (CL in Fig. 46 (d)). By adjusting the slot length, the optimal size of an internal slot can be determined for a given prototype value. Using the initial dimensions of the external (SW , SL) and internal slot (CW , CL) size as the design variables, we optimized the design variables to realize the desired frequency response. The design can be fine tuned afterwards considering the minimum and maximum of the fabrication tolerances. Then, the final variable values that match the desired frequency response can be determined.

To allow on wafer characterization using coplanar probes, the input and output probe pads have to be on the same layer which requires an embedded microstrip line to CPW vertical transition at port 2. The vertical transition consists of five stacked signal vias penetrating through circular apertures [see Fig. 49 (a)] on the ground planes (*metal 2, 3, 4 and 5*) and connecting an embedded microstrip line on *metal 6* to a CPW measurement pads on *metal 1*. In order to match to the 50Ω feedlines, the diameter of the circular apertures is optimized to be 0.57 mm for a signal via diameter of $130 \mu\text{m}$. Also, eight shielding vias (two of shielding vias: connecting *metal 1* (CPW ground planes) to 5, six of shielding vias: connecting *metal 2* to 5) are positioned around the apertures to achieve an optimum coaxial effect [58]. The number of shielding vias is determined with regard to the LTCC design rules.

The filters including CPW pads and a vertical transition were fabricated in LTCC by Asahi Glass Co. and measured on a HP8510C Vector Network Analyzer using SOLT calibration. Figure 49 (a) depicts the 3D overview of the complete structure that was simulated. The “Wincal” software gives us the ability to de-embed capacitance effects of CPW open pads and inductive effects of short pads from the measured S-parameters so that the loading shift effect could be negligible. Figure 49 (b) shows the photograph of the fabricated filter with CPW pads

and a transition whose size is $5.60 \times 3.17 \times 1 \text{ mm}^3$. The cavity size is determined to be $1.95 \times 1.284 \times 0.1 \text{ (}L \times W \times H \text{ in Fig. 42 (a)) mm}^3$.

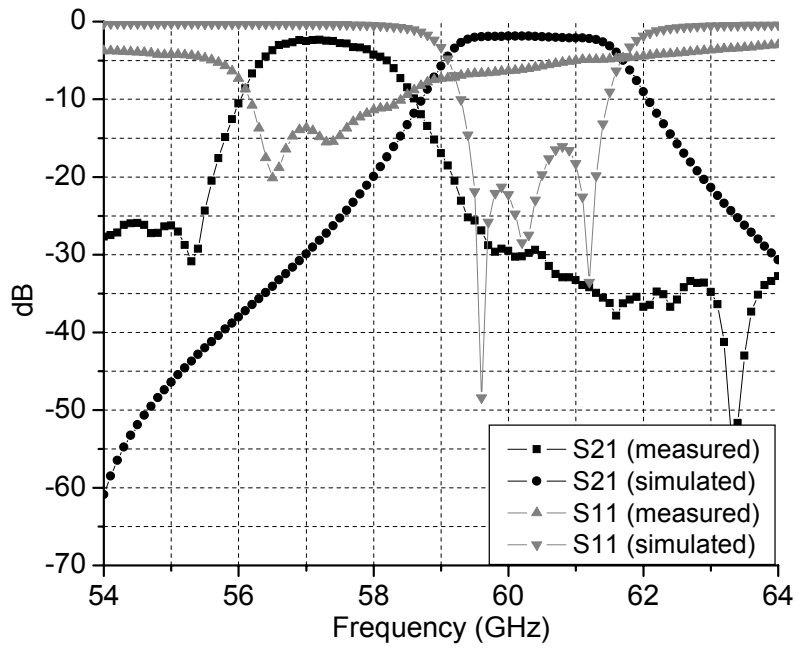


(a)

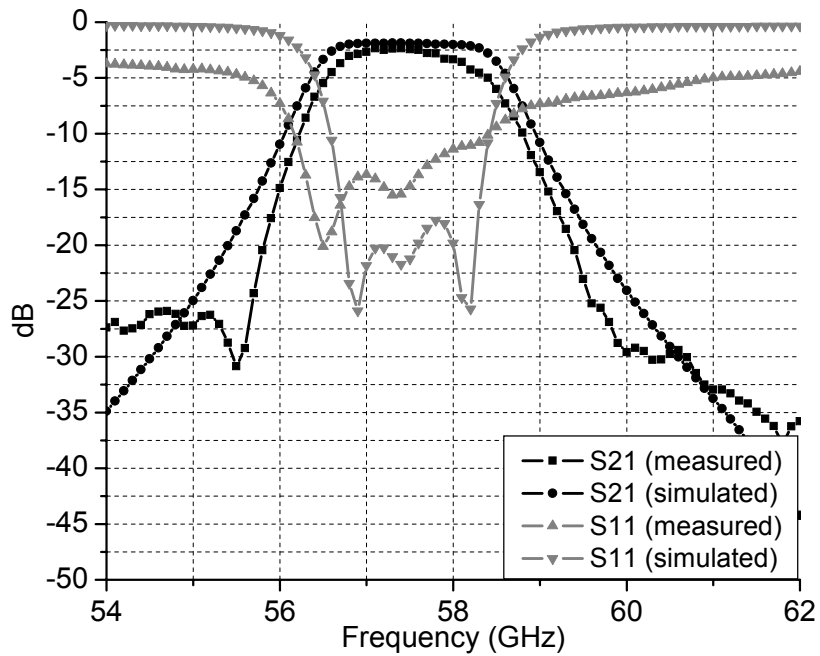


(b)

Figure 49: (a) 3D overview of vertically stacked 3-pole cavity bandpass filter with CPW pads and vertical transitions. (b) The photograph of the cavity bandpass filter fabricated on LTCC.



(a)



(b)

Figure 50: The comparison between measured and simulated S-parameters (S11 & S21) of Rx 3-pole cavity band filter (a) measurement vs. simulation with $\epsilon_r = 5.4$ and originally designed cavity size ($1.95 \times 1.284 \times 0.1 \text{ mm}^3$) (b) measurement vs. simulation with $\epsilon_r = 5.5$ and modified cavity size ($2.048 \times 1.348 \times 0.1 \text{ mm}^3$).

Figure 50 (a) shows the comparison between the simulated and the measured S-parameters of the three-pole vertically stacked bandpass filter. The filter exhibits an insertion loss <2.37 dB, which is higher than the simulated value of <1.87 dB. The main source of this discrepancy might be caused by the radiation loss from the “thru” line that could not be de-embedded because of the nature of SOLT calibration. The filter exhibits a 3-dB bandwidth about 3.5% (≈ 2 GHz) comparable to the simulated 3.82 % (≈ 2.3 GHz). The narrower bandwidth in measurements might be due to the fabrication accuracy of the slot design that has been optimized for the original resonant frequencies and not for the shifted frequencies.

The center frequency shift from 60.2 GHz to 57.5 GHz might be attributed to the dielectric constant variation at these high frequencies and the fabrication accuracy of vias positioning caused by XY shrinkage. The HFSS simulation is re-performed in terms of two aspects. (1) The dielectric constant of 5.4 was extracted using cavity resonator characterization techniques [9] at 35 GHz. The dielectric constant is expected to increase to 5.5 across 55-65 GHz [17]. (2) The tolerance of XY shrinkage is expected to be ± 15 %. XY shrinkage specification was released after design tape out; thus, we could not have accounted it at the design stage. XY shrinkage can significantly affect the via positioning that is the major factor to determine the resonant frequency of a cavity filter. From our investigation, the averaged relative permittivity was evaluated to be 5.5 across 55-65 GHz [9], and the cavity size was modified to $2.048 \times 1.348 \times 0.1$ mm³ with 5% of XY shrinkage effect. The exact coincidence between the measured center frequency (57.5 GHz) and the simulated (57.5 GHz) is observed in Fig. 50 (b). All design parameters for the modified Rx filter are summarized in Table 5.

Table 5: Design Parameters of Cavity Resonators.

<i>Design Parameters</i>	<i>1st Channel</i>	<i>2nd Channel</i>
cavity length (L)	2.048	2.048
cavity width (W)	1.348	1.266
cavity height (H)	0.100	0.100
external slot width (SW)	0.628	0.621
external slot length (SL)	0.460	0.460
external slot position(SD)	0.417	0.417
internal slot width (CW)	0.558	0.551
internal slot length (CL)	0.138	0.138
internal slot position(CD)	0.417	0.417
open stub length (MS)	0.571	0.571

Then, the same techniques were applied to the design of the cavity bandpass filter for the Tx channel (61.5 – 64 GHz). The Chebyshev prototype filter was designed for a center frequency of 62.75 GHz, a < 3dB insertion loss, a 0.1 dB band ripple and a 3.98 % 3-dB bandwidth. To meet the specified center frequency specs, the cavity width (W) was decreased. Then the cavity size was determined to be $1.95 \times 1.206 \times 0.1$ ($L \times W \times H$ in Fig. 46 (a)) mm³. The external and internal coupling slot sizes are used as the main design parameters to obtain the desired external quality factors and coupling coefficients, respectively.

The measured results of the Tx filter exhibit an insertion loss of 2.39 dB with a 3-dB bandwidth of 3.33% (~2GHz) at the center frequency of 59.9 GHz. The center frequency is downshifted approximately 2.72 GHz similarly to the Rx filter. A new theoretical simulation was

performed with $\epsilon_r=5.5$ and the 5% increase in the volume of cavity ($2.048 \times 1.266 \times 0.1 \text{ mm}^3$), and the measured and simulated results are presented in Fig. 51. The simulation showed a minimum insertion loss of 1.97 dB with a slightly increased 3-dB bandwidth of 4% ($\sim 2.4 \text{ GHz}$). The center frequency of the simulated filter was 59.9 GHz. The center frequency shift is consistent through all devices using this LTCC process because of the fabrication tolerances mentioned. All design parameters for the modified Tx filter are summarized in Table 5.

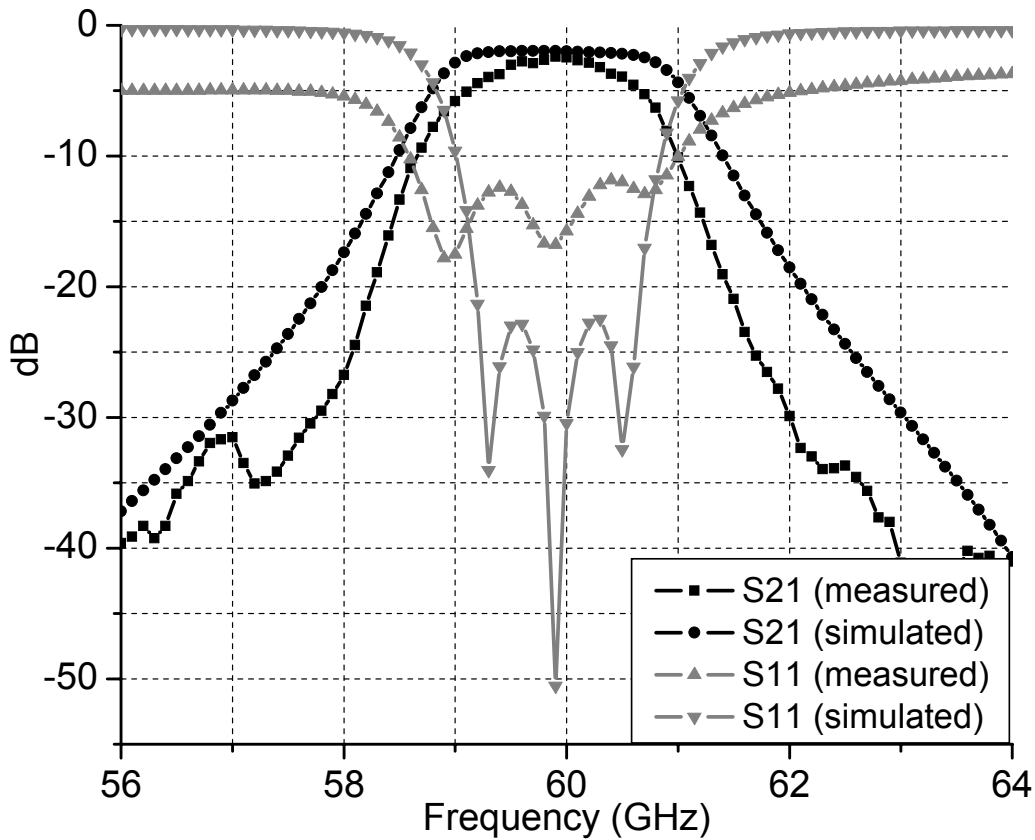
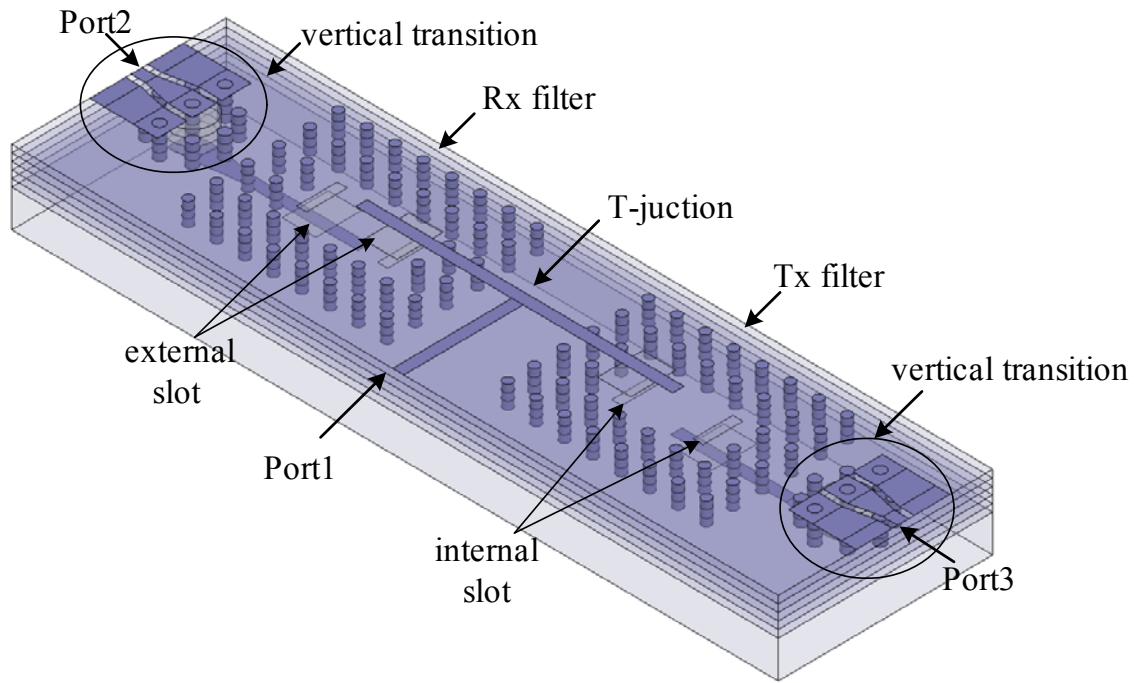


Figure 51: The comparison between measured and simulated S-parameters (S11 & S21) of Tx three-pole cavity band filter (simulation with $\epsilon_r= 5.5$ and modified cavity size ($2.048 \times 1.266 \times 0.1 \text{ mm}^3$) vs. measurement).

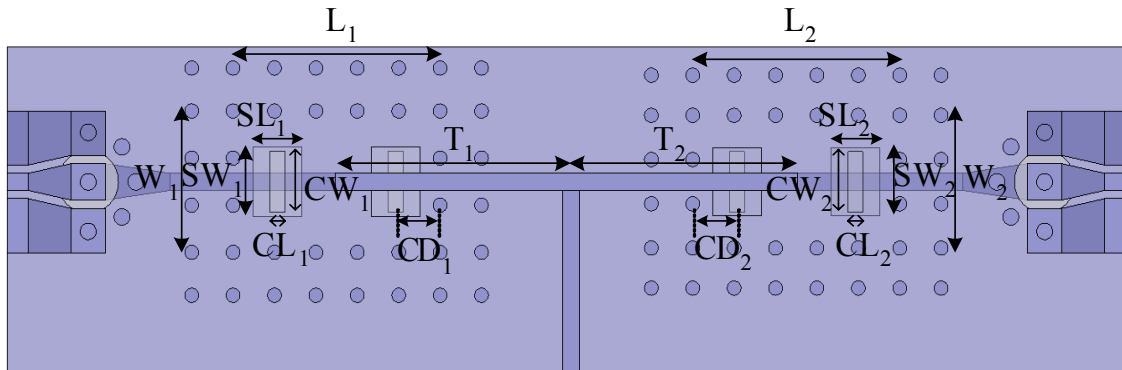
4.4.3 Duplexer (60 GHz / 62.8 GHz)

The development of a 3D fully integrated compact duplexer is crucial in a 3D 59-64 GHz ISM band transceiver front-end module to isolate the power transmit stage from a sensitive receiving stage sharing a common antenna. A low insertion loss in the transmitter and receiver paths is the most fundamental requirement because a low loss enhances the sensitivity of the receiver and prevents the excessive power consumption in the transmitter. In addition, the high channel-to-channel isolation must be accomplished by minimizing the electrical coupling level between the transmitter and the receiver.

We have designed and fabricated one duplexer consisting of the two resonant three-pole cavity filters developed in section 4.4.2 and one microstrip T-junction which connects the two filters and the common input reserved for an antenna. The two channels of the duplexer are centered at 60 GHz for the Rx channel (1st channel) and 62.8 GHz for the Tx channel (2nd channel). The insertion loss <3dB and bandwidths ≈ 2.5 GHz are desired for both channels. The 3D overview (a) and the top view (b) of the duplexer including the vertical transitions and CPW pads are illustrated in Fig. 52. The duplexer that dominates five substrate layers is implemented into a module with ten layers of LTCC tape. The remaining five substrate layers are used for burying RF circuitry that includes the antenna and integrated active devices. The 60 GHz cavity filter occupies the left portion of the duplexer and 62.8 GHz cavity filter, the right portion as shown in Fig. 52 (a) and (b). The same configurations of the 3D cavity filters [see Fig. 46] developed in section 4.2.2 are employed to the duplexer except from a slight modification of the cavity widths ($W1$ and $W2$ in Fig. 52) corresponding to the resonant frequencies of two channels. The modification was necessary to achieve the high level of channel-to-channel isolation that is aimed to be more than 30 dB over operating frequency bands.



(a)

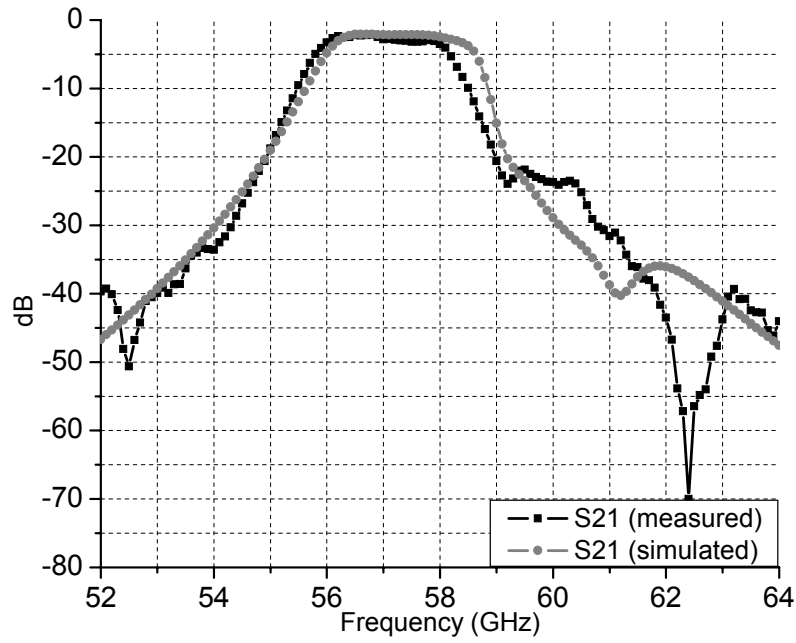


(b)

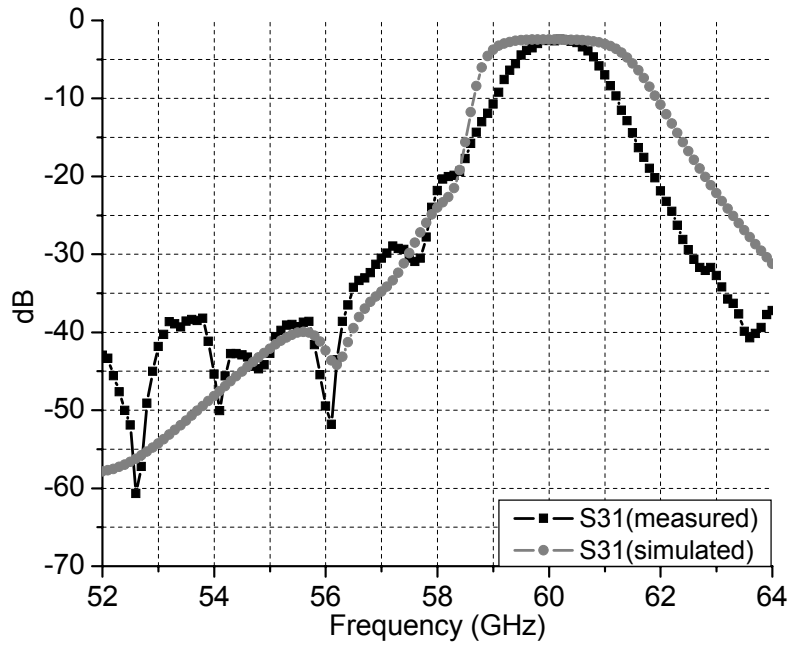
Figure 52: (a) 3D overview (b) top view of the proposed LTCC cavity duplexers using microstrip T-junction.

The cavity sizes are determined to be $1.95 \times 1.29 \times 0.1 \text{ mm}^3$ for the 1st channel and $1.95 \times 1.201 \times 0.1 \text{ mm}^3$ for the 2nd channel. The spacing of two filters is 1.6 mm. The lengths of the microstrip lines (T_1 and T_2 in Fig. 52 (b)) connecting the T-junction to the Rx and Tx filters are the most important design parameters to achieve the good isolation between two channels. First we set up T_1 and T_2 to be equal a half guided wavelength at the resonant frequencies of the 1st channel and 2nd channel filters accordingly. In our case, one guided wavelength is utilized as the initial value of T_1 and T_2 since a length equal to one half guided wavelength would cause an overlap between two filters. Then, the length of T_1 is optimized to reflect an open circuit at the resonant frequency of the 2nd channel in HFSS simulator. The length T_2 is also optimized against the 1st channel in the same way as applied to T_1 : $T_1 = 2.251 \text{ mm}$ and $T_2 = 2.135 \text{ mm}$. The optimized lengths are compensated for the fringing effects of the open stubs.

Figure 53 shows the measured and simulated insertion loss results of the LTCC duplexer for (a) the 1st channel and (b) the 2nd channel. In the simulation, the higher dielectric constant ($\epsilon_r=5.5$) and 5% increase in the volume of cavities were taken into account based on the investigation in section 4.2.2. All design parameters depicted in Fig. 52 (b) for the modified duplexer are summarized in Table 6.



(a)



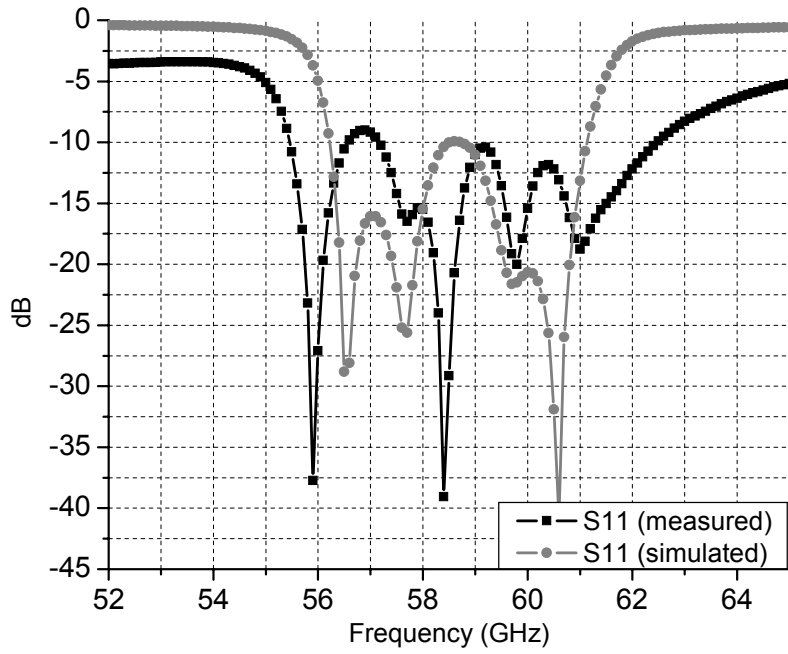
(b)

Figure 53: (a) S21 response in the 1st channel of the duplexer (measurement vs. simulation with $\epsilon_r = 5.5$ and modified cavity size ($2.048 \times 1.354 \times 0.1 \text{ mm}^3$)) (b) S31 response in the 2nd channel of the duplexer (measurement vs. simulation with $\epsilon_r = 5.5$ and modified cavity size ($2.048 \times 1.261 \times 0.1 \text{ mm}^3$)).

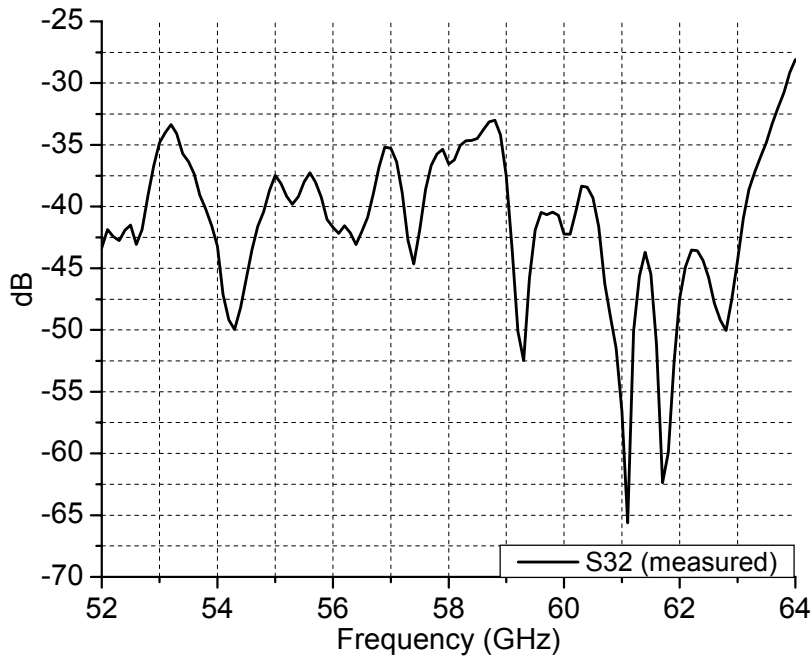
Table 6: Design Parameters of Cavity Duplexers.

<i>1st Channel</i>		<i>2nd Channel</i>	
<i>Design Parameters</i>	<i>mm</i>	<i>Design Parameters</i>	<i>mm</i>
cavity length (L_1)	2.048	cavity length (L_2)	2.048
cavity width (W_1)	1.354	cavity width (W_2)	1.261
each cavity height (H)	0.100	each cavity height (H)	0.100
ex. slot width (SW_1)	0.628	ex. slot width (SW_2)	0.621
ex. slot length (SL_1)	0.460	ex. slot length (SL_2)	0.460
ex. slot position(SD_1)	0.417	ex. slot position(SD_2)	0.417
in. slot width (CW_1)	0.558	in. slot width (CW_2)	0.551
in. slot length (CL_1)	0.138	in. slot length (CL_2)	0.138
in. slot position(CD_1)	0.417	in. slot position(CD_2)	0.417
microstrip length (T_1)	2.251	microstrip length (T_2)	2.135

The Rx filter exhibits an insertion loss <2.22 dB, which is slightly higher than the simulated value of 2.07 dB, and a 3-dB bandwidth of approximately 2.4 GHz ($\sim 4.20\%$) at the center frequency of 57.2 GHz compared to a simulated value of a 3-dB bandwidth of 2.7 GHz ($\sim 4.71\%$) at the center frequency of 57.25 GHz as shown in Fig. 53 (a). In Fig. 53 (b), the insertion loss for the 2nd channel is measured to be 2.48 dB very close to the simulated value of 2.46 dB. The Tx measurement shows a narrower 3-dB bandwidth of 1.6 GHz ($\sim 2.66\%$) at the center frequency of 60.1 GHz than the simulated 3-dB bandwidth of 2.6 GHz ($\sim 4.32\%$) at the center frequency of 60.15 GHz. The discrepancy between the measured and simulated insertion loss could be attributed to the metal loss from the roughness of screen printing on LTCC.



(a)



(b)

Figure 54: (a) S11 response of the duplexer (measurement vs. simulation with $\epsilon_r = 5.5$ and modified cavity sizes) (b) Measured S32 response in the isolation between the 1st and 2nd channels.

Table 7: Performance of Cavity Duplexers.

<i>Design Parameters</i>	<i>1st Channel</i>		<i>2nd Channel</i>	
	<i>Sim.</i>	<i>Meas.</i>	<i>Sim.</i>	<i>Meas.</i>
Insertion Loss (dB)	>2.07	>2.22	>2.46	>2.48
Bandwidth (%)	4.71	4.20	4.32	2.66
Return Loss (dB)	>16	>9	>20.67	>11.84
Center Frequency (GHz)	57.25	57.2	60.15	60.1
Isolation (dB)	>23.49	>35.18	>23.48	>38.36

The fabrication accuracy of the layer alignment could be responsible for the narrower bandwidth in the measurement because it could affect the external slots position that is a major factor to decide the bandwidth. Figure 54 shows the measured and simulated (a) return loss and the measured (b) channel-to-channel isolation. The measured isolation is better than 35.2 dB across the 1st band and better than 38.4 dB across the 2nd band. The summary of cavity duplexer results is presented in Table 7.

4.5 Cavity-Based Dual-Mode Filters

In the previous sections, we developed the single-mode cavity resonators and three-pole bandpass filters by adopting the vertically deployment of three single-mode cavity resonators. However, these single-mode devices could not satisfy optimum frequency selectivity. To achieve optimum frequency selectivity with a compact size and reduced weight, dual-mode dielectric rectangular [60]-[67] and circular waveguide filters [68]-[71] have been proposed and their basic features are well understood. The developed waveguide dual-mode filters make use of the coupling of two orthogonal modes generated from tuning screws [60]-[63], [68], [70]-[71], rectangular ridges [66]-[67], or the offsets of the feeding structure [64]-[65], [69]. Multi-pole, dual-mode cavity filters have been realized for higher frequency selectivity through the coupling between modes in adjacent dual-mode, single waveguide resonators using a cross slot [62]-[63], [68]-[69], [71] or rectangular irises [66], [70] or rectangular waveguides [65], [617]. However, these techniques not only impose a very heavy numerical burden to the modal characterization of waveguides because of the large number of evanescent modes, but also are not applicable to LTCC multilayer processes because of the fabrication limitations against a solid metal wall.

In this section, we expand previous work to a new class of 3D V-band dual-mode cavity filters and vertically stacked multi-pole filters using LTCC technologies, which enable a variety of quasi-elliptic responses by controlling the locations of transmission zeros. In Section 4.5.1, a dual-mode single cavity filter is developed for Rx and Tx channels as a complete filter solution in the design of V-band transceiver front-end module. The appearance and elimination of transmission zeros have been analyzed through multi-path coupling diagrams and lumped element models consisting of an inter-coupling through the offset of feeding structures and a cross coupling by source-to-load distance. In order to provide the additional design guideline for

the multi-pole cavity filters, the vertically stacked arrangement of two dual-mode cavities is reported for the first time ever in Section 4.5.2. The pre-synthesized dual-mode single cavity filters are stacked with two different coupling slots (rectangular and cross) between the two cavities. The feasibility of realizing a multi-pole filter has been validated with the experimental data.

4.5.1 Dual-Mode Cavity Filters

4.5.1.1 Single Dual-Mode Cavity Resonator

The square-shaped cavity resonator is first designed at a center frequency of 63 GHz to exhibit a degenerated resonance of two orthogonal modes (TE_{102} and TE_{201}) characteristic of the dual-mode operation. LTCC multilayer substrates have been used for the fabrication, and its properties are as follows: The ϵ_r is 7.1, $\tan\delta$ is 0.0017, the dielectric layer thickness is 53 μm per layer for a total of 5 layers, the metal thickness is 9 μm , and the resistivity of the metal (silver trace) is $2.7 \times 10^{-8} \Omega \cdot \text{m}$. Figure 55 shows (a) the 3D overview and (b) the top view of the proposed structure. The dual-mode cavity resonator consists of one cavity occupying two substrate layers S_2 - S_3 , the I/O microstrip feedlines on M_1 and the two coupling slots etched on the top ground plane, M_2 of the cavity. The microstrip lines are terminated with a physical short circuit realized by a metallic via (throughout S_1) to maximize the magnetic coupling through the slots. In order to determine the effective length, L , and width, W , in Fig. 55 (b) of the cavity resonator providing two orthogonal modes of TE_{mnl} and TE_{pqr} , both modes are constrained to resonate at the same frequency using the conventional resonant frequency equation of the rectangular waveguide cavity.

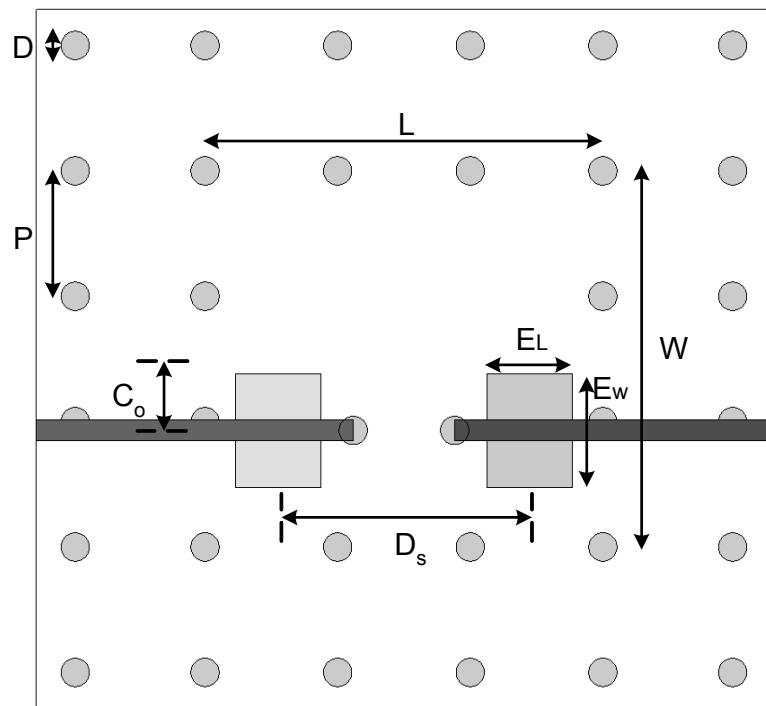
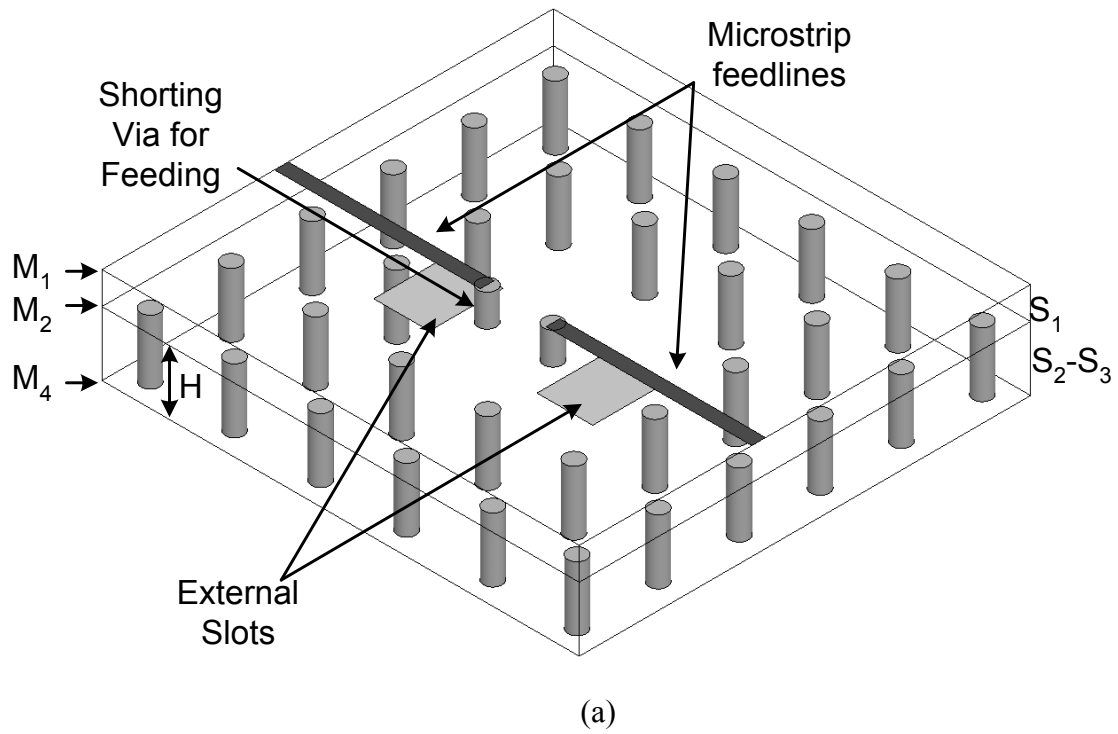
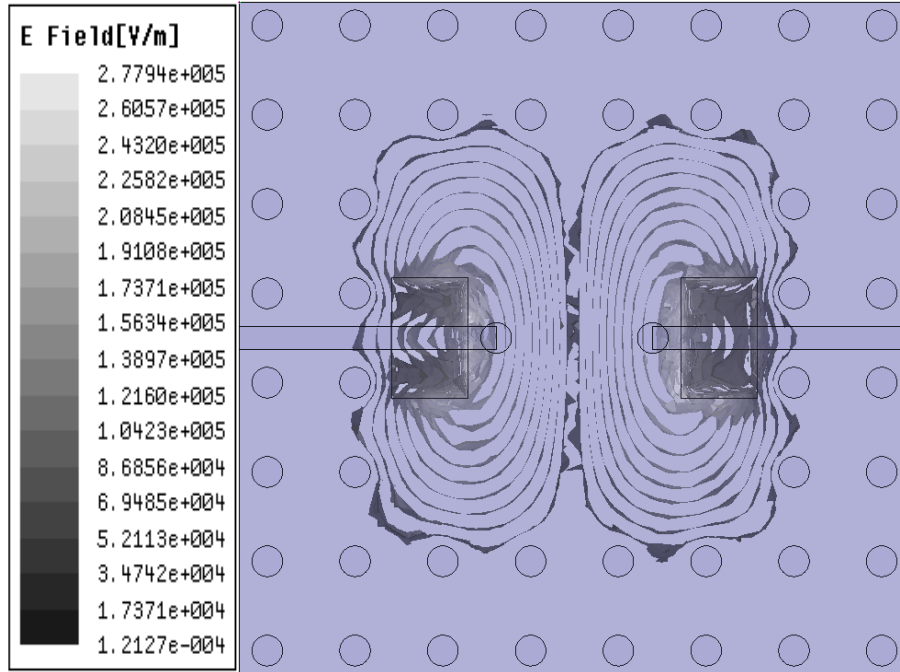


Figure 55: (a) The 3D overview (b) The top view of a quasi-elliptic dual-mode single cavity filter.

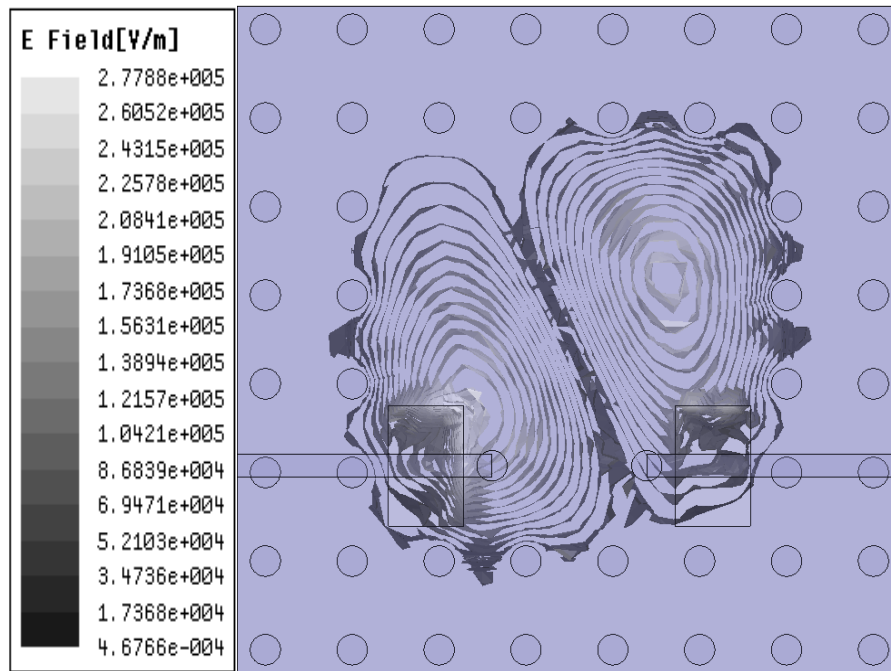
Since the modes chosen in our case are TE_{m0l} and TE_{p0r} , we impose the mode indexes of n and q to be zero so that the resonant frequency does not depend on the height of the cavity (Therefore, the degree of flexibility in the cavity height is high which makes the integration into a three-dimensional multifunctional packaging less problematic). Then, we have set the modal indices m, l and p, r to be 1,2 and 2, 1, to excite the most fundamental dual modes in the cavity and also to take advantage of the square-shaped cavity configuration that provides a higher Q_u than the rectangular-shaped configuration [49]. The final dimensions of the cavity resonator using via fences as vertical walls are determined to be $2.06 \times 2.06 \times 0.106 \text{ mm}^3$ in HFSS full-wave simulator first to resonate at 63 GHz. The size and spacing of the via posts are properly chosen according to the LTCC design rules, such as a minimum value of center-to-center vias spacing p in Fig. 55 (b) of $390 \text{ }\mu\text{m}$ and a minimum value of via diameter d in Fig. 55 (b) of $145 \text{ }\mu\text{m}$.

4.5.1.2 Internal Coupling

The centerline offset, C_o , in Fig. 55 (b) between the feeding structure and cavity position is one of major factors in realization of the dual-mode operation and controlling the mutual internal coupling of the modes, hence providing transmission zeros at the desired positions for a high selectivity. When the I/O slots are centered at the cavity interface ($C_o=0 \text{ mm}$), only the TE_{102} mode is excited so that the transmission zeros do not exist. The electric field distribution at the center frequency 62.9 GHz is illustrated in Fig. 56 (a), demonstrating the field distribution of the TE_{102} mode divided along the normal center line. The two symmetrical sections have the same magnitude but are out of phase. When a transverse offset, C_o , is applied to the position of the I/O feeding structure, the TE_{201} mode is excited as well. This mode degeneration can be used to realize dual-mode filters.



(a)



(b)

Figure 56: Magnitude of electric field distribution (TE_{102}) on horizontal plane inside the dual-mode cavity at the resonant frequency ($=62.9$ GHz) (a) when $C_o = 0$ mm (b) when $C_o = 0.6$ mm.

The basis modes are defined as even and odd mode, respectively [24], (by vectorial addition and subtraction of TE_{102} and TE_{201} modes) and the magnetic vectors of these modes calculated using HFSS simulation software are displayed in Fig. 57. These resonant frequencies are associated to the inter-coupling coefficient according to the definition of the ratio of the coupled energy to the stored energy of an uncoupled single resonator [72].

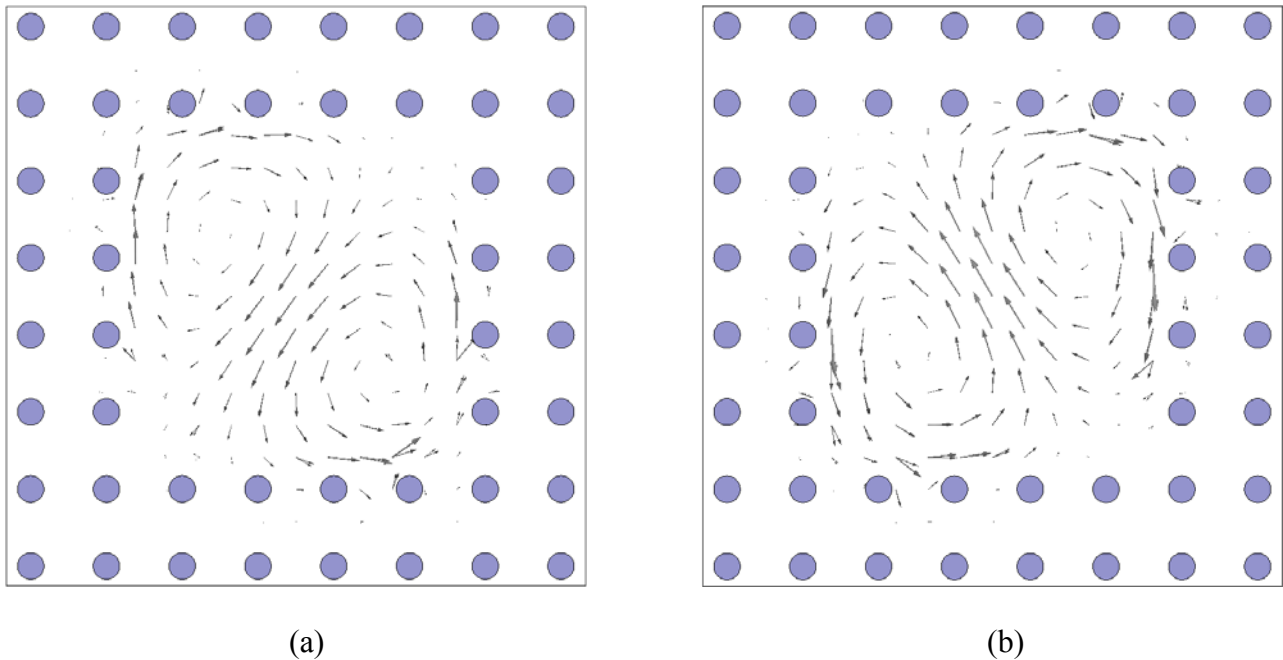


Figure 57: (a) Magnetic vector of the odd mode (b) Magnetic vector of the even mode.

Although there are numerous techniques to control the coupling coefficients by using a perturbation element such as a tuning screw and a corner cut, the transverse offset of feeding structures [64],[72] is chosen for this case. This technique can provide advantages in terms of fabrication simplicity, production cost, and reproducibility. Full-wave simulations are employed to find f_e and f_o . The value of f_e (f_o) can be derived from a symmetric structure by placing a perfect electric conductor (a perfect magnetic conductor) on the plane of the symmetry. Figure

58 displays the internal coupling coefficient as a function of the variation of the centerline offset C_o . The electric field distribution in Fig. 56 (b) corresponds to $C_o=0.6\text{mm}$, representing the dual mode that is bisected along the diagonal line.

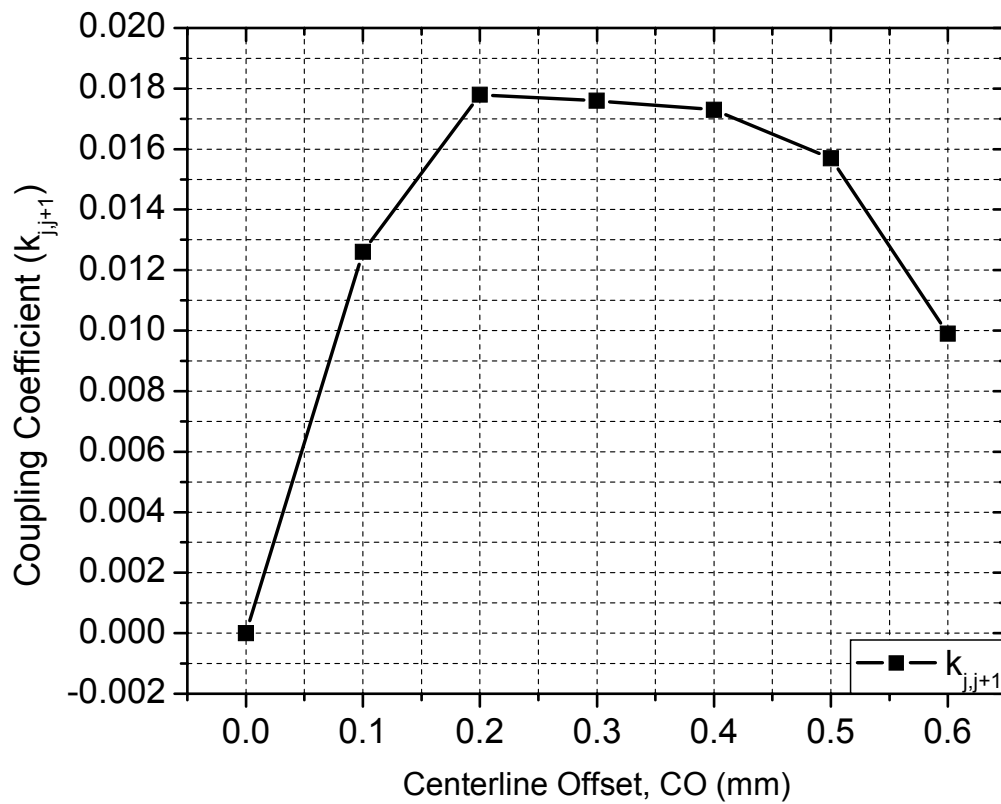


Figure 58: Internal coupling coefficient k_{jj+1} as a function of the centerline offset C_o of the feeding structures.

4.5.1.3 External Coupling

The I/O external slots on the top ground plane of the cavity are designed for the magnetic excitation of the cavity from the 50 Ω microstrip lines. In order to maximize the magnetic coupling by maximizing the magnetic currents, the microstrip lines are terminated with a physical short circuit realized by a metallic via. The spacing between the center of the via and the edge of the slot should be at least 0.165 mm according to the LTCC design rules. The accurate design of the external coupling slots that is directly related to the external quality factor, Q_{ext} , is a key issue to achieve a high- Q cavity resonator. The Q_{ext} corresponds to the resistance and the reactance and can be controlled by the position and size of the coupling slots. In order to investigate how the slot size affects the Q_{ext} , the external slots are initially placed at a quarter of the cavity length from the (front and back) edge of the cavity, and the slot length is varied with the fixed slot width ($\sim\lambda_g/4$). The issues related to the distance between external slots (D_s in Fig. 55) will be discussed in detail in section 4.5.1.4. Both single-mode case ($C_o=0$ mm) and dual-mode case ($C_o = 0.6$ mm) were tested. In the single mode case, the Q_{ext} can be determined by the relation [56] between the resonant frequency and the frequencies where a $\pm 90^\circ$ phase response in S_{11} parameter is exhibited. However, in the dual-mode case, the external coupling factor is directly related to the internal coupling coefficient according to the analytical equation [73]

$$Q_{ext} = \frac{1}{\sqrt{k_{1,2}^2 - k_{(1,2)wo}^2}} \quad (21)$$

where $k_{1,2}$ is the coupling coefficient of the dual-mode resonator with an external circuit and $k_{(1,2)wo}$ is the coupling coefficient of the dual-mode resonator without an external circuit.

Figure 59 shows the relationship between the length variation of the external slots E_L and the Q_{ext} from the simulation when the feeding structure is placed at 0.6 mm away from the center

of the cavity ($C_o = 0.6 \text{ mm}$). A larger E_L results in smaller Q_{ext} that is interpreted as a stronger external coupling.

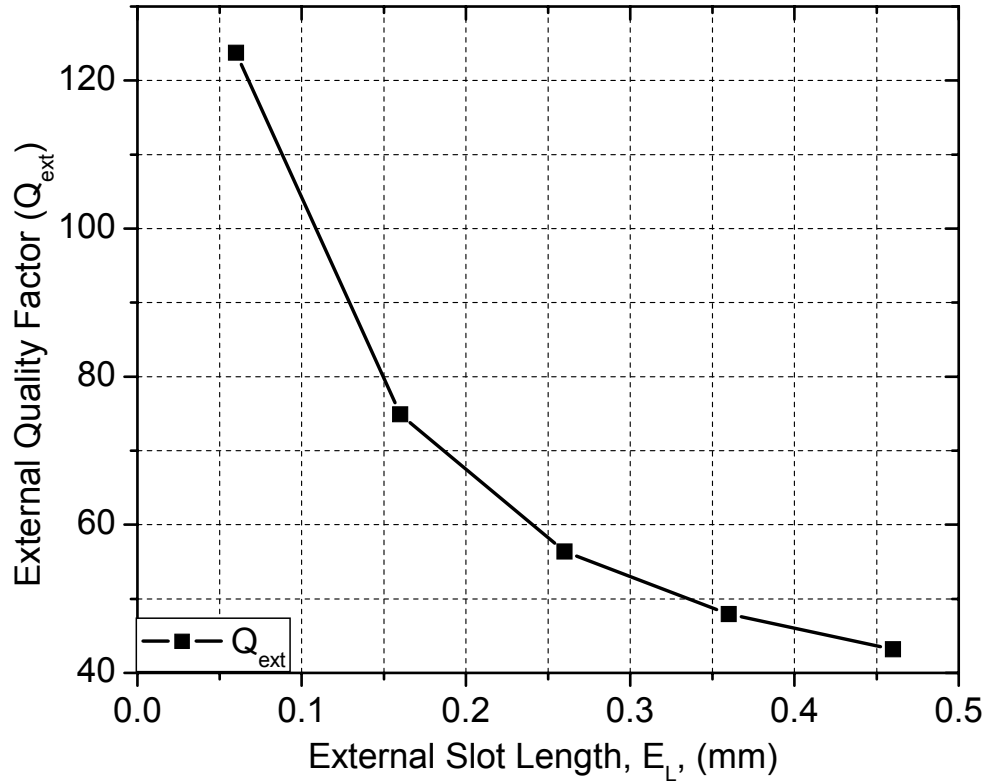
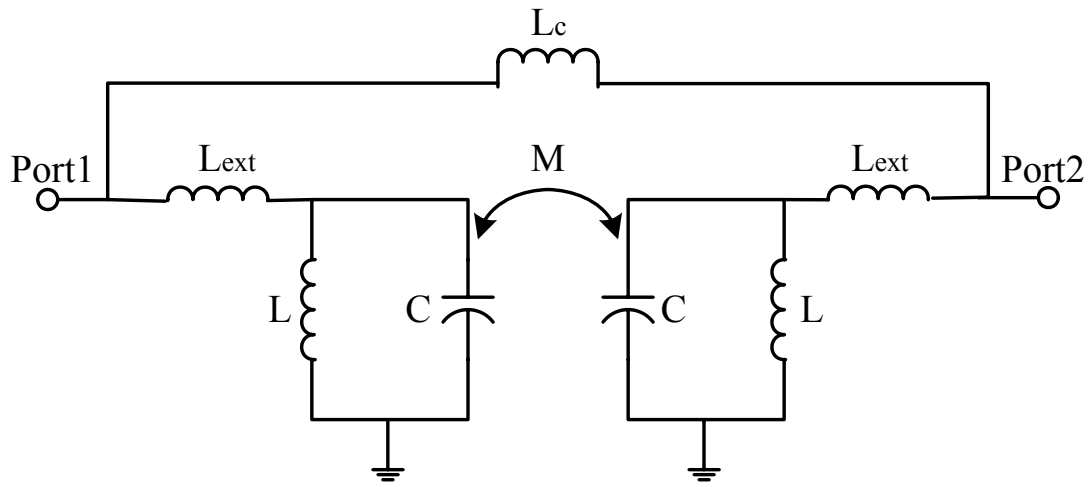


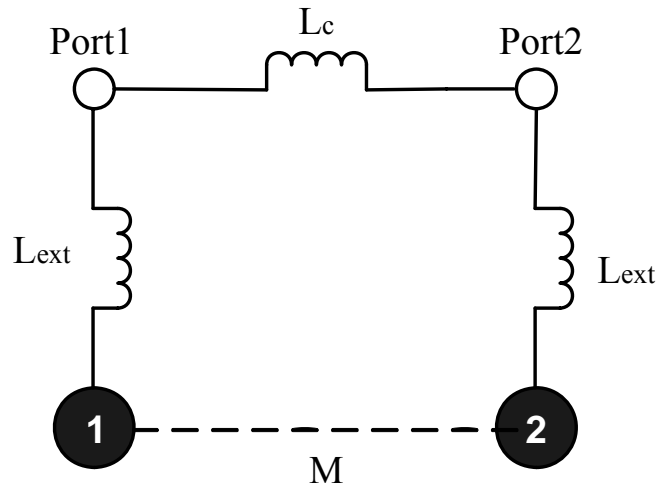
Figure 59: External quality factor Q_{ext} evaluated as a function of external slot length E_L .

4.5.1.4 Transmission Zero

Having discussed how to implement the internal and the external couplings in a dual-mode cavity resonator, the dual-mode filter realization with transmission zeros for high selectivity will be discussed in this section. The equivalent circuit model of the proposed dual-mode cavity filter is shown in Fig.60 (a).



(a)



(b)

Figure 60: (a) Equivalent circuit model of the quasi-elliptic dual-mode cavity filter (b) Multi-coupling diagram for the quasi-elliptic dual-mode cavity filter.

The filter consists of major four sections: (1) a pair of LC resonators that represent each of the degenerate dual modes in the cavity resonator, (2) mutual internal electric coupling, M , between a pair of parallel LC resonators, (3) external magnetic coupling, L_{ext} from each of the I/O external slots, and (4) magnetic cross coupling, L_c , representing the parasitic source to load coupling associated with the perturbed electric fields in the cavity [74]. A pair of transmission zeros at the upper and lower sides of the passband can be created when L_c has a 180° phase difference with respect to M with similar magnitudes. This sign reversal is attributed to a destructive interference between two modes, therefore, resulting in the construction of transmission zeros at two frequencies.

The fundamental cross coupling technique is well explained in [75] by using multipath coupling diagrams to illustrate the relative phase shifts of multiple single paths. In [75], Brian adopted the S21 phase shift, Φ_{21} , of each lumped element in the equivalent circuits of a resonator and calculated the total phase shift at the input (or output) of the resonator to predict the behavior of transmission zeros. Since transmission zeros appear away from the passband, the off-resonance behavior of each lumped component is of concern. The Φ_{21} of the series inductor and capacitor can provide a phase angle of -90° and $+90^\circ$, respectively according to the off-resonance behavior of each component. The Φ_{21} of the shunt inductor/capacitor pairs corresponds to $+90^\circ$ below the resonance and -90° above the resonance. This phenomenon is because of the fact that below (above) resonance, the inductance (capacitance) dominates on the resonator and an inductor (capacitor) in shunt is the dual of a capacitor (inductor) in series [75]. Based on this theory, the equivalent circuit for a dual-mode cavity filter can be represented by a multi-path diagram as described in Fig. 60 (b). The shunt capacitor/inductor pairs of the equivalent circuit have been replaced by the black circles, and M represents the mutual electric coupling between

two modes. The phase shift of each lumped element is used to calculate the total phase shift at the input or output of the filter for the different signal paths. In the case of the dual-mode single cavity filter, there are two possible signal paths (1) *path1: Port1-1-2-Port2* and (2) *path2: Port1-Port2*. Both paths share the common input (*Port1*) and output (*Port2*). The total phase shifts for two signal paths in the dual-mode cavity are summarized in Table 8. The total phase shift for path 1 is -90° both below and above resonance. The total phase shift for *path 2* only accounts for the cross magnetic coupling L_c between *port1* and *port2*, hence being $+90^\circ$. Therefore, two paths are out of phase both below and above resonance, meaning that destructive interferences creating transmission zeros occur both below and above the passband.

Table 8: Total phase shifts for two different paths in the dual-mode cavity filter.

<i>Paths</i>	<i>Below Resonance</i>	<i>Above Resonance</i>
Port1-1-2-Port2	$-90^\circ+90^\circ+90^\circ+90^\circ-90^\circ=+90^\circ$	$-90^\circ-90^\circ+90^\circ-90^\circ-90^\circ=-270^\circ$
Port1-Port2	-90°	-90°
Result	Out of Phase	Out of Phase

The locations of the upper and lower stopband transmission zeros for the filter can be controlled by adjusting the values of M and L_c through varying the centerline offset, C_o , and distance D_s , between the I/O external slots, respectively. Shown in Fig. 61 are the simulated responses of a dual mode filter as a function of the parameter, C_o .

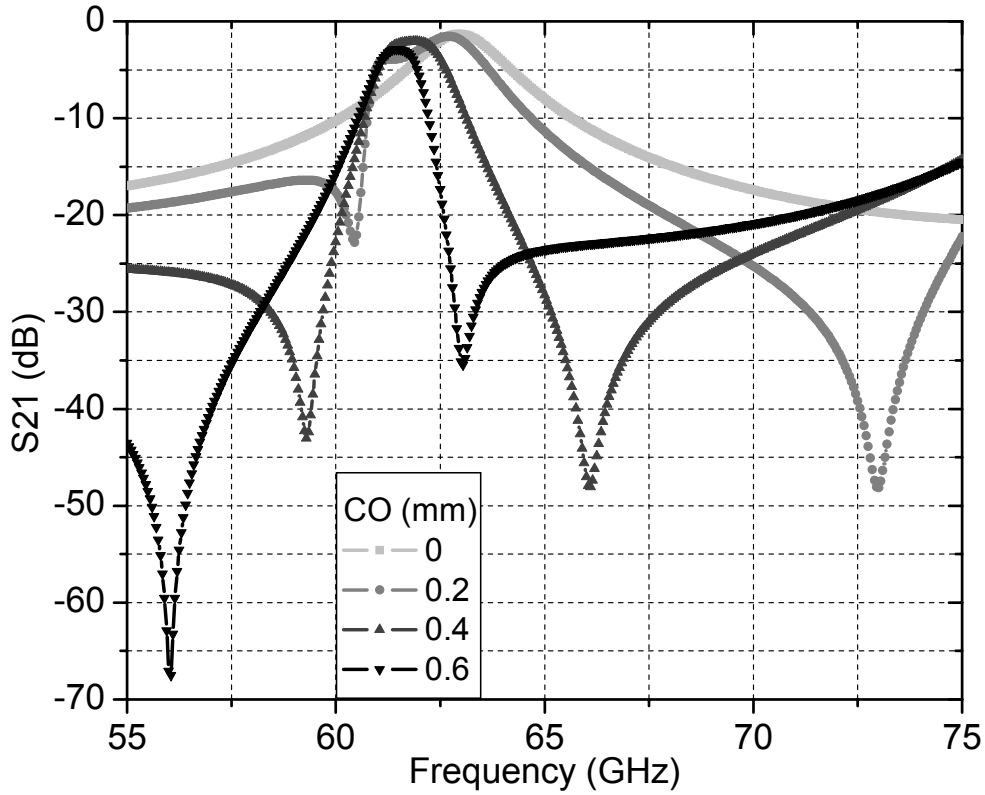
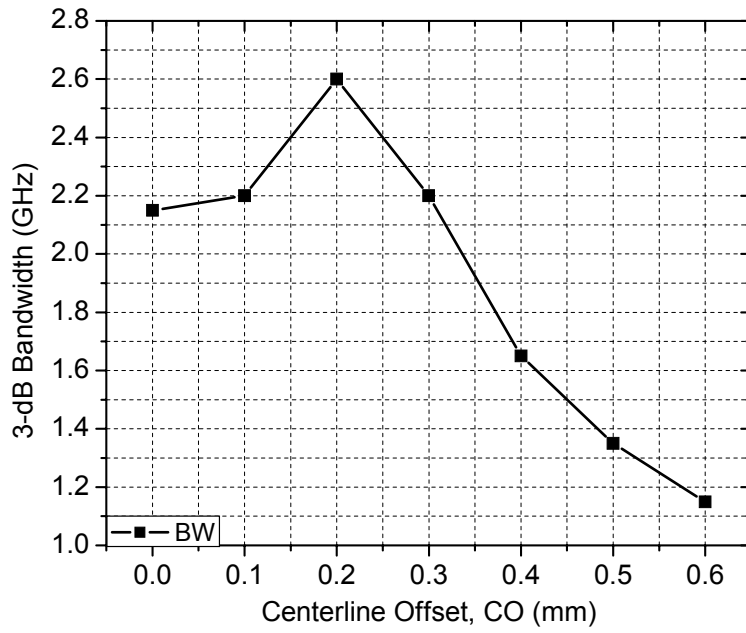


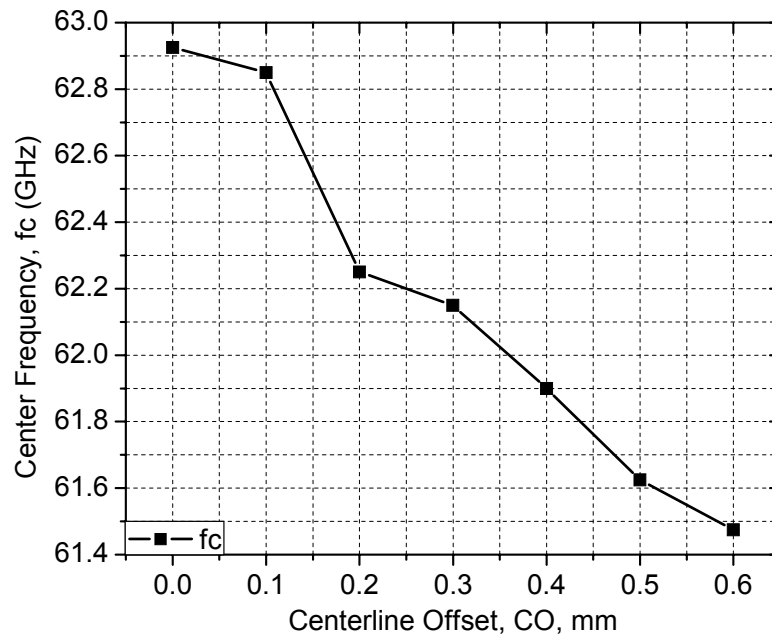
Figure 61: The simulated S_{21} parameter response of a dual mode filter as a function of the centerline offset C_o of the feeding structures.

When the feeding structure is placed at the center of the cavity ($C_o=0$ mm), only the TE_{102} mode is excited, producing no transmission zeros.

As C_o increases, the upper transmission zero moves toward the center frequency while the lower one moves away from the center frequency. Varying the centerline offset, C_o , changes the level of internal electric coupling, M , that induces the asymmetrical shift of both transmission zeros. The value of M can be obtained from the difference between f_o and f_e [56] and influences the upper transmission zeros more than the lower transmission zeros as depicted in Fig. 61.



(a)



(b)

Figure 62: Simulated responses of (a) 3-dB bandwidth and (b) center frequency f_c as a function of the centerline offset C_o of the feeding structure.

This is because when the feeding structures move from the center position the effect of M upon the upper and lower poles becomes asymmetric, resulting in that the destructive interferences creating transmission zeros occur at asymmetrical locations below and above the passband [76].

The centerline offset, C_o , affects the performance of the 3-dB bandwidth and center frequency as well. Figure 62 (a) and (b) show the simulated 3-dB bandwidth and center frequency, respectively, as C_o increases. It is observed that the maximum 3-dB bandwidth is obtained at the offset of 0.2 mm, and an increase of the offset results in a narrower bandwidth. This phenomenon could occur because the level of coupling for TE_{102} and TE_{201} changes as C_o increases. With the excitation of the TE_{201} mode, coupling between dual modes is maximized at $C_o=0.2$ mm, providing the widest bandwidth, as shown in Fig. 58. The downward shifting of the center frequency, displayed in Fig. 62 (b), could be caused by the difference between the mean frequency $((f_o + f_e)/2)$ and the original resonant frequency of the cavity resonator. Also, external coupling can be attributed to the center frequency shift because of its additional reactance effect from the feeding structures.

The transmission characteristic of the filter is investigated with respect to the values of L_c by varying the distance D_s between two external slots with a fixed centerline offset, C_o . Figure 63 displays the simulated response of a dual mode filter as a function of D_s with $C_o=0.5$ mm. As L_c decreases by increasing D_s , the lower transmission zero shifts away from the center frequency while the higher transmission zero moves toward to the center frequency. The cross coupling, L_c , causes the asymmetrical shift of both transmission zeros due to the same reason mentioned in the case of M , influencing the lower transmission zero more than the higher one. Our equivalent-circuit models are justified to validate the coupling mechanisms through the design of a

transmitter filter in the next sub-section.

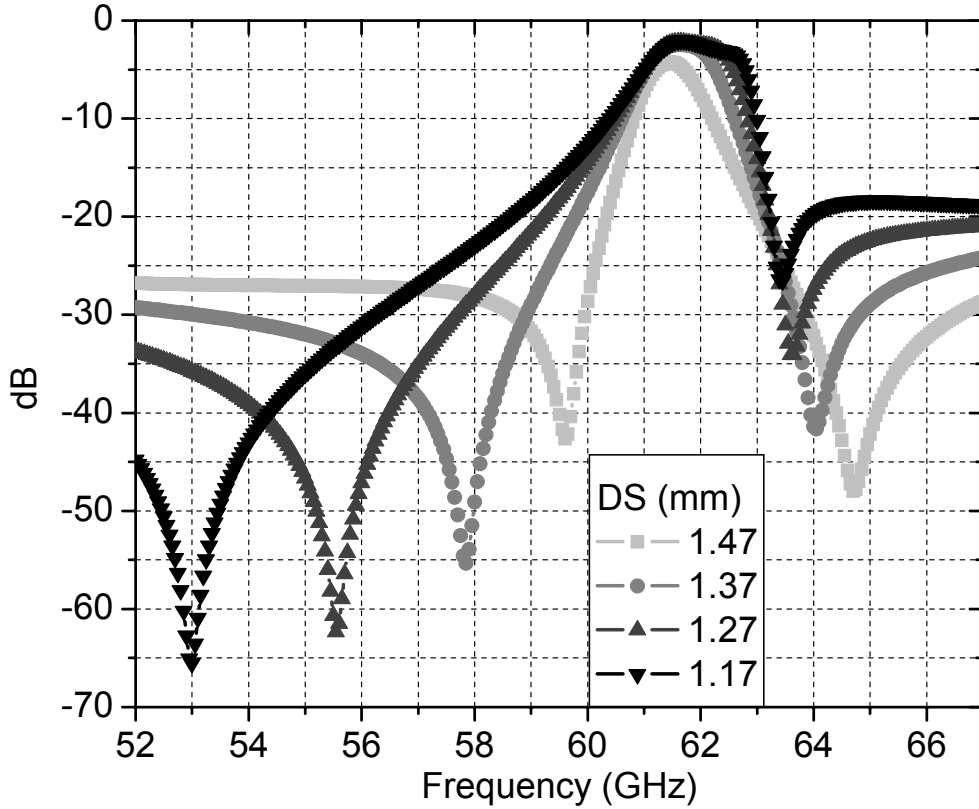


Figure 63: The simulated S_{21} parameter response of a dual mode filter as a function of the source-to-load distance D_s .

4.5.1.5 Quasi-Elliptic Dual-Mode Cavity Filter

Two dual-mode cavity filters exhibiting a quasi-elliptical response are developed as the next step for a three dimensional integrated V-band transceiver front-end module. The frequency range of interest is divided into two channels where the lower channel is allocated for a Rx, and

the higher channel allocated for a Tx. To suppress the interference between the two channels as much as possible, the upper stop-band transmission zero of the Rx channel is placed closer to the center frequency of the passband than the lower stop-band zero. In the case of a Tx filter, the lower zero is located closer to the center frequency of the passband than the upper zero.

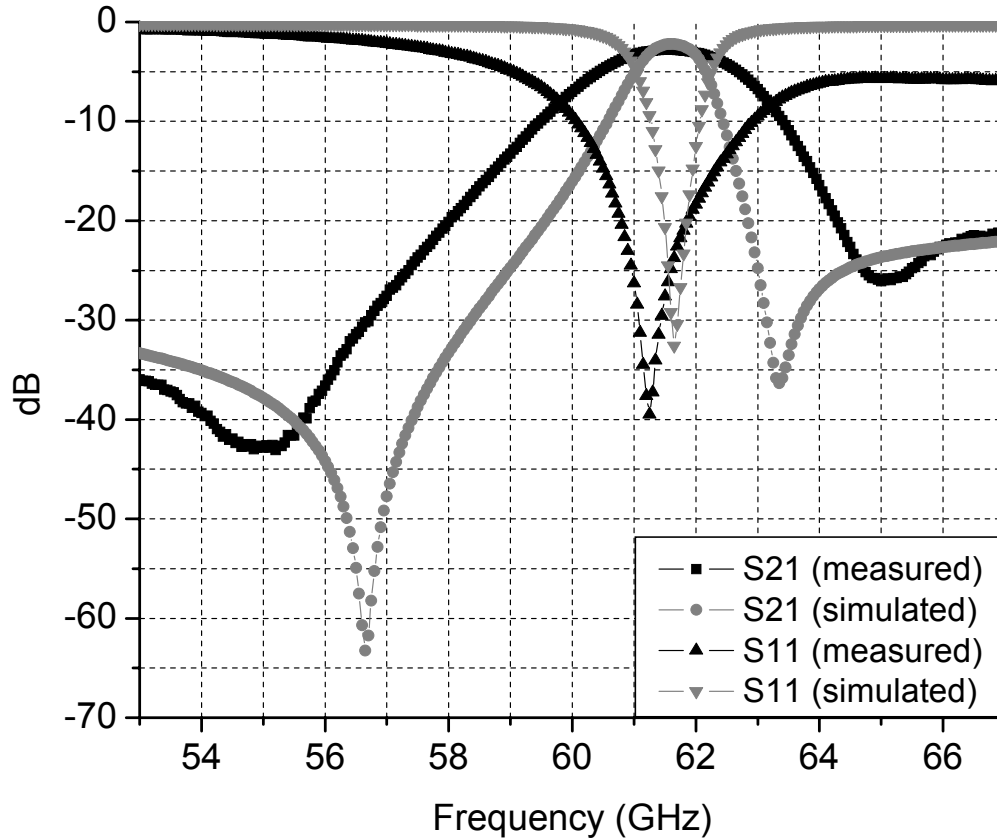


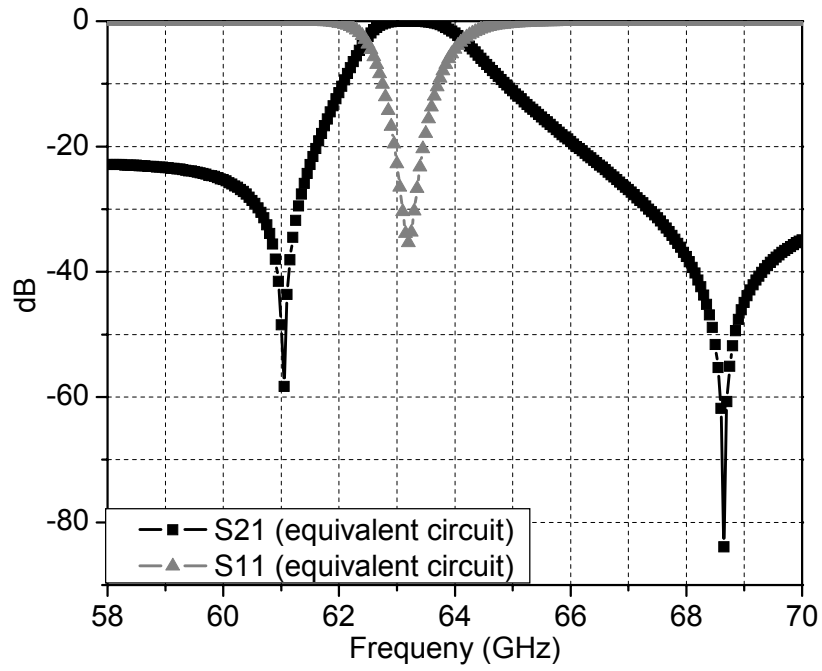
Figure 64: Measured and simulated S -parameters of the dual-mode cavity filter for a Rx channel.

First, a Rx filter was designed and validated with experimental data, as shown in Fig. 64. All of the fabricated resonators were measured using the Agilent 8510C Network Analyzer and Cascade Microtech probe station with 250 μm pitch air coplanar probes. A line-reflect-reflect-match (LRRM) method [77] was employed for calibration. In the measurement, the reference

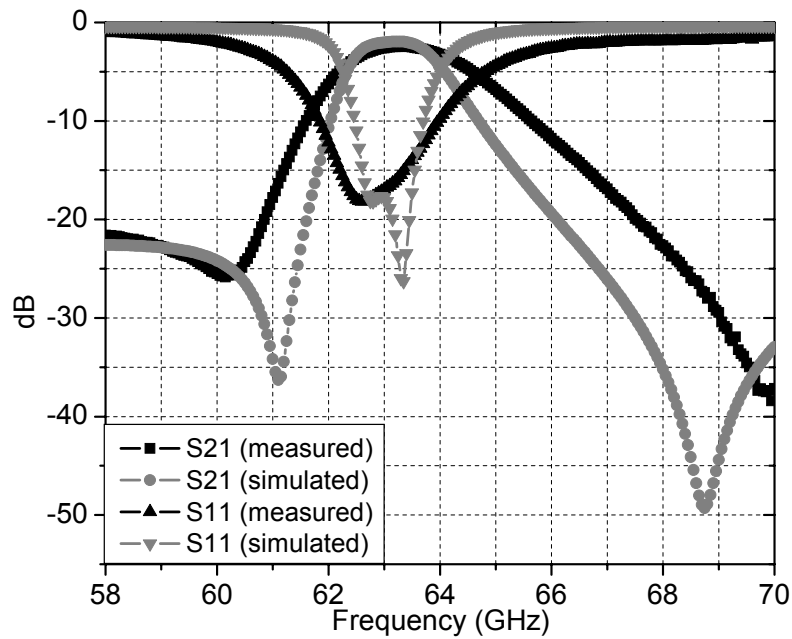
planes are decided to be at the end of the probing pads, and the capacitance and inductance effects of the probing pads are de-embedded by use of “Wincal” software so that effects, such as those due to the CPW loading, become negligible. The filter exhibits an insertion loss of <2.76 dB, center frequency of 61.6 GHz, and 3-dB bandwidth of about 4.13 % (≈ 2.5 GHz). The upper and lower transmission zeros are observed to be within 3.4 GHz and 6.4 GHz away from the center frequency, respectively.

Then, a Tx filter using a dual-mode cavity resonator is designed for a center frequency of 63.4 GHz, fractional 3-dB bandwidth of 2%, insertion loss of <3dB, and 25dB rejection bandwidth on the lower side of the passband of <2GHz. To obtain a center frequency of 63.4 GHz, the size of the via-based cavity is adjusted and determined to be $2.04 \times 2.06 \times 0.106$ ($L \times W \times H$ in Fig.55) mm^3 . The centerline offset C_o , the distance between the two external slots, and the size of each external slot are used as the main design parameters to achieve the right positions of the transmission zeros, the desired internal coupling coefficient, and the external quality factor as investigated in the previous sub-sections. The corresponding lumped-element values in the equivalent-circuit model (Fig. 60 (a)) of a Tx filter are evaluated, and their values are $L_{ext} = 0.074$ nH, $L = 0.0046$ nH, $C = 1.36$ pF, $M = 0.032$ pF and $L_c = 0.73$ nH. Figure 65 (a) shows the ideal response from the circuit model, exhibiting two transmission zeros at 61.6 and 68.7 GHz.

The measured insertion loss and reflection losses of the fabricated filter are compared to the full-wave simulation results in Fig. 65 (b). The fabricated Tx filter exhibits an insertion loss of 2.43 dB, which is slightly higher than the simulated (2.0 dB). The main source of this discrepancy might be caused by the skin and edge effects of the metal traces since the simulations assume a perfect definition of metal strips with finite thickness. The center frequency is measured to be 63.4 GHz which is in good agreement with the simulated result.



(a)



(b)

Figure 65: (a) Simulated S-parameters of the dual-mode cavity filter using equivalent-circuit model in Fig. 60 (a). (b) Measured and simulated S-parameters of the dual-mode cavity filter for a Tx channel.

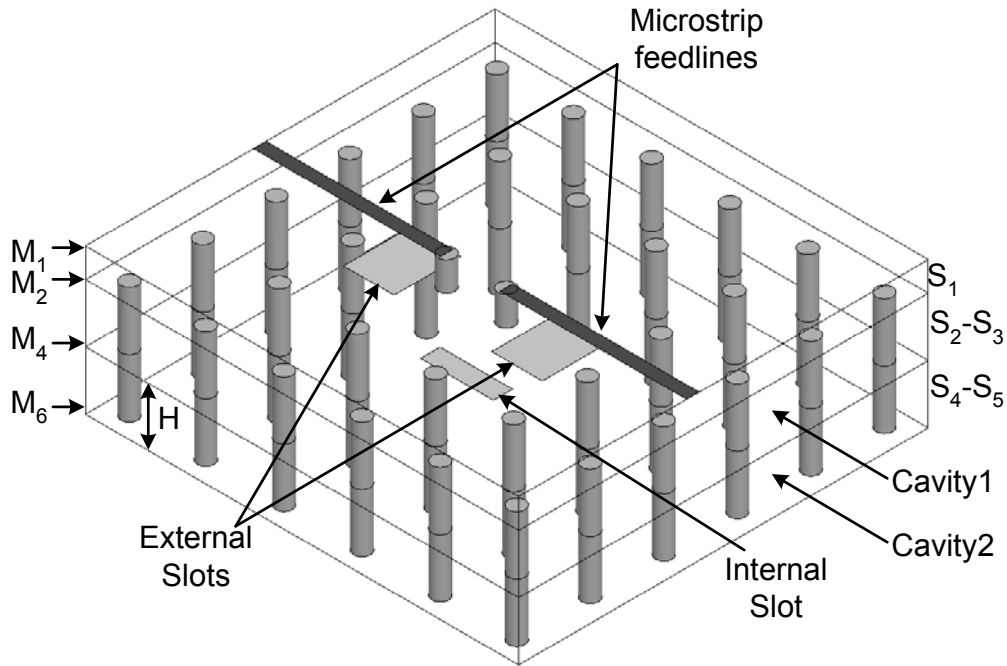
The upper and lower transmission zeros are observed to be within 6.5 GHz and 3.2 GHz away from the center frequency, respectively. Those can be compared to the simulated values that exhibit the upper and lower transmission zeros within less than 5.3 GHz and 2.3 GHz away from the center frequency. The discrepancy of the zero positions between the measurement and the simulation can be attributed to the fabrication tolerance. Also, the misalignment between the substrate layers in the LTCC process might cause an undesired offset of the feeding structure position. This could be another major contribution to a transmission zero shift. These fabrication tolerances also result in the bandwidth differences. The filter exhibits a 3-dB measured bandwidth of 4.02 % (~2.5 GHz) compared to the simulated one of 2 % (~1.3 GHz). All of the final layout dimensions optimized using HFSS are summarized in Table 9.

Table 9: Design parameters of quasi-elliptic dual-mode cavity filters.

<i>Design Parameters</i>	<i>Rx Filter(mm)</i>	<i>Tx Filter(mm)</i>
cavity length (L)	2.075	2.04
cavity width (W)	2.105	2.06
cavity height (H)	0.106	0.106
external slot length (E_L)	0.360	0.360
external slot width (E_W)	0.572	0.572
centerline offset (Co)	0.5675	0.35
Distance between external slots (D_s)	1.37	1.355

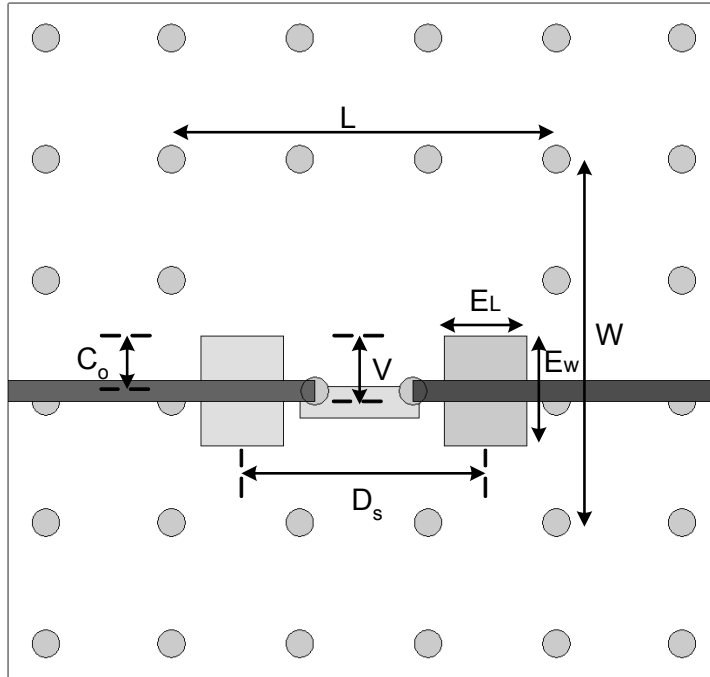
4.5.2 Multi-Pole Dual-Mode Cavity Filters

In order to provide the additional design guidelines for generic multi-pole cavity filters, the authors proceed with a vertically stacked arrangement of two dual-mode cavities. The pre-synthesized dual-mode cavities are stacked with a coupling slot in order to demonstrate the feasibility of realizing a multi-pole filter by using the dual-mode cavity filters investigated in Section 4.5.1. Two well-known types of slots (rectangular and cross-shaped) are considered as the inter-coupling structure in this study. In the past, mode matching methods [60] and scattering matrix approaches [66] have been used to analyze the modal characterization of inter-coupling discontinuities hence will not be covered in this paper. In this case, HFSS was employed to optimize the size and the position of the inter-coupling slots for the desired frequency response.

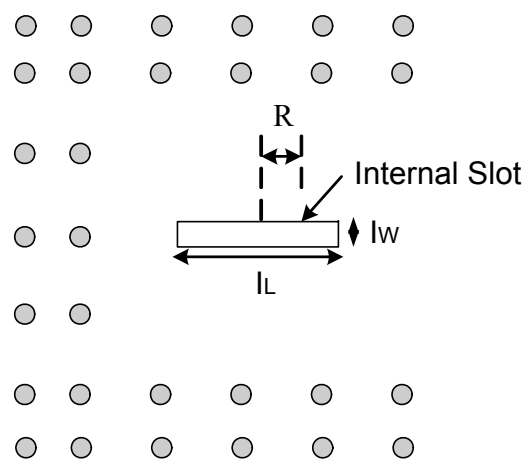


(a)

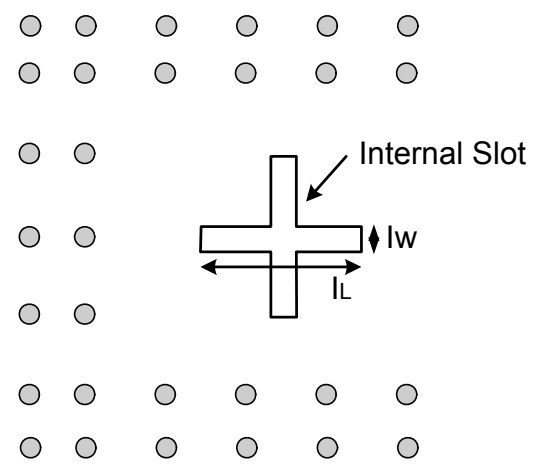
Figure 66: (a) The 3D overview (b) The top view of a vertically stacked multi-pole dual-mode cavity filter (c) Inter-coupling rectangular slot (d) Inter-coupling cross slot.



(b)



(c)



(d)

Figure 66: Continued.

The 3D overview (a), top view (b), inter-coupling rectangular slot (c) and inter-coupling cross slot (d) of the proposed cavity filter are illustrated in Fig. 66. The top five substrate layers (Microstrip line: S_1 , *Cavity1*: S_2 - S_3 , *Cavity2*: S_4 - S_5 in Fig. 66 (a)) are occupied by the filter. Microstrip lines have employed as the I/O feeding structure on the top metal layer, M_1 , and excite the first dual-mode cavity through the rectangular slots on the top ground plane, M_2 , of the *Cavity1*. Two identical dual-mode cavity resonators (*Cavity1* and *Cavity2* in Fig. 66 (a)) are vertically stacked and coupled through an inter-coupling slot to achieve the desired frequency response with high selectivity as well as a high-level of compactness.

4.5.2.1 Quasi-Elliptic Filter with a Rectangular Slot

The multi-path diagram of a vertically stacked dual-mode filter with a rectangular slot is illustrated in Fig. 67. The black circles denoted by 1 and 2 are the degenerate resonant modes in the top dual-mode cavity while the one denoted by 3 represents the excited resonant mode in the bottom cavity. The coupling, M_{12} , is realized through the electrical coupling and controlled by the offsets of the I/O feeding structures. Also, the inter-couplings, M_{13} and M_{32} , are determined by the sizes and positions of the inter-coupling slots and dominated by the magnetic coupling. It is worth noting that M_{13} is different from M_{32} since the magnitude of the magnetic dipole moment of each mode in a coupling slot is different to each other due to the nature of a rectangular slot. Since the rectangular slot is parallel to the horizontal direction, the modes polarized to the horizontal direction are more strongly coupled through the slot than the other modes that are polarized in the vertical direction. However, by adjusting the offset, we attempted to obtain the appropriate coupling level of M_{13} and M_{32} to realize the desired filter response.

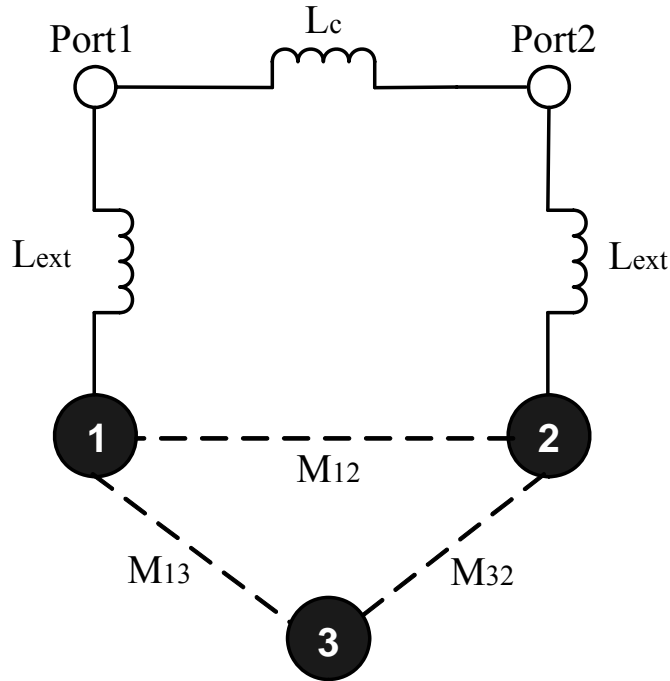


Figure 67: Multi-coupling diagram for the vertically stacked multi-pole dual-mode cavity filter with rectangular slot for inter-coupling between two cavities.

L_c (the magnetic coupling parameter) is used to implement the cross coupling between *Port1* and *Port2*. The phase shifts for three possible signal paths are summarized in Table 10. The filter with three modes can generate two transmission zeros below resonance and an additional zero above resonance.

The three-pole quasi-elliptic filters were designed to meet the following specifications: (1) center frequency: 66 GHz, (2) 3-dB fractional bandwidth: $\sim 2.6\%$, (3) insertion loss: $< 3\text{dB}$, and (4) 15 dB rejection bandwidth using triple transmission zeros (two on the lower side and one on the upper side): $< 3\text{GHz}$. A study of the dual-mode coupling in each cavity on the basis of the initial determination of the cavity size resonating at a desired center frequency (66 GHz) is performed first.

Table 10: Total phase shifts for three different signal paths in the vertically stacked dual-mode cavity filter with a rectangular slot.

<i>Paths</i>	<i>Below Resonance</i>	<i>Above Resonance</i>
Port1-1-2-Port2	$-90^\circ+90^\circ+90^\circ+90^\circ-90^\circ=+90^\circ$	$-90^\circ-90^\circ+90^\circ-90^\circ-90^\circ=-270^\circ$
Port1-Port2	-90°	-90°
Result	Out of Phase	Out of Phase
<hr/>		
1-3-2	$-90^\circ+90^\circ-90^\circ=-90^\circ$	$-90^\circ-90^\circ-90^\circ=-270^\circ$
1-2	$+90^\circ$	$+90^\circ$
Result	Out of Phase	In Phase

Then, the final configuration of the three-pole dual-band filter can be obtained through the optimization of the inter-coupling slot size and offsets via simulation. All of the design parameters for the filters are summarized in Table 11. Figure 68 shows the measured performance of the designed filters with a rectangular slot along with a comparison to the simulated results. It can be observed that the measured results with a rectangular slot produce a center frequency of 66.2 GHz with the bandwidth of 1.2 GHz (~1.81 %), and the minimum insertion loss in the passband around 2.9 dB. The simulation showed a minimum insertion loss of 2.5 dB with a slightly wider 3-dB bandwidth of 1.7 GHz (~2.58%) around the center frequency of 65.8 GHz. The center frequency shift is caused by an XY shrinkage of $\pm 3\%$.

Table 11: Design parameters of multi-pole dual-mode cavity filters with two types of inter-coupling slots.

<i>Design Parameters</i>	<i>Rectangular(mm)</i>	<i>Cross (mm)</i>
cavity length (L)	2.04	2.06
cavity width (W)	1.92	2.06
each cavity height (H)	0.106	0.106
external slot length (E_L)	0.440	0.470
external slot width (E_W)	0.582	0.472
centerline offset (Co)	0.245	0.356
internal slot length (I_L)	0.642	0.412
internal slot width (I_W)	0.168	0.145
vertical slot offset (V)	0.325	0.6075
horizontal slot offset (R)	0.065	0
distance between external slots (D_s)	1.29	1.26

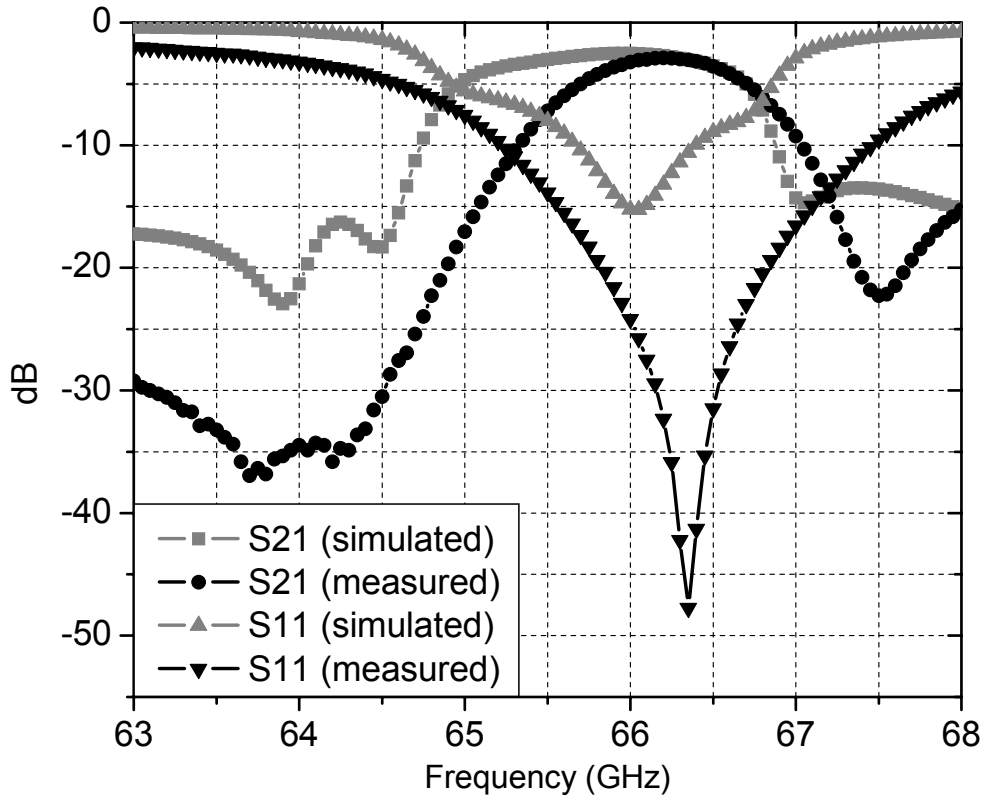


Figure 68: Measured and simulated S -parameters of the quasi-elliptic dual-mode cavity filter with a rectangular slot for inter coupling between cavities.

The two measured transmission zeros with a rejection better than 34 dB and 37 dB are observed within < 1.55 GHz and < 2.1 GHz, respectively, away from the center frequency at the lower band than the passband. One transmission zero is observed within < 1.7 GHz at the higher band than the passband. The discrepancy of the zero positions and rejection levels between the measurement and the simulation can be attributed to the fabrication tolerance as explained in Section 4.5.1.5. However, it can be observed that the behavior of transmission zeros correlates between the measurement and simulation. This type of filter can be used to generate the sharp skirt at the low side to reject local oscillator and image signals, as well the extra transmission

zero in the high skirt that can be utilized to suppress the harmonic frequencies according to the desired design specification.

4.5.2.2 Quasi-Elliptic Filter with a Cross Slot

The cross slot is applied as an alternative inter-coupling slot between the two vertically stacked cavities. The multi-paths diagram for the filter and the phase shifts for the possible signal paths are described in Fig. 69 and Table 12, accordingly. Each cavity supports two orthogonal dual modes (1 and 2 in the top cavity, 3 and 4 in the bottom cavity) since the cross slot structure excites both degenerate modes in the bottom cavity by allowing the coupling between the modes that have the same polarizations. The coupling level can be adjusted by varying the size and position of the cross slots. The couplings of M_{12} and M_{34} are realized by electrical coupling while the inter couplings of M_{13} and M_{24} are realized by magnetic coupling. The total phase shifts of the four signal paths of the proposed structure prove that they generate one zero above resonance and one below resonance.

The quasi-elliptic filters were designed for a sharp selectivity, and the simulation achieved the following specifications: (1) center frequency: 63 GHz, (2) 3-dB fractional bandwidth: $\sim 2\%$, (3) insertion loss: $< 3\text{dB}$, and (4) 40 dB rejection bandwidth using two transmission zeros (one on the lower side and one on the upper side) : $< 4\text{GHz}$.

The filter was fabricated using LTCC substrate layers, and Figure 70 shows the measured results compared to those of the simulated design. The fabricated filter exhibits a center frequency of 63.5 GHz, an insertion loss of approximately 2.97 dB, a 3-dB bandwidth of approximately 1.55 GHz ($\sim 2.4\%$), and $> 40\text{ dB}$ rejection bandwidth of 3.55 GHz.

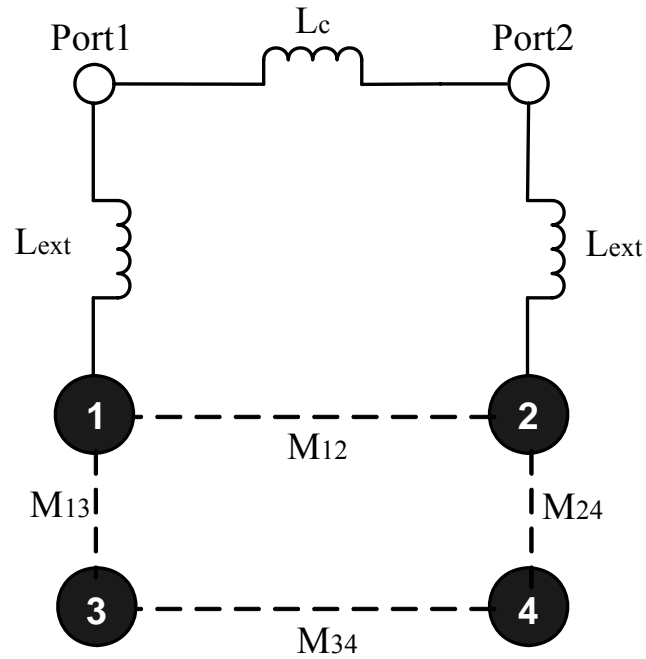


Figure 69: Multi-coupling diagram for the vertically stacked multi-pole dual-mode cavity filter with rectangular slot for inter-coupling between two cavities.

Table 12: Total phase shifts for three different signal paths in the vertically stacked dual-mode cavity filter with a cross slot.

<i>Paths</i>	<i>Below Resonance</i>	<i>Above Resonance</i>
Port1-1-2-Port2	$-90^\circ+90^\circ+90^\circ+90^\circ-90^\circ=+90^\circ$	$-90^\circ-90^\circ+90^\circ-90^\circ-90^\circ=-270^\circ$
Port1-Port2	-90°	-90°
Result	Out of Phase	Out of Phase
1-3-4-2	$-90^\circ+90^\circ+90^\circ+90^\circ-90^\circ=+90^\circ$	$-90^\circ-90^\circ+90^\circ-90^\circ-90^\circ=-270^\circ$
1-2	$+90^\circ$	$+90^\circ$
Result	In Phase	In Phase

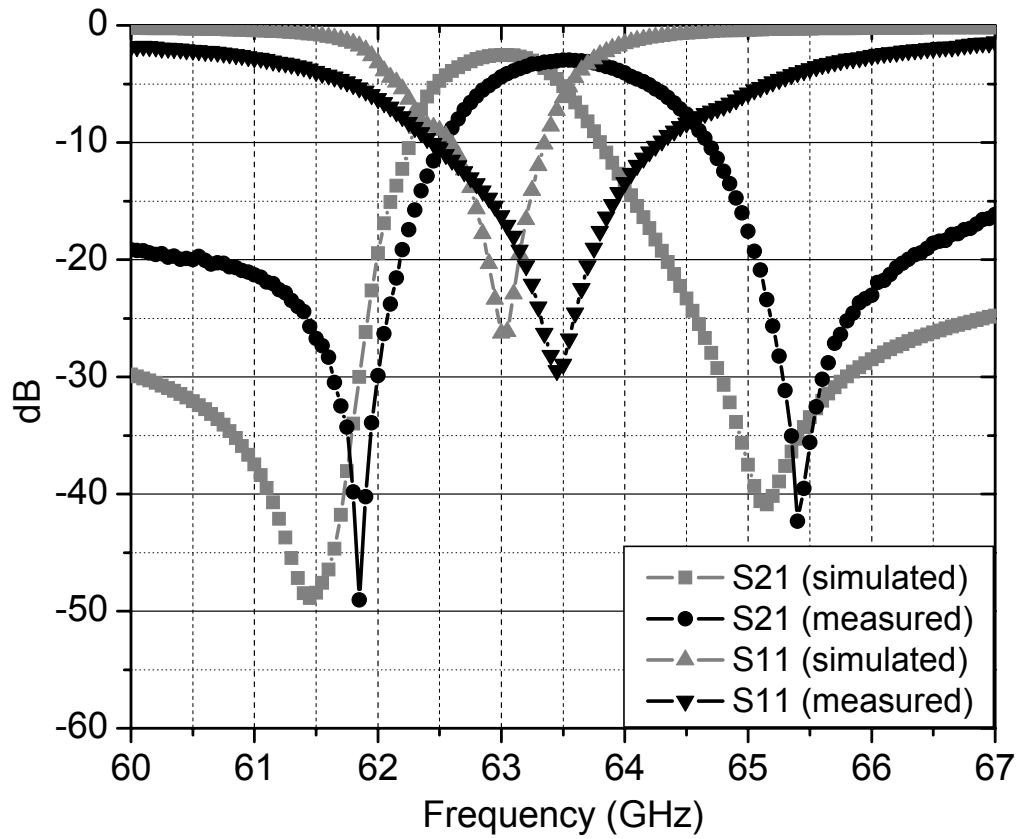


Figure 70: Measured and simulated S-parameters of the quasi-elliptic dual-mode cavity filter with a rectangular slot for inter coupling between cavities.

CHAPTER 5

3D ANTENNA ARCHITECTURES

5.1 Patch Antenna Using Soft-Surface Structure

The radiation performance of patch antennas on large-size substrate can be significantly degraded by the diffraction of surface waves at the edge of the substrate. Most of modern techniques for the surface-wave suppression are related to periodic structures, such as photonic bandgap (PBG) or EBG geometries [78]-[80]. However, those techniques require a considerable area to form a complete bandgap structure. In addition, it is usually difficult for most printed-circuit technologies to realize such a perforated structure. We apply the concept of the modern soft surface to improve the radiation pattern of patch antennas [81]. A single square ring of the shorted quarter-wavelength metal strips is employed to form a soft surface and to surround the patch antenna for the suppression of outward propagating surface waves, thus alleviating the diffraction at the edge of the substrate. Since only a single ring of metal strips is involved, the formed soft surface structure is compact and easily integrable with 3D modules.

5.1.1 Investigation of an Ideal Compact Soft Surface Structure

For the sake of simplicity, we consider a probe-fed square patch antenna operating at 15 GHz on a square grounded substrate with thickness H ($\sim 0.025\lambda_0$, λ_0 = the free-space wavelength) and a dielectric constant ϵ_r (~ 5.4). The patch antenna is surrounded by the ideal compact soft surface that consists of a square ring of metal strip short-circuited to the ground plane by a metal wall along the outer edge of the ring, as shown in Fig. 71.

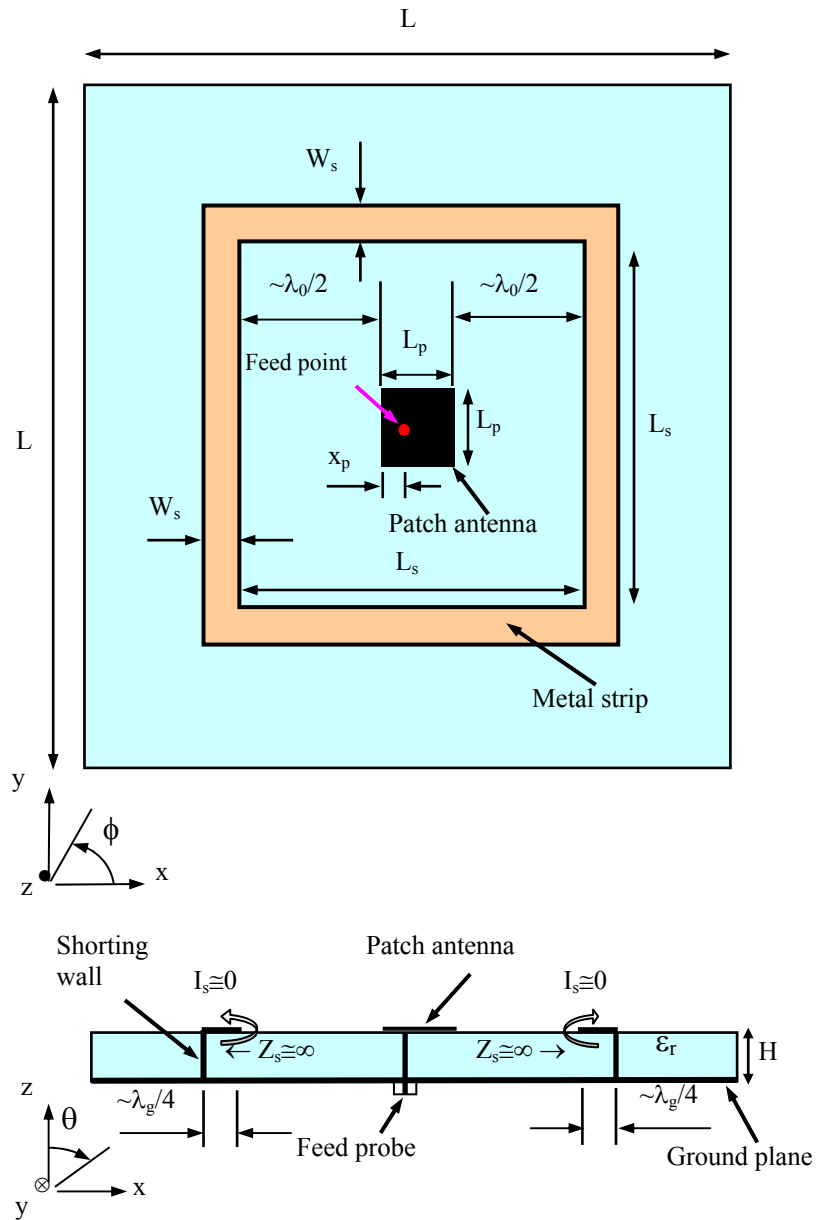
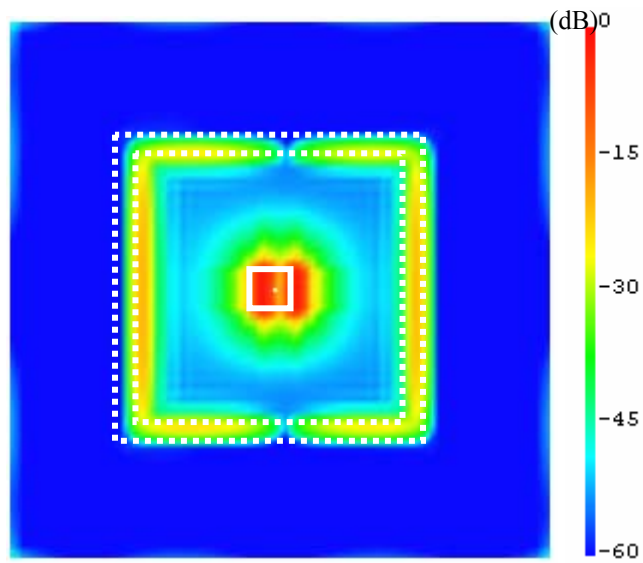
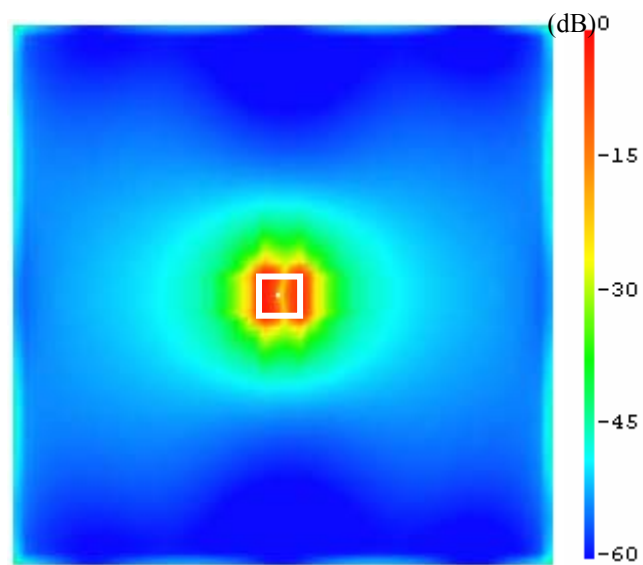


Figure 71: Patch antenna surrounded by an ideal compact soft surface structure which consists of a ring of metal strip and a ring of shorting wall (I_s =the surface current on the top surface of the soft surface ring, Z_s =the impedance looking into the shorted metal strip).



(a) With soft surface



(b) Without soft surface

Figure 72: Simulated electric field distributions on the top surface of the substrate for the patch antennas with and without the soft surface ($\epsilon_r = 5.4$).

The substrate later size is assumed to be $L \times L$ ($2\lambda_0 \times 2\lambda_0$), much larger than the size ($L_p \times L_p$) $< 0.5\lambda_g \times 0.5\lambda_g$) of the square patch. The inner length of the soft surface ring (denoted by L_s) was found to be approximately one wavelength plus L_p . The width of the metal strip (W_s) is approximately equal to a quarter of the guided wavelength.

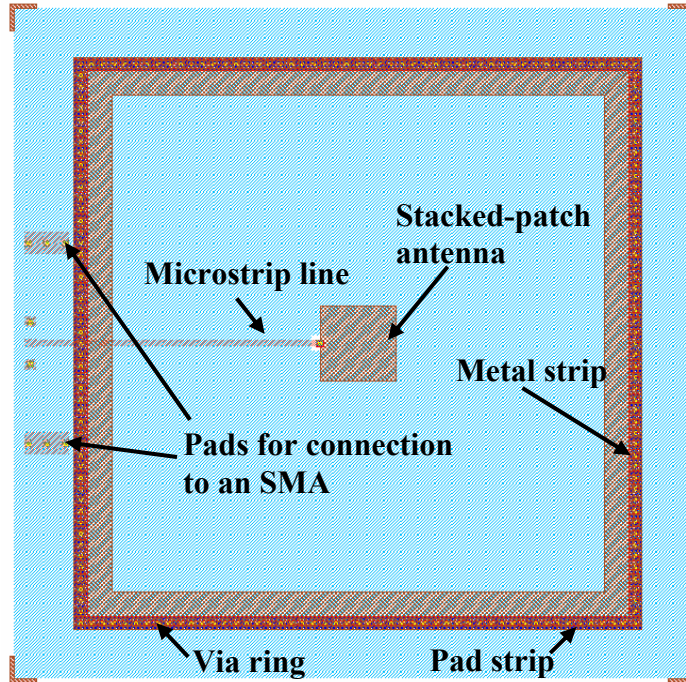
The mechanism for the radiation pattern improvement achieved by the introduction of a compact soft surface structure can be understood by considering two factors. First the quarter-wave shorted metal strip serves as an open circuit for the TM_{10} mode (the fundamental operating mode for a patch antenna). Therefore, it is difficult for the surface current on the inner edge of the soft surface ring to flow outward (also see Fig. 72). As a result, the surface waves can be considerably suppressed outside the soft surface ring, hence reducing the undesirable diffraction at the edge of the grounded substrate. This explanation can be confirmed by checking the field distribution in the substrate. Figure 72 shows the electric field distributions on the top surface of the substrate for the patch antennas with and without the soft surface. We can see that the electric field is indeed contained inside the soft surface ring. It is estimated that the field magnitude outside the ring is approximately 5 dB lower than that without the soft surface.

The second factor contributing to the radiation pattern improvement is the fringing field along the inner edge of the soft surface ring. This fringing field along with the fringing field at the radiating edges of the patch antenna forms an antenna array in the E-plane. The formed array acts as a broadside array with minimum radiation in the x-y plane when the distance between the inner edge of the soft surface ring and its nearby radiating edge of the patch is roughly half a wavelength in free space. Even though the magnitude of the fringing field along the soft surface may be much lower compared to that at the radiating edges, the size of the soft surface ring is much larger than the patch. As a result, the contribution from the soft surface ring to the radiated

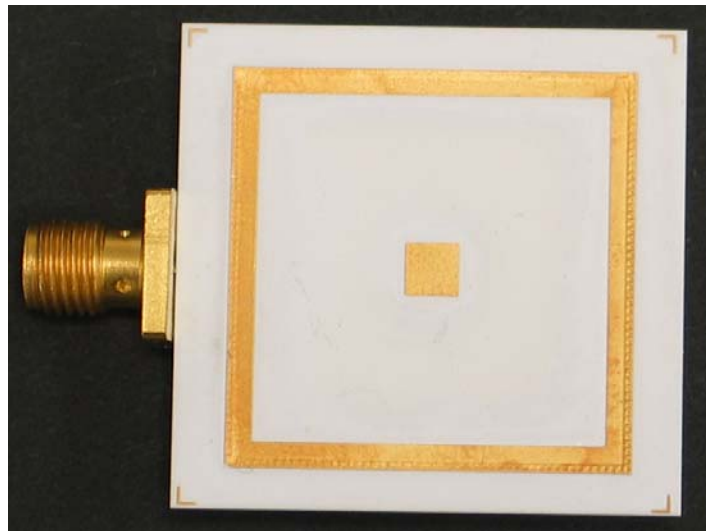
field at broadside may be significant. Therefore the radiation pattern can be considerably improved by the soft surface ring. Note that if the inner length of the soft surface ring (L_s) is further increased the fringing field will become weaker. Therefore there is an optimized value for L_s . By simulation, it is found that the optimized L_s is approximately equal to one wavelength in free space plus the length of the patch antenna (L_p). In this sense, the soft surface ring is also designed as a radiating element that launches the impinging surface wave into free space and in doing so effectively increases the size of the radiation aperture. By simulation, it is observed that the radiation pattern cannot be further improved by adding more soft surface rings, which supports the claim that the soft surface ring indeed acts as a radiating element.

5.1.2 Implementation of the Soft-Surface Structure in LTCC

To demonstrate the feasibility of this technology on the implementation of the soft surface, we first simulated a benchmarking prototype that was constructed to replace the shorting wall with a ring of vias. The utilized LTCC material had a dielectric constant of 5.4. The whole module consists of a total of 11 LTCC layers (layer thickness=100 μm) and 12 metal layers (layer thickness=10 μm). The diameter of each via was specified by the fabrication process to be 100 μm , and the distance between the centers of two adjacent vias was 500 μm . To support the vias, a metal pad is required on each metal layer. To simplify the simulation, all pads on each metal layer are connected by a metal strip with a width of 600 μm . Simulation showed that the width pad metal strips has little effect on the performance of the soft surface structure as long as it is less than the width of metal strips for the soft surface ring (W_s). The size of the LTCC board was 30 mm \times 30 mm. The operating frequency was set within the K_u -band (the design frequency $f_0=16.5$ GHz).



(a) layout

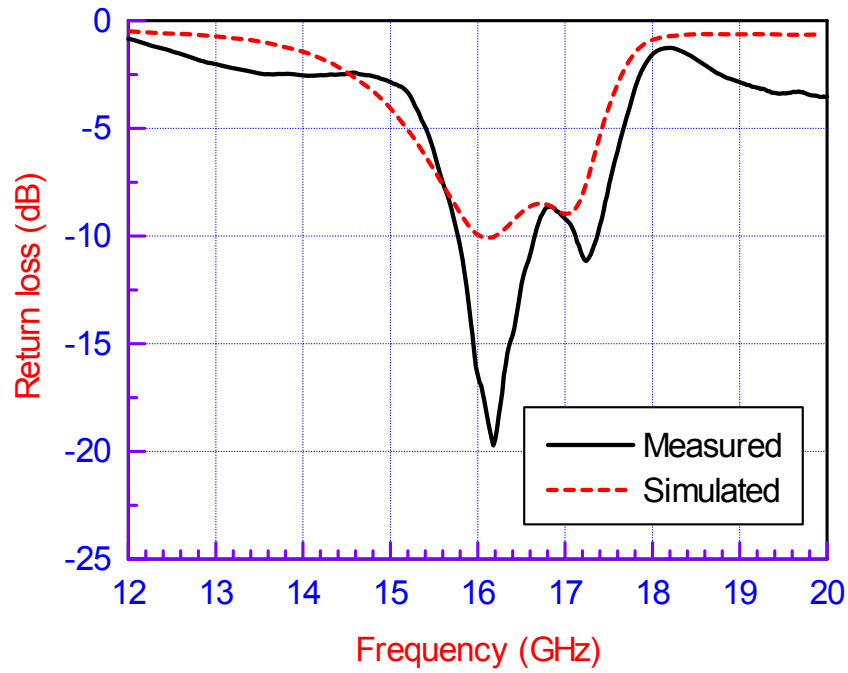


(b) Prototype

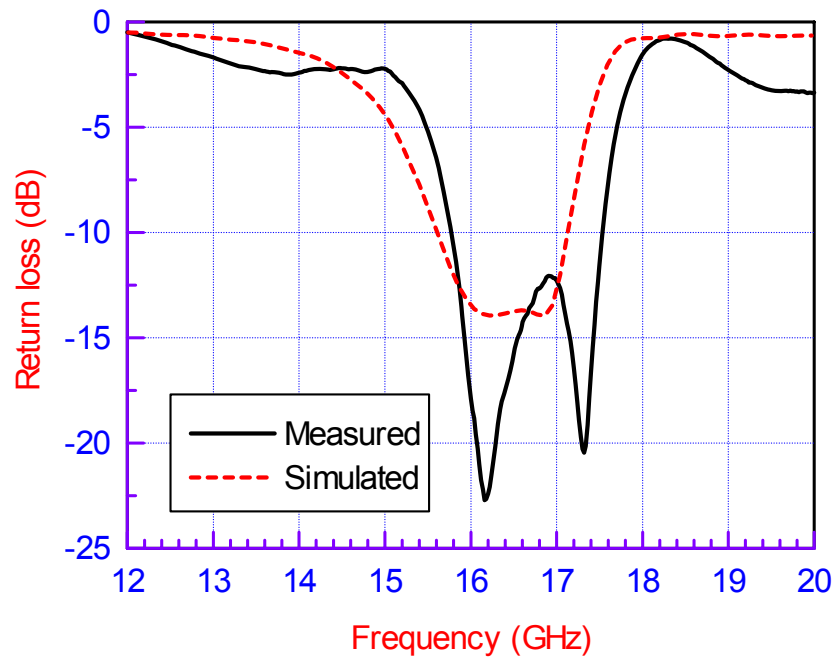
Figure 73: Layout and prototype of a stacked-patch antenna surrounded by a compact soft surface structure implemented on LTCC technology.

The optimized values for L_s and W_s were respectively 22.2 mm and 1.4 mm, which led to a total via number of 200 (51 vias on each side of the square ring). Including the width (300 μm) of the pad metal strip, the total metal strip width for the soft surface ring was found to be 1.7 mm. Since the substrate was electrically thick at $f_0=16.5$ GHz ($>0.1\lambda_g$), a stacked configuration was adopted for the patch antenna to improve its input impedance performance. By adjusting the distance between the stacked square patches, a broadband characteristic for the return loss can be achieved [82]. For the present case, the upper and lower patches (with the same size 3.4 mm \times 3.4 mm) were respectively printed on the first LTCC layer and the seventh layer from the top, leaving a distance between the two patches of 6 LTCC layers. The lower patch was connected by a via hole to a 50- Ω microstrip feed line that is on the bottom surface of the LTCC substrate. The ground plane was embedded between the second and third LTCC layers from the bottom. Figure 73 shows the layout and a prototype of the stacked-patch antenna surrounded by a compact soft surface structure implemented on the LTCC technology. The inner conductor of an SMA (semi-miniaturized type-A) connector was connected to the microstrip feed line while its outer conductor was soldered on the bottom of the LTCC board to a pair of pads that were shorted to the ground through via metallization. Note that the microstrip feed line was printed on the bottom of the LTCC substrate to avoid its interference with the soft surface ring and to alleviate the contribution of its spurious radiation to the radiation pattern at broadside. For comparison the same stacked patch antenna on the LTCC substrate but without the soft surface ring was also built.

The simulated and measured results for the return loss are shown in Fig. 74 and good agreement is observed. Note that because the impedance performance of the stacked-patch antenna is dominated by the coupling between the lower and upper patches, the return loss for



(a) With soft surface

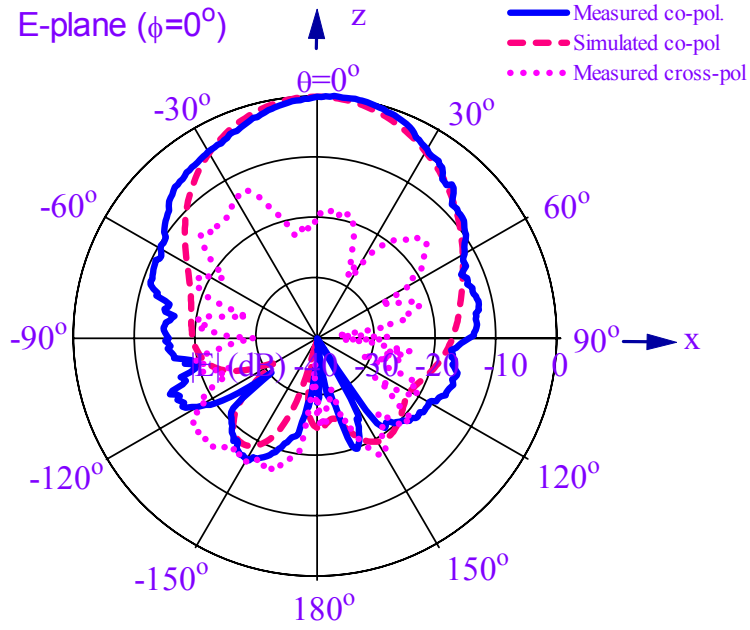


(b) Without soft surface

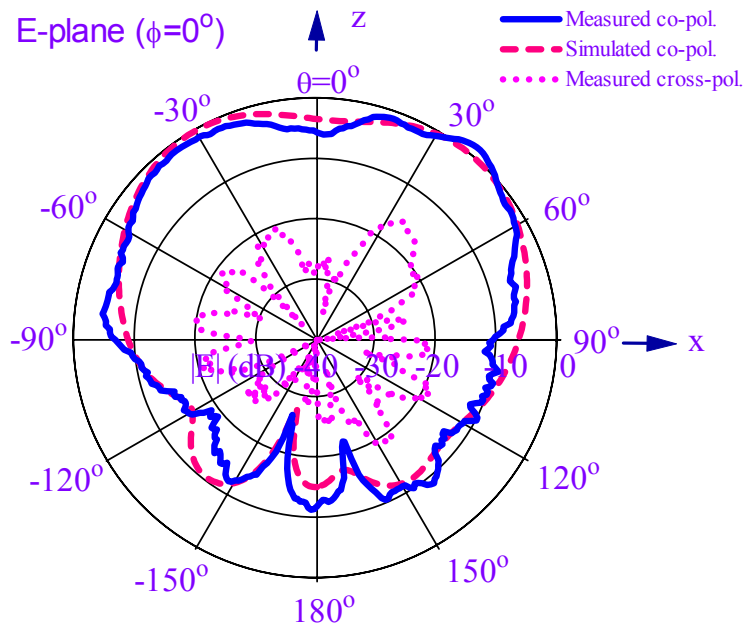
Figure 74: Comparison of return loss between simulated and measured results for the stacked-patch antennas with and without the soft surface implemented on LTCC technology.

the stacked-patch antenna seems more sensitive to the soft surface structure than that for the previous thinner single patch antenna. The measured return loss is close to -10 dB over the frequency range 15.8-17.4 GHz (about 9% in bandwidth). The slight discrepancy between the measured and simulated results is mainly due to the fabrication issues (such as the variation of dielectric constant or/and the deviation of via positions) and the effect of the transition between the microstrip line and the SMA (SubMiniature version A) connector. It is also noted that there is a frequency shift of about 0.3 GHz (about 1.5% up). This may probably be caused by the LTCC material which may have a real dielectric constant a little bit lower than the over estimated design value. Note that it is normal for practical dielectric substrates to have a dielectric constant with $\pm 2\%$ deviation.

The radiation patterns measured in the E- and H-planes are compared with simulated results in Fig. 75. The radiation patterns compared here are for a frequency of 17 GHz where the maximum gain of the patch antenna with the soft surface was observed. From Fig. 75, we can see good agreement for the co-polarized components. It is confirmed that the radiation at broadside is enhanced and the backside level is reduced. Also the beamwidth in the E-plane is significantly reduced by the soft surface. It is noted that the measured cross-polarized component has a higher level and more ripples than the simulation result. This is because the simulated radiation patterns were plotted in two ideal principal planes, i.e. $\phi=0^\circ$ and $\phi=90^\circ$ planes. From simulation, we found that the maximum cross-polarization may happen in the plane $\phi=45^\circ$ or $\phi=135^\circ$. During measurement, a slight deviation from the ideal planes can cause a considerable variation for the cross-polarized component since the spatial variation of the cross-polarization is quick and irregular.



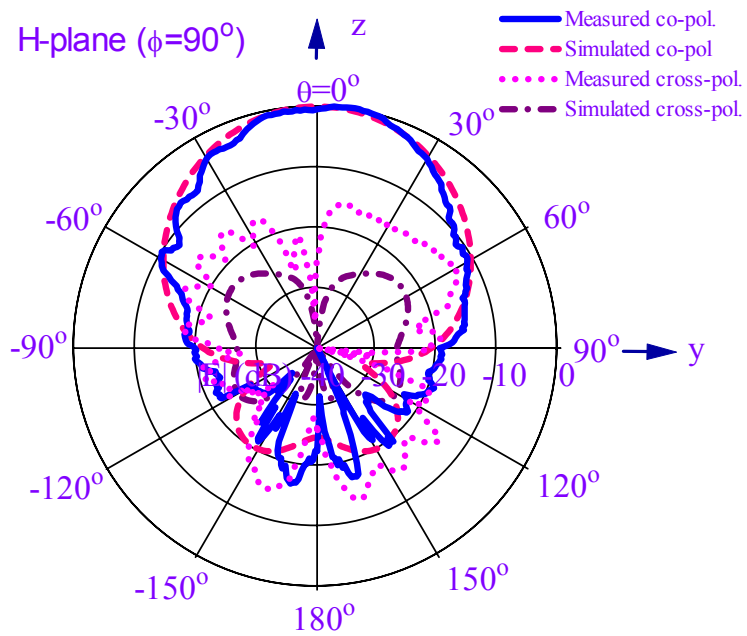
With soft surface



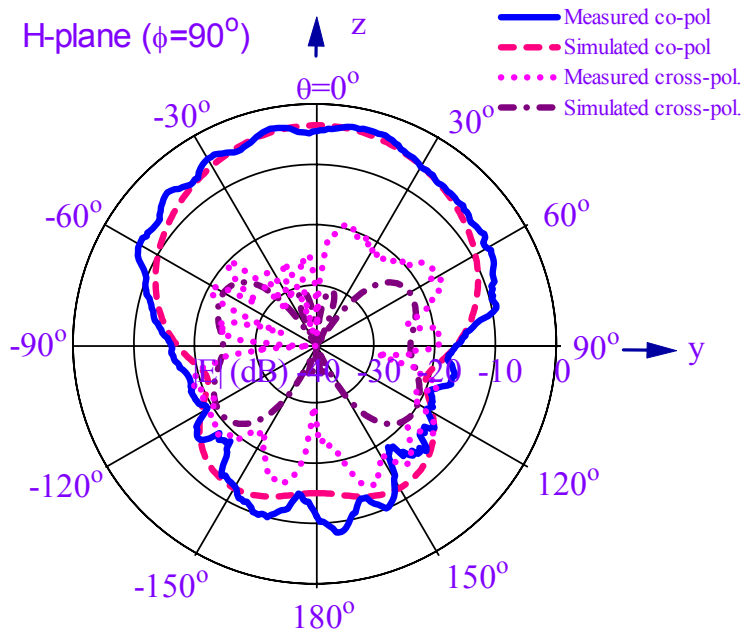
Without soft surface

(a) E-plane ($\phi=0^\circ$)

Figure 75: Comparison between simulated and measured radiation patterns for the stacked-patch antennas with and without the soft surface implemented on LTCC technology ($f_0=17$ GHz).



With soft surface



Without soft surface

(b) H-plane ($\phi=90^\circ$)

Figure 75: Continued.

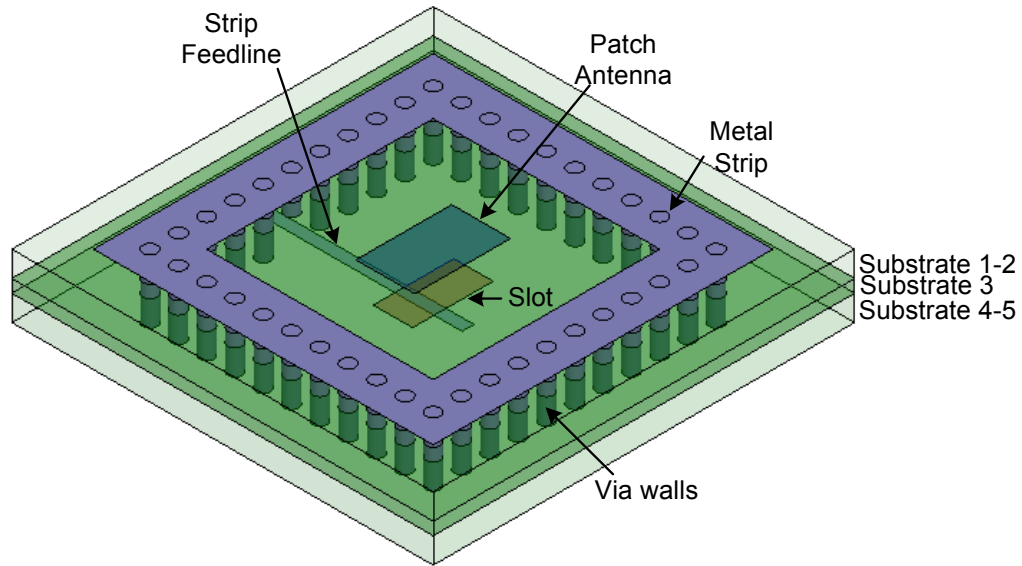
Also, a slight polarization mismatch or/and some objects nearby the antenna (such as the connector or/and the connection cable) may considerably contribute to the high cross-polarization. In addition, the maximum gain measured for the patch with the soft surface is near 9 dBi, about 3 dB higher than the maximum gain and 7 dB higher than the gain at broadside for the antenna without the soft surface.

5.2 High-Gain Patch Antenna Using Soft-Surface Structure and Stacked Cavity

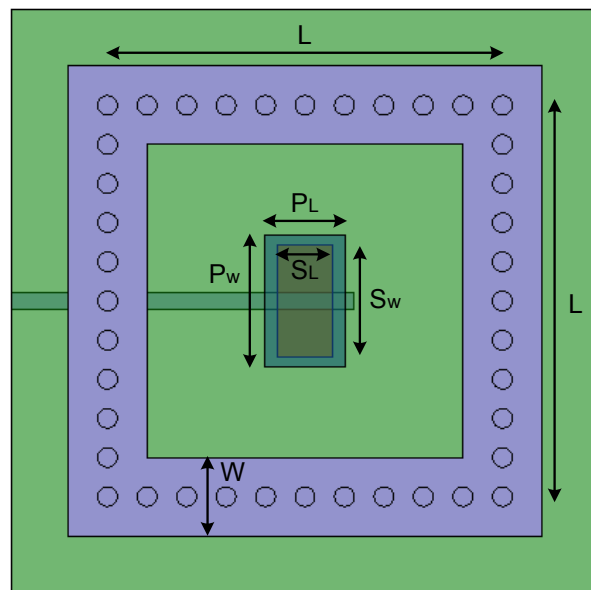
The advanced technique of the artificial soft surface consisting of a single square ring of metal strip shorted to the ground has been recently proposed with the advantages of compact size and excellent improvement in the radiation pattern of patch antennas in section 5.1. In this section, we further improve this technique by adding cavity based feeding structure on the bottom LTCC layers (*Substrate 4-5* in Fig. 76 (c)) of an integrated module to increase the gain and to reduce future the backside radiation. The back radiation is significantly reduced, and the maximum gain for the patch antenna with the soft surface and the stacked cavity is approximately 7.6 dBi which is 2.4 dB higher than 5.2 dBi for the “soft-enhanced” antenna without the backing cavity.

5.2.1 Antenna Structure Using a Soft-Surface and Stacked Cavity

The 3D overview, top view and cross-section view of the topology chosen for the microstrip antenna using a soft-surface and a vertically stacked cavity are shown in Fig. 76 (a), (b) and (c), respectively. The antenna is implemented into 5 LTCC substrate layers (layer thickness = 117 μm) and 6 metal layers (layer thickness = 9 μm).

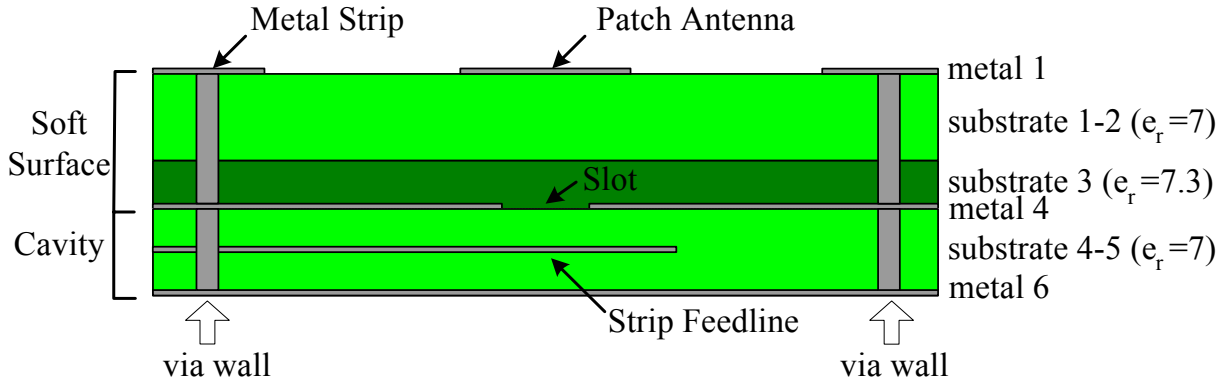


(a)



(b)

Figure 76: (a) The 3D overview (b) cross-section view (c) cross-section view of a patch antenna with the soft surface and sacked cavity.



(c)

Figure 76: Continued.

The utilized LTCC is a novel composite material of high dielectric constant ($\epsilon_r \sim 7.3$) in the middle layer (*substrate 3* in Fig. 76 (c)) and slightly low dielectric constant ($\epsilon_r \sim 7.0$) in the rest of the layers (*Substrate 1-2* and *4-5* in Fig. 76 (c)). A 50Ω stripline is utilized to excite the microstrip patch antenna (*metal 1*) through the coupling aperture etched on the top metal layer (*metal 4*) of the cavity as shown in Fig. 76 (c). In order to realize the magnetic coupling by maximizing magnetic currents, the slot line is terminated with a $\lambda_g/4$ open stub beyond the slot. The probe feed could not be used for the feeding structure because the size of the patch at the operating frequency of 61.5 GHz is too small to be connected to a probe via according to the LTCC design rules. The patch antenna is surrounded by a soft surface structure that consists of a square ring of metal strips that are short-circuited to the ground plane (*metal 4* in Fig. 76 (c)) for the suppression of outward propagating surface waves. Then, the cavity (Fig.76 (c)) that is realized utilizing the vertically extended via fences of the “soft surface” as its sidewalls is stacked right underneath the antenna substrate layers (*substrate 4-5* in Fig. 76 (c)) to improve

the gain and to reduce backside radiation. The operating frequency is chosen to be 61.5 GHz. The optimized size ($P_L \times P_W$) of patch is $0.54 \times 0.88 \text{ mm}^2$ with the rectangular coupling slot ($S_L \times S_W = 0.36 \times 0.74 \text{ mm}^2$). The size ($L \times L$) of the square ring of metal strip and the cavity is optimized to be $2.6 \times 2.6 \text{ mm}^2$ to achieve the maximum gain. The width of metal strip (W) is found to be 0.52 mm to serve as an open circuit for the TM_{10} mode of the antenna, alleviating the surface current flowing outward (transversely to the via walls of the soft surface). The ground planes are implemented on *metal 4* and *6*.

We achieved the significant miniaturization on the ground planes because their size excluding the feeding lines is the same as that of the soft surface ($\approx 3.12 \times 3.12 \text{ mm}^2$). In addition, the underlying cavity is used as both a dual-mode filter to separate TM_{10} mode whose phase and amplitude contain the information transmitted through short-range indoor WPAN and a reflector to improve the gain.

5.2.2 Simulation and Measurement Results

The full antenna structure is analyzed with the aid of a FEM-based full-wave simulator (HFSS). The simulated and measured results for the return loss are shown in Fig. 77 and good agreement is observed. The measured return loss is close to -10 dB over the frequency range 58.2-62.3 GHz (about 6.6 % in bandwidth). The slight discrepancy between the measured and simulated results is mainly due to the fabrication issues, such as the variation of dielectric constant or/and the deviation of via positions. From our investigation on the impedance performance, it is noted that the soft-surface structure vertically stacked by the cavity does not provide significant effect on the bandwidth of the patch with the soft surface only.

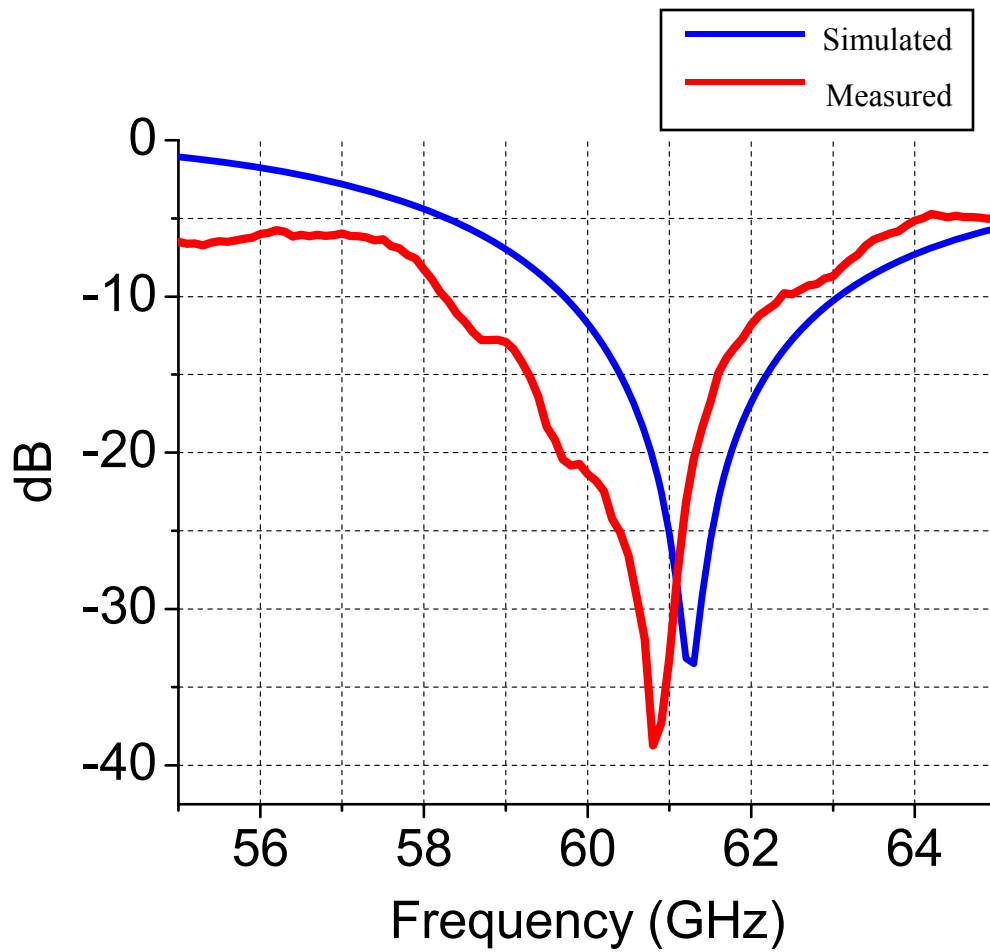


Figure 77: Comparison of return loss between simulated and measured results for a patch antenna with the soft surface and the stacked cavity implemented on LTCC technology.

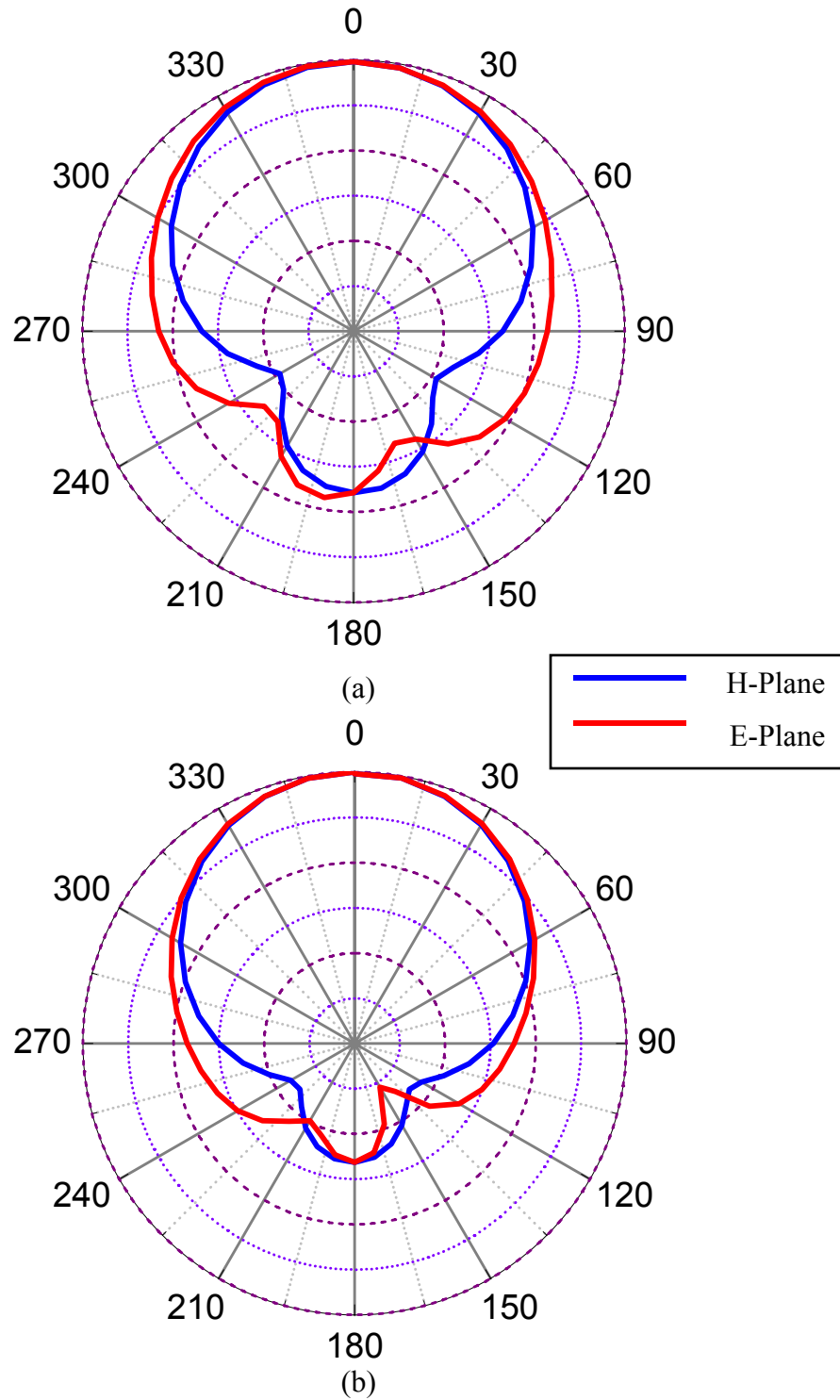


Figure 78: The radiation characteristics at 61.5 GHz of patch antennas (a) with the soft surface and (b) with the soft surface and the stacked cavity.

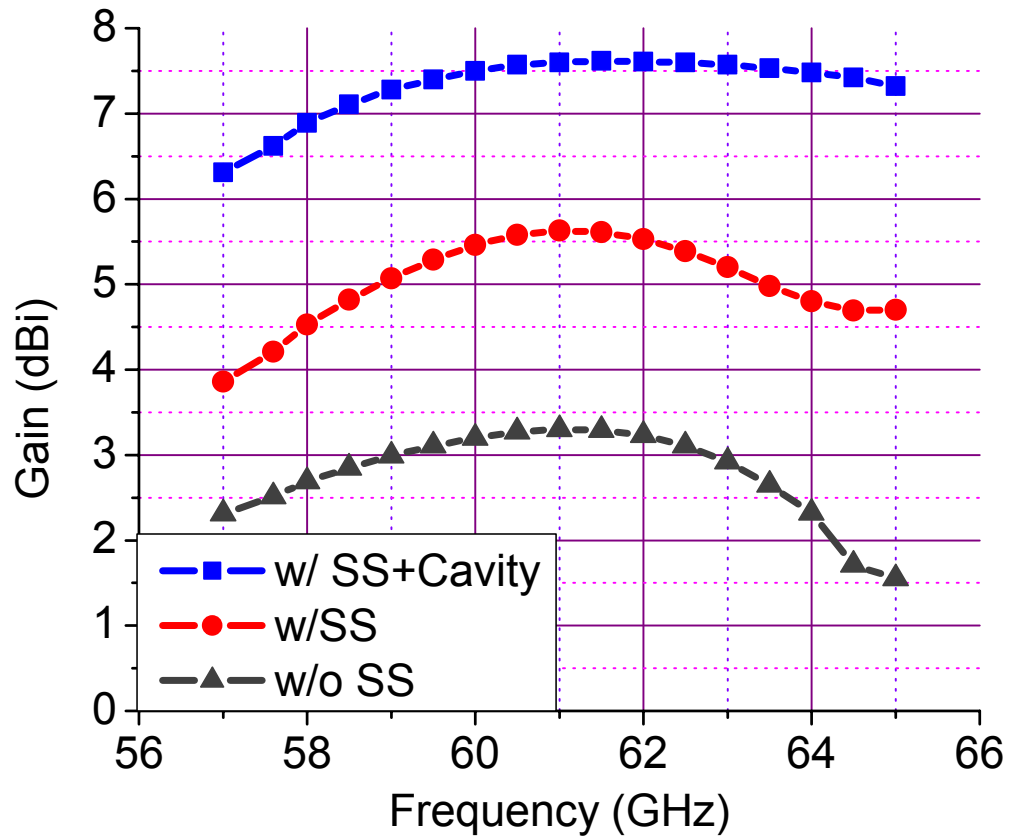


Figure 79: Comparison of simulated and measured gains at broadside between the stacked-patch antennas with and without the soft surface implemented on LTCC technology

The radiation patterns simulated in E and H planes of patch antennas with the soft surface only and with the soft surface/stacked cavity are shown and compared in Figs. 78 (a) and (b), respectively. The radiation patterns compared here are for a frequency of 61.4 GHz where the maximum gain of the patch antenna with the soft surface was observed. It is confirmed that the radiation at broadside is enhanced by 2.4 dB and the backside level is significantly reduced by 5.1 dB by stacking the cavity to the patch antenna with the soft surface. Also the beamwidth in the E-plane is reduced from 74° to 68° with the addition of the stacked cavity.

Finally let us compare the gains among the patch antennas with the soft-surface and the stacked cavity, with the soft surface only, and without the soft surface. The simulated gains at broadside (i.e. the z-direction) are shown in Fig. 79. The simulated gain was obtained from the numerically calculated directivity in the z-direction and the simulated radiation efficiency, which is defined as the radiated power divided by the radiation power plus the ohmic loss from the substrate and metal structures ($\tan\delta=0.0024$ and $\sigma=5.8\times 10^7$ S/m were assumed). From Fig. 79, we can see that the simulated broadside gain around the design frequency of the patch antenna with the soft surface and the stacked cavity is more than 7.6 dBi, about 2.0 dB improvement as compared to one with the soft surface only and 4.3 dB improvement as compared to one without the soft surface. More gain enhancement could be possible with the thicker substrate since the thicker substrate excites stronger surface waves while the soft surface blocks and transforms the excited surface waves into space waves.

5.3 Dual-Polarized Cross-Shaped Microstrip Antenna

A cross-shaped antenna has been designed for the transmission and reception of signals that cover two bands between 59-64 GHz. The first band (channel 1) covers 59-61.25 GHz, while the second band (channel 2) covers 61.75-64 GHz. This antenna can be easily integrated within a wireless millimeter-wave module containing the components of the previous section. Its structure is dual-polarized for the purpose of doubling the data output rate transmitted and received by the antenna. The cross-shaped geometry was utilized to decrease the cross-polarization which contributes to unwanted side lobes in the radiation pattern [33].

5.3.1 Cross-Shaped Antenna Structure

The antenna, shown in Fig. 80, was excited by proximity-coupling and had a total thickness of 12 metal layers and 11 substrate layers (each layer was 100 μm thick). Proximity-coupling is a particular method for feeding patch antennas where the feedline is placed on a layer between the antenna and the ground plane. When the feedline is excited, the fringing fields at the end of the line strongly couple to the patch by electromagnetic coupling. This configuration is a non-contact, non-coplanar method of feeding a patch antenna. The use of proximity-coupling allows for different polarization reception of signals that exhibits improved cross-channel isolation in comparison to a traditional coplanar microstrip feed.

There were two substrate layers separating the patch and the feedline, and two substrate layers separating the feedline and the ground layer. The remaining seven substrate layers are used for burying RF circuitry beneath the antenna that includes the filter, integrated passives and other components. The size of the structure was $8 \times 7 \text{ mm}^2$. A right angle bend in the feedline of channel 2 is present for the purpose of simplifying the scattering parameter measurements on the network analyzer.

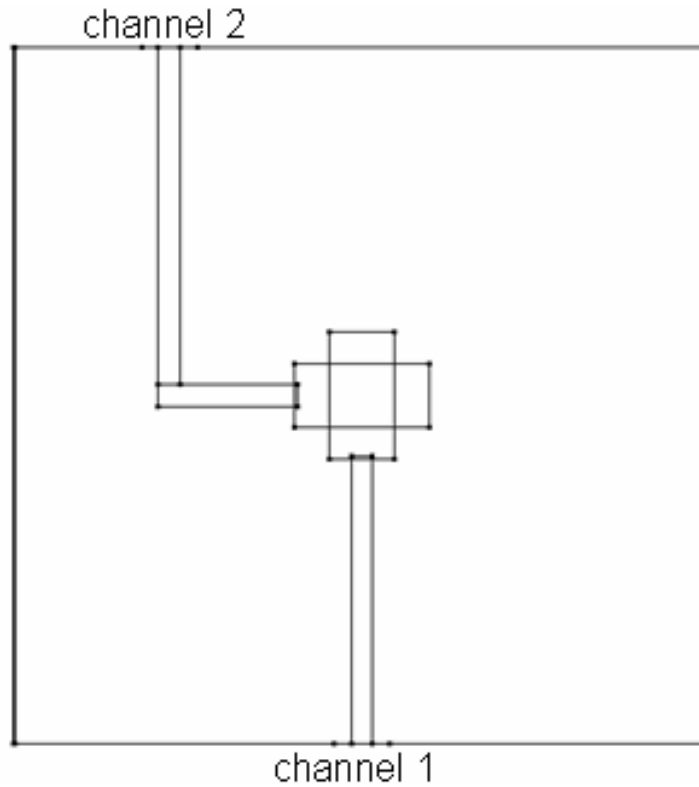
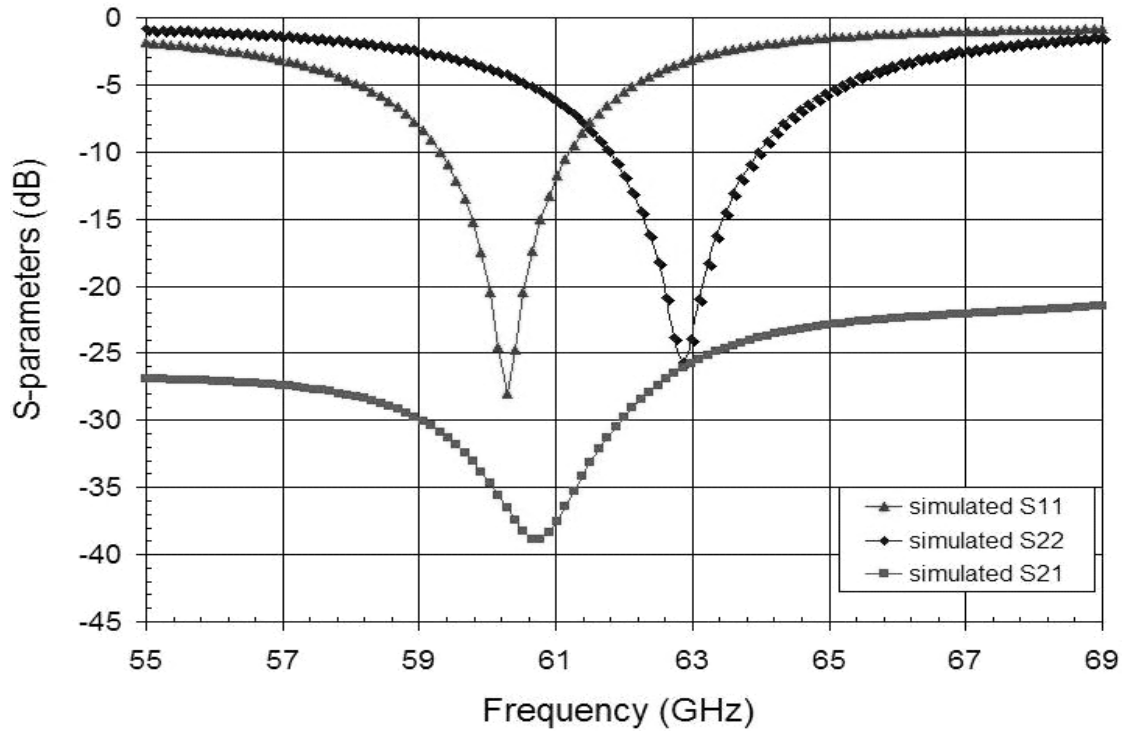


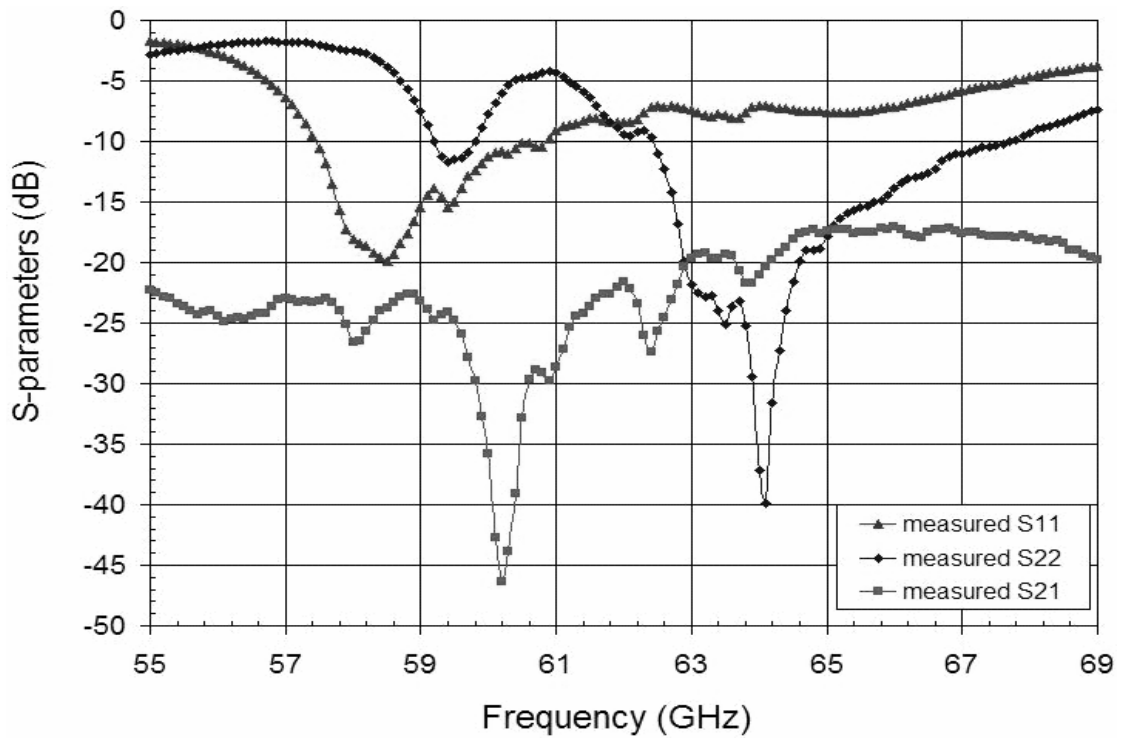
Figure 80: Cross-Shaped Antenna Structure in LTCC.

5.3.2 Simulation and Measurement Results

The design was simulated using the TLM-based, 3D full-wave solver MicroStripes 6.0. Figure 81 (a) shows the simulated scattering parameters versus frequency for this design. The targeted frequency of operation was around 60.13 GHz for channel 1 (S11) and 62.87 GHz for channel 2 (S22). The simulated return loss for channel 1 was close to -28dB at $f_r = 60.28$ GHz, while for channel 2, the return loss was ~ -26 dB at $f_r = 62.86$ GHz. The simulated frequency for channel 1 was optimized in order to cover the desired band based on the antenna structure.



(a)



(b)

Figure 81: (a) Simulated and (b) measured S-Parameter data versus frequency.

Channel 2 has a slightly greater bandwidth (3.49%) than that of channel 1 (3.15%) primarily due to the right angle bend in the feedline that can cause small reflections to occur at neighboring frequencies near resonance point of the lower band. The upper edge frequency (f_H) of the lower band is 61.21 GHz; while the lower edge frequency (f_L) of the higher band is 61.77 GHz.

Figure 81 (b) shows the measured scattering parameters versus frequency for the design. The measured return loss for channel 1 (-20dB @ $f_r = 58.5$ GHz) is worse than that obtained through the simulation (-26dB). Conversely, the -40dB of measured return loss at $f_r = 64.1$ GHz obtained for channel 2 is significantly better than the simulated return loss of -28dB. The diminished return loss of channel 1 is acceptable due to minor losses associated with measurement equipment (cables, connectors, etc...). The enhanced return loss of channel 2 could result from measurement inaccuracies or constructive interference of parasitic resonances at or around the TM_{10} resonance. The asymmetry in the feeding structure may account for this difference in the measured return loss. Frequency shifts for both channels are present in the measured return loss plots. Additionally, the bandwidths of the two channels are wider than those seen in simulations (5.64% for channel 1 and 8.26% for channel 2). Small deviations in the dimensions of the fabricated design as well as measurement tolerances may have contributed to the frequency shifts, while the increased bandwidths may be attributed to radiation from the feedlines and other parasitic effects that resonate close to the TM_{10} mode producing an overall wider bandwidth. The upper edge frequency (f_H) of the lower band is 61 GHz, while the lower edge frequency (f_L) of the higher band is 62.3 GHz. The simulated cross-coupling between channels 1 and 2 (Fig. 81) is below -22 dB for the required bands. On the other hand, the measured cross-coupling between the channels is below -22dB for the lower band and below -

17dB for the upper band. Due to the close proximity of the feeding line terminations of the channels, the cross-coupling is hindered, but these values are satisfactory for this application.

5.4 Series-Fed Antenna Array

A series fed 1×4 linear antenna array of four microstrip patches [83] covering the 59-64 GHz band, which has been allocated world wide for dense wireless local communications [84], has been designed on LTCC substrate.

5.4.1 Antenna Array Structure

The top and cross-section views of a series-fed 1×4 linear antenna array are illustrated in Figs. 82 (a) and (b), accordingly. The proposed antenna employs a series feed instead of a corporate feed because of its easy-to-design feeding network and low level of radiation from the feed line [83]. The matching between neighbouring elements is achieved by controlling the width (PW in Fig. 82 (a)) of the patch elements. The antenna was screen-printed on the top metal layer (*metal 1* in Fig. 82 (b)), and uses six substrate layers to provide the required broadband matching property and high gain. The targeted operation frequency was 61.5 GHz. First, the single patch resonator ($0.378\lambda_g \times 0.627\lambda_g$) resonating at 61.5 GHz is designed. The width-to-line ratio of the patch is determined to obtain the impedance matching and the desired resonant frequency. In our case, identical four patch resonators are linearly cascaded using thin microstrip lines ($w=0.100$ mm in Fig. 82 (a)) to maximize the performance at the center frequency of 61.5 GHz. The distance (g in Fig. 82 (a)) between patch elements is the critical design parameter to achieve equal amplitude and co-phase (equal phase) excitation and control the tilt of the maximum beam direction. It was optimized to be 0.780 mm ($\sim 0.387\lambda_g$) for 0° tilted fan beam antenna. Its physical length was determined to be 1.108 mm (T_L in Fig. 82 (a)).

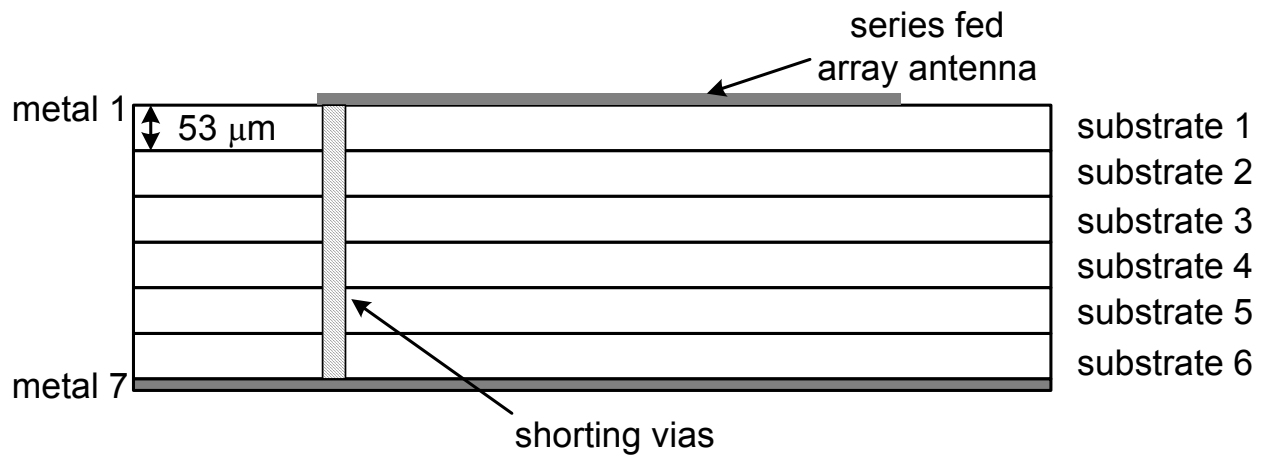
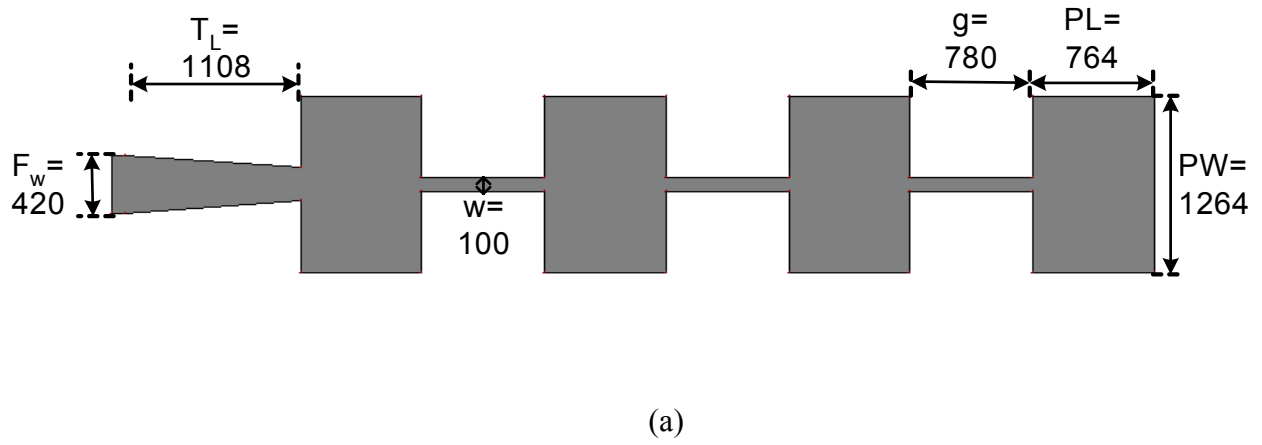


Figure 82: (a) Top view and (b) cross-section view of a series fed 1×4 linear array of four microstrip patches. All dimensions indicated in (a) are in mm.

5.4.2 Simulation and Measurement Results

Figure 83 shows very good correlation between the measured and simulated return loss (S11) versus frequency for the design. The measured 10-dB BW is 55.4-66.8 GHz (~18.5 %) compared to the simulated which is 54-68.4 GHz (~23.4%). The narrower BW might be due to the band limiting effect from the CPW measurement pad ($0.344 \times 1.344 \text{ mm}^2$).

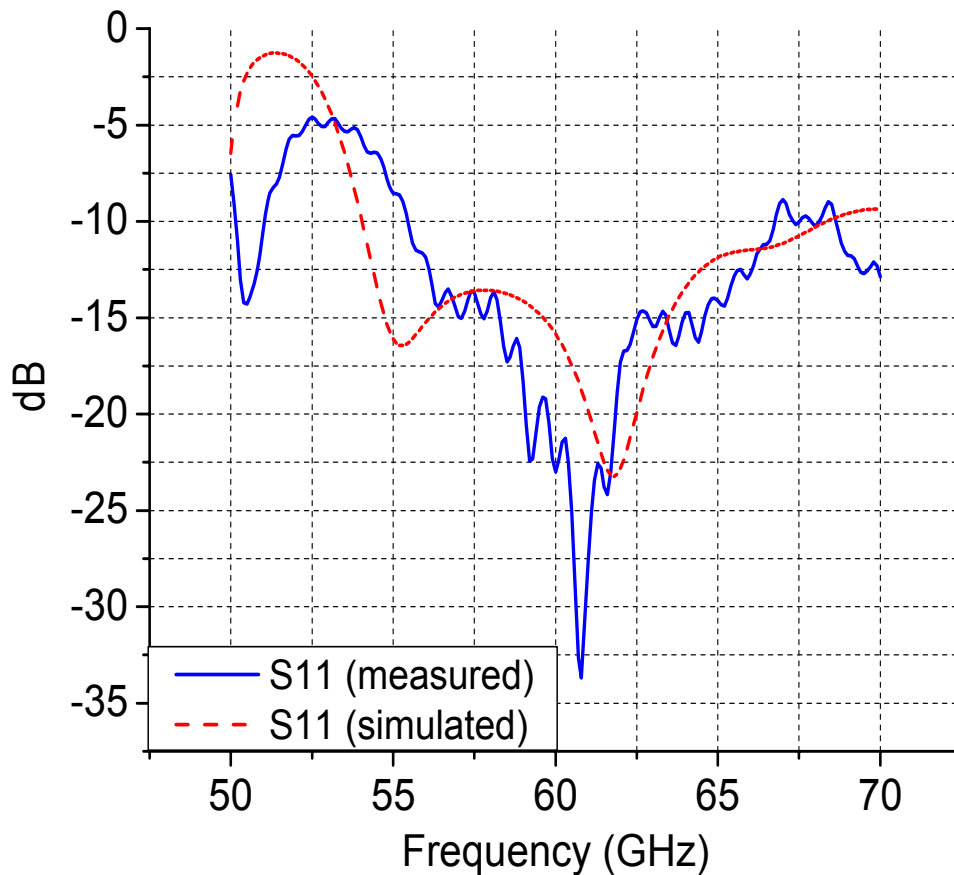


Figure 83: Measured and simulated return loss (S11) at 61.5 GHz of the series fed 1×4 antenna array.

Figure 84 presents E-plane and H-plane radiation patterns at the center frequency of 61.5 GHz. We can easily observe the 0° beam tilt from the radiation characteristics. The maximum gain of this antenna is 12.6 dBi.

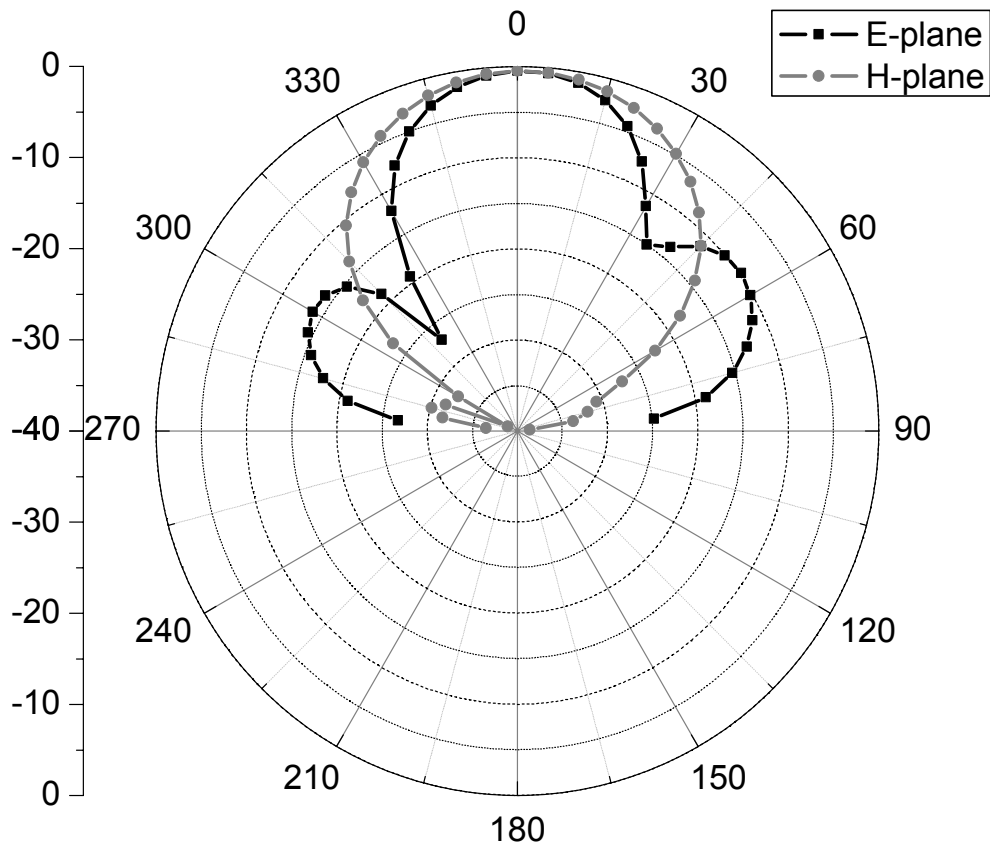


Figure 84: Simulated radiation patterns at 61.5 GHz of the series fed 1x4 antenna array.

CHAPTER 6

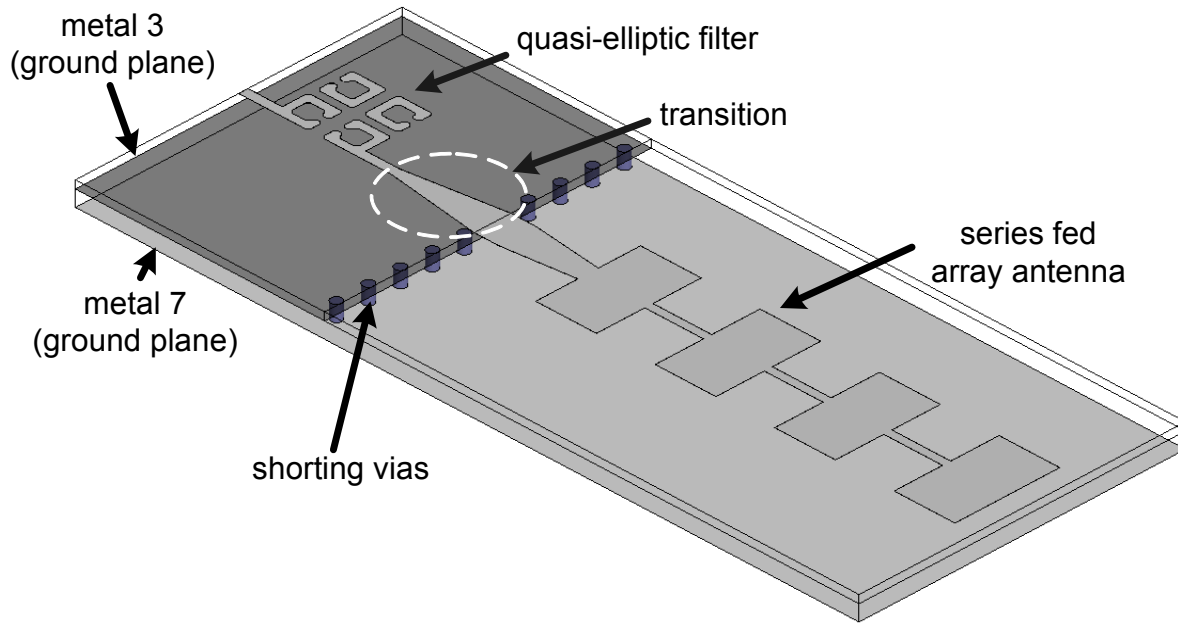
FULLY INTEGRATED 3D PASSIVE FRONT-ENDS

6.1 Passive Front-Ends for 60 GHz Time-Division Duplexing (TDD) Applications

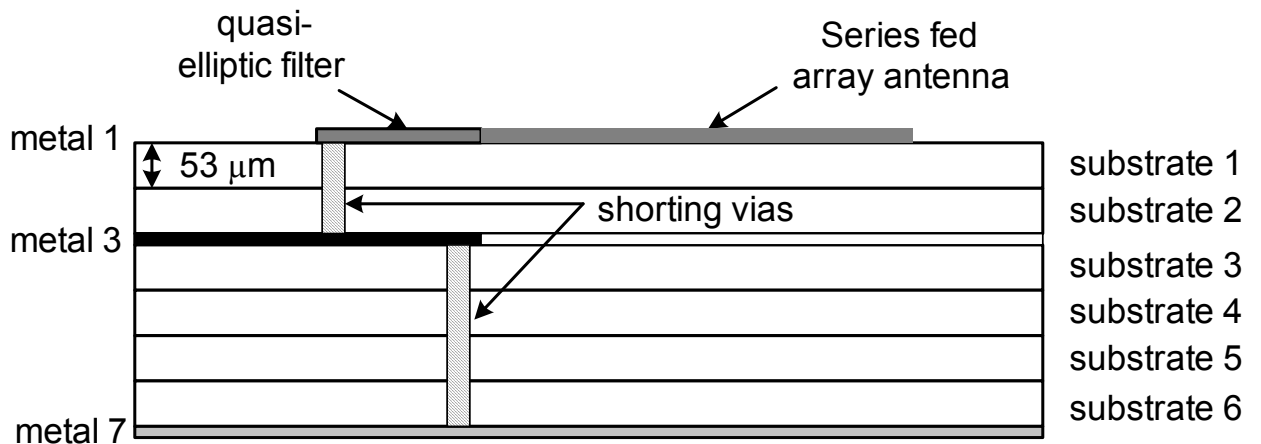
In the 60 GHz front-end module development, the compact and efficient integration of the antenna and filter is a crucial issue in terms of real estate efficiency and performance improvement, such as high level of band selectivity, the reduced parasitics and low filtering loss. Particularly, when the integration is constructed in a high- ϵ_r material such as LTCC, the excitation of strong surface waves also causes the unwanted coupling between the antenna and other components on the board. Using the developed quasi-elliptic filter and the series-fed array antenna, it is now possible to realize a V-band compact integrated front-end.

6.1.1 Topologies

The 3D overview and cross-section view of the topology chosen for the integration are shown in Figs. 85 (a) and (b) respectively. The four-pole quasi-elliptic filter and the 1×4 series fed array antenna are located on the top metallization layer (*metal 1* in Fig. 85 (b)) and are connected together with a tapered microstrip transition [46] as shown in Fig. 85 (a). The design of the tapered microstrip transition aims to annihilate the parasitic modes from the 50Ω microstrip lines discontinuities between the two devices and to maintain a good impedance matching (20 dB bandwidth $\approx 10\%$). The ground planes of the filter and the antenna are located on *metal 3*, on *metal 7*, respectively. The ground plane of the filter is terminated with a $175 \mu\text{m}$ extra metal pad from the edge of the antenna feedline due to LTCC design rules, and the two ground planes on *metal 3* and *7* are connected together with a via array as presented in Fig. 85.



(a)



(b)

Figure 85: (a) Top view and (b) cross-section view of a series fed 1×4 linear array of four microstrip patches. All dimensions indicated in (a) are in mm.

The fabricated integrated front-end occupies an area of $9.616 \times 1.542 \times 0.318 \text{ mm}^3$ including the CPW measurement pads.

6.1.2 Performance Discussion

Figure 86 shows the simulated and measured return losses of the integrated structure. It can be observed that the 10-dB return loss bandwidth is approximately 4.8 GHz (59.2 – 64 GHz) that is slightly wider than the simulation of 4 GHz (60-64 GHz). The slightly increased bandwidth may be attributed to the parasitic radiation from the feedlines and from the transition, as well as from the edge effects of the discontinuous ground plane.

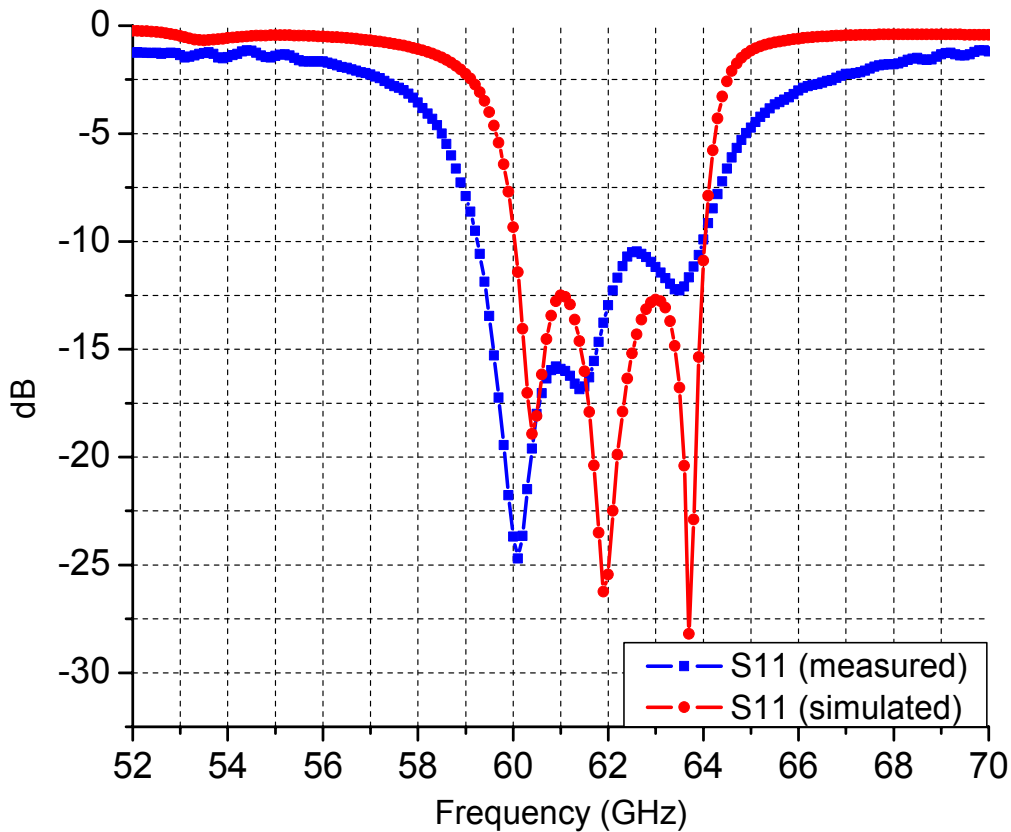


Figure 86: The comparison between measured and simulated return loss (S11) of the integrated filter and antenna functions.

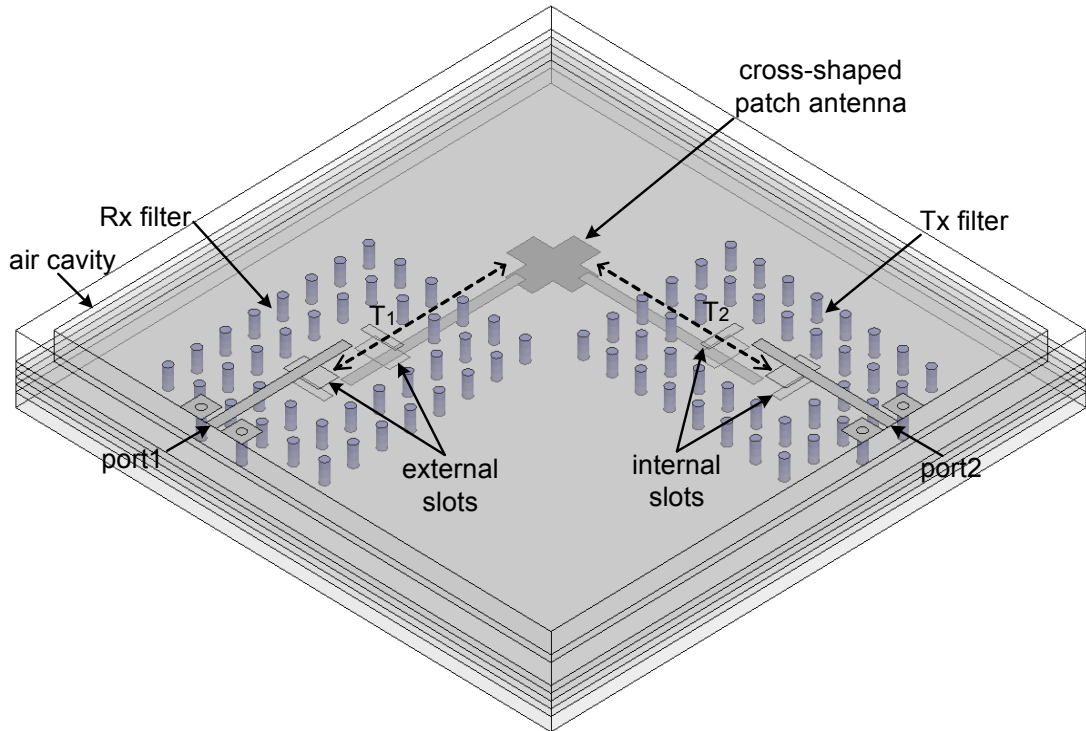
6.2 Passive Front-Ends for 60 GHz Frequency-Division Duplexing (FDD) Applications

The optimal integration of antennas and duplexers into a 3D 59-64 GHz frequency-division duplexing (FDD) transceiver module is significantly desirable since it not only reduces cost, size and system complexity but also achieves a high-level of band selectivity and spurious suppression, providing a high-level of isolation between two channels. Although cost, electrical performance, integration density and packaging capability are often at odds in RF front-end designs, the performance of the module can be significantly improved by employing the 3D integration of filters and antennas using the flexibility of multilayer architecture on LTCC.

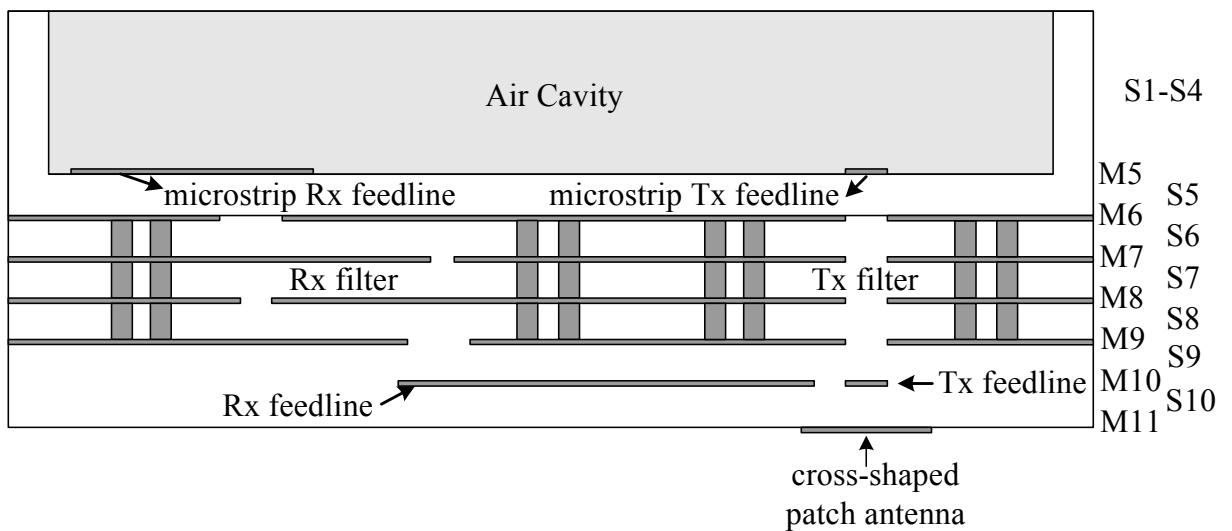
In this section, the fully integrated Rx and Tx filters and the dual-polarized cross-shaped antenna that covers Rx (1st) and Tx (2nd) channels are proposed employing the presented designs of the filters. The filters' matching (>10 dB) toward the antenna and the isolation (> 45 dB) between Rx and Tx paths comprise the excellent features of this compact 3D design. The stringent demand of high isolation between two channels induces the advanced design of a duplexer and an antenna as a fully integrated function for V-band front-end module.

6.2.1 Topologies

The 3D overview and the cross-section view of the topology chosen for the integration are shown in Figs. 87 (a) and (b), respectively. A cross-shaped patch antenna designed in section 5.3 to cover two bands between 59-64 GHz (1st channel: 59-61.5GHz, 2nd channel: 61.75-64 GHz) is located at the most bottom metal layer (*M11* in Fig. 87 (b)). The cross-shaped geometry was utilized to decrease the cross-polarization, which contributes to unwanted side lobes in the radiation pattern. The cross-channel isolation can be improved by receiving and transmitting signals in two orthogonal polarizations.



(a)



(b)

Figure 87: (a) 3D overview and (b) cross-section view of the 3D integration of the filters and antennas using LTCC multilayer technologies.

The feedlines and the patch are implemented into different vertical metal layers ($M10$ and $M11$, respectively), and then the end-gap capacitive coupling is realized by overlapping the end of the embedded microstrip feedlines and the patch. The overlap distance for Rx and Tx feedline is approximately 0.029 and 0.03 mm, respectively. The common ground plane for the feedlines and the patch is placed one layer above the feedlines as shown in Fig. 87 (b).

The two antenna feedlines (Rx feedline and Tx feedline in Fig. 87 (b)) are commonly utilized as the filters' feedlines that excite the Rx and Tx filters accordingly through external slots placed at $M9$ in Fig. 87 (b). The lengths of Rx and Tx feedlines (T_1 and T_2 in Fig. 87 (a)) connecting the cross-shaped antenna to the Rx and Tx filters, respectively, are initially set up to be one guided wavelength at the corresponding center frequency of each channel and are optimized using HFSS simulator in the way discussed in section 4.4.3 (T_1 : 2.745 mm, T_2 : 2.650 mm).

The 3D Rx and Tx filters [see Fig. 46] designed in section 4.4.2 are directly integrated to the antenna, exploiting the design parameters listed in Table 5. The integrated filters and antenna function occupies six substrate layers ($S5-S10$: 600 μm). The remaining four substrate layers ($S1-S4$ in Fig. 87 (b)) are dedicated to the air cavities reserved for burying RF active devices (RF receiver and transmitter MMICs) that are located beneath the antenna on purpose not to interfere with the antenna performance and to be highly integrated with the microstrip (Rx/Tx) feedlines, leading to significant volume reduction, as shown in Fig. 87. The cavities are fabricated removing the inner portion of the LTCC material outlined by the successively punched vias. The deformation factor of a cavity that is defined to be the physical depth difference between the designed one and the fabricated one is stable in LTCC process when the depth of the cavity is less than a two third of the height of the board. Since we have chosen the

air cavity depth of 400 μm , which is suitable for Rx/Tx MMIC chipsets, to enable the full integration of MMICs and passive front-end components, we can limit the fabrication tolerances effect of an air cavity to the other integrated circuitries. Figure 88 shows the photograph of the integrated device which is equipped with one air cavity at the top layers. The device occupies an area of $7.94 \times 7.82 \times 1 \text{ mm}^3$ including the CPW measurement pads.

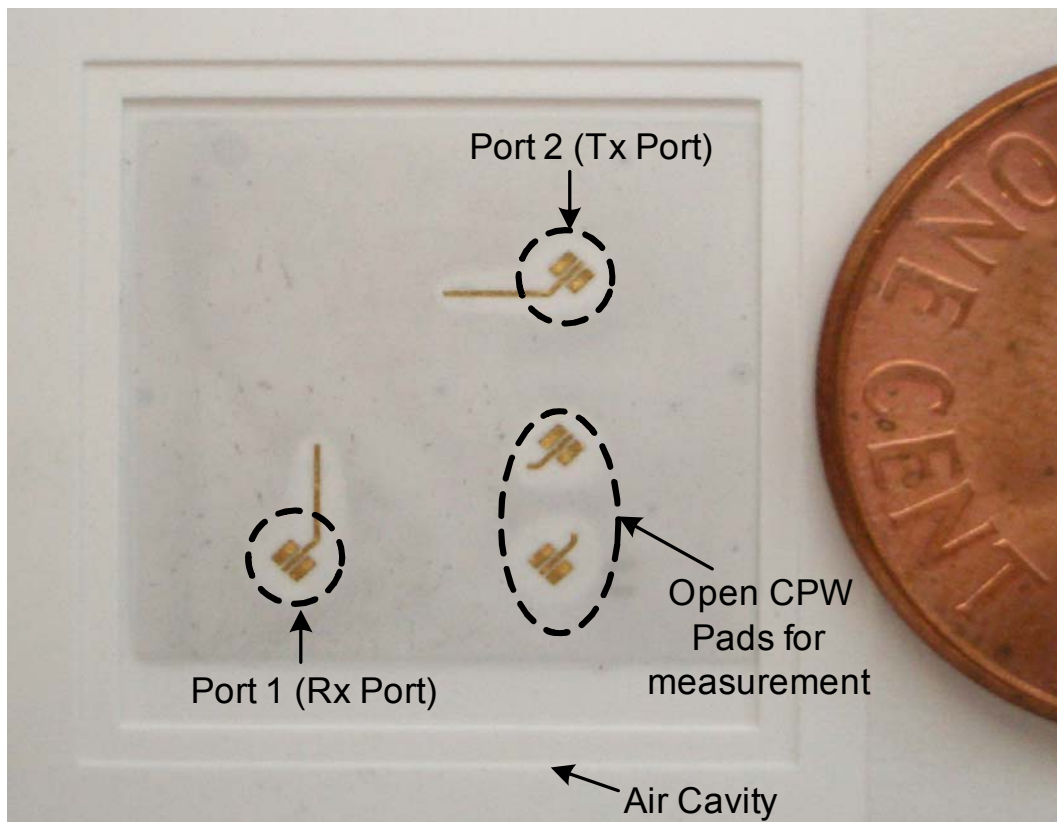
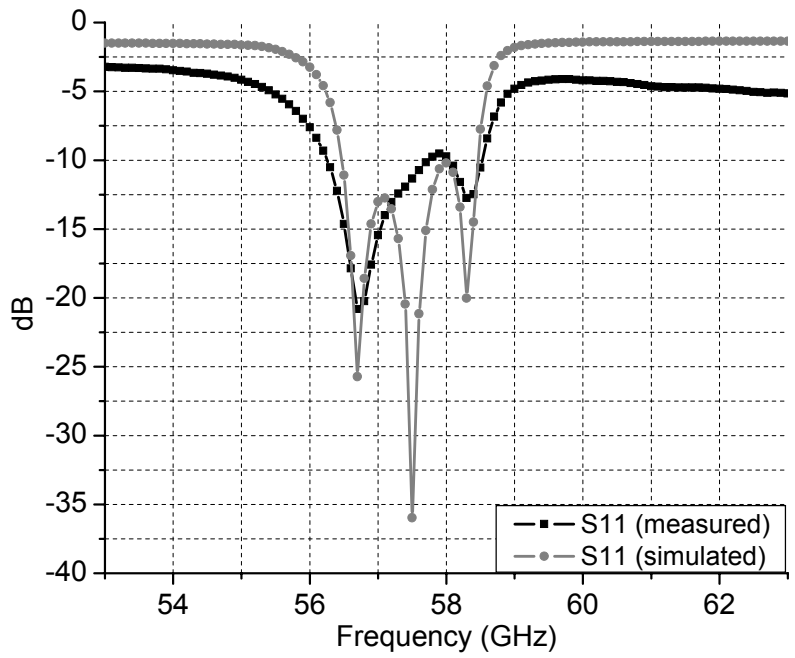


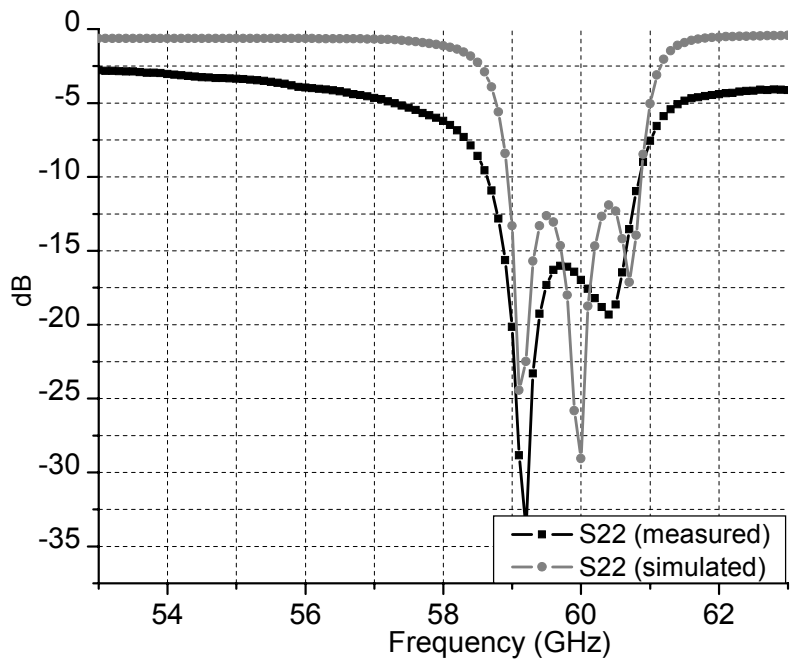
Figure 88: The photograph of the top view of the integrated function of Rx/Tx cavity filters and cross-shaped patch antenna with the air cavity top.

6.2.2 Performance Discussion

Figure 88 shows the simulated and measured return losses (S_{11}/S_{22}) of the integrated structure. In the simulation, the higher dielectric constant ($\epsilon_r=5.5$) and 5% increase in the volume of cavity were applied. It is observed from the 1st channel that the 10-dB return loss bandwidth is approximately 2.4 GHz ($\sim 4.18\%$) at the center frequency of 57.45 GHz that is slightly wider than the simulation of 2.1 GHz ($\sim 3.65\%$) at 57.5 GHz as shown in Fig. 88 (a). The slightly increased bandwidth may be attributed to parasitic radiation from the feedlines or the measurement pads. In Fig. 88 (b), the return loss measurement from the 2nd channel exhibits also a wider bandwidth of 2.3 GHz ($\sim 3.84\%$) at the center frequency of 59.85 GHz compared to the simulated value of 2.1 GHz ($\sim 3.51\%$) at that of 59.9GHz. The measured channel-to-channel isolation is illustrated in Fig. 89. The measured isolation is better than 49.1 dB across the 1st band (56.2-58.6 GHz) and better than 51.9 dB across the 2nd band (58.4-60.7 GHz), which is significantly improved in comparison with the cavity duplexer using the T-junction presented in section 4.4.3.



(a)



(b)

Figure 89: The comparison between measured and simulated return loss (a) S11 of the 1st channel (b) S22 of the 2nd channel.

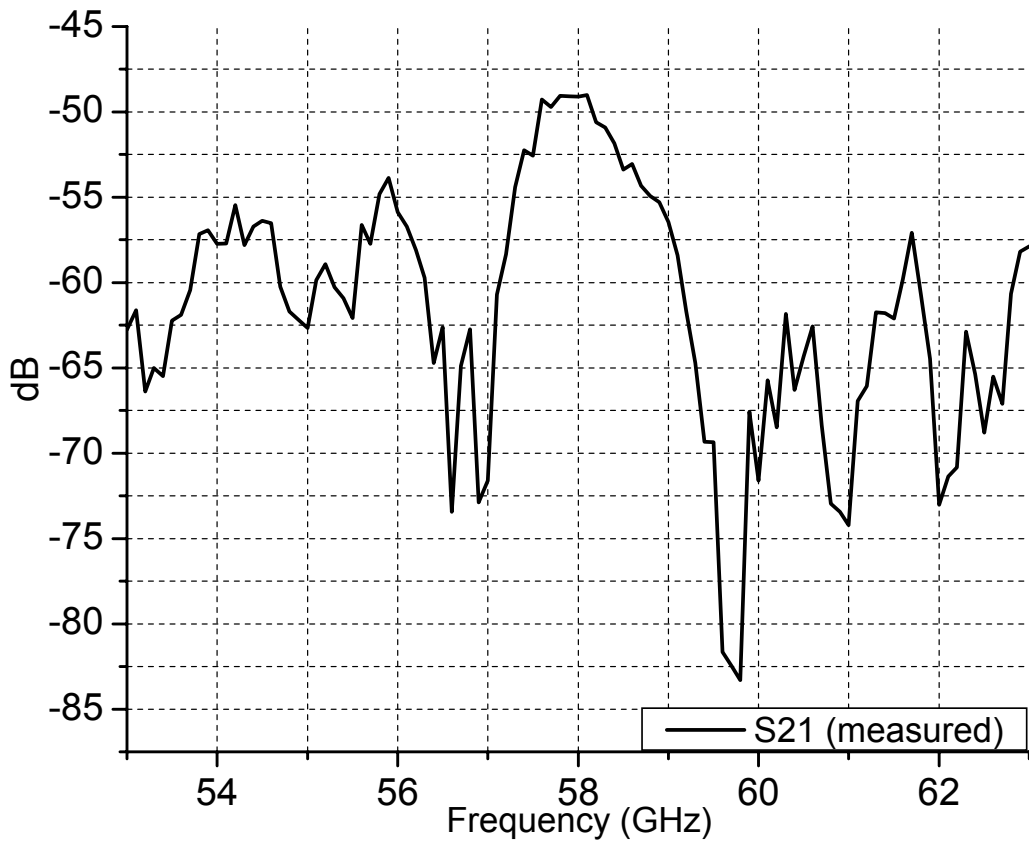


Figure 90: The measured channel-to-channel isolation (S21) of the integrated structure.

CHAPTER 7

CONCLUSIONS

The development of various advanced 3D filters/duplexers and antennas has been presented as a SOP passive solution of compact, low-cost, LTCC wireless front-end modules to be used in millimeter-wave frequency ranges. The SOP allows efficient integration of complete passive RF front-end functional building blocks, such as filters and antennas. Recent development of thin-film RF materials and process makes it possible to bring the concept of SOP into the RF world to meet the stringent needs in wireless communication area. Especially, LTCC has been widely used as a packaging material because of its process maturity/stability and its relatively high dielectric constant that enables a significant reduction in the module/function dimensions. The very mature multilayer fabrication capabilities of LTCC up to as many as metal layers make LTCC attractive for 3D integrated embedded components in a compact and cost-effective manner to meet millimeter-wave design requirements.

A new class of compact and easy-to-design microstrip passive functions, such as filters has been demonstrated with excellent performance and high integration potential. The patch resonator filter that uses vertical coupling overlap and transverse cuts as design parameters achieves a high level of miniaturization and a great compromise between size and power handling. The excellent performance of the patch resonator filter is verified through a measured insertion loss better than 2.3 dB and a return loss larger than 18.2 dB over the pass-band, and a bandwidth of about 6.4%. On the basis of the single-mode patch resonator, a multilayer compact diplexer and multistage (3pole & 5pole) bandpass filters have been fully characterized and have demonstrated performances suitable for V-band mobile communication and inter-satellite wideband applications. In addition, we discuss the development of a four-pole cross-coupled

quasi-elliptic filter, targeting high selectivity and compactness. It exhibits an insertion loss < 3.5 dB, a return loss > 15 dB over the pass band (~ 3.4 GHz) and a 3dB bandwidth of about 5.46 % (~ 3.4 GHz) at the center frequency of 62.3 GHz.

We presented for the first time a comparative study validated by measured data of three different excitation techniques for 3D LTCC integrated cavity resonators. Three excitation techniques (slot excitation with a shorting via, slot excitation with a $\lambda_g/4$ open stub, probe excitation) were comparatively evaluated in terms of S-parameters, bandwidth, external coupling (Q_{ext}), Q_u , and fabrication accuracy/simplicity based on electromagnetic simulations and experimental results. For millimeter-wave wideband applications, the probe excitation exhibited a relatively wide bandwidth nature ($\sim 1.8\%$) with the strongest external coupling based on the lowest Q_{ext} . The slot excitation with open stub exceeded the other techniques in terms of the lowest insertion loss (~ 0.84 dB) over the 3dB bandwidth around the center frequency of 59.2 GHz as well as fabrication simplicity. The shorting via exhibits excellent blockage of the electrical coupling between two microstrip feedlines along with a much simpler fabrication process than the probe excitation. The presented slot excitation with open stub is used in the development of 3D cavity resonators and bandpass filters. The 3-D integrated cavity resonators and three-pole filters composed of via walls have been successfully demonstrated with excellent performance using LTCC technology at 60GHz. The resulting strong-coupling cavity demonstrated excellent performances in terms of a low insertion loss (~ 0.84 dB) at 59.2 GHz and a 3dB bandwidth of about 1.5 % (~ 0.89 GHz) as well as fabrication simplicity. A low-loss, fully integrated three-pole bandpass filter employing a slot excitation with an open stub has been implemented for the first time for 60GHz WLAN narrowband (~ 1 GHz) applications. It exhibited an insertion loss of 2.14 dB at a center frequency of 58.7 GHz, a return loss ≥ 16.39 dB

over the passband and a 3-dB fractional bandwidth about 1.38% (~0.9 GHz). To the best of the authors' knowledge, this is the lowest loss reported for a LTCC 3D integrated narrowband filter at 60 GHz.

As an alternative of a compact bandpass filter solution, vertically stacked 3D low-loss cavity bandpass filters are developed for Rx and Tx channels to realize a compact duplexer integrated into a 3D V-band transceiver module. Excellent performance for both channels was observed with low insertion loss such as <2.37 and <2.39 dB, respectively. The resonant frequency downshift about 2.7 GHz was observed through all devices fabricated on this LTCC process. The fabrication tolerances such as the dielectric constant variation (5.5 vs. 5.4) at these high frequencies and the accuracy of vias positioning caused by XY shrinkage (~5%) were interpreted as major factors for these phenomena and considered in the simulations of the rest devices. Then, The duplexer consisting of the developed cavity filters are demonstrated with the specific passband characteristics (4.2% at 57.2 GHz, 2.66 % at 60.1 GHz), low insertion loss (2.22/2.48dB), and high level of channel-to-channel isolation (35.2/38.4 dB). For a high level of selectivity and compactness, a novel concept of three dimensional integrated V-band dual-mode cavity filters, which permit the realization of a variety of quasi-elliptic responses by creating transmission zeros, has been demonstrated using multilayer low-temperature co-fired ceramic technology. A single cavity resonator is designed to generate a degenerate resonance of two orthogonal modes (TE_{102} and TE_{201}), enabling dual-mode operation. The appearance and elimination of transmission zeros have been analyzed through the multi-path coupling diagrams and lumped elements models. Then, the quasi-elliptic, dual-mode filters with the appropriate locations of the transmission zeros are developed for receiver and transmitter channels of a V-band transceiver module. Two pre-synthesized, dual-mode cavity filters are vertically stacked

with two types of inter-coupling slots (1. rectangular 2. cross) to realize the multi-pole filters for 60 GHz wireless local area network narrowband applications. These proposed filters are the first to be reported and have great potential to be integrated into miniaturized V-band low-temperature co-fired ceramic transceiver modules.

The effectiveness of a modern soft surface concept on the radiation-pattern improvement of a patch antenna on a large-size substrate has been investigated. The new soft surface structure consists of a ring of short-circuited metal strips with a strip width of a quarter guided wavelength, much more compact than typical PBG/EBG structures. The mechanism for the radiation-pattern improvement has been analyzed and it has been revealed that the optimal length of the soft surface ring is approximately one wavelength in free space plus the patch size. The compact soft surface structure can be easily implemented in 3D modules, such as those fabricated using LTCC technology. Experimental results show that it is feasible to make use of the via-metallization process on the LTCC technique for realization of a shorting wall required by the compact soft surface structure. The maximum gain measured for the patch with the soft surface is near 9 dBi, about 3 dB higher than the maximum gain and 7 dB higher than the gain at broadside for the antenna without the soft surface. To improve further radiation patterns, A patch antenna integrated with a soft surface and the stacked cavity has been investigated on LTCC multilayer technology. A higher gain is achieved by stacking the cavity underneath the soft surface, and the significant reduction of the backside radiation is observed as compared to the patch antenna with the soft surface. The compact antenna with the soft surface and the stacked cavity can be easily integrated into 3D 60 GHz modules. A double fed cross-shaped microstrip antenna has been designed for the purpose of effectively doubling the data through-put by means of dual polarized wireless channel, covering the band between 59-64 GHz. In addition, a series fed 1×4 linear

antenna array of four microstrip patches exhibiting high gain and fan-beam radiation pattern has been designed. Its 10 dB bandwidth is experimentally validated to be 55.4-66.8 GHz (~18.5 %).

Finally, the developed quasi-elliptic microstrip filters and series-fed 1×4 antennas have been combined together, leading to a complete passive TDD front-end integration with high level of selectivity over the band of interest covering 59-64 GHz. The excellent performance of the integrated solution is verified through a 10 dB return loss bandwidth of 4.8 GHz (59.2 – 64 GHz). As a complete passive solution for 60 GHz FDD transceiver modules, the fully integrated functions of Rx and Tx filters and the dual-polarized antenna that covers Rx and Tx channels are proposed employing a novel 3D deployment of embedded components with an air cavity. The excellent overall performance of the integration is verified through 10-dB bandwidth of 2.4 GHz (~4.18%) at 57.45 GHz and 2.3 GHz (~3.84%) at 59.85 GHz and the measure isolation better than 49 dB across the Rx band and better than 51.9 dB across the Tx band. The proposed 3D integrated functions can be easily integrated with Rx/Tx MMICs to realize a LTCC V-band FDD transceiver front-end module.

After the development of the complete 3D passives integration, novel LTCC transceiver architectures will be developed to realize the future 60 GHz gigabit radio, using the latest advancement in CMOS, BiCMOS and GaAs technologies toward an agile 60-GHz frequency operation. The optimum combination and co-design of active and passive circuits is the key for the successful deployment of ultra-high speed, high capacity, 60 GHz WLAN access for very dense urban network and hot spot coverage. The future research effort will continue toward developing a novel millimeter-wave cognitive radio using state-of-the-art SOP technologies. Such a development will go through two major phases. First, novel front-ends having adaptive or tunable characteristics must be designed for multimode and multiband operation in millimeter

frequencies. A genetic adaptive beamforming antenna array, which could be directly integrated into the package, could be a possible radiator solution. In order to support multi-gigabit-per-second data rates, the multi-antennas should be combined in array form, providing the high directivity and gain, spatial diversity, and electronic beam stability. Active interference-cancellation approaches will be required for high efficiency, range and directivity. The development of a novel millimeter-wave ultra-wide band (30-110GHz) antenna exhibiting great pattern stability is one of keys to realizing a compact millimeter-wave reconfigurable radio with no need of multiple antennas architectures. In millimeter-wave reconfigurable “cognitive” radios, the replacement of fixed frequency filters by switchable/tunable filters or filter banks will be needed to allow transceiver performance to be dynamically optimized to the requirements of different frequency bands and modulation schemes. The RF MEMS technology can contribute significantly to the successful low-power compact development of such switchable/tunable filters. Finally, the organic- or ceramic-material 3D packaging technology is key to overcome various interconnect design constraints and to cope with the rapid increase in system complexity. Extra attention is required for the minimizing of coupling, crosstalk, interference and loss at mm-W frequencies through the use of patterned grounds and via arrays. Extensive use of system-level and module-level hybrid EM/mechanical simulation tools will allow for the accurate modeling and optimization of multilayer cognitive modules. At the board level, attention should be paid to mixed-signal interfaces especially regarding shared grounds partitioning, transmission lines, isolation and shielding of sensitive lines, clean power supply distribution network to subblocks, and prevention of unwanted radiation by noisy digital circuits.

References

- [1] K. Lim, S. Pinel, M. F. Davis, A. Sutono, C. -H. Lee, D. Heo, A. Obatoynbo, J. Laskar, E. M. Tentzeris, and R. Tummala, "RF-system-on-package (SOP) for wireless communications," *IEEE Microwave Magazine*, vol.3, no.1, pp.88-99, Mar. 2002.
- [2] C. H. Doan, S. Emami, D. A. Sobel, A. M. Niknejad, and R. W. Brodersen, "Design considerations for 60GHz CMOS radios," *IEEE Communication Magazine*, vol. 42, no. 12, pp. 132-140, Dec 2004.
- [3] H.H.Meinel, "Commercial applications of millimeter waves History, Present Status, and Future Trends," *IEEE Transaction on Microwave Theory and Technique*, vol. 43, no. 7, pp. 1639-1653, July 1995.
- [4] http://rfdesign.com/mag/radio_passive_integration_technology/. November 2002.
- [5] D. B. Rutledge, D. P. Neikirk, and D. P. Kassailigam, *Integrated-Circuit Antennas*, New York, NY/USA: Academic, 1983.
- [6] M. Singer, A. Stiller, K. M. Strohm, J. -F. Luy, and E. M. Biel, "A SIMMWIC 76 GHz front-end with high polarization purity," in *1996 IEEE MTT-S Int. Microwave Sym. Dig.*, Philadelphia, PA, June 1996, pp. 1079-1082.
- [7] G. P. Gauthier, J. -P. Raskin, L. P. B. Katehi, and G. M. Rebeiz, "A 94 GHz aperture-coupled micromachined microstrip antenna," *IEEE Transaction on Antennas Propagation* , vol. 47, no. 12, pp. 1761-1766, Dec. 1999.
- [8] M. M. Tentzeris, J. Laskar, J. Papapolymerou, D. Thompson, S. Pinel, R. L. Li, J. H. Lee, G. DeJean, S. Sarkar, R. Pratap, R. Bairavasubramanian and N. Papageorgiou, "RF SOP for multi-band RF and millimeter-wave systems," *Advanced Packaging Magazine*, pp. 15-16, April 2004.
- [9] D. C. Thompson, O. Tantot, H. Jallageas, G. E. Ponchak, M. M. Tentzeris and J. Papapolymerou, "Characterization of Liquid Crystal Polymer (LCP) Material and Transmission Lines on LCP Substrates from 30-110 GHz," *IEEE Transactions on Microwave Theory and Techniques*, vol.52, no.4, pp.1343-1352, April 2004.
- [10] J.Lee, K.Lim, S.Pinel, G.DeJean, R.L.Li, C.-H.Lee, M.F.Davis, M.Tentzeris, and J.Laskar, "Advanced System-on-Package (SOP) Multilayer Architectures for RF/Wireless Systems up to Millimeter-Wave Frequency Bands," in *Proc. Asian Pacific Microwave Conference*, Seoul, Korea, Nov. 2003, pp. FA5_01.
- [11] V.Kondratyev, M.Lahti, and T.Jaakola, "On the design of LTCC filter for millimeter-waves," in *2003 IEEE MTT-S Int. Microwave Sym. Dig.*, Philadelphia, PA., June 2003, pp. 1771-1773.

- [12] R.L.Li, G.DeJean, M.M.Tentzeris, J.Laskar, and J.papapolymerou, "LTCC Multilayer based CP Patch Antenna Surrounded by a Soft-and-Hard Surface for GPS Applications," in *2003 IEEE-APS Symposium*, Columbus, OH, June 2003, pp.II.651-654.
- [13] C.H.Lee, A.Sutono, S.Han, K.Lim, S.Pinel, J.Laskar, and E.M.Tentzeris, "A Compact LTCC-based Ku-band Transmitter Module," *IEEE Transactions on Advanced Packaging*, Vol.25, No.3, , Aug. 2002, pp.374-384.
- [14] Y.Rong, K.A.Zaki, M.Hageman, D.Stevens, and J.Gipprich, "Low-Temperature Cofired Ceramic (LTCC) Ridge Waveguide Bandpass Chip Filters," *IEEE Transaction on Microwave Theory and Technique*, Vol. 47, No. 12, pp. 2317-2324, Dec. 1999.
- [15] Yong Huang, "A Broad-Band LTCC Integrated Transition of Laminated Waveguide to Air-Filled Waveguide for Millimeter-Wave Applications," *IEEE Transaction on Microwave Theory and Technique*, Vol. 51, No. 5, pp. 1613-1617, May 2003.
- [16] W.-Y.Leung, K.-K.M.Cheng, and K.-L.Wu, "Multilayer LTCC Bandpass Filter Design with Enhanced Stopband Characteristics," *IEEE Microwave and Wireless Components Letters*, Vol.12, No. 7, pp. 240-242, May 2002.
- [17] Y. Rong, K.A.Zaki, M.Hageman, D.Stevens, and J.Gipprich, "Low Temperature Cofired Ceramic (LTCC) Ridge Waveguide Multiplexers," in *2000 IEEE MTT-S Int. Microwave Sym. Dig.*, Boston, MA., June 2000, pp. 1169-1172.
- [18] R.Lucero, W.Qutteneh, A.Pavio, D.Meyers, and J.Estes, "Design of An LTCC Switch Diplexer Front-End Module for GSM/DCS/PCS Application," in *2001 IEEE Radio Frequency Integrated Circuit Sym.*, Phoenix, AZ., May 2001, pp. 213-216.
- [19] C.H.Lee, A.Sutono, S.Han, K.Lim, S.Pinel, J.Laskar, and E.M.Tentzeris, "A Compact LTCC-based Ku-band Transmitter Module," *IEEE Transactions on Advanced Packaging*, Vol.25, No.3, pp.374-384, Aug. 2002.
- [20] B.G.Choi, M.G.Stubbs, and C.S.Park, "A Ka-Band Narrow Bandpass Filter Using LTCC Technology," *IEEE Microwave and Wireless Components Letters*, Vol.13, No.9, pp. 388-389, Sep. 2003.
- [21] V.Piatnitsa, E. Jakku, and S.Leppaevuori, "Design of a 2-Pole LTCC Filters for Wireless Communications," *IEEE Transactions on Wireless Communications*, Vol.3, No.2, Mar. 2004, pp. 379-381.
- [22] M.J.Hill, R.W.Ziolkowski, and J.Papapolymerou, "Simulated and Measured Results from a Duroid-Based Planar MBG Cavity Resonator Filter," *IEEE Microwave and Wireless Components Letters*, Vol.10, No.12, pp. 528-530, Dec. 2000.

- [23] H.-J.Hsu, M.J.Hill, J.Papapolymerou, and R.W.Ziolkowski, "A Planar X-Band Electromagnetics Band-Gap (EBG) 3-Pole Filter," *IEEE Microwave and Wireless Components Letters*, Vol.12, No.7, pp. 255-257, July 2002.
- [24] C.A.Tavernier, R.M.Henderson, and J.Papapolymerou, "A Reduced-Size Silicon Micromachined High-Q Resonator at 5.7 GHz," *IEEE Transaction on Microwave Theory and Technique*, Vol. 50, NO. 10, pp. 2305-2314, Oct. 2002.
- [25] A.El-Tager, J.Bray, and L.Roy, "High-Q LTCC Resonators For Millimeter Wave Applications," in *2003 IEEE MTT-S Int. Microwave Sym. Dig*, Philadelphia, PA., June 2003, pp. 2257-2260.
- [26] P.Ferrand, D.Baillargeat, S.Verdeyme, J.Puech, M.Lahti, and T.Jaakola, "LTCC reduced-size bandpass filters based on capacitively loaded cavities for Q band application," in *2005 IEEE MTT-S Int. Microwave Sym. Dig*, Long Beach, CA., June 2005, pp. 1789-1792.
- [27] X.Gong, W.J.Chappell, and L.P.B.Katehi, "Multifunctional Substrates For High-Frequency Applications," *IEEE Microwave and Wireless Components Letters*, Vol.13, No.10, pp. 428-430, Oct. 2003.
- [28] M.Ito, K.Marubishi, K.Ikuina, T.Hashiguchi, S.Iwanaga, and K.Ohata, "60-GHz-band Dielectric Waveguide Filters with Cross-coupling for Flip-chip Modules," in *2002 IEEE MTT-S Int. Microwave Sym. Dig*, Seattle, WA., June 2002, pp. 1789-1792.
- [29] Y.C.Lee, W.-I.Chang, Y.H.Cho, and C.S.Park, "A Very Compact 60GHz Transmitter Integrating GaAs MMICs on LTCC Passive Circuits for Wireless Terminals Applications," in *2004 IEEE MTT-S Int. Microwave Sym. Dig*, Fort Worth, TX., Oct. 2004, pp. 313-316.
- [30] K.Ohata, T.Inoue, M.Funabashi, A.Inoue, Y.Takimoto, T.Kuwabara, S.Shinozaki, K.Marubishi, K.Hosaya, and H.Nagai, "Sixty-GHz-Band Ultra-Miniature Monolithic T/R Modules for Multimedia Wireless Communication Systems," *IEEE Transaction on Microwave Theory and Technique*, vol.44, no. 12, pp. 2354-2360, Dec. 1996.
- [31] K.Ohata, K.Marubishi, M.Ito, S.Kishimoto, K.Ikuina, T.Hashiguchi, K.Ikeda, and N.Takahashi, "1.25 Gbps Wireless Gigabit Ethernet Link at 60 GHz-Band," in *2003 IEEE MTT-S Int. Microwave Sym. Dig*, Philadelphia, PA, June 2003, pp. 373-376.
- [32] J.Mizoe, S.Amano, T.Kuwabara, T.Kaneko, K.Wada, A.Kato, K.Sato, and M.Fujise, "Miniature 60 GHz Transmitter/Receiver Modules on AlN Multi-Layer High Temperature Co-Fired Ceramic," in *1999 IEEE MTT-S Int. Microwave Sym. Dig*, Anaheim, CA, June 1999, pp. 475-478.
- [33] A.Tavakoli, N.Darmvandi, and R.M.Mazandaran, "Analysis of cross-shaped dual-polarized microstrip patch antennas," in *1995 IEEE AP-S Int. Sym. Dig.*, Newport Beach, CA., June 1995, pp. 994 – 997.

- [34] M. F. Davis, A. Sutono, A. Obatoyinbo, S. Chakraborty, K. Lim, S. Pinel, J. Laksar, and R. Tummala, "Integrated RF architectures in fully-organic SOP technology," in *Proc. 2001 IEEE EPEP Topical Meeting*, Boston, MA, Oct. 2001, pp. 93-96.
- [35] K. Lim, A. Obatoyinbo, M. F. Davis, J. Laksar, and R. Tummala, "Development of planar antennas in multi-layer package for RF-system-on-package applications," in *Proc. 2001 IEEE EPEP Topical Meeting*, Boston, MA, Oct. 2001, pp. 101-104.
- [36] M. F. Davis, A. Sutono, K. Lim, J. Laksar, V. Sundaram, J. Hobbs, G. E. White, and R. Tummala, "RF-microwave multi-layer integrated passives using fully organic system-on-package (SOP) technology," in *Proc. 2001 IEEE International Microwave Symposium*, vol. 3, Phoenix, AZ, May 2001, pp. 1731-1734.
- [37] J. M. Hobbs, S. Dalmia, V. Sundaram, L. Wan, W. Kim, G. White, M. Swaminathan, and R. Tummala, "Development and characterization of embedded thin-film capacitors for mixed signal applications on fully organic system-on-package technology," in *Proc. IEEE 2002 Radio and Wireless Conference, RAWCON 2002*, Boston, MA, Aug. 2002, pp. 201-204.
- [38] R. Ulrich and L. Schaper, Eds., *Integrated Passive Component Technology*: IEEE Press/Wiley, 2003.
- [39] J. Laksar, M. Tentzeris, K. Lim, S. Pinel, M. Davis, A. Rhagavan, M. Maeng, S. -W. Yoon, and R. Tummala, "Advanced system-on-package RF front-ends for emerging wireless communications," in *Proc. 2002 Asian-Pacific Microwave Symposium*, Kyoto, Japan, Nov. 2002, pp. III. 1703-1708.
- [40] M. M. Tentzeris, J. Laskar, J. Papapolymerou, S. Pinel, V. Palazzari, R. Li, G. DeJean, N. Papageorgiou, D. Thompson, R. Bairavasubramanian, S. Sarkar, J. -H. Lee, "3-D-integrated RF and millimeter-wave functions and modules using liquid crystal polymer (LCP) system-on-package technology," *IEEE Transaction on Advanced Packaging*, vol. 27, no. 2, pp. 332-340, May 2004.
- [41] K. Lim, A. Obatoyinbo, A. Sutuno, S. Chakraborty, C. Lee, E. Gebara, A. Raghavan, and J. Laskar, "A highly integrated transceiver module for 5.8 GHz OFDM communication system using multi-layer packaging technology," in *IEEE MTT-S Int. Microwave Symp, Dig.*, vol. 1, 2001, pp. 65-68.
- [42] W. Diels, K. Vaesen, K. Wambacq, P. Donnay, S. De Raedt, W. Engels, and M. Bolsens, "A single-package integration of RF blocks for a 5 GHz WLAN application," *IEEE Trans. Comp. Packaging. Technol. Adv. Packag.* pt. B, vol. 24, Aug. 2001, pp. 384-391.
- [43] P. G. Barnwell and L. Wood, "A novel thick-film on ceramic MCM technology offering MCM-D performance," in *6th International Conf. on MCMs*, Denver, CO, 1997, pp. 48-52.

- [44] P. G. Barnwell, C. E. Free, and C. S. Aitchison, "A novel thick-film on ceramic microwave technology," in *Proc. 1998 Asian-Pacific Microwave Symposium*, Yokohama, Japan, Dec. 1998, pp. 189-192.
- [45] B. Geller, B. Thaler, A. Fathy, M. J. Liberatore, H. D. Chen, G. Ayers, V. Pendrick, and Y. Narayan, "LTCC-M: An enabling technology for high performance multilayer RF systems," in *IEEE MTT-S Int. Microwave Symp., Dig.*, Anaheim, CA, June 1999, pp. 189-192.
- [46] D.M.Pozar, *Microwave Engineering*, 2nd ed. New York:Wiley, 1998.
- [47] M. Ito, K. Maruhashi, K. Ikuina, T. Hashiguchi, S. Iwanaga, and K. Ohata, "A 60-GHz-band planar dielectric waveguide filter for flip-chip modules," *IEEE Transaction on Microwave Theory and Technique*, vol.49, no. 12, pp. 2431-2436, Dec. 2001.
- [48] D.M.Pozar and D.H.Schauber, *Microstrip Antennas*, Piscataway, NJ/U.S.A.:IEEE press, 1995.
- [49] Robert E. Collin, *Foundations for Microwave Engineering*, New York, NY/U.S.A: McGraw Hill, 1992.
- [50] Y.Rong, K.A.Zaki, M.Hageman, D.Stevens, and J.Gipprich, "Low Temperature Cofired Ceramic (LTCC) Ridge Waveguide Multiplexers," in *2000 IEEE MTT-S Int. Microwave Sym. Dig.*, Boston, MA., June 2000, pp. 1169-1172.
- [51] Wojciech Wiatr, "Coplanar-Waveguide-to-Microstrip Transition Model," in *2000 IEEE MTT-S Int. Microwave Sym. Dig*, Boston, MA., June 2000, pp. 1797-1800.
- [52] J.-S.Hong and M.J.Lancaster, "Coupling of microstrip square open-loop resonators for cross-coupled planar microwave filters," *IEEE Transaction on Microwave Theory and Technique*, Vol. 44, No. 12, pp. 2099-2109, Dec. 1996.
- [53] J.-S.Hong and M.J.Lancaster, "Design of Highly Selective Microstrip Bandpass Filters with a Single Pair of Attenuation Poles at Finite Frequencies," *IEEE Transactions on Microwave Theory and Techniques*, vol.48, pp. 1098-1107, July 2000.
- [54] J.-G.Yook, N.I.Dib, and L.P.B.Katehi, "Characterization of High Frequency Interconnects Using Finite Difference Time Domain and Finite Element Methods," *IEEE Transactions on Microwave Theory and Techniques*, vol.42, pp. 1727-1736, Sept. 1994.
- [55] Y. Cassivi and K.Wu, "Low Cost Microwave Oscillator Using Substrate Integrated Waveguide Cavity," *IEEE Microwave and Wireless Components Letters*, Vol.13, No.2, pp. 48-50, Feb. 2003.
- [56] J.-S. Hong and M.J.Lancaster, *Microstrip Filters for RF/Microwave Applications*, New York, NY/U.S.A: John Wiley & Sons, Inc., 2001.

- [57] J.-H.Lee, S.Pinel, J.Papapolymerou, J.Laskar, and M.M.Tentzeris, "Low Loss LTCC Cavity Filters Using System-on-Package Technology at 60 GHz," *IEEE Transaction on Microwave Theory and Technique*, vol. 53, no. 12, pp. 231-244, Dec. 2005.
- [58] J.Heyen, A.Gordiyenko, P.Heide and A.F.Jacob, "Vertical Feedthroughs for Millimeter-Wave LTCC Modules," in *2003 IEEE European Microwave Conference*, Munich, Germany, Oct. 2003, pp. 411-414.
- [59] J.-H.Lee, N.Kidera, G.DeJean, S.Pinel, J.Laskar, and M.M.Tentzeris, "A V-band front-end with 3-D integrated cavity filters/duplexers and antenna in LTCC technologies," *IEEE Transaction on Microwave Theory and Technique*, vol.54, no. 7, pp. 2925-2236, July 2006
- [60] H.-C.Chang, K.A.Zaki, "Evanescent-mode coupling of dual-mode rectangular waveguide filters," *IEEE Transaction on Microwave Theory and Technique*, vol.39, no. 8, pp. 1307-1312, Aug. 1991.
- [61] K.Sano and M.Miyashita, "Application of the planar I/O terminal to dual-mode dielectric-waveguide filters," *IEEE Transaction on Microwave Theory and Technique*, vol.48, no. 12, pp. 2491-2495, Dec. 2000.
- [62] A.I.Atia and A.E.Williams, "Narrow-bandpass waveguide filters," *IEEE Transaction on Microwave Theory and Technique*, vol. MTT-20, no. 4, pp. 258-265, April 1972.
- [63] A.I.Atia and A.E.Williams, "Nonminimum-phase optimum-amplitude bandapss waveguide filters," *IEEE Transaction on Microwave Theory and Technique*, vol. MTT-22, no. 4, pp. 425-431, April 1974.
- [64] D.Deslandes and K.Wu, "Substrate Integrated Waveguide Dual-Mode Filters for Broadband Wireless Systems," in *2003 Radio and Wireless Conf.*, Boston, MA, Aug. 2003, pp. 385-388.
- [65] M.Guglielmi, P.Jarry, E.Kerherve, O.Roquerbrun, and D.Schmitt "A new family of all-inductive dual-mode filters," *IEEE Transaction on Microwave Theory and Technique*, vol. 49, no. 10, pp. 1764-1769, Oct. 2001.
- [66] P.Savi, D.Trincherro, R.Tascone, and R.Orta "A new approach to the design of dual-mode rectangular waveguide filters with distributed coupling," *IEEE Transaction on Microwave Theory and Technique*, vol. 45, no. 2, pp. 221-228, Feb. 1997.
- [67] J.-F.Liang, X.-P.Liang, K.A.Zaki, and A.E.Atia "Dual-mode dielectric or air-filled rectangular waveguide filters," *IEEE Transaction on Microwave Theory and Technique*, vol. 42, no. 7, pp. 1330-1336, July. 1994.
- [68] A.E.Williams and A.E.Atia, "Dual-mode canonical waveguide filters," *IEEE Transaction on Microwave Theory and Technique*, vol. MTT-25, no. 12, pp. 1021-1026, Dec 1977.

- [69] C.Kdsia, R.Cameron, and W.-C.Tang, "Innovations in microwave filters and multiplexing networks for communications satellite systems," *IEEE Transaction on Microwave Theory and Technique*, vol. 40, no. 6, pp. 1133-1149, June 1992.
- [70] L.Accatino, G.Bertin, and M.Mongiardo, "Elliptical cavity resonators for dual-mode narrow-band filters," *IEEE Transaction on Microwave Theory and Technique*, vol. 45, no. 12, pp. 2393-2401, Dec. 1997.
- [71] A.E.Williams, "A Four-Cavity Elliptic Waveguide Filter," *IEEE Transaction on Microwave Theory and Technique*, vol. MTT-18, no. 12, pp. 1109-1114, Dec. 1970.
- [72] I.Awai, A.C.Kundu, and T.Yamashita, "Equivalent-circuit representation and explanation of attenuation poles of a dual-mode dielectric-resonator bandpass filter," *IEEE Transaction on Microwave Theory and Technique*, vol. 46, no. 12, pp. 2159-2163, Dec. 1998.
- [73] M.Sagawa, K.Takahashi, and M.Makimoto, "Miniaturized hairpin resonator filters and their application to receiver front-end MIC's," *IEEE Transaction on Microwave Theory and Technique*, vol. 37, no. 12, pp. 1991-1997, May 1989.
- [74] K.A.Zaki, C.Chen, and A.E.Atia, "A circuit model of probes in dual-mode cavities," *IEEE Trans. Microwave Theory Tech.*, vol. 36, pp. 1740-1746, Dec. 1988.
- [75] J.B.Thomas, "Cross-coupling in coaxial cavity filters – a tutorial overview," *IEEE Transaction on Microwave Theory and Technique*, vol. 51, no. 4, pp. 1368-1376, April 2003.
- [76] L.K.Yeung and K.-L.Wu, "A compact second-order LTCC bandpass filter with two finite transmission zeros," *IEEE Transaction on Microwave Theory and Technique*, vol. 51, no. 2, pp. 337-341, Feb. 2003.
- [77] F.Purroy and L.Pradell, "New theoretical analysis of the LRRM calibration technique for vector network analyzers," *IEEE Transaction on Instrumentation and Measurement*, vol. 50, issues 5, pp. 1307-1314, Oct. 2001.
- [78] M. J. Vaughan, K. Y. Hur, and R. C. Compton, "Improvement of microstrip patch antenna radiation patterns," *IEEE Trans. Antennas Propagat.*, vol. 42, no. 6, pp. 882-885, June 1994.
- [79] R. Gonzalo, P. de. Maagt, and M. Sorolla, "Enhanced patch-antenna performance by suppressing surface waves using photonic-bandgap substrates," *IEEE Trans. Microwave Theory Tech.*, vol. 47, no. 11, pp. 2131-2138, Nov. 1999.
- [80] R. Coccioli, F.-R. Yang, K.-P. Ma, and T. Itoh, "Aperture-coupled patch antenna on UC-PBG substrate," *IEEE Trans. Microwave Theory Tech.*, vol. 47, no. 11, pp. 2123-2130, Nov. 1999.

- [81] R. L. Li, G. DeJean, J. Papapolymerou, J. Laskar, and M. M. Tentzeris, "Radiation-pattern improvement of patch antennas on a large-size substrate using a compact soft surface structure and its realization on LTCC multilayer technology," *IEEE Trans. Antennas and Propagation*, vol. 53, no. 1, pp. 200-208, Jan. 2005.
- [82] M. Tentzeris, R. L. Li, K. Lim, M. Maeng, E. Tsai, G. DeJean, and J. Laskar, "Design of compact stacked-patch antennas on LTCC technology for wireless communication applications," *Proceedings of IEEE Antenna and Propagation Society International Symposium*, vol. 2, pp. 500-503, June 2002.
- [83] C. Balanis, *Antenna Theory*. Canada: John Wiley & Sons, Inc, 1997.
- [84] P.F.M. Smulder, "Exploiting the 60 GHz Band for Local Wireless Multimedia Access: Prospects and Future Directions," *IEEE Communications Magazine*, vol. 40, pp. 140-147, Jan. 2002.
- [85] L. Xue, C. C. Liu, H.-S. Kim, and S. Tiwari, "Three-dimensional integration: technology, use, and issues for mixed-signal applications," *IEEE Trans. on Electron Devices*, vol. 50, no. 3, pp. 601-608, Mar. 2003.
- [86] S. Kawamura, N. Sasaki, I. Iwai, M. Nakano, and M. Takagi, "Three-dimensional CMOS IC's fabricated by using beam recrystallization," *IEEE Electron Device Lett.*, vol. EDL-4, pp. 601-608, Mar. 2003.
- [87] Y. Akasaka and T. Nishimura, "Concept and basic technologies for 3-D IC structure," in *IEDM Tech. Dig.*, 1986, pp. 488-491.
- [88] T. Kunio, K. Oyama, Y. Hayashi, and M. Morimoto, "Three-dimensional IC's, having four stacked active device layers," in *IEDM Tech. Dig.*, 1989, pp. 837-840.
- [89] K. Yamazaki, Y. Itoh, A. Wada, K. Morimoto, and Y. Tomita, "4-layer 3-D IC technologies for parallel signal processing," in *IEDM Tech. Dig.*, 1990, pp. 599-602.
- [90] K. W. Lee, T. Nakamura, T. Ono, Y. Yamada, T. Mizukusa, H. Hashimoto, K. T. Park, H. Kurino, and M. Koyanagi, "Three-dimensional shared memory fabricated using wafer stacking technology," in *IEDM Tech. Dig.*, 2000, pp. 165-168.
- [91] M. B. Kleiner, S. A. Kuhn, P. Ramm, and W. Weber, "Performance improvement of the memory hierarchy of RISC-systems by application of 3-D technology," *IEEE Trans. on Comp. Packag. Manufact. Technol.*, vol. 19, pp. 709-718, Nov. 1996.
- [92] R. L. V. Tuyl, "Unlicensed millimeter wave communications: A new opportunity for MMIC technology at 60 GHz," in *IEEE GaAs IC Symp.*, 1996, pp. 3-5.
- [93] H. Daembkes, "GaAs MMIC based components and frontends for millimeter-wave communication and sensor system," in *Microwave Sys. Conf.*, 1995, pp. 83-86.

- [94] S. Reynolds, "60 GHz transceiver circuits in SiGe Bipolar Technology," in *IEEE Int'l Solid-State Circuits Conf. Dig. Tech. Papers*, Feb. 2004, pp. 442-443.
- [95] T. Yao, M. Q. Gordon, K. K. W. Tang, K. H. K. Yau, M.-T Yang, P. Schvan, S. P. Voinigescu, "Algorithmic design of CMOS LNAs and PAs for 60-GHz radio," *IEEE Journal of Solid-State Circuit*, vol. 42, no. 5, pp. 1044-1057, May 2007.
- [96] B. Razavi, "A 60-GHz CMOS receiver front-end," *IEEE Journal of Solid-State Circuit*, vol. 41, no. 1, pp. 17-22, Jan. 2006.
- [97] V. A. Chiriac and T. -Y. T. Lee, "Thermal assessment of RF-integrated LTCC front end modules," *IEEE Trans. on Adv. Packag.*, vol. 27, no. 3, pp. 545-557, Aug. 2004.